Western Graduate&PostdoctoralStudies

Western University
Scholarship@Western

Electronic Thesis and Dissertation Repository

4-26-2012 12:00 AM

New Mechatronic Systems for the Diagnosis and Treatment of Cancer

Jeffrey S. Bax
The University of Western Ontario

Supervisor
Dr. Aaron Fenster
The University of Western Ontario

Graduate Program in Biomedical Engineering
A thesis submitted in partial fulfillment of the requirements for the degree in Doctor of Philosophy
© Jeffrey S. Bax 2012

Follow this and additional works at: https://ir.lib.uwo.ca/etd

Part of the Biomedical Engineering and Bioengineering Commons

Recommended Citation
Bax, Jeffrey S., "New Mechatronic Systems for the Diagnosis and Treatment of Cancer" (2012). *Electronic Thesis and Dissertation Repository*. 522.
https://ir.lib.uwo.ca/etd/522

This Dissertation/Thesis is brought to you for free and open access by Scholarship@Western. It has been accepted for inclusion in Electronic Thesis and Dissertation Repository by an authorized administrator of Scholarship@Western. For more information, please contact wlswadmin@uwo.ca.

NEW MECHATRONIC SYSTEMS FOR THE DIAGNOSIS AND TREATMENT OF CANCER

(Spine title: Mechatronic Systems for the Diagnosis and Treatment of Cancer)

(Thesis format: Integrated Article)

by

Jeffrey Scott Bax

Graduate Program in Biomedical Engineering

A thesis submitted in partial fulfillment
of the requirements for the degree of
Doctor of Philosophy

The School of Graduate and Postdoctoral Studies
The University of Western Ontario
London, Ontario, Canada

© Jeffrey Bax 2012

THE UNIVERSITY OF WESTERN ONTARIO
School of Graduate and Postdoctoral Studies

CERTIFICATE OF EXAMINATION

Supervisor	Examiners
Dr. Aaron Fenster	Dr. Maria Drangova
Supervisory Committee	Dr. Grace Parraga
Dr. Terry Peters	Dr. Kathleen Surry
Dr. Cesare Romagnoli	Dr. Ivan Yeung

The thesis by

Jeffrey Scott Bax

entitled:

A New Generation of Mechatronic Systems for the Diagnosis and Treatment of Cancer

is accepted in partial fulfillment of the
requirements for the degree of
Doctor of Philosophy

Date	Chair of the Thesis Examination Board

Abstract

Both two dimensional (2D) and three dimensional (3D) imaging modalities are useful tools for viewing the internal anatomy. Three dimensional imaging techniques are required for accurate targeting of needles. This improves the efficiency and control over the intervention as the high temporal resolution of medical images can be used to validate the location of needle and target in real time. Relying on imaging alone, however, means the intervention is still operator dependant because of the difficulty of controlling the location of the needle within the image. The objective of this thesis is to improve the accuracy and repeatability of needle-based interventions over conventional techniques: both manual and automated techniques.

In this thesis, I propose that by combining the remote center of motion concept using spherical linkage components into a passive or semi-automated device, the physician will have a useful tracking and guidance system at their disposal in a package, which is less threatening than a robot to both the patient and physician. This design concept offers both the manipulative transparency of a freehand system, and tremor reduction through scaling currently offered in automated systems. In addressing each objective of this thesis, a number of novel mechanical designs incorporating an remote center of motion architecture with varying degrees of freedom have been presented. Each of these designs can be deployed in a variety of imaging modalities and clinical applications, ranging from preclinical to human interventions, with an accuracy of control in the millimeter to sub-millimeter range.

Keywords

Percutaneous needle intervention; image guided intervention; medical robotics; small animal imaging; ultrasound guidance; x-ray micro-computed tomography; three-dimensional imaging; and image registration.

Co-Authorship Statement

Chapter 2 was published in Medical Physics as: Jeffrey Bax, Derek Cool, Lori Gardi, Kerry Knight, David Smith, Jacques Montreuil, Shi Sherebrin, Cesare Romagnoli, Aaron Fenster, "Mechanically Assisted 3D Ultrasound Guided Prostate Biopsy System", *Med Phys*., vol 35, no 12, pp 5397-5410, 2008. I designed and calibrated the mechanical tracking device and spring loaded counterbalance, which was manufactured by our laboratory machinists, Mr. Jacques Montreuil and Mr. Kevin Barker. Mr. David Smith was responsible for designing the hydraulic stabilizer and cart restraint system to which the tracking apparatus was attached. I solved the kinematics and Mr. Shi Sherebrin developed the control software for the system. In addition, Shi designed and constructed the electric hardware with the assistance of our electrician, Mr. Janos Bartha. Ms. Lori Gardi developed the software for the image reconstruction and visualization. Dr. Derek Cool developed the methods and software to collect and characterize the systems performance, and carried out the analysis, while Lori Gardi and I performed the experiments. The clinical studies performed using the system was in collaboration with the London Health Sciences Center (University Hospital): Dr. Cesare Romagnoli, performed the biopsy procedures and assisted in the design of the clinical prototype. The work presented in this chapter was performed under the supervision of Dr. Aaron Fenster.

Chapter 3 was published in Medical Physics as: Jeffrey Bax, David Smith, Laura Bartha, Jacques Montreuil, Shi Sherebrin, Lori Gardi, Chandima Edirisinghi, Aaron Fenster, "A Compact Mechatronic System for 3D Guided Prostate Interventions", *Med Phys*., vol 38, no 2, pp 1055-69, 2011. I designed, calibrated and performed all of the experiments with the prototype mechatronic device. With the assistance of Mr. David Smith and Mr Jacques Montreuil, we constructed the first prototype device. The system components were manufactured by Mr. Jacques Montreuil with the assistance of Mr. Kevin Barker. I developed the kinematic control software for the system with help from Mr. Shi Sherebrin. Shi designed and constructed the electric hardware with the assistance of our electrician, Mr. Janos Bartha. Dr. Chandima Edirisinghi and Ms. Lori Gardi developed the software for dosimetry planning, image reconstruction, dynamic dosimetry re-planning, and needle placement verification. I was responsible developing the methods and Ms. Laura Bartha was responsible for developing the software to collect, register, and characterize the systems performance by carrying out the analysis. I worked on this project under the supervision of Dr. Aaron Fenster.

Chapter 4 was submitted to Medical Physics with the author list: Christopher Waring, Jeffrey S. Bax, Amila Samarabandu, David W. Holdsworth, James C. Lacefield and Aaron Fenster. I designed and constructed the calibration phantom. I also developed the method to measure the calibration phantom to a traceable standard. The construction and measurement of the phantom was completed by me with assistance from the laboratory machinists Mr. Jacques Montreil and Mr. Kevin Barker. Mr. Chris Warring developed the algorithm and software for processing the micro-CT images of the phantom to characterize the scanner geometric accuracy. Mr. Amila Samarbandu a summer research assistant, assisted in the development of the software. Chris was responsible for collecting images of the phantom and performing all image analysis. The work presented in this chapter was performed under the supervision of Drs. David W. Holdsworth, James C. Lacefield and Aaron Fenster.

Chapter 5 is to be submitted to Medical Physics with author list: Jeffrey S. Bax, Christopher Waring, Shi Sherebrin, Shawn Stapleton, James C. Lacefield and Aaron Fenster. For this study, I designed and calibrated the prototype robotic device that was constructed by our laboratory machinists, Jacques Montreuil and Kevin Barker. I developed the kinematic control software for the robot and Shi Sherebrin coded the kinematics. Shi designed and constructed the electric hardware with the assistance of our electrician, Janos Bartha. I developed the calibration methods and Chris developed the registration methods and software. Chris developed the methods and software to collect, register, and characterizes the systems performance by carrying out the analysis. I performed the experiments to characterize the systems performance. Shawn acquired all of the CT images and in addition, designed and performed the animal experiments. I worked on this project under the supervision of James C. Lacefield and Aaron Fenster.

Acknowledgments

I would like to acknowledge the many people who have contributed to my education, and offered their support and guidance during my time at Robarts Research Institute at The University of Western Ontario.

First, I would like to thank my supervisor Dr. Aaron Fenster for his support and guidance throughout this project. I would also like to thank my clinical collaborators and advisors on this project, Drs. Cesare Romagnoli, David DSouza, Nikhilesh Patil, and Terry Peters for serving on my advisory committee and offering many helpful suggestions.

Special thanks to my colleagues in the Graduate Program in Biomedical Engineering: Ms. Diana Timmermans and Ms. Kayley Ma. I would also like to thank the many individuals from the Fenster group including the technical staff: Mr. Jacques Montreuil, Mr. Kevin Barker, Ms. Lori Gardi, Dr. Chandima Edirisinghi, Dr. Igor Gyacskov, Mr. Shi Sherebrin, Mr. Kerry Knight, Mr. David Tessier, Mr. Adam Krasinski, and Ms. Kimbery Perry.

I have been financially supported by a Canada Graduate Scholarship from the Natural Sciences and Engineering Research Council of Canada.

Table of Contents

List of Tables

List of Figures

List of Appendices

Chapter 1

1 Introduction

1.1 Mechatronic Surgical Assistants

Since the introduction of the Horsley and Clarke apparatus in 1908[1], considerable effort has been devoted to the development of image-guided systems that are more user friendly. Based on the idea that the physician using the system should be inconvenienced to a bare minimum, a great deal of effort has been devoted to developing systems that provide the surgeons with a new set of tools to extend their ability and perform more complex tasks.

With the rapid development of computing power, coupled with improvements in imaging modalities, a number of new products offering varying levels of automation are evolving. Table 1.1 is a summary of some of the systems that are in routine clinical and preclinical use today. Commercially available image-guided systems available to researchers and healthcare workers vary in automation from freehand tracking devices to fully automated systems that can perform preprogrammed tasks, like the Cyberknife (Sunnyvale, CA), or telesurgical systems like the da Vinci robot (Sunnyvale, CA) where the physician controls the robot remotely.

1.1.1 Freehand Surgical Navigation Systems

One method to link the current orientation of the tool to the image is to use frameless stereotaxy. This involves attaching a tracking device to the surgical tool, like electromagnetic, optical or sonic transmitters.[14] Once the tracking system is registered to the image, a computer provides real-time visual feedback of the tool in the image to assist in needle or tool placement. The primary advantage of this type of navigation system is that the physician can perform the intervention without compromising his/her dexterity and natural haptic feedback, making this a simple and feasible option for procedures like needle-guided interventions.[14]

Table 1.1: A summary of computer-assisted surgical tracking systems.

System Name	**Institution**	**Subject**	**Mount**	**Type**
AESOP[2]	Computer Motion	Human	Cart	Serial link robot
Cyberknife[3]	Accuray	Human	Floor	Serial link robot
da Vinci[4]	Intuitive Surgical	Human	Cart	Bar type parallelogram RCM telerobotic system
Neuro Mate[5]	Integrated Surgical Systems	Human	Cart	Serial link robot
PinPoint[6]	Philips	Human	Ceiling	Passive serial linkr
ROBODOC[7]	Integrated Surgical Systems	Human	Floor and Patient	Serial link robot
RX-90[8]	ortoMarquet	Animal	Floor	Serial link robot
SurgiScope[9]	Humboldt University	Human Animal	Ceiling	Parallel robot
Zeus[10]	Computer Motion	Human	Patient Bed	Telerobotic system
Micron Tracker[11]	Claron Technology Inc.	Human	Freehand	Optical Video-metric
Polaris[12]	Northern Digital Inc.	Human	Freehand	Optical Active/Passive
Aurora[12]	Northern Digital Inc.	Human	Freehand	Electromagnetic
microBIRD[13]	Ascension Technology Corp.	Human	Freehand	Electromagnetic

There are two different types of freehand tracking systems commercially available: optical, and electromagnetic.[14] Optical tracking systems identify marker patterns using charge-coupled device (CCD) images from two different viewpoints to triangulate the tool location in space (see Figure 1.1). Because of their high accuracy and large field of view, these systems can be adapted easily into a large number of clinical applications. However, the line of sight between the markers and at least two CCD cameras must be maintained at all times. This limits its use to procedures where at least a portion of the tool is outside the patient's body. Optical trackers commercially available today include the videometric system available from Claron Technology Inc. (Toronto, Canada),[11] and the active/passive infrared system from Northern Digital (Waterloo, Canada).[12]

Another method for tracking tools inside the patient is to use an electromagnetic tracking device. Electromagnetic systems use pulsed field generators to track the position of miniature field sensors about the size of a grain of rice (see Figure 1.2). Northern Digital (Waterloo, Canada)[12] and Ascension Technology (Burlington, Vermont)[13] offer electromagnetic tracking systems for a variety of medical applications.

Figure 1.1: Photograph of an infrared optical tracking system from Northern Digital. The three optical markers attached to the tool are imaged from two different angles to determine its position.

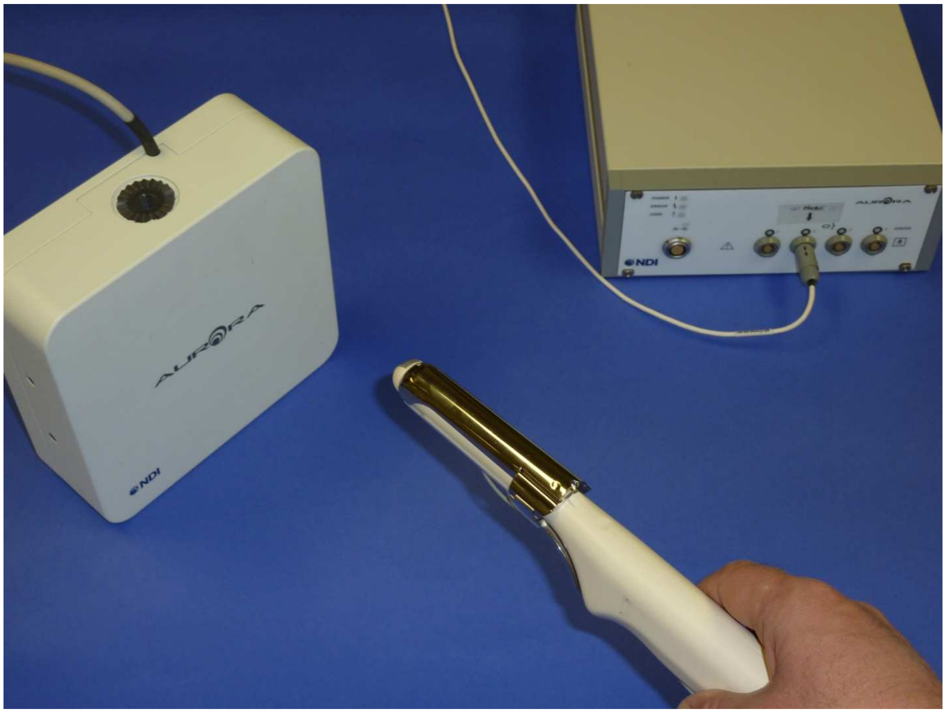

Figure 1.2: Photograph of an electromagnetic tracking system from Northern Digital. The position of the ultrasound probe is tracked using a small coil of wire mounted near the tip of the probe.

1.1.2 Passive and Semi-automated Devices for Needle placement

Although few researchers have proposed the use of passive or semi-automated devices for needle placement, these systems offer an effective alternative for needle interventions in ultrasound,[15-17] CT[18-20] and MRI[21]. These designs are based on an early form of a freehand tracking system where articulated arms of various configurations determine the position of the tool tip by measuring the angles between the arms within the linkage.[19, 20]

PinPoint

The PinPoint system, available from Phillips (Cleveland, OH) is a passive tracking arm to assist the physician in planning and performing biopsies using CT data.[6] Similar in appearance to the serial link robot, this device is a modified 3D digitizer from Immersion Inc., which uses a series of sliding counterweights via a hidden parallelogram linkage to support the structure. Since this system is physically attached to the CT scanner, the physician can use this tool, with little additional training, to freely guide a needle while the system passively tracks the needle within the preoperative CT image. In addition, this system is highly back drivable and counterbalanced, allowing the physician to use the system with little risk to the patient. A disadvantage with this design is the use of counterweights in the tracker. This limits the payload carrying capabilities to small objects like lasers and needle guides as the size and inertia of the counterweights needed for larger payloads becomes prohibitively large.

Passive systems with minimal automation offer a less expensive alternative than fully automated systems as these systems are of reduced complexity and easier to use. However, since the device does not interfere with the physician’s movements in any way, the advantages of tremor reduction and motion scaling provided by a robotic system are not available here. Since the development of freehand localizers, mechanically articulated arms have become unpopular as they offered little advantage over freehand techniques.

1.1.3 Robotic/Fully Automated Surgical Assistants

The advantages of a robot in an interventional procedure is that the surgeon can manipulate multiple instruments through complex trajectories quickly and accurately, and work virtually in hazardous imaging environments or confined spaces that are not possible for the physician to work in. Robots give the physician improved dexterity and accuracy by applying motion scaling and eliminating hand tremor.[22] Most surgical robotic systems work with the surgeon and are usually controlled remotely using a specially designed joystick, voice control or a computer vision system to track the physician's movements.[23]

Many of these designs are based on the industrial serial link robot architecture with their many degrees-of-freedom, which has the advantage of low development cost, high accuracy, and high rigidity.[24] These designs offer a convenient, off-the-shelf solution for experimentation or proof-of-concept for a specific clinical application.[25] This approach of using industrial robots has shown success in clinical areas like imaging, radiation therapy,[3] and orthopedic surgery[26], to name a few.

1.1.4 Commercial Robotic Systems for Surgery

CyberKnife, NeuroMate, ROBODOC, and RX-90serial link robot

Each of these robots have a serial link design, which provides the greatest level of flexibility and largest workspace possible, making it potentially useful for a many different procedures from imaging[3, 27] to milling operations in orthopedic surgery.[26] The CyberKnife, developed by Accuray, uses a Fanuc (Fanuc Robotics North America, Rochester Hills, MI) serial link robot for radiosurgery.[3] The system directs a high energy X-ray stream to a fixed target and uses X-ray imaging to adjust the robot and attached accelerator to maintain alignment to the target.

ROBODOC[7] and NeuroMate[5] are both serial link robots developed by Integrated Surgical Systems (Sacramento, CA). The NeuroMate system positions a needle guide over the target for manual insertion, while the ROBODOC system uses the same robot architecture for joint replacement surgery. With the patient's bone rigidly attached to the robot base via a fixation device, the surgeon hand guides the robotic arm to the starting point using a force sensor attached to the robot. Once the correct implant geometry has been selected by the surgeon, the robot then automatically cuts the desired shape in the bone to accept the implant.

Industrial robot designs have also shown success in applications involving interventions on animals. The Staubli RX 90 clean environment robot (Bayreuth, Germany) was successfully used as a part of a synergistic guidance system, similar to ROBODOC, by a research group at Karlsruhe University (Germany).[8]

SurgiScope

This robot architecture is commonly known as a delta robot, which uses three parallelograms, each of which is connected through a universal joint to construct a parallel manipulator with three translational and one rotational degree-of-freedom.[9] The three parallelograms restrict the end effector movement to three degrees-of-translation, and the fourth degree-of-rotation is controlled by a fourth arm which extends from the robot base to the end effector. This design was patented by Reymond Clavel in 1980, to manipulate small objects at a high rate of speed.[28] The advantage of this design is that the robot is mounted on the ceiling allowing the medical staff to work with it without obstructions, despite its large footprint.

AESOP, Zeus and the daVinci robot

The Zeus robotic system (Computer Motion Inc., Goleta, CA) was developed as a surgical assistant for laparoscopic surgery, which integrates the Automated Endoscopic System for Optimal Positioning (AESOP) platform.[10] The system has three robotic arms: an AESOP unit for endoscope positioning, and at least two additional arms for holding surgical tools. Each of the arms was designed to be mounted onto the surgical table, and fitted with articulating wrists, giving a total of six DOF. The AESOP module was developed to support and maneuver an endoscopic camera.[2] This is a 7 DOF robotic system, with three passive joints from the base to the elbow joint, and four motorized joints controlled via voice control.

The daVinci system illustrated in Figure 1.3, below, replaced the Zeus robotic system in 2003 when Computer Motion merged with Intuitive Surgical (Sunnyvale, CA). The daVinci robotic system consisted of at least three robotic arms attached to a cart.[4] A binocular camera was attached to one of the robotic arms and various tools or instruments could be mounted to the other arms. The camera image was transmitted to the binocular viewport where the physician controled the robot. Controlling the instruments through the console allowed for improved accuracy through motion scaling and filtration of movement tremors.

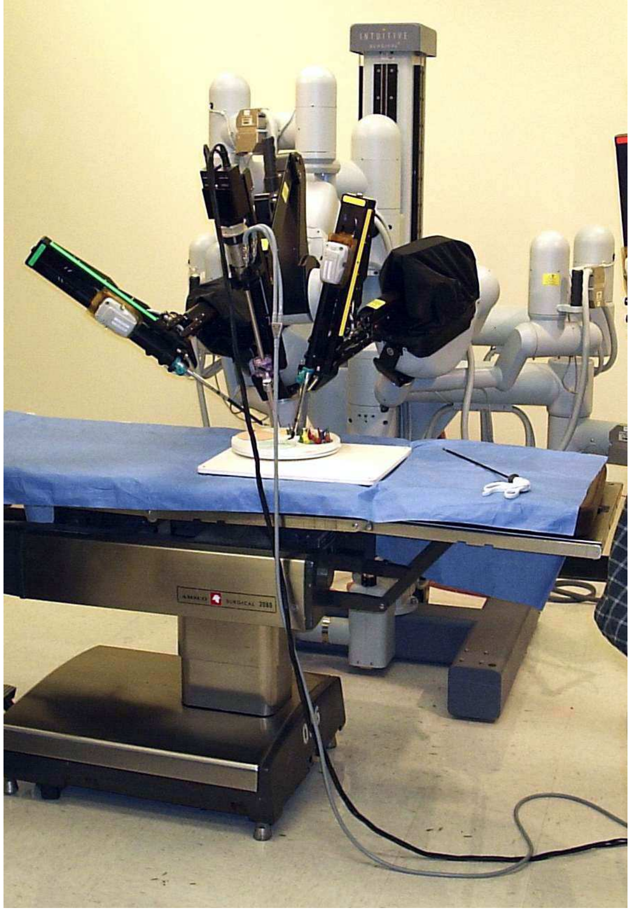

Figure 1.3: Photograph of the DaVinci surgical robotic system. Copyright © 2000, 2001, 2002 Free Software Foundation, Inc.; 51 Franklin St, Fifth Floor, Boston, MA 02110-1301 USA.

Despite the daVinci being one of the most successful surgical robotic systems to date, one shortcoming preventing its widespread use is its prohibitive cost.[29] The setup time and calibration of the instruments requires a special team and in many cases a dedicated surgical suite for the robot.[30] The large footprint of the robotic arms also restricts its use to procedures on adults, as the arms may collide with each other for smaller patients or animals.[31] In addition, haptic feedback is absent in these systems, which could result in excessive force being applied to the patient without the surgeon realizing it.[31] Although the daVinci system is capable of precise relative motion control, it is known to have a poor absolute positioning accuracy,[32] which imposes limitations on using this system for guiding needles in conjunction with high resolution scanners.

1.2 Devices for Needle Based Interventions

Needle guided interventions through the skin is preferred to surgery as there are fewer complications and quicker, less-painful recovery times. As a result, percutaneous needle interventions have become the standard of care for diagnoses, such as biopsies, and minimally invasive treatment of diseases. Examples of needle-based interventions are prostate brachytherapy, where needles are used to deliver about 80-100 small radiation sources into the prostate,[33] and radiofrequency and microwave ablation of liver tumours.[34]

Less complicated than other forms of surgery like tissue dissection, needle interventions usually require only three decoupled tasks:

(1) placing the needle at the desired insertion point on the skin, requiring three independent translational motions,

(2) pivoting the needle at the entry point to align the expected needle path with the target, and

(3) inserting the needle through the skin entry point to the intended target in the image.

Therefore, robots for needle insertion require a minimum six degrees of freedom: three to define the location of the point of entry on the patient's skin, two rotational degrees of freedom at the point of entry, and insertion of the needle into the body.[29, 30]

1.2.1 Remote Center of Motions Designs

Of particular interest are the robotic systems that were designed according to the specifications outlined by Taylor et al.,[35] where the tasks of needle placement, orientation and insertion are mechanically decoupled using a remote center of motion (RCM). By decoupling the motion of the needle about the RCM, it is no longer necessary to control multiple degrees-of-freedom simultaneously to control the needle insertion, which is the most delicate part of the procedure. By aligning the needle axis to the RCM of the machine, the needle can be pivoted about a fixed point and inserted through a predetermined entry point without the need to adjust the translational placement of the machine.

There are two different methods to create an RCM: creating a mechanically constrained linkage locked by the kinematics of the machine, or using the robot controller to coordinate the movement of a general purpose robot with many degrees-of-freedom. This can be achieved with an industrial robot[3] or custom robotic designs like the serial/parallel manipulator by Stacco and Salcudean.[36] In terms of the robot architecture, the fixed RCM robot design is preferred to general purpose robots as the fixed RCM robots are better suited to a specific task in confined spaces. In particular, fixed RCM devices allow higher angular mobility in the confined space of closed bore scanners.[23]

Surgical robots have used one of two approaches to produce a mechanically constrained RCM: either a parallelogram or spherical link design. The parallelogram linkage is the most popular design and uses either a parallelbar,[4] or belt drive[37-39]. The spherical link mechanism is a linkage where the axis of each revolute or sliding joint intersects at a common point in space and can incorporate any combination goniometric arcs,[40, 41] or pinned connections (like the universal joint used in the AESOP robotic arm[10]). The Horsley and Clarke apparatus is an example of a spherical linkage, which is composed of one revolute joint and one goniometer arc to create a RCM with two DOF: pitch and yaw.[1]

The double parallelogram linkage is the most popular design in medical systems as the actuators can be mounted on the stationary part of the mechanism to reduce the inertia of the linkage, and the parallelogram can be counterbalanced more easily than spherical linkages because cables can be routed through the mechanism more easily than curved beams.[42] As a result, spherical linkage designs have been restricted to applications like a joystick design in a master-slave manipulator or end-of-arm tooling in a robotic manipulator.[4, 10]

1.3 Design Considerations for Medical Devices

One of the many technical challenges in designing an interventional device is the human-machine interface. The interface must allow the physician to work cooperatively with the machine. Thus, in order to successfully integrate the machine, factors such as ergonomics and the surgical work flow must be considered at the initial phase of design. Standard input devices used for computers, like the keyboard and mouse, are not appropriate in a surgical environment as there is not an intuitive way the physician can use the input device to perform an intervention where the tool is handled in a very different manner. This has led to the development of special purpose manipulators to control the robot in surgical systems.[4]

An example of a special purpose manipulator is the daVinci surgeon's console.[4] This system provides an 3D view by projecting a binocular image of the surgical site over top of the surgeon's arms and hands, giving the physician the illusion the robot is an extension of his/her arms. The console allows the physician to control two robots at a time using two manipulators, one each for the left and right hand. Each manipulator has a total of seven degrees-of-freedom to control each robot arm: three translational and rotational, plus an additional control for gripping. In addition, there are foot pedals at the base of the console to control other features of the system such as switching control to any of the robot arms, or switching control over the clutch, allowing the robot to be back driven manually.

1.3.1 Safety

A significant barrier preventing widespread integration of automated robotic systems into the healthcare system is the potential safety hazard to both the patient and surgeon in the event of equipment failure, making it difficult to get regulatory approval. In contrast to robots used in an industrial setting, surgical robots are often in the same workspace as the physician, staff and patient. Therefore, the use of these systems is strictly regulated by the authorities (like Health Canada or FDA in the United States of America), and requires a risk analysis to determine the risks and benefits for both the patient and staff.

Health Canada classifies the risk level of a medical device into one of four categories based on the level of control needed to assure the effectiveness and safety of the device. A Class 1 device poses the lowest potential risk and does not require Health Canada approval for use on human or animal subjects. A Class II device requires a risk analysis from the manufacturer of the device. Common methods used to identify the safety of a device are: failure modes effects analysis (FMEA) or failure modes effects and critically analysis (FMECA).[43] These methods are used to identify all component failures and access the probability of occurrence, delectability of the problem and the severity of the failure. Low risk failures where no harm can come to both the patient and staff are considered to be a category II risk level. Failure modes that can cause serious injury or death are classified as either a level III or IV and are subject to in-depth scrutiny, which inevitably increases both the lead time and cost of integrating the system into a clinical setting.

Another aspect affecting the safety of a mechatronic device is the stiffness of the kinematic frame and drive system. The advantage of a rigid frame and a non-back drivable transmission is that they allow for an accurate tool positioning and high load carrying capabilities. The problem with this design is that the physician must interact with the device using some sort of input device (joystick, voice command, etc.. The robotic device could become unusable and possibly hazardous if there is a failure in the electronic control loop. As a result, these types of systems are generally classified as a higher risk, thus requiring redundancies in the system design, and possibly increasing the time for regulatory approval of the device.

Redundancy in the kinematics and sensing are the most common means to improve the safety of a robot used for surgery.[23] Kinematic redundancy can be accomplished by constraining the motion of the robot: for example, the addition of physical stops to prevent the robot from colliding with a tool or patient. Sensing redundancy is another option and is typically accomplished by using multiple sensors in serial at either end of the transmission chain to verify the pose of the robot.

On the other hand, a robot with low stiffness and high back drivability are inherently safer in a surgical environment as the system exerts less force on the patient.[23] Also, if the system loses power, it may be possible to still use the device by directly manipulating the tool. The disadvantage of this approach is these systems are less accurate due to the flexibility and low gear ratio transmission, and can create a possible hazard due to the possibility of dropping or driving a heavy tool into the patient/physician in the event of a control failure.

To overcome this difficulty, one can design a gravity balance into the system as a means to improve the safety. Active gravity balances used in industrial robot designs are not sufficient to reduce the risk level of the robot. Alternately, counterweights provide a simple and safe alternative to an active anti-gravity balance, but are limited to small designs and payloads where the range of motion of the device is limited.

Another method that can be used to counterbalance a linkage is to use springs in place of counterweights. Most springs, like gas, compression, or torsion springs, exert a force (or torque), which is proportional to the change in length, and offer a point of adjustment to compensate for an unknown or variable payload. However, conventional linear springs do not adequately balance the robot except at one or two configurations. To compensate for drift, the designer is forced to accept a compromise between using friction or motors[44] at the joints, or adding a purity of additional linkage elements and springs,[45] which increases both the complexity and inertia of the device, making this option unsuitable for designs that need to be back drivable. Another option is to use a constant force spring, which consists of a flat piece of metal tightly wound around a drum, and exerts a nearly constant force as it is unwound. Since the force exerted by this type of spring is typically small, they are usually found only in small devices like mechanical timepieces.

Ideally, any of these robotic designs described can be used to improve the safety, accuracy and speed of a procedure; however, this is not the case for many minimally invasive procedures, which make use of imaging systems like ultrasound (US), that are not harmful to either the patient or physician. In addition, since many decisions are made during surgery, the time saved by having the robot automatically insert the needle to the correct location would be compromised by the additional hazards of incorrectly placing the needle as the physician does not have complete control over this action.

Since many of the devices described cannot be rear-driven, the physician must rely on interaction with the computer interface to correctly position the needle. Although the inability to rear drive the system can provide rigidity for needle insertion, the physician does not have direct control over needle placement. Without a sufficient amount of training, it may be difficult to successfully integrate a fully automated system and result in added complexity to the procedure.

In cases where the physician is not exposed to any hazards (like radiation or hazardous chemicals), it is difficult to justify the use of an automated system to place and insert a needle if there is a solution with a minimum level of automation and complexity. In addition, following the current protocol will not only solve the clinical issue at hand in many cases, but also gain acceptance more easily as there is little training required.

1.4 Hypothesis

Both 2D and 3D imaging modalities are useful tools for viewing the internal anatomy. Three dimensional imaging techniques are required for accurate targeting of needles. They improve the efficiency and control of the intervention as the high temporal resolution of 2D/3D imaging can be used to validate the location of needle and target in real time. Relying on imaging alone, however, means the intervention is still operator dependant because of the difficulty of controlling the physical location of the needle within the image.

The **overarching hypothesis** of the research program described in this thesis is that **integrating 2D and/or 3D imaging with a mechatronic device to constrain the**

needle movement will improve the accuracy and repeatability of needle intervention over conventional techniques. An image-guided mechatronic system will enhance the intervention as there will be a direct link between the coordinates of the image and device supporting the needle. Integration of various imaging systems with a mechanical device allows 2D/3D guidance throughout the entire procedure including visualization, intervention planning, validation and correction in an integrated interventional system.

1.5 Research Objectives

The long-term objective of this research project is to improve the outcome of needle-based interventions over conventional techniques: both manual and automated techniques. This includes increasing the accuracy and repeatability of these procedures to minimize the invasiveness of the procedure. The specific objectives in this thesis are:

- Develop a highly dexterous and compact mechatronic needle guidance system that can be deployed in a variety of imaging modalities and clinical applications, from preclinical to human interventions.

- Develop an interactive needle guidance system with the precision of a robot, but with the interactive transparency of handheld tools currently in use with an accuracy of control in the millimeter to sub-millimeter range.

- Improve real-time tracking and stabilization of the equipment used for intervention using a low inertia spring balance.

In this thesis, I proposed that by combining the remote center of motion concept using spherical linkage components into a passive or semi-automated device, physicians will have a useful tracking system at their disposal in a package, which is less threatening to both the patient and physician. This design concept offers both the manipulative transparency of a freehand system, and tremor reduction through scaling currently offered in automated systems. I proposed three novel designs for needle interventions with improved accuracy and minimum complexity, each based on the spherical kinematics designs implementing each of the parallelogram, goniometer arc, and hinged spherical linkage with the third being the common element among the following proposed designs:

- 3D ultrasound-guided prostate biopsy system,
- 3D ultrasound-guided prostate therapy system, and
- 3D micro-CT-guided needle positioning system for small animal research.

1.6 Thesis Outline

Achievement of each specific research objective listed above is presented in the following four chapters, the first two published,[46, 47] and the third and fourth in preparation for submission to peer-reviewed journals. The next four chapters form the body of the thesis, and are summarized as follows:

1.6.1 Chapter 2: Mechanically assisted 3D ultrasound guided prostate biopsy system

Currently there are limitations associated with the prostate biopsy procedure, which is the most commonly used method for a definitive diagnosis of prostate cancer. With the use of 2D transrectal ultrasound (TRUS) for needle guidance in this procedure, the physician has restricted anatomical reference points for guiding the needle to target sites. Also, any motion of the physician's hand during the procedure may cause the prostate to move or deform to a prohibitive extent. These variations make it difficult to establish a consistent reference frame for guiding a needle. We have developed a 3D navigation system for prostate biopsy, which addresses these shortcomings. This system is composed of a 3D US imaging subsystem and a passive mechanical arm to minimize prostate motion. To validate our prototype, a series of experiments were performed on prostate phantoms. The 3D scan of the string phantom produced minimal geometric distortions, and the geometric error of the 3D imaging subsystem was 0.37 mm. The accuracy of 3D prostate segmentation was determined by comparing the known volume in a certified phantom to a reconstructed volume generated by our system and was shown to estimate the volume with less than 5% error. Biopsy needle guidance accuracy tests in agar prostate phantoms showed that the mean error was 2.1 mm and the 3D location of the biopsy core was recorded with a mean error of 1.8 mm. In this paper, we described the mechanical design and validation of the prototype system using an *in vitro* prostate phantom. Preliminary results from an ongoing clinical trial show that in-plane prostate motion is small with an in-plane displacement of less than 1 mm during the biopsy procedure.

1.6.2 Chapter 3: A Compact Mechatronic System for 3D Guided Prostate Interventions

Ultrasound imaging has improved the treatment of prostate cancer (PCa) by producing increasingly higher quality images and influencing sophisticated targeting procedures for the insertion of radioactive seeds during brachytherapy. However, it is critical that the needles be placed accurately within the prostate to deliver the therapy to the planned location and avoid damaging surrounding tissues. We have developed a compact mechatronic system, as well as an effective method for guiding and controlling the insertion of transperineal needles into the prostate. This system has been designed to allow guidance of a needle obliquely in 3D space into the prostate thereby reducing pubic arch interference. Choice of needle trajectory and location in the prostate can be adjusted manually or with computer control.

To validate our system, a series of experiments were performed on phantoms. The 3D scan of the string phantom produced minimal geometric error, which was less than 0.4 mm. Needle guidance accuracy tests in agar prostate phantoms showed that the mean error of bead placement was less than 1.6 mm along parallel needle paths that were within 1.2 mm of the intended target and 1º from the preplanned trajectory. At oblique angles of up to 15º relative to the probe axis, beads were placed to within 3.0 mm along a trajectory that was within 2.0 mm of the target with an angular error less than 2º. By combining 3D TRUS imaging system to a needle tracking linkage, this system should improve the physician's ability to target and accurately guide a needle to selected targets without the need for the computer to directly manipulate and insert the needle. This would be beneficial as the physician has complete control of the system and can safely maneuver the needle guide around obstacles like previously placed needles.

1.6.3 Chapter 4: Micro-CT Geometric Accuracy Phantom for Improved Fiducial Localization in Image-Guided Needle Positioning Systems

In this paper, a compact quality assurance phantom qualified to a traceable standard is presented for routine evaluation of the geometric accuracy of micro-CT scanners. An automated algorithm is described that processes micro-CT images of the phantom to characterize the geometric accuracy of the scanner and calculate correction factors to reduce the geometric error of the images. The phantom and algorithm are used to evaluate the geometric accuracy of five micro-CT scanners representing four different models of micro-CT systems. The calculated correction factors are then applied to measurements of fiducial markers in each of the five scanners to evaluate their ability to improve fiducial localization. The techniques developed in this study allow the micro-CT end user to guarantee the highest level of geometric fidelity in images. This ability is crucial for applications such as mechatronic needle positioning systems, which cannot be successful without high geometric accuracy.

In all three of the scanners, the geometric error was minimal, and statistically significant correction factors were derived; in many applications, these corrections would be practically negligible. In some applications they could be important, and stable, traceable corrections factors are possible in all three axis. Each of these three scanners was found to have sub-voxel accuracy in localization of bead centroids. In two of the scanners tested, or 40% of the total, a correctable geometric inaccuracy was detected in the image. The error was found to be anisotropic in nature and required different correction values for the in-plane and out-of-plane directions. However, application of correction factor allowed these two scanners to achieve sub-voxel accuracies. Use of a calibration phantom should therefore be considered for any application that demands high geometric fidelity in images. The geometric errors detected within micro-CT images by this study are not immediately obvious but could be serious in an application (such as a micro-CT guided small animal interventions) that may require targeting accuracies < 200 µm. The calibration phantom is an easily implemented assurance to micro-CT end users of the geometric fidelity of their images.

1.6.4 Chapter 5: 3D Image-Guided Robotic Needle Positioning System for Small Animal Interventions

This paper presents the design of a micro-CT guided small animal robotic needle positioning system. In order to simplify the robotic design and maintain a small targeting error, a novel implementation of the RCM is used in the system. The system has been developed with the objective of achieving a mean targeting error of < 200 µm while maintaining a high degree of user friendliness. The robot is compact enough to operate within the micro-CT bore. Small animals can be imaged and the intervention performed without the need to transport the animal from one workspace to another. Not requiring transport of the animal reduces opportunities for targets to shift from their localized position in the image and simplifies the workflow of interventions. An improved method of needle calibration is also presented that better characterizes the calibration using the position of the needle tip in photographs rather than the needle axis. A calibration fixture was also introduced, which dramatically reduces the time requirements of calibration while maintaining calibration accuracy. Two registration modes have been developed to correspond the robot coordinate system with the coordinate system of the micro-CT scanner. The two registration modes offer a balance between the time required to complete a registration and the overall registration accuracy. The development of slow high accuracy and fast low accuracy registration modes provides users with a degree of flexibility in selecting a registration mode best suited for their application. The errors of the high accuracy primary registration were fiducial registration error ($FRE_{primary}=21 \pm 6$ µm) and target registration error ($TRE_{primary}=31 \pm 12$ µm). The error in the low accuracy combined registration was $TRE_{combined}=139 \pm 63$ µm. Both registration modes are therefore suitable for small-animal needle interventions. The targeting accuracy of the robotic system was then characterized using targeting experiments in tissue-mimicking gelatin phantoms. The results of the targeting experiments were combined with the known calibration and needle deflection errors to provide a more meaningful measure of the needle positioning accuracy of the system. The combined targeting errors of the system were 149 ± 41 µm and 218 ± 38 µm using the primary and combined registrations respectively. Finally, pilot *in vivo* experiments were completed to demonstrate the performance of the system in a biomedical application.

1.7 References

1. Horsley V, Clarke RH. The structure and function of the cerebellum examined by a new method. *Brain.* 1908;31(1):45–124.

2. Kasalicky MA, Svab J, Fried M, Melechovsky D. [AESOP 3000--computer-assisted surgery, personal experience]. *Rozhl Chir.* Jul 2002;81(7):346-349.

3. Adler JR, Murphy MJ, Chang SD, Hancock SL. Image-guided robotic radiosurgery. *Neurosurgery.* Jun 1999;44(6):1299-1306.

4. Guthart G, Salisbury JK. The Intuitive Telesurgery System: Overview and application. *Proceedings of 2000 Ieee International Conference on Robotics and Automation.* 2000:618-621.

5. Li QH, Zamorano L, Pandya A, Perez R, Gong J, Diaz F. The application accuracy of the NeuroMate robot--A quantitative comparison with frameless and frame-based surgical localization systems. *Comput Aided Surg.* 2002;7(2):90-98.

6. Hevezi J, Blough M, Hoffmeyer D, Yanof J. Brachytherapy usingCT PinPoint. *MEDICAMUNDI.* 2002;46(3):22–27.

7. Yao J, Taylor RH, Goldberg RP, et al. A C-arm fluoroscopy-guided progressive cut refinement strategy using a surgical robot. *Comput Aided Surg.* 2000;5(6):373-390.

8. Burghart C, Krempien R, Redlich T, et al. Robot assisted craniofacial surgery: First clinical evaluation. *Cars '99: Computer Assisted Radiology and Surgery.* 1999;1191:828-833.

9. Heissler E, Hein A, Bolouri S, et al. Robot supported insertion of catheters for hyperthermia and brachytherapy. *Car '98 - Computer Assisted Radiology and Surgery.* 1998;1165:660-663.

10. Ghodoussi M, Butner SE, Wang YL. Robotic surgery - The transatlantic case. *2002 Ieee International Conference on Robotics and Automation, Vols I-Iv, Proceedings.* 2002:1882-1888.

11. www.clarontech.com/platforms_micron.tracker.php. Accessed Oct. 10, 2011.

12. www.ndigital.com/medical/index.php. Accessed Oct.10, 2011.

13. Schneider M, Stevens C. Development and testing of a new magnetic-tracking device for image guidance - art. no. 65090I. *P Soc Photo-Opt Ins.* 2007;6509:I5090-I5090.

14. Cleary K, Peters TM. Image-Guided Interventions: Technology Review and Clinical Applications. *Annu Rev Biomed Eng.* 2010;12:119-142.

15. Springer ML, Sievers RE, Viswanathan MN, et al. Closed-chest cell injections into mouse myocardium guided by high-resolution echocardiography. *Am J Physiol-Heart C.* Sep 2005;289(3):H1307-H1314.

16. Olsson M, Campbell K, Turnbull DH. Specification of mouse telencephalic and mid-hindbrain progenitors following heterotopic ultrasound-guided embryonic transplantation. *Neuron.* Oct 1997;19(4):761-772.

17. Slevin JC, Byers L, Gertsenstein M, et al. High resolution ultrasound-guided microinjection for interventional studies of early embryonic and placental development in vivo in mice. *Bmc Dev Biol.* Feb 27 2006;6.

18. Watanabe E, Watanabe T, Manaka S, Mayanagi Y, Takakura K. 3-Dimensional Digitizer (Neuronavigator) - New Equipment for Computed Tomography-Guided Stereotaxic Surgery. *Surg Neurol.* Jun 1987;27(6):543-547.

19. Blough MM, Hevezi JM, Eng TY, Dahiya RS, Chopra S. CT guided prostate brachytherapy using pinpoint stereotactic arm. *Cancer J.* Nov-Dec 2002;8(6):505-506.

20. Kosugi Y, Watanabe E, Goto J, et al. An articulated neurosurgical navigation system using MRI and CT images. *Biomedical Engineering, IEEE Transactions on.* 1988;35(2):147-152.

21. Krieger A, Susil RC, Menard C, et al. Design of a novel MRI compatible manipulator for image guided prostate interventions. *IEEE T Bio-Med Eng.* Feb 2005;52(2):306-313.

22. Riviere CN, Thakor NV. Modeling and canceling tremor in human-machine interfaces. *IEEEe Eng Med Biol.* May-Jun 1996;15(3):29-36.

23. Taylor RH, Stoianovici D. Medical robotics in computer-integrated surgery. *Ieee T Robotic Autom.* Oct 2003;19(5):765-781.

24. Kwoh YS, Hou J, Jonckheere EA, Hayati S. A robot with improved absolute positioning accuracy for CT guided stereotactic brain surgery. *IEEE Trans Biomed Eng.* Feb 1988;35(2):153-160.

25. Wei ZP, Wan G, Gardi L, Mills G, Downey D, Fenster A. Robot-assisted 3D-TRUS guided prostate brachytherapy: System integration and validation. *Med Phys.* Mar 2004;31(3):539-548.

26. Taylor RH, Mittelstadt BD, Paul HA, et al. An Image-Directed Robotic System for Precise Orthopedic-Surgery. *IEEE T Robotic Autom.* Jun 1994;10(3):261-275.

27. Chang SD, Murphy M, Geis P, et al. Clinical experience with image-guided robotic radiosurgery (the Cyberknife) in the treatment of brain and spinal cord tumors. *Neurol Med-Chir.* Nov 1998;38(11):780-783.

28. Clavel R, Inventor. Device for the movement and positioning of an element in space. US patent US 4 976 582. 1990-12-11, 1990.

29. Cadeddu JA, Stoianovici D, Kavoussi LR. Robotics in urologic surgery. *Urology.* Apr 1997;49(4):501-507.

30. Stoianovici D, Whitcomb LL, Anderson JH, Taylor RH, Kavoussi LR. A modular surgical robotic system for image guided percutaneous procedures. *Medical Image Computing and Computer-Assisted Intervention - MICCAI'98.* 1998;1496:404-410.

31. Sim HG, Yip SK, Cheng CW. Equipment and technology in surgical robotics. *World J Urol.* Jun 2006;24(2):128-135.

32. Hager GD, Okamura AM, Kazanzides P, Whitcomb LL, Fichtinger G, Taylor RH. Surgical and Interventional Robotics: Part III: Surgical Assistance Systems. *IEEE Robot Autom Mag.* Dec 1 2008;15(4):84-93.

33. Lucas JN. *Trends in prostate cancer research*. New York: Nova Biomedical Books; 2005.

34. Sindram D, Swan RZ, Lau KN, McKillop IH, Iannitti DA, Martinie JB. Real-time three-dimensional guided ultrasound targeting system for microwave ablation of liver tumours: a human pilot study. *HPB (Oxford).* Mar 2011;13(3):185-191.

35. Taylor R FJ, Grossman D, Karidis J, LaRose D, Inventor. Remote center-of-motion robot for surgery. US patent 5,397,323.

36. Stocco LJ, Salcudean SE, Inventors. Hybrid serial/parallel manipulator. US patent US 6 047 6102000.

37. Jensen JF, Inventor. Remote Center Positioing Device With Flexible Drive. US patent 5 817 084. Oct. 6, 1998, 1998.

38. Taylor RH, Funda J, Eldridge B, et al. A Telerobotic Assistant for Laparoscopic Surgery. *Ieee Eng Med Biol.* May-Jun 1995;14(3):279-288.

39. Kobayashi E, Masamune K, Sakuma I, Dohi T, Hashimoto D. A new safe laparoscopic manipulator system with a five-bar linkage mechanism and an optical zoom. *Comput Aided Surg.* 1999;4(4):182-192.

40. Davies BL, Hibberd RD, Ng WS, Timoney AG, Wickham JE. The development of a surgeon robot for prostatectomies. *Proc Inst Mech Eng H.* 1991;205(1):35-38.

41. Harris SJ, ArambulaCosio F, Mei Q, et al. The Probot - an active robot for prostate resection. *P I Mech Eng H.* 1997;211(4):317-325.

42. Bassan HS, Patel RV, Moallem M. A Novel Manipulator for Percutaneous Needle Insertion: Design and Experimentation. *IEEE-ASME T Mech.* Dec 2009;14(6):746-761.

43. Davies B. A discussion of safety issues in medical robots. In: Taylor R, Lavallee S, Burdea G, Moesges R, eds. *Computer Integrated Surgery*. Cambridge, MA: MIT Press; 1996:287-296.

44. Lessard S, Bigras P, Bonev IA. A New Medical Parallel Robot and Its Static Balancing Optimization. *Journal of Medical Devices.* 2007;1(4):272-278.

45. Wang JG, Gosselin CM. Static balancing of spatial three-degree-of-freedom parallel mechanisms. *Mech Mach Theory.* Apr 1999;34(3):437-452.

46. Bax J, Cool D, Gardi L, et al. Mechanically assisted 3D ultrasound guided prostate biopsy system. *Med Phys.* Dec 2008;35(12):5397-5410.

47. Bax J, Smith D, Bartha L, et al. A compact mechatronic system for 3D ultrasound guided prostate interventions. *Med Phys.* Feb 2011;38(2):1055-1069.

Chapter 2

2 Mechanically Assisted 3D Ultrasound Guided Prostate Biopsy System

2.1 Introduction

Digital rectal exams and prostate-specific antigen (PSA) blood tests are common screening tests for prostate cancer (PCa) in asymptomatic men. Combined with the public's increased awareness of PCa and PSA testing, the proportion of men diagnosed with early stage prostate cancer has increased.[1, 2] When diagnosed at an early stage, the disease is treatable;[3, 4] and even at later stages, treatment can be effective. However, if a tumour has extended beyond the prostate, the risk of metastases increases significantly.

The definitive diagnosis of PCa requires histological assessment of tissue cores drawn from the prostate during a biopsy procedure. The physician uses a conventional 2D transrectal ultrasound (TRUS) probe to guide the needle into the prostate. Biopsies are commonly performed with an 18-gauge needle mounted on a spring-loaded biopsy "gun". This gun is connected to an "end-firing" 2D TRUS probe by a guide that forces the needle to stay in the imaging plane so it is always visible in the US image. The TRUS probe is held by the physician and inserted into the patient's rectum in order to image the prostate through the rectal wall (Figure 2.1). Typically, an average of 10 biopsy cores is obtained in a single biopsy procedure.[5] Each core is separately identified as to its location within the prostate so that the pathologist can report the extent and grade of cancer.

While the TRUS-guided prostate biopsy has become a commonly performed urological procedure, it is not without limitations. Many patients' initial biopsy will be negative for PCa; however, because the sensitivity of the procedure is poor, PCa cannot be ruled out in these patients. Physicians currently try to obtain occult cancer samples by taking biopsies from predetermined regions of the prostate that have a high probability of harboring cancer. Not only is the volume of the biopsy sample small but the presence of PCa is also often multi-focal, involving only a small part of the prostate in the early stages of the disease.[3, 6] As a result, a patient may be informed of a negative biopsy result but in fact may be harboring an occult early stage cancer. The management of these patients, in addition to patients diagnosed with early stage disease, is currently a major challenge.

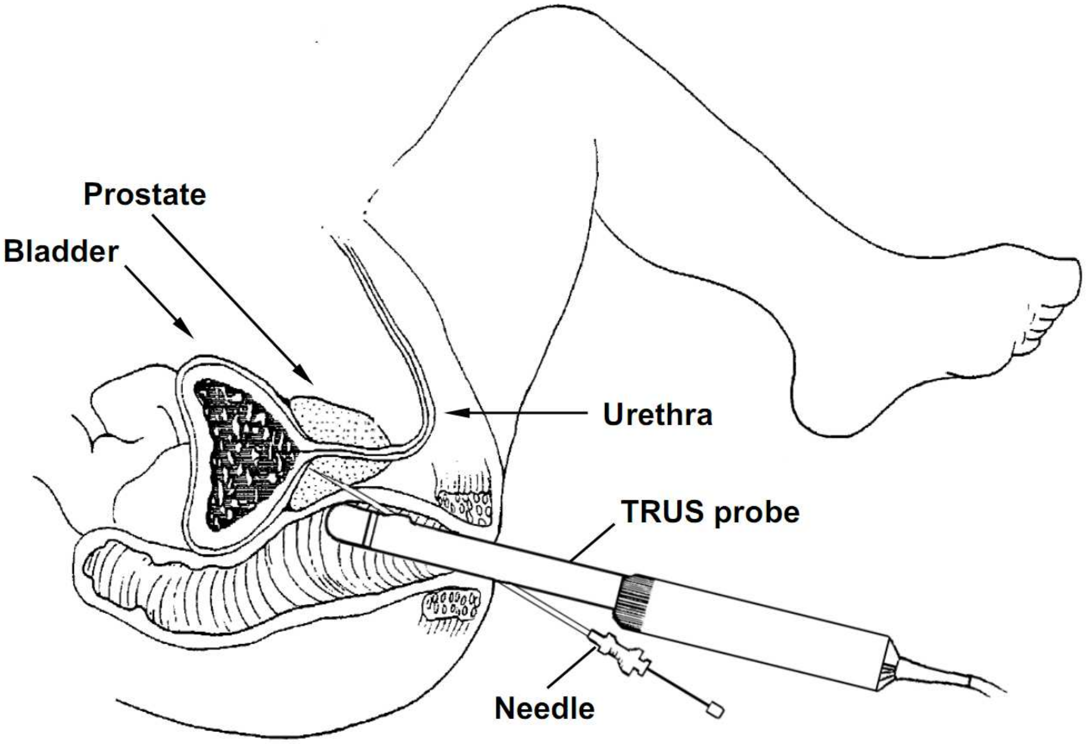

Figure 2.1: Schematic drawing of a biopsy procedure illustrates how a forward viewing probe captures images of the prostate and nearby organs (bladder and urethra). The needle guide constrains the needle path to stay in the imaging plane of the TRUS probe so it is always visible in the US image.

Since a negative result does not preclude the possibility of a missed cancer,[7] patients undergo repeat biopsies when indicated by clinical suspicion and in cases when a positive biopsy for cancer would have therapeutic consequences. Since there are an appreciable number of men with false-negative biopsy who, in fact, harbor curable PCa, the physician is faced with a difficult challenge. Sometimes these patients are imaged with other modalities and undergo a second or even a third biopsy, in which the physician tries to avoid the location of the first negative biopsy.

Various reports have shown that the detection rate of PCa for repeat biopsy procedures range from 10% to 25% (after initial biopsy results were shown to be negative).[3, 8-10] Because PCa is present in at least a tenth to a quarter of patients who have undergone an initial negative biopsy, current biopsy procedures are still suboptimal.[6, 11, 12] If an initial biopsy fails to detect cancer, how should a repeat biopsy be directed? Should the repeat (and initial) biopsy be lesion-directed, random, or based on the details of the patient's anatomy (*e.g*., prostate regions, volume, shape)?[3, 13]

Another important challenge facing physicians is men diagnosed on biopsy to have pre-malignant lesions, *i.e*. high-grade prostatic intraepithelial neoplasia, and particularly atypical small acinar proliferation (ASAP).[14] These are challenging to manage as there is a 40-50% chance of finding cancer on repeat biopsy with ASAP.[15] Since co-existing cancer might be present, especially with ASAP, where the pathologist finds only a small amount of histological "atypia" but not enough material to confidently diagnose cancer, these patients require a repeat biopsy soon after the first. In these situations, it is vital to re-biopsy the same area.[14] Currently, 2D US provides only a vague location of the abnormal findings, and it is not possible to be certain that the same area has been sampled by the repeat biopsy.

Due to the increasing number of younger men with potentially early and curable PCa undergoing repeated prostate biopsy, it is important not to re-biopsy the same area if the original biopsy was negative, and it is particularly vital to re-biopsy the exact area if a possible abnormal area was detected on first biopsy.[14, 15] Thus, the locations of the cores obtained in 3D from the prostate must be known accurately to help guide the physician during the repeat biopsy[16, 17] to help in correlating any imaging evidence of the disease, and to provide improved planning for any subsequent therapy.

As there is a clinical need for a prostate biopsy system allowing recording of the core locations, and guiding tools to allow sampling of specific targets in 3D, special purpose TRUS biopsy systems have emerged in the marketplace. Envisoneering Medical Technologies (St. Louis, MO) has developed a system that uses a stationary endorectal ultrasound probe for biopsy. The Voluson prostate biopsy system (General Electric) is a

3D handheld US imaging system that allows for real-time imaging of the prostate. Several groups have reported using 3D prostate systems in both phantom and patient studies.[18-21] These studies have shown an improvement in the positional and diagnostic accuracy of the procedure.[20-1] However, there is still a group of patients with ultrasound occult cancers.[20] As a result, the use of real-time 3D US probes suffers from the same problems as 2D probes.[20]

MRI imaging using high resolution T2 weighted images, and MRI spectroscopy are promising methods that can improve the detection of prostate cancer.[22] Several groups have proposed and developed a number of potential solutions that use CT or MRI for prostate biopsy.[23-25] Fichtinger et al. integrated CT with a side-firing TRUS system to guide the needle to a preplanned target using a robotic arm.[19] MRI has also been used to identify potential malignant tumors while a robotic device has been used to guide the biopsy needle.[24,25] The DaVinci robot (Intuitive Surgical Inc., Sunnyvale, CA) has been used extensively for prostate surgery, and can also be adapted to guide a biopsy needle. However, these solutions require physicians to use CT,[23] MRI,[24, 25] or specially modified biopsy systems, which are costly. As well, the workflow for each of the new designs differs significantly from current biopsy protocols, requiring physicians to retrain. Furthermore, since there are more than one million biopsies performed each year,[26] it would be beneficial to develop a biopsy system that utilizes ultrasound equipment currently in use for the procedure. Also, the use of 3D US coupled to a mechanical navigation system has the potential to provide a reproducible record and allow for image fusion with other imaging modalities like MRI, assisting the physician in planning a repeat biopsy. This system can potentially eliminate most of the user variability of conventional non-fixed hand-held probes that render them unsuitable for precision biopsy, while preserving some of the user familiarity.

In this paper, we describe the development and testing of a mechanically assisted 3D TRUS prostate biopsy system, which addresses the limitations of current prostate biopsy procedures and also minimizes adoption cost and physician retraining. We also report briefly on the initial clinical use of this system for prostate biopsy.

2.2 System Design

Our 3D TRUS system is an integrated 3D workstation, with mechanical guidance system and software tools to record the core locations and guide the needle to its target. It allows real-time tracking and recording of the 3D position and orientation of the biopsy needle as the physician manipulates the US transducer. The system uses (1) passive mechanical components for guiding, tracking, and stabilizing the position of a commercially available end-firing transrectal US transducer, (2) software components for acquiring, storing, and reconstructing (in real time) a series of 2D US images into a 3D US image, and (3) software that displays a model of the 3D scene to guide and record the biopsy core locations in 3D.

2.2.1 Mechanical Tracking System

The mechanical assembly consists of a passive four degree-of-freedom tracking device, an adaptable transducer cradle and a hydraulic support (Figure 2.2). The transducer cradle mechanically locks and fastens a commercially available end-firing TRUS transducer. The tracking device and transducer cradle are secured by the hydraulic support, which stabilizes the mechanical assembly while the physician performs a biopsy. When the TRUS probe is maneuvered, the software records the 3D position and orientation of the transducer tip via absolute encoders as described below.

The end-firing TRUS transducer (with the biopsy needle guide in place) is mounted to the mechanical tracking mechanism where the US probe is free to rotate and slide along its long axis (Figure 2.3, wrist joint axis of rotation: J_3). This allows the physician to insert the TRUS transducer through the patient's rectum to view the prostate and to rotate the TRUS transducer to acquire a 3D image. The tracking linkage contains angle-sensing encoders (Figure 2.3) mounted to each joint to transmit the angle between the arms to the computer. This encoder arrangement allows for the continuous computation of the position of the transducer needle guide as the transducer is manipulated in the rectum.

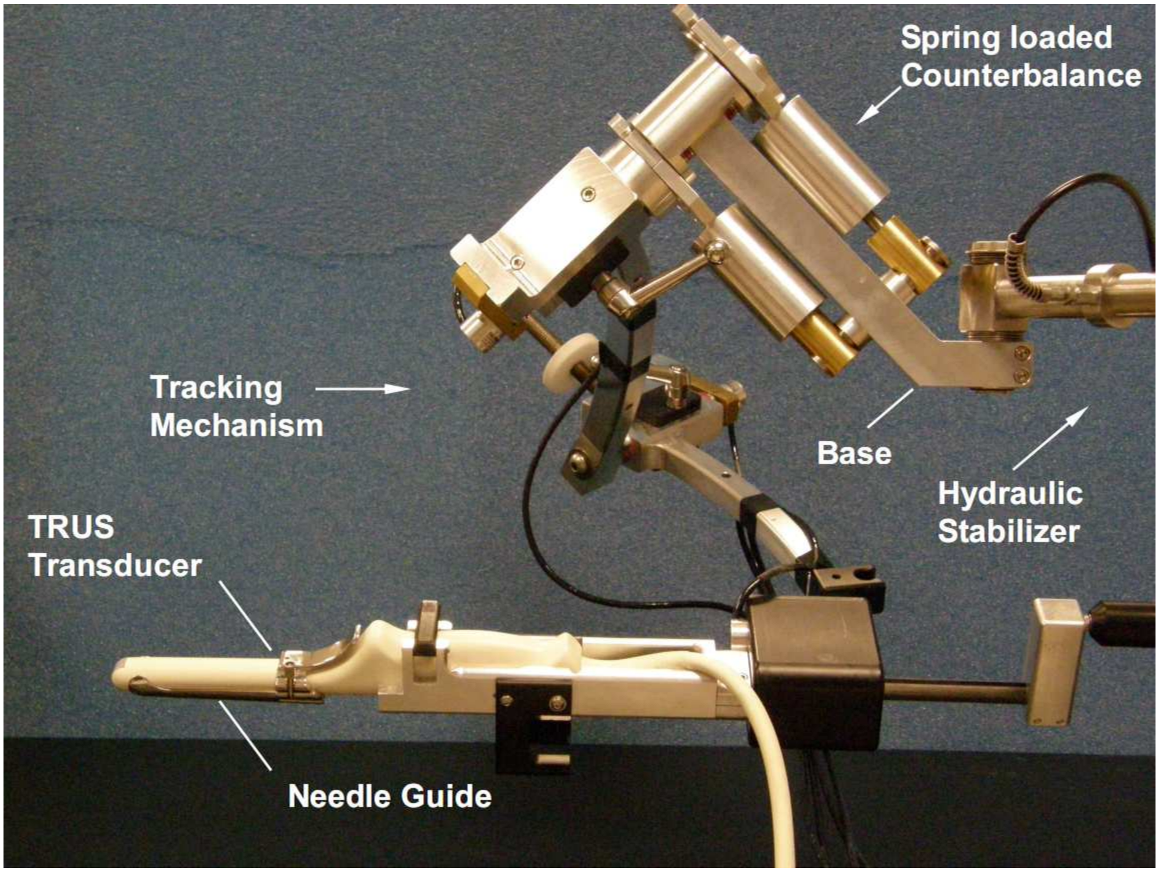

Figure 2.2: Photograph of the tacking system to be used for 3D US guided prostate biopsy. The system is mounted at the base to a hydraulic actuated stabilizer while the linkage allows the TRUS transducer to be manually manipulated about a RCM, to which the center of the probe tip is aligned. The spring loaded counterbalance was designed to fully support the weight of the system throughout its full range of motion about the RCM.

The mechanical tracking device is a spherical linkage assembly that consists of three links and three hinged connections. The axis of each hinged connection converges to a common point to produce a remote center of motion (RCM).[27-29] The base link (Figure 2.3, L_1) defines the reference axis of the proposed coordinate system and is fixed to a multi-jointed stabilizer (Figure 2.3: L_1) that attaches to a cart. The angle between each hinged connection in the mechanism defines the size and shape of the operating envelope of the kinematics frame, which allows for two degrees of rotation (pitch and yaw) about the RCM.

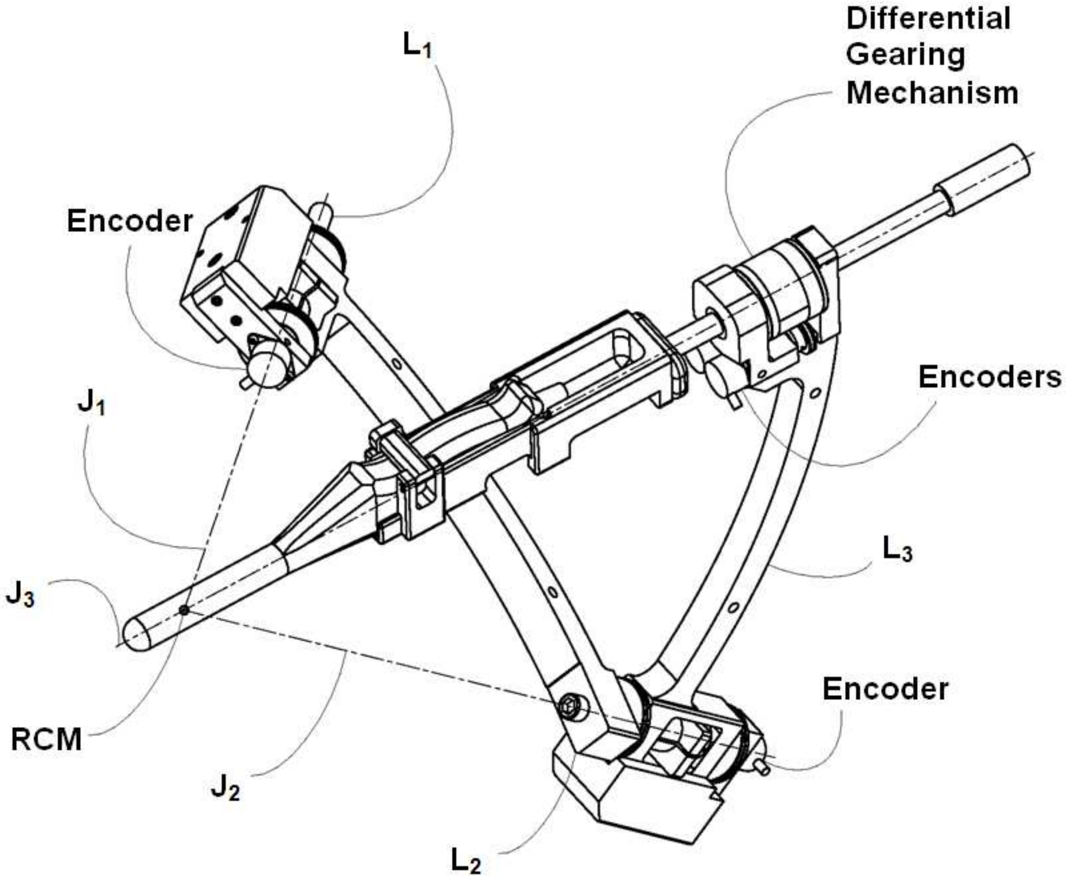

Figure 2.3: A front perspective view of the mechanical tracker, which in turn is attached to a multi-jointed stabilizer at L_1. The RCM is at the intersection of the primary, secondary and tertiary axes. The encoders mounted at the pivot J is used to measure the relative angles between the two successive links L_2 and L_3. The encoder at pivot J_2 measures the angle between L_1 and L_2. The differential gearing mechanism, which is coupled to the tracking linkage, decouples the two DOF provided by the cylindrical joint J_3 supporting the shaft, which in turn is mounted to the transducer cradle. These two degrees of mobility represent the probe penetration and angular orientation about its longitudinal axis respectively. Two additional encoders, mounted onto the wrist joint, J_3, are required to measure the angle and depth of penetration of the probe through the differential gear train.

The linkage assembly supports the TRUS transducer through the distant pinned connection (Figure 2.3, wrist joint axis: J_3) such that the long axis of the probe passes through its RCM. Therefore, the angular position of the axis of the probe relative to the base is determined by measuring the angle between two successive joint axes. Two encoders mounted at the pivots (shoulder joint axis: J_1 and elbow joint axis: J_2) are used to measure the relative angles between the two successive linkages (Figure 2.3, links L_1 and L_2) and between the link L_1 and stabilizer respectively.

The probe is supported through the revolute axis by a sleeve and pivots and slides freely along the axis of the revolute joint (Figure 2.3, wrist joint axis J_3). This compound joint gives the tracking mechanism an additional two DOF where the probe penetration and relative rotation angle to the supporting frame are defined. As illustrated in Figure 2.3, the differential gearing mechanism, which is coupled to the tracking mechanism, decouples the motion through the compound joint. These two degrees of mobility represent the probe penetration and angular orientation about its long axis (i.e. roll angle) respectively.

2.2.1.1 Forward Kinematics Equations of Motion

The unit vector $\hat{\mathbf{r}}$ defines the 3D orientation of the TRUS tip in spherical coordinates relative to its fulcrum (O) (Figure 2.4):

$$\hat{r} = \begin{bmatrix} x \\ y \\ z \end{bmatrix} = \begin{bmatrix} \cos\theta\sin\phi \\ \sin\theta\sin\phi \\ \cos\phi \end{bmatrix}. \qquad [1]$$

In this description, the position of the probe tip $\hat{\mathbf{r}} = f(\phi, \theta)$ is specified by the angle ϕ, the angle long axis of the probe makes with the z-axis, and the angle θ, which is the orientation of the TRUS transducer in the x-y plane. The relationship between the tracker coordinate system $\hat{\mathbf{r}} = f(\phi, \theta)$ and the reference frame defined by the encoders connected at each of the hinged connections is illustrated in Figure 2.4. The tracker arm configuration measured by the encoders is defined by the spherical triangle (ABC), and is linked to the global reference frame by the spherical triangle (APC).

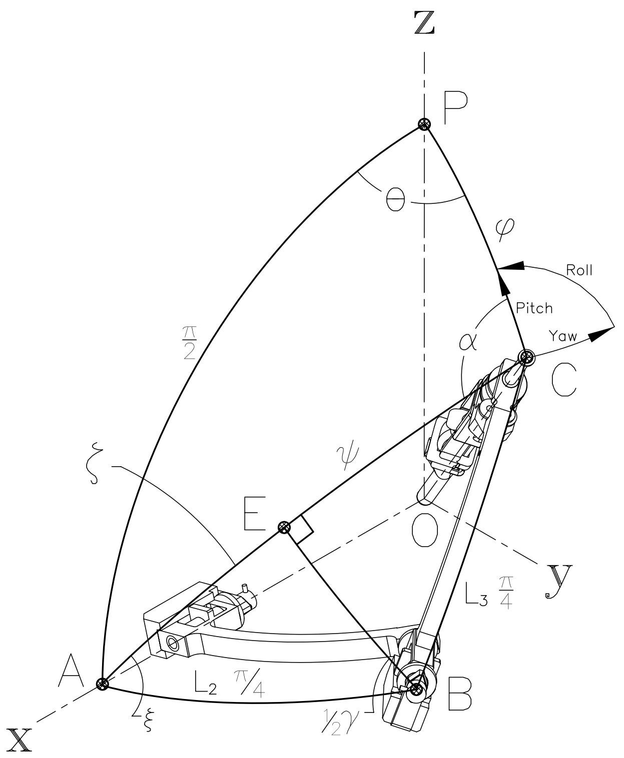

Figure 2.4: Diagram illustrating the relationship between the tracker linkage orientations relative to the global Cartesian reference frame. The angle between the joints A and B in link L_2 (<AOB) is π/4. Likewise, the angle between the joints B and C connections in link L3 (<BOC) is also π/4.

The forward kinematics equations of motion for the open-chain linkage (Eqs. 2a, 2b and 2c) were derived by applying the Napier analogies to spherical triangle APC (Figure 2.4).[28]

$$\tan\frac{1}{2}(\theta+\alpha)=\cos\frac{1}{2}\left(\psi-\frac{\pi}{2}\right)\sec\frac{1}{2}\left(\psi+\frac{\pi}{2}\right)\cot\frac{1}{2}\zeta \qquad \text{[2a]}$$

$$\tan\frac{1}{2}(\theta-\alpha)=\sin\frac{1}{2}\left(\psi-\frac{\pi}{2}\right)\csc\frac{1}{2}\left(\psi+\frac{\pi}{2}\right)\cot\frac{1}{2}\zeta \qquad \text{[2b]}$$

$$\tan\frac{1}{2}\varphi=\tan\frac{1}{2}\left(\psi-\frac{\pi}{2}\right)\sin(\theta+\alpha)\cos(\theta-\alpha) \qquad \text{[2c]}$$

This defines spherical coordinates of the vector $\hat{\mathbf{r}} = f\ (\phi,\ \theta)$ in terms of the geometric configuration of the linkage angles ψ and ζ (see Figure 2.4).

Equations 3a and 3b, which define the configuration of the linkage in terms of the angles measured by the encoders at the shoulder and elbow joints respectively, were derived by solving the right spherical triangle (ABE).[28]

$$\tan\frac{1}{2}\psi = \cos\xi \qquad [3a]$$

$$\cot\frac{1}{2}\psi = \frac{1}{\sqrt{2}}\tan\gamma \qquad [3b]$$

The position of each arm (AB and BC in Figure 2.4) in the linkage was determined by measuring the spherical angles at each of the pinned couplings A and B respectively. The encoder mounted at A measures the angle ($\xi + \zeta$) between L_1 and the x-z plane, and the encoder mounted at B measures the angle γ between the two arms (L_1 and L_2). Equation (3b) is needed to decouple the values for (ξ) and (γ), required to solve equations (2a-c).

2.2.2 Software for Acquiring and Reconstructing 3D US Images

Before the physician acquires a 3D image of the prostate, the tracking arm is locked into place to prevent the TRUS probe from changing its pitch, yaw and depth of penetration while the probe is rotated. As the physician rotates the transducer manually about its long axis (Figure 2.3, wrist joint axis: J_3) to acquire a 3D scan composed of 200 images in one-degree increments, the 2D US images from the US machine are digitized using a frame grabber, and reconstructed into a 3D image.[30] The last 20 images in the overlap region (from 180º to 200º and 0º to 20º of transducer rotation) are merged by averaging the duplicate images to remove any slight discontinuities that may arise from image lag[31] or small patient motion. Our software has a graphical software interface to provide information to the physician on the proper rotational speed. The software interface provides a visual queue to indicate if the rotation was too rapid and the 2D US image was not acquired properly. Once the 3D TRUS image has been acquired, the software then displays the image in a cube view (Figure 2.5).[30]

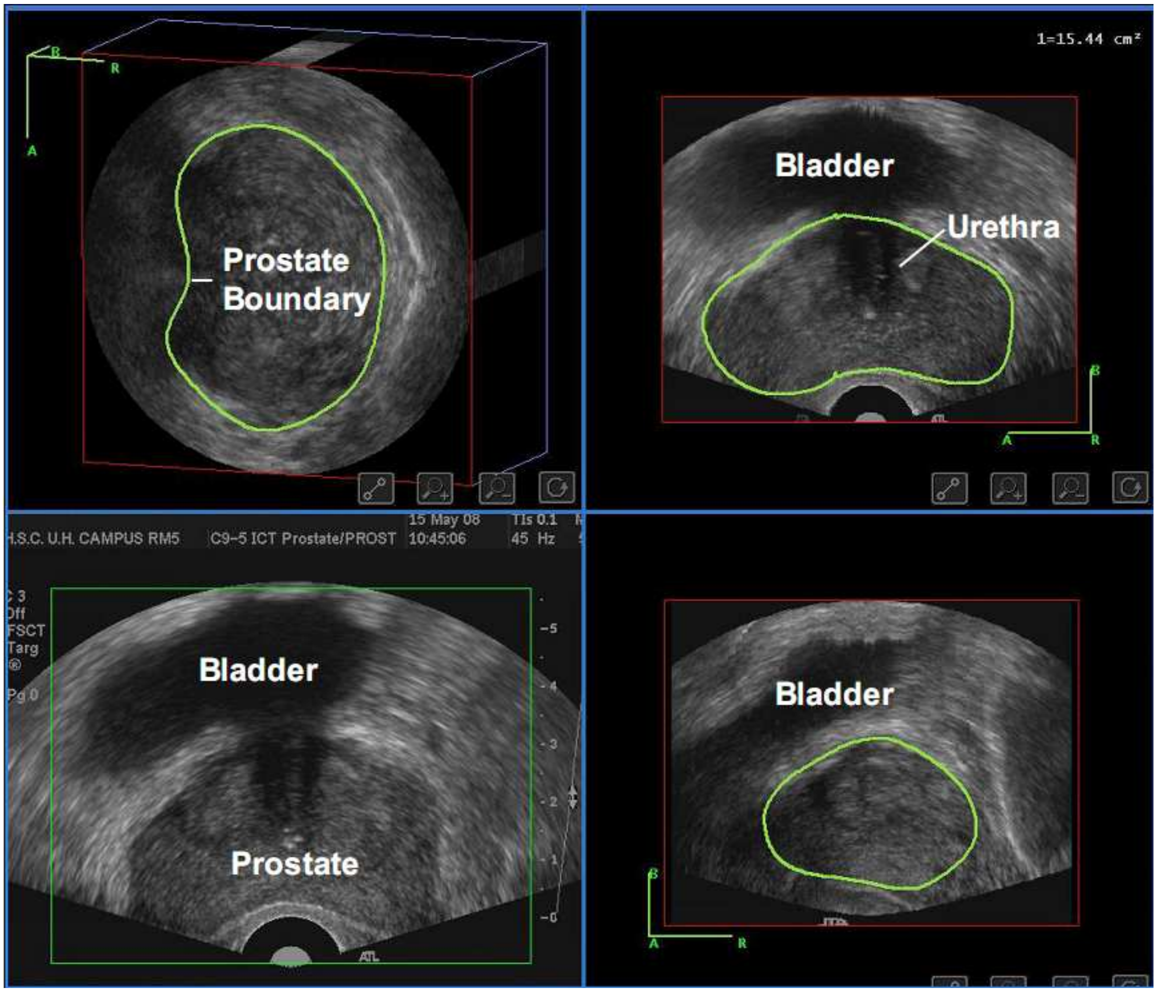

Figure 2.5: Axial (top left), sagittal (top right) and coronal views (bottom right) of the 3D TRUS image of a patient's prostate. The coronal view of the prostate is not possible using the current 2D TRUS biopsy procedure. The image in the bottom left shows the live video stream from the US machine. The image within the green bounding box was digitized by a frame grabber as the physician rotated the TRUS transducer and then reconstructed into the 3D image shown in the other three windows. The bladder (hypoechoic region anterior to the prostate boundary) and urethra are visible within the axial and sagittal views.

A model of the prostate is then generated from the 3D image by a semi-automatic 3D segmentation algorithm developed in our laboratory and described in detail elsewhere.[31, 32] The segmentation algorithm requires that the physician selects four points around the boundary of a 2D prostate cross-section. The algorithm then segments the prostate by fitting a dynamic deformable contour to match the boundary of the prostate. The contour is then used in the adjacent slice as a template and deformed around the prostate boundary; the result is propagated through 180° and refined for each succeeding image slice.[32] After the software reconstructs the image and the model, the physician can slice through the 3D TRUS image to select target biopsy locations. If the procedure is a re-biopsy, then previous biopsy locations can be viewed for planning (see Figure 2.6.)

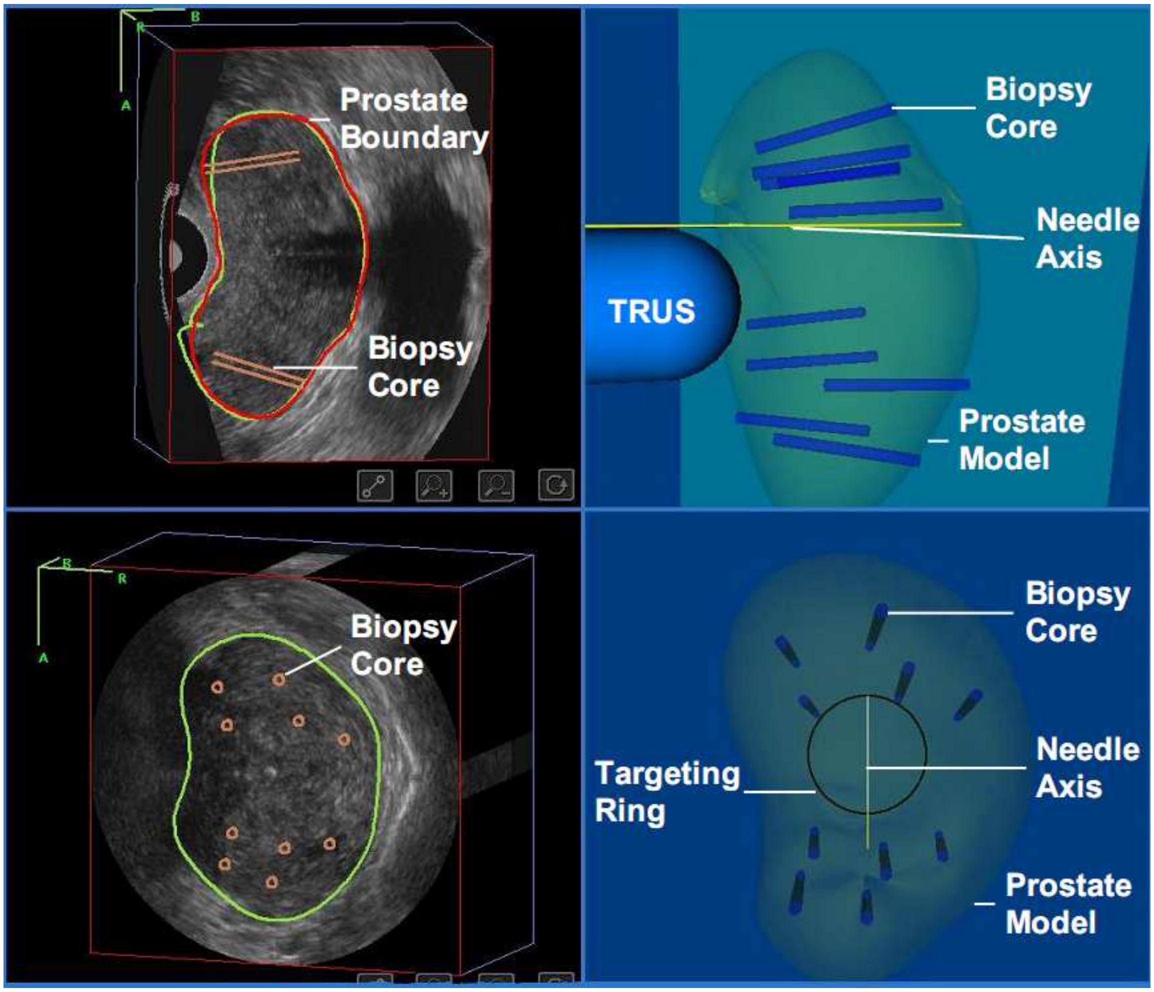

Figure 2.6: For rebiopsy, the patient's prostate can be viewed to show the previous biopsy plan (top left). In addition, the physician can also evaluate the registration by comparing the previously segmented prostate boundary (red line) with the currently segmented boundary (green line, bottom left corner). The coronal view of the patient's prostate with the segmented boundary and circles representing the location of the previous biopsy cores (top and bottom right). The 3D locations of the biopsy core are displayed within the

3D prostate models. The targeting ring in the bottom right window shows all the possible needle paths that intersect the selected target by rotating the TRUS about its long axis.

2.2.3 Software Components for 3D Tracking and Recording

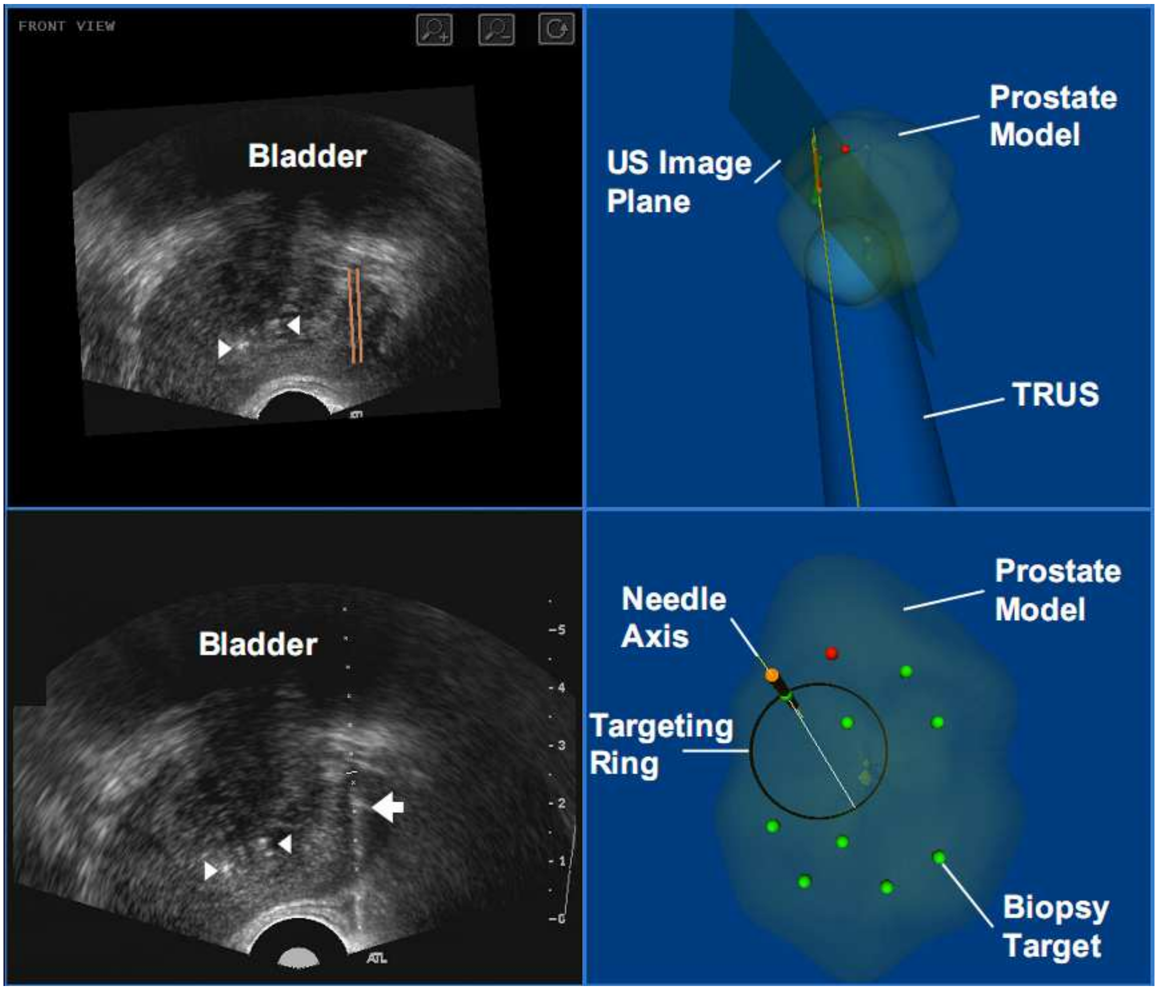

Figure 2.7: The 3D biopsy system interface is composed of four windows: (top left) the 3D TRUS image dynamically sliced to match the real-time TRUS probe 3D orientation, (bottom left) the live 2D TRUS video stream, (right side) and the 3D location of the targets displayed within the 3D prostate models. The targeting ring in the bottom right window shows all the possible needle paths that intersect the preplanned target by rotating the TRUS about its long axis. This allows the physician to maneuver the TRUS to the target (highlighted by the red dot) in the shortest possible distance. The biopsy needle (arrow) is visible within the real-time 2D TRUS image. The bladder (hypoechoic region anterior to prostate) and calcifications within the prostate (arrow head) illustrate anatomical correspondence between the real-time and static 3D image.

Once the 3D image scanning and biopsy plan are complete, the system displays a 3D needle guidance interface to facilitate the systematic targeting of each biopsy location. Throughout the biopsy procedure, the 3D location and orientation of the TRUS transducer is tracked and displayed in real time. Figure 2.7 shows the biopsy interface, which is composed of 4 windows: the 2D TRUS video stream, the 3D TRUS image, and two 3D model views. The 2D TRUS window (bottom left) displays the real-time 2D TRUS image streamed from the ultrasound machine. The 3D TRUS window (top left) contains the 3D TRUS image sliced in real time to correspond to the orientation and position of the TRUS probe. This correspondence allows the physician to compare the static 3D image with the real-time 2D image. Finally, the two 3D targeting windows show (i) the coronal and perspective views of the 3D prostate model, (ii) the real-time position of the 2D TRUS image plane, (iii) and the expected path of the biopsy needle as defined by the biopsy guide.

The targeting windows aid the physician in guiding the needle to each preplanned target. The targeting circle on the screen (Figs. 2.6 and 2.7) illustrates all accessible needle trajectories by rotating the US probe about its long axis. This shows the physician the shortest distance to each preplanned target.

2.3 System Validation Methods

We used an HDI 3500 US system and C9-5 (9-5 MHz) TRUS probe (Philips Medical Systems, Seattle, WA) in the following experiments. The resolution of the Philips scan head was determined experimentally by measuring the diameter of a wire (full width at half maximum) within a preset focal zone 3 cm deep in a bath of distilled water and 7% glycerol by weight, giving a speed of sound of 1540 m/s at a temperature of 20°C. The axial, lateral and elevational resolutions were 1.2, 1.4 and 2.5mm respectively.

2.3.1 Geometric Reconstruction

The accuracy of 3D geometric reconstruction of the TRUS image based on manual rotation of the transducer was verified using a string phantom,[33] which was immersed in a bath of distilled water and 7% glycerol (by weight). The string phantom consists of four layers of orthogonally intersecting monofilament nylon string with a diameter of 0.10 mm, which are anchored to the sides of a brass frame of the following dimensions: 12.2 cm (length) by 12.2 cm (width) by 3.0 cm (height). The intersections of the strings and each of the layers are spaced 10 mm apart, and each layer is offset by 2.5 mm so that upper layers of strings do not shadow the subsequent layers.

The tracking apparatus was positioned with the tip of the TRUS transducer placed below the surface of the glycerol solution. The transducer was then manually rotated 200° around its long axis (z-direction) to acquire a 3D US image of the string phantom. Using this 3D image, the spacing between the strings was measured in the three principal views {(x,y), (x,z), and (y,z)}. The measurements for each plane were then repeated fifteen times, and the mean, standard deviation, and the standard error for Δx, Δy, Δz were then determined.

2.3.2 3D Segmentation

A certified Ultrasound Calibration Phantom, which is constructed of Zerdine®, (Computerized Imaging Reference Systems Inc, Norfolk, Virginia) was used to assess the accuracy of volumetric measurements. The phantom had an embedded 21.5 cm^3 egg-shaped object 1 cm below the surface of the phantom, simulating the location and size of a small-to-medium sized prostate.

To verify the 3D segmentation accuracy of our system, the reconstructed volume of the embedded egg-shaped object was compared to that of its known volume. A 3D TRUS image of the phantom was acquired and the semi-automated segmentation algorithm was used to generate a 3D model of the embedded object. The volume of the segmented model was then compared to the certified volume of the object to quantify the volume measurement error of the 3D segmentation. The phantom was independently scanned 15 times and each object was semi-automatically segmented using the software described in section 2.2 to calculate mean and standard deviation values for the volume error. The volume error $V^{error}(V, V^*)$ was defined as the percentage difference between the reconstructed volume, V, and the known volume of the scanned object V^*:

$$V_{error} = \frac{V - V^*}{V^*} \qquad [4]$$

To determine the impact the semi-automated segmentation algorithm has on the volume error, the following volume metrics were used to compare the reconstructed volume to a manually segmented volume as a gold standard.[34] The sensitivity S(V, V^{man}) was used to determine the portion of the reconstructed volume, V, that intersects the manually segmented volume V^{man}:

$$S = \frac{V \bigcap V^{man}}{V^{man}} \quad . \qquad [5a]$$

The difference D(V, V^{man}) was used to measure the proportion of the segmented volumes that is not correctly overlapped:

$$D = \frac{V \bigcup V^{man} - V \bigcap V^{man}}{V^{man}} \quad . \qquad [5b]$$

2.3.3 Mock Biopsy on Prostate Phantoms

Mock biopsy procedures were performed on an agar-based tissue-mimicking phantom to quantify the accuracy of the 3D TRUS system for guiding biopsies and recording the 3D location of the biopsy core. The agar phantom consisted of an agar-based prostate model[35] embedded in surrounding background agar.[34, 35] The background and prostate model were constructed by adding 7% by mass of glycerol solution with agar powder to produce a speed of sound similar to that of human tissue (1540 m/s).[30] The mould of the prostate model was generated from segmented 3D image of a human prostate (volume = 21.5 cm^3). The background material contained cellulose (15% by weight) to create acoustic backscattering in US, making the surrounding region appear bright relative to the prostate. Tungsten powder (1% by weight) was added to the prostate model to increase the X-ray attenuation within the prostate, making it visible in the CT image. Finally, stainless steel ball bearings of 1 mm diameter were placed in a geodesic configuration within the background material, surrounding the prostate model. These ball bearings served as fiducials for coordinate registration between the 3D TRUS and CT images.

Six independent mock biopsies were performed on five prostate phantoms for a total of 30 cores, using the 3D TRUS biopsy system. To start the procedure, the tracking apparatus was positioned with the tip of the TRUS transducer contacting the surface of the agar phantom and aligned with the center of the prostate gland immediately adjacent to its posterior aspect. A 3D TRUS image of the prostate was then acquired (and reconstructed) by manual 200° rotation of the TRUS probe about its long axis and was reconstructed in a cartesian reference frame with isometric voxel dimensions (0.194 mm^3). A semi-automated segmentation was then used to generate a 3D segmented model of the prostate.[30-32, 34] A traditional sextant biopsy plan was followed, with contralateral biopsy targets placed at the base, mid-gland, and apex of the prostate. A systematic biopsy of each target was performed and the location of each biopsy core was recorded within the 3D system (e.g. Figure 2.7).

The agar phantom was imaged, post-biopsy, in an eXplore Locus Ultra Pre-Clinical CT scanner (GE Healthcare, London, ON), which is used for small animal micro-imaging. The high resolution CT image (isometric voxel dimensions of 0.15 mm^3) served as the gold standard for the true location of each biopsy core. In the CT image, a biopsy core was evident as an air track left from the insertion of the 18-gauge needle into the agar phantom. The location of a biopsy core was extracted from a CT image by selecting multiple points along the center of the air track, from the base to the tip. A linear regression of the points was used to define the 3D trajectory of the needle, and the location of the 19 mm biopsy core was defined relative to the tip of the air track. The centers of the 1 mm fiducial markers surrounding the prostate were manually selected from corresponding CT and 3D TRUS images to co-register the two coordinate systems.

2.3.3.1 Biopsy System Errors

The 3D biopsy system was evaluated for its ability to (a) guide a biopsy needle to a 3D target and (b) record the location of the biopsy core in 3D following the methods described by Cool et al.[34] The process of directing a biopsy needle toward a target using the 3D TRUS system has human, machine, and tissue factors as all potential sources of error. The needle guidance error, *NGE*, measured the mean complete error associated with a user guiding the biopsy needle to predefined targets. This error was quantified for all biopsy sites, *n* as the perpendicular distance between the i^{th} target location (a_i) and the corresponding "true" biopsy core identified in the 3D CT image (b_i^{CT}):

$$NGE = \frac{\sum_{i=1}^{n} D\left(a_i, b_i^{CT}\right)}{n}, \qquad [6]$$

where $D(\ )$ is a function measuring the 3D minimum distance between a 3D target point, a_i, and a 3D biopsy core line segment, b_i^{CT}. *NGE* is composed of two quantifiable errors: one related to human guidance error, *NGHE*, and the other related to the needle trajectory error, *NTE*. Conceptually, *NGHE* represents the ability of the user to align the biopsy target within the center of the expected needle path of the biopsy system. *NGHE* was measured by comparing the 3D Euclidean distance between the biopsy targets, a_i, and the expected path of the biopsy needle, p_i, within the 2D TRUS image:

$$NGHE = \frac{\sum_{i=1}^{n} \left|a_i - p_i\right|}{n}. \qquad [7]$$

It should be noted that the preplanned biopsy targets, a_i, were virtual targets, fixed within the 3D TRUS system tracking space, not within the real 3D world. Therefore, both the target, a_i, and the expected needle path, p_i, were within the same 3D tracking space and *NGHE* was only influenced by human errors and not by errors in the 3D system, such as positional tracking error, inaccurate system calibration, poor 3D TRUS image to world correspondence, etc.

Needle trajectory error, *NTE*, was calculated to determine how well the biopsy needle traveled along the expected biopsy needle path, p_i, defined by the TRUS manufacturer. *NTE* was measured within the 2D TRUS image plane and defined as the minimum distance between the actual needle trajectory, b^{TRUS}, and the expected needle trajectory, p_i :

$$NTE = \frac{\sum_{i=1}^{n} D\left(p_i, b_i^{TRUS}\right)}{n}. \qquad [8]$$

The accuracy of the biopsy system to record biopsy core locations in 3D (Biopsy Localization Error or *BLE*) was quantified using three metrics: BLE^{min}, BLE^{center}, and BLE^{θ}. BLE^{min} is defined as the minimum distance between the "true" biopsy core from CT, b_i^{CT}, and the record 3D TRUS biopsy core, b_i^{TRUS}.

$$BLE^{\min} = \frac{\sum_{i=1}^{n} D\left(b_i^{CT}, b_i^{TRUS}\right)}{n}, \qquad [9]$$

where *D*( ) measures the minimum distance between two 3D biopsy core line segments. BLE^{θ} is the angle between the cores when projected on a plane perpendicular to BLE^{min}:

$$BLE^{\theta} = \frac{\sum_{i=1}^{n} \theta\left(b_i^{CT}, b_i^{TRUS}\right)}{n}, \qquad [10]$$

where $\theta(\boldsymbol{u},\boldsymbol{v})$ is the function that calculates the minimum angle between vectors $\boldsymbol{u}$ and $\boldsymbol{v}$. BLE^{center} is the center-to-center distance between corresponding biopsy cores:

$$BLE^{center} = \frac{\sum_{i=1}^{n} \left| b_i^{CT}(0.5) - b_i^{TRUS}(0.5) \right|}{n}, \qquad [11]$$

where *b*(0.5) represents the center point of the 19 mm biopsy core *b*.

2.3.4 Clinical Evaluation

The 3D biopsy system was tested clinically on three patients to determine the extent of prostate motion and deformation, and the system's impact on workflow. All subjects provided written consent to the study protocol approved by The University of Western Ontario Standing Board on Human Ethics prior to imaging. The workflow of the current 2D standard procedure was maintained with the addition of a 10-second 3D US scan at the start and end of the procedure. Anatomical landmarks such as the prostate boundary or calcifications within the patient's prostate were used for qualitative comparison of the real-time 2D TRUS image with the 3D TRUS image to identify correspondence issues resulting from prostate deformation, patient motion or tracking inaccuracies.

An in-plane quantitative assessment of prostate motion and deformation was evaluated by measuring the distance between calcifications found in the 2D slices of a 3D TRUS image, which is generated at the start of the procedure to the real-time 2D US images obtained at a later time. We defined the in-plane displacement as the absolute distance between the true location of the landmark and its location within the initial 3D image.

2.4 Results

2.4.1 Geometric Reconstruction

A 3D TRUS image of the string phantom was successfully reconstructed without significant visible discontinuity or probe alignment artifacts. Table 2.1 show the distances between the strings within the phantom measured in the three orthogonal views {(x, y), (x, z), (y, z)}. The distance measured in each plane overestimated the known manufactured inter-string distance, with measured errors varying from 3.1% to 4.0%.

Table 2.1: Results from the 3D geometric reconstruction experiment illustrating the mean distance between the strings, the measurement error ($|u-u_0|$), standard deviation (STD), and the number of data points (n).

	Y-Z Plane		***X-Z Plane***		***X-Y Plane***	
	y	*z*	*x*	*z*	*x*	*y*
Mean	10.38	10.65	10.40	10.62	10.37	10.38
$\lvert u-u_0 \rvert$ (mm)	0.38	0.35	0.40	0.32	0.37	0.38
Error (%)	3.80	3.40	4.00	3.11	3.70	3.80
STD (mm)	0.11	0.14	0.13	0.14	0.14	0.12
n	45	45	45	45	45	45

2.4.2 3D Segmentation

Table 2.2 shows the results from the scan of the phantom and the segmentations of the 3D object. Multiple 3D TRUS images were successfully reconstructed from the certified industrial US phantom. The egg shaped object resembling a prostate was segmented using both the semi-automatic segmentation algorithm with a mean volume error of 4.7%. Furthermore, the reconstructed prostate models overlapped with the gold standard volumes with a sensitivity of 95.4%, and difference error of 7.5%.

Table 2.2: The volume of the segmented model was compared to the certified volume of the object to quantify the volume measurement error of the 3D segmentation. The volume error (eq. 4) compares the difference between the reconstructed volume, V, and the known volume of the scanned object, V^{*}=21.5 cm^3. The following volume metrics were used to compare the semi-automated segmented volume to a manually segmented volume. The sensitivity (eq. 5a) was used to determine the portion of the reconstructed volume, V that intersects the manually segmented volume V^{man}, and the difference (eq. 5b) measured the proportion of the segmented volumes that is not correctly overlapped:

Volume-based Metrics	
Semi-automatic segmented Volume	20.49±0.16
Manually Segmented Volume (cm^3)	20.83±0.16
Overlap Volume (cm^3)	19.88±0.26
Volume Error (%)	4.69
Sensitivity (%)	95.44
Difference **(%)**	7.50

2.4.3 Needle Guidance

The quantitative results for 3D biopsy needle guidance and recording of biopsy cores are summarized in Table 2.3. Navigation of the biopsy needle to each target had a mean *NGE* = 2.13 ± 1.28 mm. A one-tailed t-test showed the needle-guidance error was statistically less than 5mm ($p<0.001$, B=0.2, n=30), which is the smallest tumour considered clinically significant.[36] Figure 2.8 shows a plot of the *NGE*, which is decomposed into in- and out-of-plane errors. The needle deflection is primarily in-plane with little out-of-plane error. Human navigation error in directing the probe to the biopsy target, *NGHE*, had a mean error of 0.54±0.41 mm. Trajectory error of the biopsy needle deviating from the expected needle path, *NTE*, was 2.08±1.59 mm. Figure 2.9a shows a comparison of the 3D biopsy cores for an 18-gauge needle. The biopsy cores overlapped

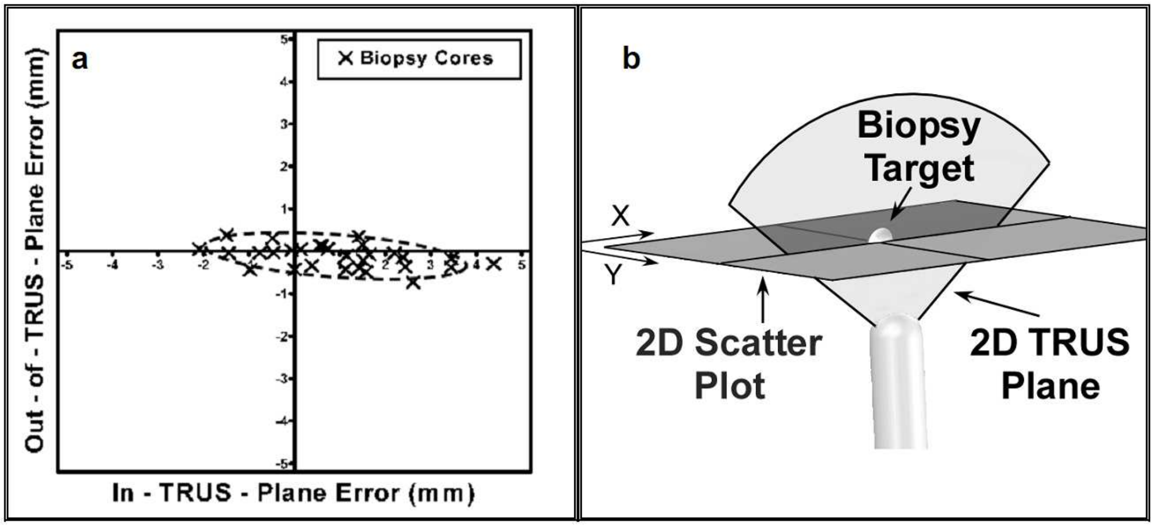

Figure 2.8: (a) Scatter plot of the in-TRUS plane vs. out-of-TRUS plane needle guidance error, *NGE*. The diagram (b) illustrates the relative orientation of the TRUS to the target and the scatter plot. The scatter plot in is a cross-sectional plane, perpendicular to the 2D TRUS image plane, where the plot's x-axis corresponds the x-axis of the TRUS image (positive and negative x values are more lateral and more medial in the TRUS image, respectively) and the plot's y-axis is parallel to the normal of the 2D TRUS image plane. The origin of the plot is centered on each biopsy target point, x_i, with the "true" biopsy core location, b_i^{CT}, plotted with an "x". This diagram illustrates the relative orientation of the TRUS.

with each target (white spheres) showing that the needle was successfully guided to each biopsy target location. Figure 2.9b shows a qualitative comparison of the 3D biopsy cores recorded using the 3D TRUS system (black) with the gold standard cores (white). The biopsy cores were accurately localized to 1.51±0.92 mm (BLE^{min}) and with a mean angulation difference of 6.68±2.23° ($BLE^{\square}$). The center-to-center distance (BLE^{center}) between corresponding biopsy cores was larger than BLE^{min}, at 3.87±1.81 mm.

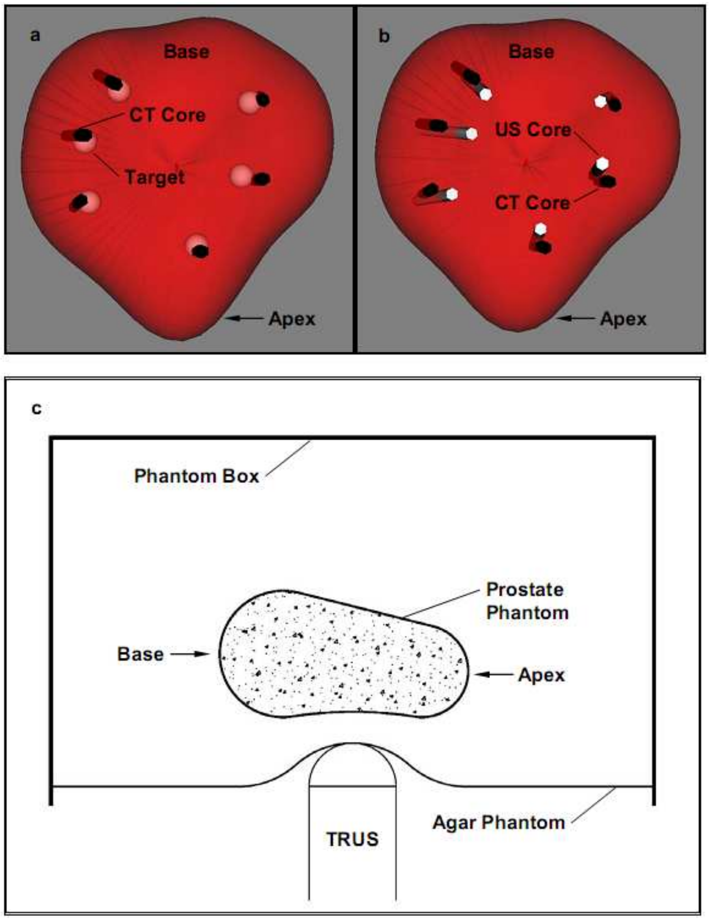

Figure 2.9: (a) Coronal view of the prostate as viewed from the end of the TRUS probe shows the CT gold standard biopsy cores (black cylinders) and the corresponding biopsy targets (grey dots). (b) The image on the right shows the coronal view of the prostate model with the US biopsy cores recorded within the 3D biopsy system (black) and the corresponding CT gold standard biopsy cores (white). The cylinders represent the 18-gauge biopsy core tissue samples. The data highlighted in Table 2.3 was used to construct the phantom images. (c) Illustration of the simulated prostate orientation within the agar phantom with respect to the TRUS probe.

Table 2.3: 3D biopsy system accuracy based on the biopsy core analysis described in section 2.3.3. Needle guidance error, NGE (eq. 6), needle guidance human error, NGHE (eq. 7), and needle trajectory error, NTE (eq. 8), all evaluate biopsy targeting accuracy. The biopsy localization metrics BLE^{min}, BLE^{center} and BLE^{θ} (see eq. 9-11), indicate the errors in recording the 3D location of the biopsy cores. 95% CI represents the confidence interval of the mean. All of the values are reported as Mean±STD. The results from the experiment highlighted in bold are illustrated in Figure 2.9.

	System Accuracy			***Localization Error Metrics***		
Experiment	*NGE* *(mm)*	*NGHE* *(mm)*	*NTE* *(mm)*	BLE^{min} *(mm)*	BLE^{center} *(mm)*	BLE^{θ} *(degrees)*
1	3.79±0.86	0.37±0.51	4.41±0.27	1.93±0.75	3.98±1.45	5.65±2.04
2	0.70±0.32	0.27±0.12	1.44±0.46	1.08±0.61	3.82±2.52	5.61±3.30
3	1.95±0.39	0.19±0.09	1.97±0.59	2.39±0.98	4.07±1.22	7.76±2.01
4	2.21±1.39	0.99±0.08	2.06±1.94	1.20±0.67	4.34±3.17	6.46±2.55
5	1.99+0.77	0.90±0.11	0.50±0.51	0.97±0.92	3.13±2.00	7.93±1.20
Mean	2.13+1.28	0.54±0.41	2.08±1.59	1.51±0.92	3.87±1.81	6.68±2.23
95% CI	(1.7, 2.6)	(0.4, 0.7)	(1.5, 2.7)	(1.2, 1.8)	(3.2, 4.5)	(5.9, 7.9)

2.4.4 Clinical Evaluation

Figure 2.5 shows axial, sagittal and coronal views of the 3D TRUS image of a patient's prostate that were obtained during a biopsy procedure. There were no obvious discontinuities or artifacts within the 3D image, even in the coronal plane, which lies perpendicular to the axis of rotation for 3D scanning.

Figure 2.10 shows a sequence of images that were captured during a sextant biopsy at the start (top row), mid-point (3rd) biopsy (middle row), and at the end (bottom row) of the procedure. The 2D slice from the 3D static image (Figure 2.10, left column) is shown with the prostate boundary in green. The corresponding 2D real time video stream (Figure 2.10, middle column) displays a dotted outline of the prostate boundary from the 3D image. The images in the right column show the real time 2D TRUS images after needle insertion (Figure 2.10, white arrow). There is a strong correlation between the real-time 2D TRUS image (middle column) and the original 3D image (left column) time point, suggesting that there were no major changes in the prostate at each location and morphology during the biopsy procedure. Alignment between the initial 3D and real-

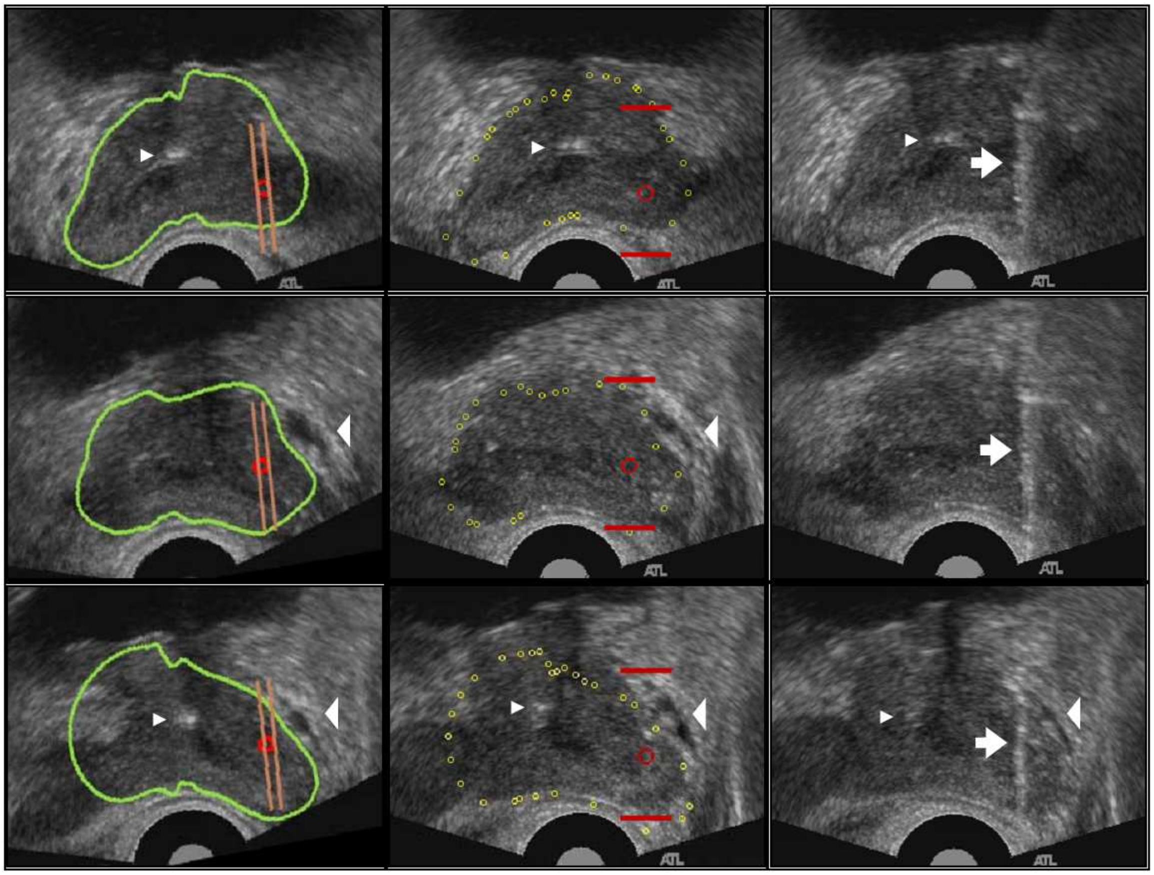

Figure 2.10: A sequence of images captured at the beginning (top row), midpoint (middle row) and end (bottom row) of a sextant biopsy procedure. Left column: The 2D slice from the 3D static image is shown with the prostate boundary segmented in green. The circle represents the pre-planned target, and the parallel lines show the estimated location of the biopsy core. Center column: The corresponding 2D real-time video stream displays a dotted outline of the prostate boundary from the 3D image in the left column. The location of the pre-planned target is highlighted by the circle on the 2D image, and the extents of the biopsy notch (19 mm) are designated by the two horizontal lines. Spatial correspondence is maintained even after needle insertion (white arrow) as seen in the real time 2D TRUS images (right column). White speckled calcifications within the prostate boundary (small arrowheads), cysts (large arrowheads) and the location of the segmented prostate boundary show good correspondence between the real-time (center column) and static 3D image (left column) throughout the entire procedure.

time image was maintained throughout the entire procedure, even after six biopsies (bottom row). Similar anatomical landmarks (Figure 2.10, calcifications) were visible in both the 3D and real-time 2D images, indicating a good correlation. The mean in-plane displacement of calcifications used as anatomical markers identified in images obtained within the prostates of 20 patients was 0.74±0.71 mm (see Table 2.4).[37] The measured in-plane displacements of calcifications as well as the maintenance of good correlation between the images in each row suggest that the prostate did not move or deform to a prohibitive extent.

Table 2.4: Mean in-plane displacement of anatomical landmarks identified in three patients participating in an ongoing clinical trial. The standard deviation (STD), maximum and minimum displacement, and the number of landmarks (n) identified in the images are reported.

	Displacement *(mm)*
Mean	0.74
Maximum	6.78
Minimum	0.03
STD	0.71
n	670

Figure 2.11 shows a case where the patient moved during the procedure. The 2D axial slice from the initial 3D image does not correlate well with the 2D TRUS image from the US machine. The prostate has moved from its original scanned position and the shape of the prostate boundary has also changed.

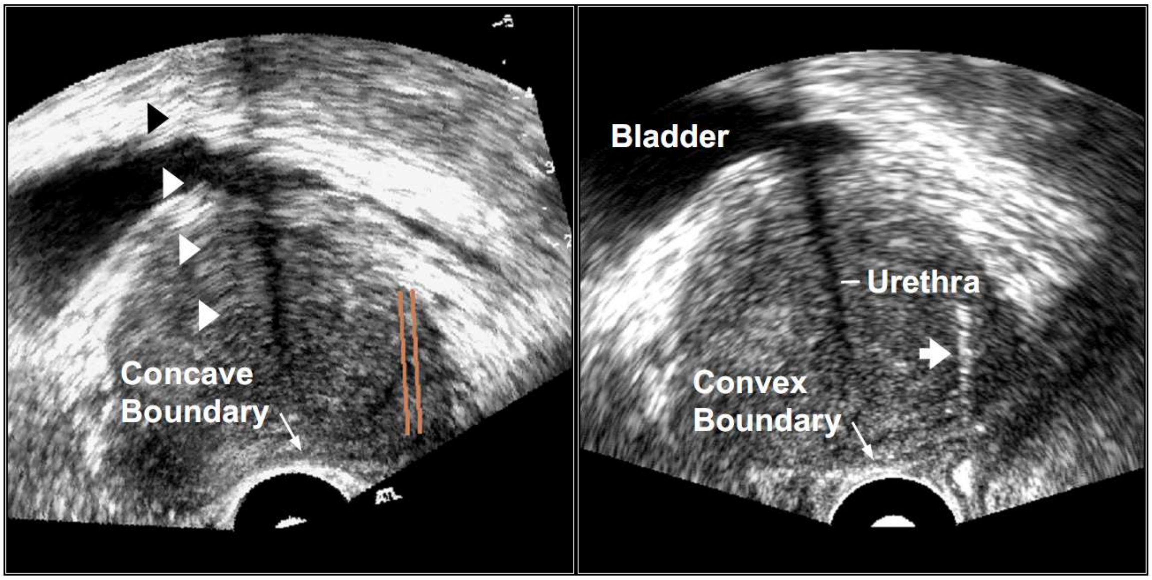

Figure 2.11: Comparison of (a) the 2D axial slice of the 3D TRUS image with (b) the real-time 2D TRUS image captured immediately after the biopsy gun was fired; the needle is still visible in the image on the right (arrow). If the patient moves during the procedure, not only does the prostate move from its original scanned position, but also its shape changes. The prostate boundary next to the TRUS tip is concave in the 2D axial slice, and convex in the real time snapshot. The discontinuity in the 3D image highlighted by the arrowheads was the result of patient motion during a 3D scan. The bladder (hypoechoic region anterior to the prostate boundary) and urethra are visible in each image.

2.5 Discussion

Volume calculations from the ultrasound phantoms were within five percent of the certified standard and the shape-based metrics (sensitivity = 95%, error = 4.7%) show a high degree of overlap correspondence. Together with the string phantom results they suggest that geometrical distortion due to manual rotation of the transducer and semi-automatic segmentation algorithm were not significant.

The user was able to use the system to accurately guide a biopsy needle in vitro to predefined targets with an average error of 2.1 mm. This error was primarily due to the large NTE as a result of needle deflection in our prostate phantom.[34] In spite of this error, the targeting accuracy was within the 5 mm radius of the smallest tumours considered clinically significant (tumour radius less than 0.5 cm is considered insignificant).[36]

From the results of our ongoing patient study, we were able to guide the biopsy needle to pre-determined targets and maintain proper correspondence of our real-time 2D and 3D images by minimizing prostate motion through a variety of mechanical and software mechanisms. By providing mechanical means to stabilize and support the US probe, constant pressure between the probe and rectal wall was maintained. The remote fulcrum (located at the anus) further stabilized the pressure by minimizing motion between the RCM and probe tip. Further, constant pressure on the prostate was maintained with the probe tip by simply pivoting about the RCM. To complement this mechanical feature, we implemented a visual ring representation in the software interface where the axis of the needle intersects the depth of the pre-selected target (Figure 2.5). This ring provides visual guidance in manipulating and orienting the probe to the target in the shortest distance possible, while minimizing motion of the probe and maintaining constant pressure on the prostate. The shortest path is the minimum yaw and pitch angle needed to align the needle guide to a predetermined target. This is accomplished by rolling the probe and changing the pitch angle to align the needle axis with the target. Although minimizing probe motion and its effects on the prostate would be preferred, it is also important the physician avoids the urethra and nearby organs (including the bladder). This imposes restrictions on the entry points as it is necessary for the physician to be able to see sensitive areas so they can be avoided.

Patient motion on the biopsy table that cannot be controlled (see Figure 2.11) or prostate motion would result in the real-time 2D image not matching the 2D corresponding slice from the 3D TRUS image. This would provide a visual warning to the physician that the pre-selected targets are no longer valid, requiring the physician to perform another 3D scan. Prostate motion can be corrected by registering the planned and recorded biopsy locations in the 3D US image to the current image after the prostate has moved. Although patient motion during the procedure is infrequent, correction for patient motion errors is a focus of our future work.

2.6 Conclusions

By adding 3D information to the prostate biopsy procedure, our system should improve the recording procedure as well as the physician’s ability to accurately guide the biopsy needle to selected targets identified using other imaging modalities. This would be beneficial in cases where the patient was diagnosed on biopsy to have ASAP and requires the physician to rebiopsy the same area. Using the 3D TRUS image, the physician was able to observe the patient's prostate in views currently not possible in 2D procedures. Overall, our 3D system should result in prostate biopsy procedures that are stereotactic and more reproducible, which may lead to higher cancer detection rates and improve the yield on repeat biopsy

Finally, integration of our system into the current prostate biopsy procedure requires minimal physician retraining as procedural workflow is maintained. By adhering to the imaging tools and protocols of current biopsy procedures, clinical integration of our 3D system should be cost effective.

2.7 References

1. Horner M, Ries L, Krapcho M, et al, eds. SEER Cancer Statistics Review, 1975–2006. Bethesda, MD: National Cancer Institute; 2009.

2. Fink KG, Hutarew G, Esterbauer B, et al. Evaluation of transition zone and lateral sextant biopsies for prostate cancer detection after initial sextant biopsy. *Urology.* Apr 2003;61(4):748-753.

3. Nelson WG, De Marzo AM, Isaacs WB. Prostate cancer. *N Engl J Med.* Jul 24 2003;349(4):366-381.

4. Eastham JA, Scardino PT. Early diagnosis and treatment of prostate cancer. *Dis Mon.* Sep 2001;47(9):421-459.

5. Eskew LA, Bare RL, McCullough DL. Systematic 5 region prostate biopsy is superior to sextant method for diagnosing carcinoma of the prostate. *J Urol.* Jan 1997;157(1):199-202; discussion 202-193.

6. Djavan B, Remzi M, Schulman CC, Marberger M, Zlotta AR. Repeat prostate biopsy: who, how and when?. A review. *Eur Urol.* Aug 2002;42(2):93-103.

7. Presti JC, Jr., O'Dowd GJ, Miller MC, Mattu R, Veltri RW. Extended peripheral zone biopsy schemes increase cancer detection rates and minimize variance in prostate specific antigen and age related cancer rates: results of a community multi-practice study. *J Urol.* Jan 2003;169(1):125-129.

8. Djavan B, Zlotta AR, Ekane S, et al. Is one set of sextant biopsies enough to rule out prostate Cancer? Influence of transition and total prostate volumes on prostate cancer yield. *Eur Urol.* Aug 2000;38(2):218-224.

9. Karakiewicz PI, Bazinet M, Aprikian AG, et al. Outcome of sextant biopsy according to gland volume. *Urology.* Jan 1997;49(1):55-59.

10. Keetch DW, Catalona WJ, Smith DS. Serial prostatic biopsies in men with persistently elevated serum prostate specific antigen values. *J Urol.* Jun 1994;151(6):1571-1574.

11. Park SJ, Miyake H, Hara I, Eto H. Predictors of prostate cancer on repeat transrectal ultrasound-guided systematic prostate biopsy. *Int J Urol.* Feb 2003;10(2):68-71.

12. Kranse R, Beemsterboer P, Rietbergen J, Habbema D, Hugosson J, Schroder FH. Predictors for biopsy outcome in the European Randomized Study of Screening for Prostate Cancer (Rotterdam region). *Prostate.* Jun 1 1999;39(4):316-322.

13. Coplen DE, Andriole GL, Yuan JJ, Catalona WJ. The ability of systematic transrectal ultrasound guided biopsy to detect prostate cancer in men with the clinical diagnosis of benign prostatic hyperplasia. *J Urol.* Jul 1991;146(1):75-77.

14. Iczkowski KA, Chen HM, Yang XJ, Beach RA. Prostate cancer diagnosed after initial biopsy with atypical small acinar proliferation suspicious for malignancy is similar to cancer found on initial biopsy. *Urology.* Nov 2002;60(5):851-854.

15. Iczkowski KA, Bassler TJ, Schwob VS, et al. Diagnosis of "suspicious for malignancy" in prostate biopsies: predictive value for cancer. *Urology.* May 1998;51(5):749-757; discussion 757-748.

16. San Francisco IF, DeWolf WC, Rosen S, Upton M, Olumi AF. Extended prostate needle biopsy improves concordance of Gleason grading between prostate needle biopsy and radical prostatectomy. *J Urology.* Jan 2003;169(1):136-140.

17. Thorson P, Humphrey PA. Minimal adenocarcinoma in prostate needle biopsy tissue. *Am J Clin Pathol.* Dec 2000;114(6):896-909.

18. Andriole GL, Bullock TL, Belani JS, et al. Is there a better way to biopsy the prostate? Prospects for a novel transrectal systematic biopsy approach. *Urology.* Dec 2007;70(6A):22-26.

19. Long JA, Daanen V, Moreau-Gaudry A, Troccaz J, Rambeaud JJ, Descotes JL. Prostate biopsies guided by three-dimensional real-time (4-D) transrectal ultrasonography on a phantom: comparative study versus two-dimensional transrectal ultrasound-guided biopsies. *Eur Urol.* Oct 2007;52(4):1097-1104.

20. Abul FT, Arun N, Abu-Assi MA, Asbeutah AM. Transrectal ultrasound guided biopsy for detecting prostate cancer: can random biopsies be reduced using the 4-dimensional technique? *Int Urol Nephrol.* 2007;39(2):517-524.

21. Megwalu II, Ferguson GG, Wei JT, et al. Evaluation of a novel precision template-guided biopsy system for detecting prostate cancer. *Bju International.* Sep 2008;102(5):546-550.

22. Hricak H, Choyke PL, Eberhardt SC, Leibel SA, Scardino PT. Imaging prostate cancer: A multidisciplinary perspective. *Radiology.* Apr 2007;243(1):28-53.

23. Fichtinger G, DeWeese TL, Patriciu A, et al. System for robotically assisted prostate biopsy and therapy with intraoperative CT guidance. *Acad Radiol.* Jan 2002;9(1):60-74.

24. Krieger A, Susil RC, Menard C, et al. Design of a novel MRI compatible manipulator for image guided prostate interventions. *IEEE T Bio-Med Eng.* Feb 2005;52(2):306-313.

25. Barnes AS, Haker SJ, Mulkern RV, So M, D'Amico AV, Tempany CM. Magnetic resonance spectroscopy-guided transperineal prostate biopsy and brachytherapy for recurrent prostate cancer. *Urology.* Dec 2005;66(6):131913-131915.

26. American Cancer Society: Detailed Guide: Prostate Cancer. http://wwwcancer.org/docroot/CRI/CRI_2_3x.asp?dt=36. Accessed November 7, 2007.

27. Taylor RH, Funda J, Eldridge B, et al. A Telerobotic Assistant for Laparoscopic Surgery. *Ieee Eng Med Biol.* May-Jun 1995;14(3):279-288.

28. Bax J, Cool D, Gardi L, Fenster A, Inventors. Apparatus for guiding a medical tool. US patent Pending. Sept 17, 2009, 2009.

29. Bax J, Cool D, Gardi L, et al. 3D transrectal ultrasound prostate biopsy using a mechanical Imaging and needle-guidance system - art. no. 691825. *Medical Imaging 2008: Visualization, Image-Guided Procedures, and Modeling, Pts 1 and 2.* 2008;6918:91825-91825.

30. Fenster A, Downey DB, Cardinal HN. Three-dimensional ultrasound imaging. *Phys Med Biol.* May 2001;46(5):R67-99.

31. Ladak HM, Mao F, Wang Y, Downey DB, Steinman DA, Fenster A. Prostate boundary segmentation from 2D ultrasound images. *Med Phys.* Aug 2000;27(8):1777-1788.

32. Wang Y, Cardinal HN, Downey DB, Fenster A. Semiautomatic three-dimensional segmentation of the prostate using two-dimensional ultrasound images. *Med Phys.* May 2003;30(5):887-897.

33. Wei Z, Wan G, Gardi L, Mills G, Downey D, Fenster A. Robot-assisted 3D-TRUS guided prostate brachytherapy: system integration and validation. *Med Phys.* Mar 2004;31(3):539-548.

34. Cool D, Sherebrin S, Izawa J, Chin J, Fenster A. Design and evaluation of a 3D transrectal ultrasound prostate biopsy system. *Med Phys.* Oct 2008;35(10):4695-4707.

35. Rickey DW, Picot PA, Christopher DA, Fenster A. A wall-less vessel phantom for Doppler ultrasound studies. *Ultrasound Med Biol.* 1995;21(9):1163-1176.

36. Epstein JI, Sanderson H, Carter HB, Scharfstein DO. Utility of saturation biopsy to predict insignificant cancer at radical prostatectomy. *Urology.* Aug 2005;66(2):356-360.

37. Bax J, Williams J, Cool D, Gardi L, Montreuil J, Karnik V, Sherebrin S, Romagnoli C, Fenster A, Mechanically assisted 3D prostate ultrasound imaging and biopsy needle-guidance system, *Proc. SPIE*, 2010; 7625, 76252Q.

Chapter 3

3 A Compact Mechatronic System for 3D Guided Prostate Interventions

3.1 Introduction

There has been an increase of 20% in the number of men diagnosed with prostate cancer (PCa) in the last decade, and this trend is projected to continue in the future, due to the demographic shift towards higher proportions of older men and the increased use of the prostate-specific antigen (PSA) blood test.[1-4] The use of the PSA test for early detection of PCa and the public's increased awareness about the disease have combined to increase the proportion of PCa diagnosed at an early and organ-confined stage, and in younger men.[1, 5] Improvements in transrectal ultrasound (TRUS) imaging, computer-aided dosimetry, and new treatment options have stimulated investigators to develop minimally invasive therapies for localized PCa, such as brachytherapy, cryosurgery, high-intensity focused ultrasound, and laser thermal ablation. Although transperineal TRUS-guided brachytherapy is the most advanced because of its high-dose delivery rates and low risk of incontinence and impotence, intense research is ongoing into improved and alternative forms of minimally invasive prostate therapy. However, in all these transperineal therapy techniques, it is critical that the needles be placed accurately within the prostate to deliver the therapy to the planned location and avoid damaging surrounding tissues.[6, 7]

A limitation of current TRUS-guided prostate brachytherapy involves the use of a template-based technique, which restricts the placement of radioactive seeds within the prostate. This technique uses a square template, which contains a series of holes spaced 5mm apart in a Cartesian grid. Using this template, needles are guided by the grid parallel to the long axis of the US transducer. However, due to the 5 mm spacing increments between the guidance holes, positioning of needles during the procedure is limited. Moreover, the use of this template is problematic for patients with enlarged prostates as a portion of the prostate may be occluded by the pubic arch. With the interference of the pubic arch, a parallel needle insertion is inadequate for targeting this occluded region of the prostate. As a result, there may be sub-optimal dose coverage of the prostate.[8]

There are an estimated 50,000 prostate brachytherapy procedures performed each year in the United States,[9] of which 17 to 27% of these patients have been reported to have preoperative pubic arch interference (PAI), and 6 to 19% of these cases had intra-operative PAI requiring the physician to alter the preplanned needle trajectory.[10, 11] These estimates could be higher as seed implants are not recommended for men with prostates larger than 60cm[3, 12]. One method currently used to deal with this problem is downsizing of the prostate using androgen deprivation therapy. Unfortunately, there are many drawbacks with using hormones, because negative side effects include sexual dysfunction, endocrine abnormalities, cardiovascular disease,[13] and increased health care costs.[10] To overcome intra-operative PAI, techniques like extending the lithotomy position, changing the probe angle,[10] gently bending the template guided needle using a manipulation ruler,[14] or inserting the needle using the freehand technique have shown success.[10] The problem with changing the patient orientation or probe angle is that the position of the prostate will change with respect to the preoperative image the plan was created on. Also, by using the manipulation ruler or freehand technique, the needle becomes decoupled from the image, thus forcing the physician to visualize the needle trajectory relative to the anatomy displayed in the image. It would be beneficial to develop an interactive needle guidance system for the procedure while preserving some of the user familiarity.

As there is a clinical need for an improved prostate therapy system, special purpose robotic TRUS therapy systems have emerged in the literature. Several researchers have developed robotic systems to improve targeting accuracy and needle coverage of the prostate. Phee et al. (2006) developed an automated system that delivers needles through a single entry point on the perineum, requiring only two degrees of rotation about a remote-center-of-motion (RCM).[15] A remote center of motion is a constrained motion where a portion of the machine can only pivot about a fixed point in space.[16] However, the problem with this approach is that inserting many needles through a single entry point would result in significant tissue damage at the entry point. To overcome the issue of using a fixed entry point, Bassan et al. (2009)[17] developed a robotic system that consists of a five degree-of-freedom (DOF) RCM manipulator supported by an adjustable passive arm (Yousef et al., 2006)[18] to position the robot. The advantage of these two systems is that the robotic devices can be manually positioned by the physician with little training. Fichtinger et al. (2006) developed a six DOF robotic arm to control a needle with three degrees of translation and three degrees of rotation about a RCM.[19] Wei et al. (2004) demonstrated that an industrial serial link robot can also be adapted to the procedure.[20] The limitations with these designs is that the imaging system is not directly coupled to the robotic needle manipulator, thus requiring an elaborate calibration procedure before each use.

To eliminate the need to recalibrate the system, Yu. et al. (2007) developed a 16 DOF robotic system to control both the TRUS probe and the needle,[21] which were fixed to a common base. Hu et al. (2007) also developed an automated system that is coupled directly to the US transducer.[22] This system consists of a three DOF needle positioning gantry, a two DOF US probe, a two DOF needle driver, and a one DOF seed pusher. Unfortunately, these systems are too bulky, and obstruct the physician’s view making them difficult to integrate into a clinical setting.

More recently, Salcudean et al. (2008) have developed a compact four DOF robot design and needle driving apparatus that can be mounted on a standard brachytherapy stepper.[23] Other compact robotic designs incorporating rotary and/or linear stages have also been developed by Hungr et al. (2009)[24], and Meltsner et al. (2007)[25]. Fichtinger et al. (2008) also designed a compact 4 DOF robotic device for the TRUS procedure by coupling the needle to computer controlled x-y stages using spherical misalignment bushings.[26] This system was originally developed by Kettenbach et al. (2005) for US guided biopsy,[27] and offers an improvement to the earlier prototypes. Not only are these robotic manipulators relatively compact, but by fixing the robot directly to the TRUS probe, the system does not need to be recalibrated before each procedure. However, since these devices, as well as the other robotic devices previously described, cannot be rear-driven, the physician must rely on the software or manual adjustment knobs to control the system and align the needle with the target while avoiding obstacles like previously inserted needles or the TRUS probe. Although the inability to rear drive a system can provide rigidity for needle insertion,[23] the physician does not have direct control over the needle placement. Without sufficient training, it may be difficult to successfully manipulate the needle positioning device and this may result in added complexity to the procedure.

Other groups have developed image guided robotic systems that use CT[28] and MRI[29]. Numerous other approaches including needle drilling[30] and tapping[31] have shown a decrease in prostate motion during needle insertion. However, these designs are non-standard techniques that require a modified surgical procedure.

Commercial robotic systems like the da Vinci Surgical System for endoscopic surgical procedures (Intuitive Surgical, Sunnyvale California), *B-RobII* designed for CT interventions (ARC Seibersdorf Research GmbH, Vienna, Austria), or the INNOMOTION MRI-compatible device (Innomedic, Herxheim & FZK Karlsruhe Germany & TH Gelsenkir) could also be adapted to guide a brachytherapy needle. An advantage of a commercial system is that these systems are FDA/Health Canada approved, which may reduce the time required to adapt to a new procedure. However, the workflow required to operate these systems differs significantly from current US guided brachytherapy protocols, thus requiring physicians to retrain themselves. Additionally, surgical robotic systems are expensive; it would be beneficial to develop an affordable solution without monopolizing the use of expensive equipment.

Ideally, any of the previously described robotic devices can be used to improve the needle placement accuracy before insertion and reduce procedure time by automatically placing the needle in the correct orientation at the patient's perineum.[19, 21] However, since US does not produce any harmful radiation and the risk of exposure from brachytherapy seed loading devices like the Mick® applicator (Mick Radio-Nuclear Instruments, Inc., Mount Vernon, NY) is not a concern, it is difficult to justify the use of an automated needle placement and insertion approach to improve safety or PAI. Although many robotic devices have been used successfully in a clinical setting, guiding a tool within the human body under computer guidance can produce potential hazards if the robot malfunctions.

Our objective is to develop a mechanical assisted prostate therapy system, which facilitates the physician in performing transperineal prostate therapy procedures, in which the needle can be positioned (i.e., readied for insertion) manually with improved resolution and flexibility, and the needle insertion into the prostate is done manually by the physician. Our approach to the problem differs from the robotic systems previously developed in that many of the benefits of a robotic system (accuracy and improved needle coverage) can be realized with the option to control the needle location and trajectory (including oblique) manually.

Our system has undergone a number of important design changes since our first computer-controlled needle positioning prototype.[32] Although the device can be computer controlled, to deal with the safety issues of using a fully automated robotic device, we propose this device should be used manually in a clinical setting. Since the system is back drivable when the unit is powered down, we could simply disconnect the power from the motors (except for the 3D scanning motor) or physically remove the motors. By doing so, the system becomes a needle tracking device with many flexible degrees of freedom, where the counterbalanced linkage and attached encoders support and track the needle position, giving the physician the same feel and level of control over the needle orientation as the free hand technique currently used. This will give the physician the freedom to position a needle at the desired location and appropriate angle, before manually inserting the needle.

By combining the original design with the principle of a fixed remote center of motion (RCM) and the use of 3D transrectal ultrasound (TRUS), the physician can interact directly with the device. Our design offers similar benefits as the design proposed by Phee et al. (2006) or Bassan et al. (2009), where the device can be used manually by the physician, with minimal training.[15, 17] The advantage offered with our system is that the needle entry into the patient’s skin can be adjusted with two DOF over the patient’s skin. The ability to adjust the needle entry point is an important feature as this allows the physician to perform both parallel and oblique needle insertions. To create a mechanically constrained RCM, we combined the design concept of a spherical linkage originally incorporated into our mechanically assisted prostate biopsy system[33] with our original prototype[32] to create a dynamically adjustable system with two degrees of translation in front of the patient's perineum and two degrees of rotation about a fixed point on the patient's skin. We used a spherical linkage instead of the goniometric arc design used by Phee et al. (2006)[15] or parallelogram linkage by Bassan et al. (2009)[17] because the spherical linkage is more compact and does not interfere with the physician's ability to see the needle entry point on the perineum.

3.2 System Design

3.2.1 Mechatronic Device

The needle positioning device as illustrated in Figure 3.1 comprises of an ultrasound transducer supported by a cradle and attached to a motorized assembly for 3D image acquisition, and a linkage to support the needle.[32, 34] The apparatus fixes the ultrasound probe to a common shaft from below to which all drive motors, position encoders, and linkage assembly are mounted. To automatically control the needle positioning device, we used four DC micromotors (MicroMo Electronics Clearwater, Florida) with a reduction ratio of 139:1, and integrated magnetic encoder (512 pulses per rev.). The motors were coupled to the needle positioning device in series to an external differential gear train and slip clutch. The differential gear train provided an additional point of manual adjustment for the physician through an adjustment knob (see Fig 3.1a, motor body), and the adjustable slip clutch protected the drive train when the system is rear driven by the physician. For the 3D scanning motor, we also used a DC micromotor (MicroMo Electronics Clearwater, Florida) with a reduction ratio of 590:1 and integrated magnetic encoder (512 pulses per rev.), connected in series to a slip clutch as a means to rotate the transducer for acquiring 3D images.

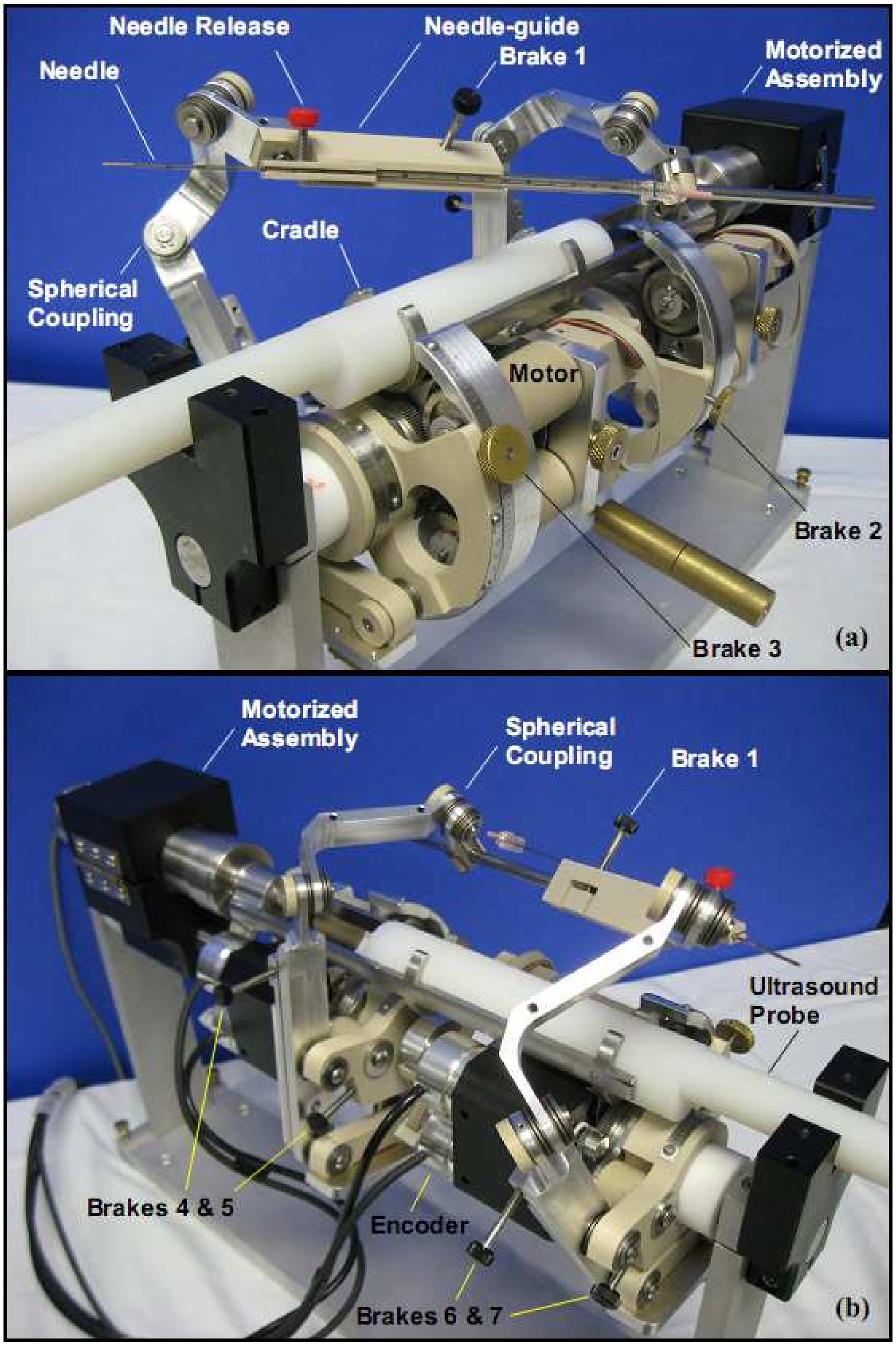

Figure 3.1: Photograph of the mechanical apparatus showing the (a) four motors and (b) four encoders that drive the linkage. The needle positioning device mounted below the ultrasound transducer is supporting the needle through a pair of spherical couplings at a compound angle relative to the long axis of the ultrasound transducer. The transducer is connected to a cradle, which in turn is attached to a motorized assembly to rotate the transducer about its long axis for 3D ultrasound acquisition.

The TRUS probe is also mounted onto the central shaft in order to provide a fixed reference and to facilitate a one-time calibration of the probe to the machine reference frame. By mounting the linkage and supporting electronics below the transducer, the physician's field of view is not obstructed. The central shaft provides a fixed reference for all movements of the apparatus and can be used to secure the apparatus to a surgical table or other operating room fixture (e.g., RTP-6000 Precision Stabilizer from Radiation Therapy Products, Seattle, WA).

Referring to Figures 3.1a and 3.1b, the mechatronic apparatus comprises of a telescoping needle guide that supports the needle through a removable needle holder. The needle holder with an aperture complementary to the needle diameter extends from the needle guide. The needle holder shown was designed to support an 18-gauge needle for implantation of radioactive seeds during prostate brachytherapy. Since the needle holder can be removed, other tools or needles can be adapted to the apparatus (e.g. cryotherapy needles or a biopsy gun and needle).

The needle guide is supported by two parallelogram linkages by means of a pair of spherical couplings. The RCM of each spherical coupling (Figure 3.2, point O) and attached needle guide ($O^F N$) is permitted to telescope between the front and rear RCM points (O^F and O^R). When the first and second parallelograms are differentially moved, the spherical couplings and telescoping needle guide allow the needle to be adjusted to any desired angular orientation in space relative to the central shaft ($U^R U^F$) supporting the needle positioning device. Since the needle guide axis is also aligned with each stationary point, any movement from either parallelogram will result in the needle guide axis pivoting about the stationary point of the opposing spherical linkage, thus resulting in no linear displacement of the intersection point "O" (O^F or O^R). A desired angle of tool insertion can therefore be attained by calculating the corresponding positions of the RCM points, which are mechanically constrained by the parallelogram linkages to move in a plane that is perpendicular to the long axis of the supporting shaft. Since the needle axis ($O^F N$) is also angled to the needle guide axis to intersect the RCM of the front spherical coupling (O^F), its motion becomes mechanically decoupled through the front spherical coupling.

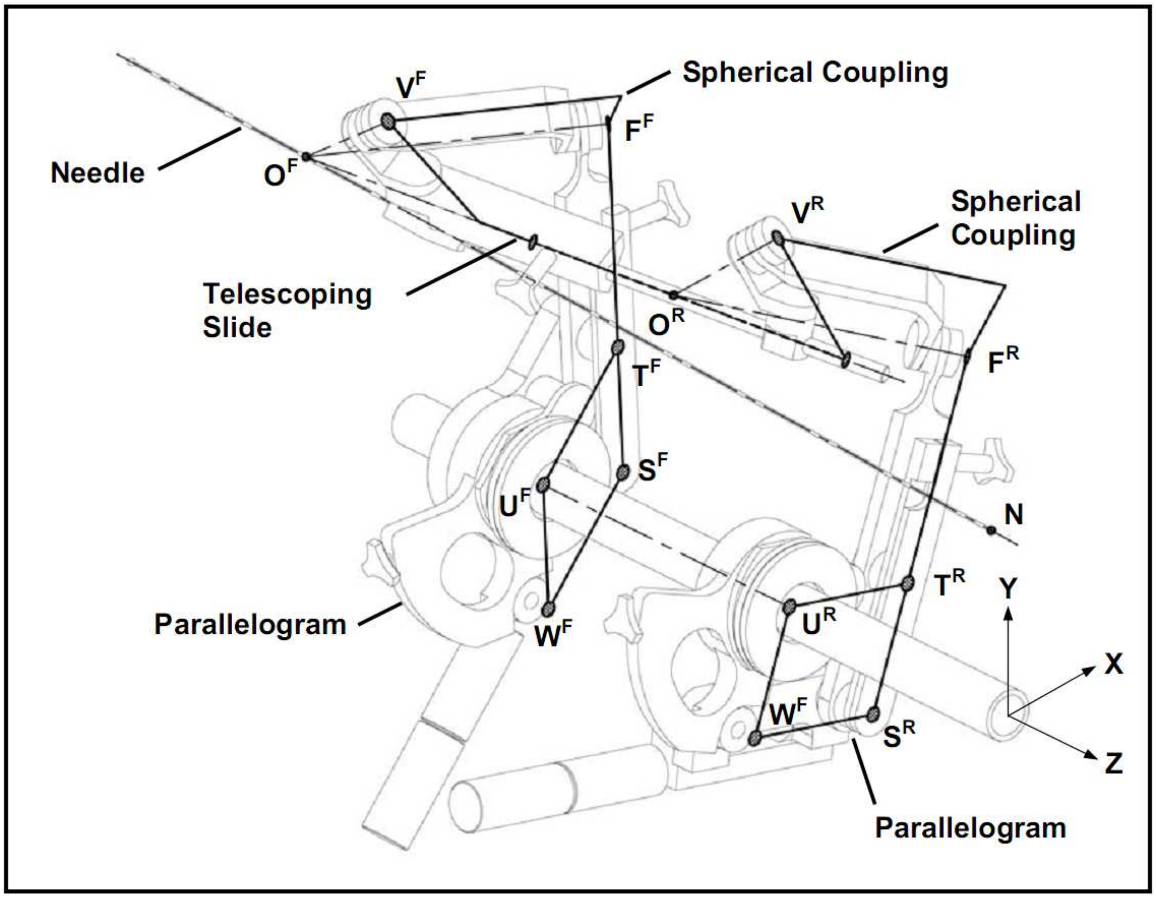

Figure 3.2: A partial rear perspective view of the device illustrating the different components of the linkage mechanism. The linkage is pinned to a common shaft that serves as the coordinate reference frame for the needle positioning device. This mechanism is an overconstrained linkage where 13 linkage components are configured in a manner where the needle is confined to four DOF about two points in space. The mechanism consists of two pinned parallelograms supporting a needle guide through a pair of spherical couplings. The needle guide is pinned to the forward and connected to the rear spherical coupling via a telescoping slide.

By aligning the front RCM to the patient's skin, the planar mobility of the needle at the patient's skin is decoupled from the rotational motion about the RCM and provides a visual queue to allow the physician to align the needle to the target within the image in two simple steps. First, the physician aligns the front RCM on the patient's skin at the point of entry by manipulating the front parallelogram linkage as shown in Figure 3.3a. The rear RCM remains fixed while the front parallelogram is moved and this changes the location of the needle tip, which is aligned to the front RCM. This gives the physician the flexibility to change the needle insertion point on the patient's skin.

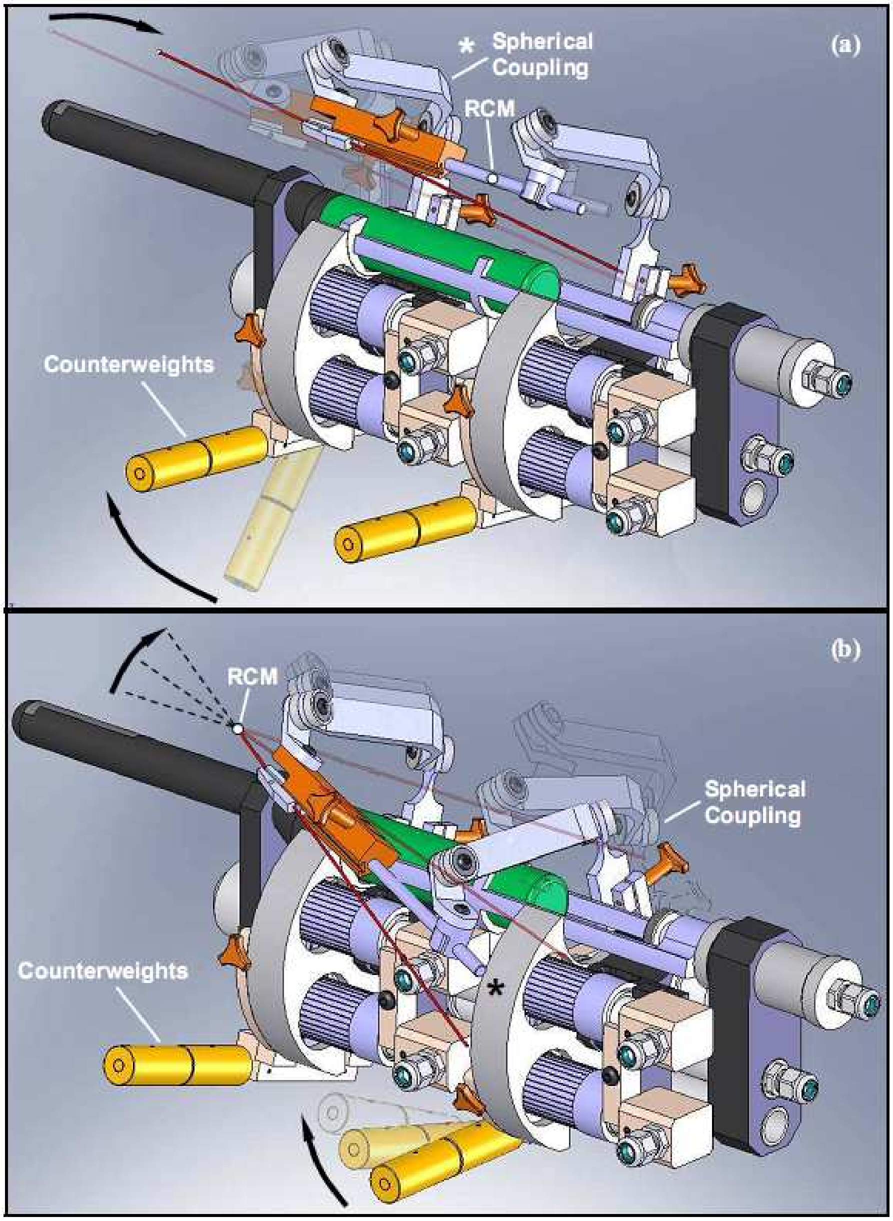

Figure 3.3: The device is decoupled through two remote pivot points created from the spherical couplings pinned to each parallelogram. Since the needle guide axis is also aligned with each stationary point, any movement from either parallelogram will result in the needle guide axis pivoting about the stationary point of the opposing spherical linkage, thus resulting in no linear displacement of the intersection point. The physician can manually align the needle axis in two simple steps. (a) First, the physician aligns the forward RCM by moving the forward parallelogram (the physician would manipulate the apparatus from *). (b) Then by moving the rear arms (from the point *), the physician can target a point of interest within the

patient’s anatomy by pivoting the needle about the forward RCM to the target. The counterweights support the weight of the needle guide and prevent the linkage from drifting when the brakes are not applied.

Then by manipulating the rear parallelogram from a point, as illustrated in Figure 3.3b in the second step, a point of interest within the ultrasound image can be targeted by angulating the needle through the front RCM to the target. Since the linkage mimics a simple lever that pivots about a stationary point on the patient’s skin when manipulated, as illustrated in Figure 3.3b, the physician can target a point of interest within the image with a mechanical advantage greater than unity. The mechanical advantage is defined as the ratio of the distance between the point where the physician handles the needle guide and the front RCM, to the distance between the RCM and target within the image (represented by a dashed line in Figure 3.3b). The parallelogram linkages were designed to mimic the workspace of a standard 6 cm square template commonly used for prostate interventions. By using the same parallelogram configuration in the rear, the linkage is capable of positioning the needle guide to a maximum angle of 28º relative to the longitudinal axis of the transducer.

Once the needle guide is in the correct position, it can be locked, allowing the needle to be inserted without concern that the apparatus will move. As such, four mechanical brakes are integrated into the design of the system so that each of its decoupled movements is constrained, allowing the progressive reduction in degrees of freedom (brakes 2, 3, 5 and 7 in Figs. 3.1a and b). Each of the four mechanical brakes was designed to reduce the mobility of the apparatus by constraining each link in the parallelogram that is pinned to the central shaft. Each of the brakes comprises of a locking knob attached to a clamping screw that exerts a clamping pressure on a split ring that resides inside each link.

After the needle has been inserted, three additional brakes can be used by the physician to safely release the needle from the grip of the device in a controlled manner. This can be accomplished by applying the three constraint brakes, two parallel (brakes 4 and 6, Figure 3.1b) and one needle guide brake (brake 1, Figure 3.1b), then releasing the brakes on each parallelogram linkage. This will constrain the linkage to only one degree of rotational freedom about the base shaft. This coordination can be used by the physician to release the needle manually from the mechatronic device in a controlled manner or serve to mechanically coordinate the motion of the four motors driving the linkage. Four motors (Figure 3.1a) and position encoders in association with each motor are mounted on the central shaft and are used for computer-controlled adjustment of the mechanism. By reducing the linkage to one degree of freedom about the main shaft, each motor in the needle positioning device becomes mechanically constrained to rotate at the same speed and direction to free the needle from the needle positioning device's grip.

3.2.2 Software components for 3D tracking and targeting

The TRUS probe, which is equipped with a side-firing linear array, is rotated about its long axis under the power of a DC motor (Figure 3.1) to acquire a 3D scan.[35] The 2D TRUS images from the US machine are digitized using a frame grabber and then reconstructed into a 3D image for viewing in a cube interface.[36] The 3D TRUS image of the prostate is then available for dosimetry planning and dynamic preplanning of needle trajectories.

Once the 3D image scanning and therapy plan are complete, the system displays a 3D needle guidance interface to facilitate the systematic targeting of each needle. Throughout the brachytherapy procedure, the 3D location and orientation of the needle axis within the image is tracked and displayed in real-time. Figure 3.4a shows the targeting interface, illustrating the location of the needle track in each image. The image displays the current path of the needle (yellow) and the planned needle path (pink) by displaying two points on the needle path. The cross illustrates the piercing point between the needle axis and patient's skin projected onto the transverse image plane, and the circle represents the intersection of the needle axis to the transverse image plane showing the location of the intended target.

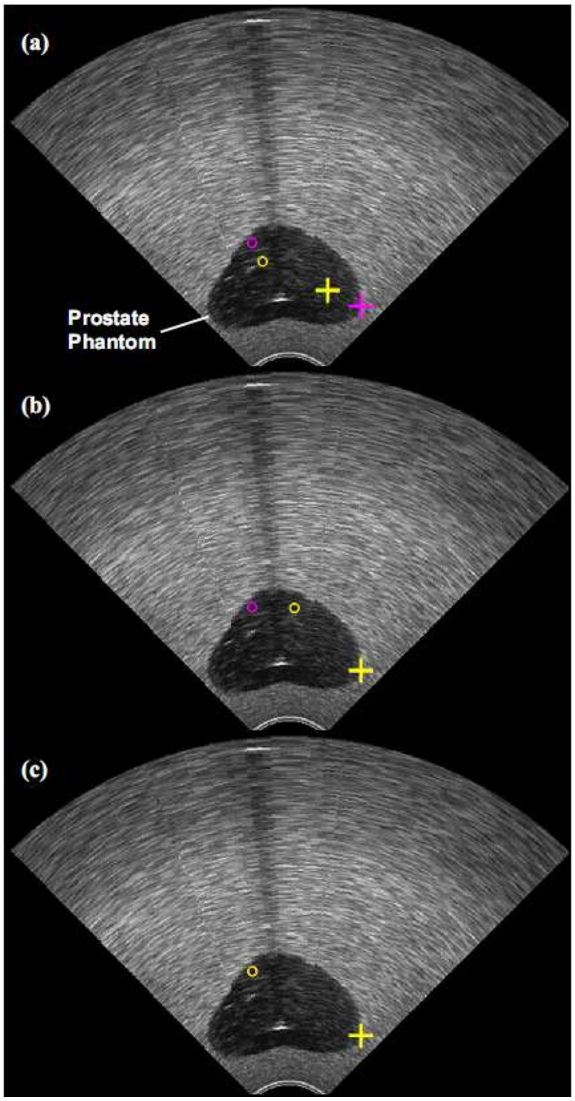

Figure 3.4: Illustration of the 3D needle guidance interface to facilitate the systematic targeting of each needle. (a) Shows the targeting interface, illustrating the location of the needle track. The image displays the current path of the needle (yellow) and the planned needle path (pink) by displaying two points on the needle path. The cross illustrates the piercing point between the needle axis and patient’s skin projected onto the transverse image plane, and the circle represents the intersection of the needle axis to the transverse image plane showing the location of the intended target. To align the needle to the planned trajectory in a therapy procedure, the physician would first align the needle piercing point over the patient’s skin by moving the front parallelogram linkage as seen in figure 3.3a. (b) Then, by manipulating the rear parallelogram, the physician would adjust the needle trajectory about the RCM until the needle is aligned to the target, when the yellow circle is superimposed onto the pink circle in (c). Since the front RCM remains stationary while the physician manipulates the needle, the alignment of the pink and yellow crosses does not change.

To align the needle to the planned trajectory in a therapy procedure, the physician would first align the needle piercing point over the patient's skin by moving the front parallelogram linkage, as illustrated in Figure 3.3a, until the yellow cross lies on top of the pink cross (as indicated by the software interface illustrated in Figure 3.4b). Then, by manipulating the rear parallelogram, as illustrated in Figure 3.3b, the physician would then adjust the needle trajectory about the RCM until the needle is aligned to the target, when the yellow circle is superimposed onto the pink circle (Figure 3.4c). Since the front RCM remains stationary while the physician manipulates the needle illustrated in figure 3.3b, the alignment of the superimposed pink and yellow crosses does not change. This correspondence allows the physician to directly interact with the mechanical apparatus and maintain direct control over its movements.

Once the needle is aligned to the target, the physician would then apply the brakes to make the device rigid and then insert the needle using the 3D US image as a guide (i.e. with the guidance of the software interface as the tracked trajectory is annotated on the 3D US image). This is accomplished by continuously rotating the TRUS probe back and fourth over a narrow range to cover the intended needle track.[37] The transverse, sagittal, and coronal views would then be updated in near real time and allow the physician to insert the needle to the correct depth and verify the actual needle path in the 3D image.[38] On the other hand, if the needle deviates from its intended trajectory, the physician can make small corrections to the needle trajectory while using the 3D image as a guide.[39]

3.3 System Calibration Methods

Any side-firing TRUS probe can be used with our system; however, the reported experimental results were obtained with a Falcon 2101 EXL Scanner and model 8808 transducer (B-K Medical, Herlev, Denmark). The axial, lateral and elevational resolutions were 1.1, 1.3 and 2.0 mm respectively. The resolution of the B-K Medical transducer was determined experimentally by measuring the diameter of a wire (0.1 mm), full width at half maximum within a preset focal zone 3 cm deep in a bath of distilled water and 7% glycerol by weight, giving a speed of sound of 1540 m/s at a temperature of 20ºC.

Two calibration steps are required to link the image coordinate system to the needle positioning device reference: the device coordinate system calibration, and the image to machine calibration.[20] First, the device coordinate system is calibrated to determine the variability and eliminate any bias resulting from the propagation of machining tolerances within the assembly. Secondly, the image to machine calibration determines the relationship linking the two coordinate systems.

3.3.1 Coordinate system calibration

The needle positioning device coordinate system, which is fixed to the ground, and the linkage orientation define the location of the needle guide relative to the needle positioning device frame. In order to validate and calibrate the position of the needle guide, it was manually positioned to 49 parallel positions covering every second hole of a standard 6 cm square brachytherapy template commonly used for brachytherapy (seven rows and seven columns spaced 1 cm apart). The orientation of the needle guide was determined by measuring the position of the RCM of each coupling, which gives the location of two points along the axis of the needle guide.

As shown in Figure 3.5, the needle positioning device was mounted onto a dividing head, which in turn sat on a granite surface plate and served as the reference plane for the calibration procedure. The needle positioning device was attached to a dividing head, which a milling machine accessory was used to precisely divide the circumference of the work-piece into equally spaced divisions. For this experimental setup, the dividing head was used to precisely rotate the needle positioning device by ±90º. Since the height gauge illustrated in Figure 3.5 can only be used to measure the height of the tooling balls relative to the surface plate, rotating the dividing head by 90º allowed both the horizontal and vertical location of toolling balls to be precisely measured using the this set-up.

The tooling ball is a locating component, which consists of a hardened ball bearing (∅9.5mm and ∅12.7mm mounted to front and rear spherical couplings respectively) fixed to a pedestal and ground to close tolerances (5 μm misalignment between ball bearing center and axis of the cylindrical pedestal). By fixing the center of the tooling ball to the RCM of each coupling, two points along the trajectory of the needle guide axis were determined by measuring their location using the height gauge (Figure 3.5).

In order to determine the variability of the calibration procedure, the tool guide was manually positioned to nine parallel positions over a standard 6 cm square template (three rows and three columns spaced 3cm apart). The measurements were repeated five times at each of the nine parallel positions to determine the mean and standard deviation for Δx and Δy-the error components along the coordinate axis, which are in the plane perpendicular to the axis of the TRUS probe (Figure 3.2).

Another factor that contributes to the positioning error of the device is the alignment error between the needle guide axis and center of the tooling ball. The impact of this misalignment appears when the needle guide is oriented at an oblique angle. The maximum error was determined relative to nine parallel positions (three rows and three columns spaced 3 cm apart) by repositioning the rear coupling RCM to the other eight positions to create a total of 72 oblique angles and measuring the x, y and z components of the displaced tooling ball using the height gauge.

The measured positioning error along the x and y axes (Figure 3.2) for both the forward and rear tooling ball relative to its predicted location is illustrated in Table 3.1. The total displacement of the tooling ball varied from a minimum of 0.12 mm nearest to the encoder home position (A3 in Table 3.1) to a maximum of 0.68 mm, which corresponds to the most distant point from the encoder home position (F1 in Table 3.1). The encoder home position was measured by constraining the parallelogram arms to a square configuration and parallel to the x axis of the mechatronic needle guidance system using the height gauge and attached indicator (Figure 3.4), and recording the encoder readouts.

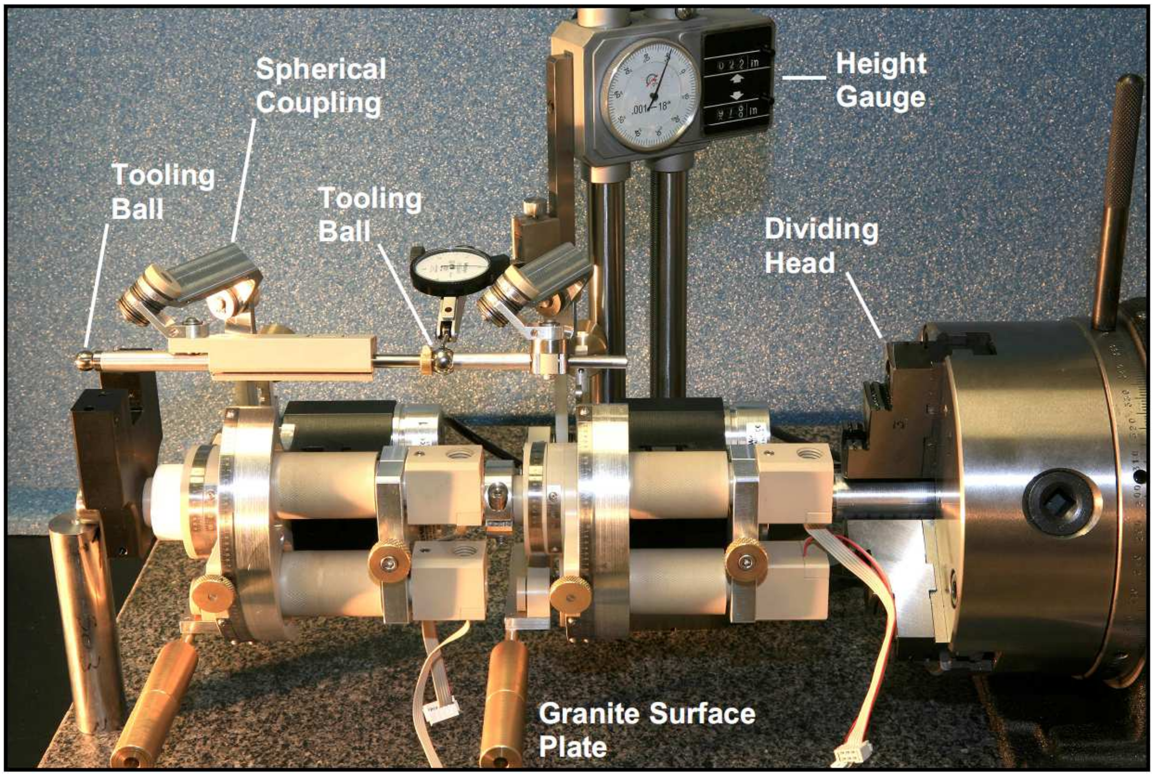

Figure 3.5: The device was coupled to a dividing head, which in turn sat on a granite surface plate and served as the reference plane for the calibration procedure. The dividing head was used to measure both the horizontal (x axis) and vertical position (y axis) of the tooling ball relative to the surface plate by indexing the chuck (and attached robot) by ±90 degrees. The height gauge was used to determine the height of the tooling balls that were aligned to the RCM of the spherical couplings.

The variability of the calibration procedure for nine parallel positions for both the forward and rear arms was determined from five repeated measurements over three rows and three columns spaced 3cm apart. The mean error values of the Δx and Δy are highlighted in grey in Table 3.1, and the standard deviation varied little, from (0.01, 0.01) to a maximum of (0.02, 0.04), and are not tabulated. As the positional variability of the system is small (standard deviation < .045 mm) relative to the measured bias (mean error < 0.68mm), the accuracy of the system could be improved by eliminating the bias. Although the errors contributed by each parallelogram linkage are less than 1mm, the cumulative effect of this error is additive and would be amplified by the linkage, resulting in an accumulated error that may exceed the ultrasound resolution. To eliminate this undesirable effect, the calibration results were integrated into the kinematics equations and then subsequently used for the mock seed implantation experiment described in section 4.1.

Table 3.1: Measurement results of the calibration errors (Δx, Δy) for both the forward and rear parallelogram arms of the mechatronic device. The location of the tooling ball was measured five times to determine the mean position (highlighted in grey) at 3 cm increments in x and y over the entire area of a 6cm square grid typically used for brachytherapy (consisting of at least seven rows [A-G] and columns [1-7]). All other values not highlighted in grey contain only one measurement.

Forward Parallelogram (mm, mm)								
		Horizontal Location						
		A	B	C	D	E	F	G
Vertical Location	7	*0.05, 0.24*	*0.09, 0.30*	*0.15, 0.37*	*0.18, 0.30*	*0.19, 0.30*	*0.20, 0.30*	*0.22, 0.33*
	6	*0.05, 0.25*	*0.08, 0.30*	*0.15, 0.38*	*0.17, 0.34*	*0.17, 0.27*	*0.20, 0.27*	*0.21, 0.38*
	5	*0.07, 0.34*	*0.10, 0.30*	*0.13, 0.31*	*0.16, 0.30*	*0.17, 0.25*	*0.19, 0.26*	*0.20, 0.24*
	4	*0.10, 0.30*	*0.11, 0.21*	*0.15, 0.27*	*0.16, 0.26*	*0.17, 0.26*	*0.20, 0.27*	*0.20, 0.27*
	3	*0.07, 0.29*	*0.12, 0.29*	*0.22, 0.34*	*0.26, 0.34*	*0.20, 0.34*	*0.06, 0.30*	*0.26, 0.29*
	2	*0.05, 0.30*	*0.15, 0.36*	*0.35, 0.38*	*0.46, 0.33*	*0.35, 0.29*	*0.11, 0.31*	*0.38, 0.26*
	1	*0.01, 0.29*	*0.15, 0.29*	*0.43, 0.29*	*0.57, 0.26*	*0.48, 0.22*	*0.40, 0.24*	*0.44, 0.20*

Rear Parallelogram (mm, mm)								
		Horizontal Location (mm, mm)						
		A	B	C	D	E	F	G
Vertical Location	7	*0.44, 0.20*	*0.48, 0.24*	*0.58, 0.19*	*0.53, 0.25*	*0.60, 0.21*	*0.64, 0.15*	*0.66, 0.21*
	6	*0.33, 0.19*	*0.40, 0.25*	*0.42, 0.24*	*0.44, 0.22*	*0.48, 0.19*	*0.52, 0.21*	*0.66, 0.20*
	5	*0.20, 0.19*	*0.29, 0.21*	*0.31, 0.16*	*0.33, 0.21*	*0.34, 0.19*	*0.44, 0.19*	*0.57, 0.20*
	4	*0.01, 0.12*	*0.12, 0.19*	*0.19, 0.19*	*0.19, 0.17*	*0.24, 0.13*	*0.33, 0.17*	*0.35, 0.19*
	3	*0.01, 0.08*	*0.07, 0.12*	*0.14, 0.15*	*0.20, 0.19*	*0.22, 0.19*	*0.43, 0.20*	*0.39, 0.25*
	2	*-.07, 0.07*	*-.03, 0.16*	*0.05, 0.20*	*0.16, 0.29*	*0.31, 0.34*	*0.40, 0.29*	*0.41, 0.26*
	1	*-.21, 0.07*	*-.03, 0.21*	*0.13, 0.38*	*0.24, 0.53*	*0.41, 0.48*	*0.53, 0.43*	*0.48, 0.39*

The impact of the misalignment of the needle guide axis to the RCM has on the calibration is illustrated in Table 3.2, where the maximum displacement of the forward tooling ball was determined relative to the rear tooling ball position (see Figure 3.5). This shows an increasing error for larger oblique angles, with the maximum RCM misalignment of 0.18 mm when the forward and rear tooling balls are displaced from one another by 6 cm in the x and y directions (highlighted in bold, Table 3.2). This configuration corresponds to an oblique angle of 28° relative to the calibrated parallel needle path.

Table 3.2: Results illustrating the maximum tooling ball displacement (mm) for various rear RCM locations relative to the forward tooling ball. The maximum displacement was determined from a total of 72 different oblique trajectories where the rear tooling ball was displaced from nine different parallel trajectories in 3 cm increments over a 6 cm square grid except for the values in bold where only one data point was available for the given configuration (i.e. forward and rear tooling balls are in opposite corners of the 6cm grid pattern used in this experiment).

		x-axis				
	Location (cm)	6	3	**0**	3	6
y-axis	6	***0.14***	*0.11*	*0.09*	*0.10*	***0.07***
	3	*0.10*	*0.08*	*0.05*	*0.12*	*0.11*
	0	*0.12*	*0.05*	-	*0.07*	*0.13*
	3	*0.12*	*0.08*	*0.05*	*0.09*	*0.17*
	6	***0.13***	*0.11*	*0.10*	*0.11*	***0.18***

3.3.2 Image to tracker calibration

The image coordinate system is physically linked to the needle positioning device reference frame to provide a fixed relationship between the image and needle positioning device coordinate system, thus requiring only a one-time calibration. To determine the relationship between the tracker and image coordinate systems, a multilayered string phantom[20] was constructed and mounted to the needle positioning device to constrain the string intersections to a known location. The string phantom consisted of four layers of orthogonally intersecting monofilament nylon strings (diameter = 0.25 mm), which were anchored to the sides of a brass frame of the following dimensions (Figure 3.6a): 12.2 cm square by 3.0 cm (height). They were spaced 10 mm apart, and each layer was offset by 2.5 mm to prevent the strings closer to the transducer from shadowing the adjacent layers.

The mechanical apparatus was positioned with the tip of the TRUS transducer placed below the surface in a bath of distilled water and 7% glycerol (by weight), giving a speed of sound of 1540 m/s at a temperature of 20°C.[35] The transducer was then rotated around its long axis under power of the motor as described earlier to acquire a 3D TRUS image of the string phantom (Figure 3.6b).[36] The acquired 3D image was then displayed using multi-planar reformatting in a cube view, which can be manipulated and sliced to view different sections within the image to identify the different string intersections.[36] The spacing between the strings and their location in the image coordinate system was then measured by manually selecting each string intersection. Each intersection measurement was repeated five times to determine the mean and standard deviation.

To determine the impact that the speed of the motor driving the TRUS probe and the ultrasound frame rate has on the image to needle positioning device calibration, the motor speed and the number of focal zones selected on the US machine were varied to produce nine different 3D images. The motor speed was varied to produce three different scan times: 4, 5.7 and 22 seconds. Three different focal zones were selected on the US machine to vary the frame rate: 8Hz 15Hz, and 30Hz. For each combination of motor speed and frame rate, four non-coplanar string intersections were then manually selected in each of the nine images and a rigid body transformation was found between the image under investigation and the image with the slowest motor speed and fewest focal zones (i.e., scan time = 22s and frame rate = 30Hz) by solving the orthogonal Procrustes problem.[40] The image rotation about the z axis of the machine coordinate system represented the image lag angle, with the assumption that the 22 s / 30 Hz image had no image lag.

A 3D TRUS image of the string phantom was successfully reconstructed without any visible discontinuities or probe misalignment artifacts. Table 3.3 shows the distances between the strings within the phantom measured in the three orthogonal views {(x, y), (x, z), (y, z)}. The distance measured in each plane overestimated the known manufactured inter-string distance, with measured errors less than 0.40 mm (Table 3.3). The transformation between the image and machine coordinate system revealed an image lag rotation that varied from 0 to 4.5 degrees about the z-axis of the machine coordinate system (Figure 3.6). This rotation due to image lag is caused by a mismatch between the measured transducer rotation angle and the actual angle of the 2D TRUS image digitized by the computer. The image lag is a function of the motor speed and the number of focal zones selected on the US machine.

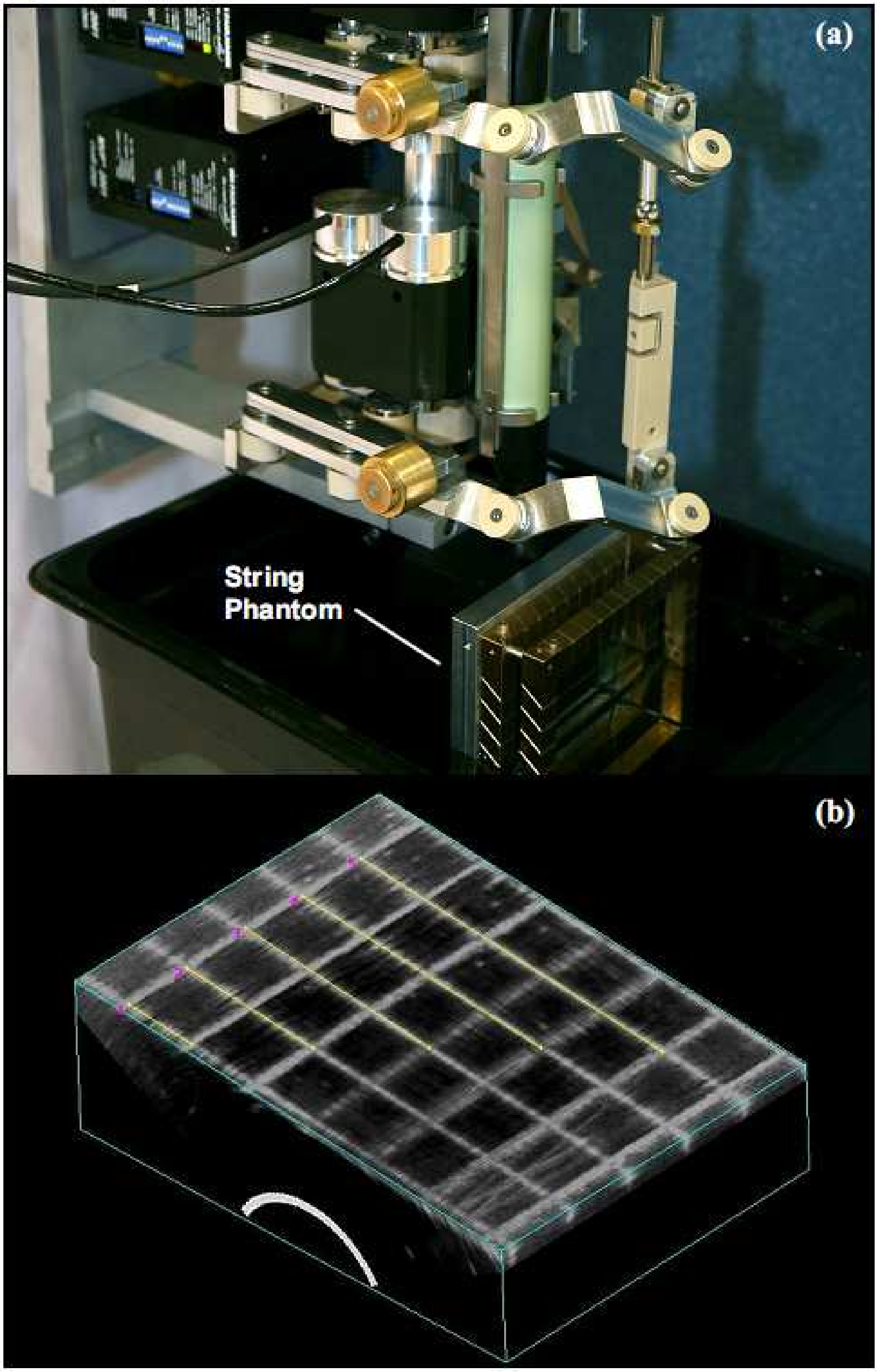

Figure 3.6: (a) Photograph of the experimental setup used to align the ultrasound image (b) to the coordinate reference frame of the needle positioning device. To determine the relationship between the coordinate systems, a multilayered string phantom was constructed and mounted to the needled positioning device to constrain the string intersections to a known location.

Table 3.3: Measurement results of string separations from the 3D geometric reconstruction experiment illustrating the mean distance between the strings, the measurement error ($u-u_0$) where u_0=10mm, and standard deviation (STD).

	Y-Z Plane		***X-Z Plane***		***X-Y Plane***	
	y	*z*	*x*	*z*	*x*	*y*
Mean	10.65	10.30	10.38	10.40	10.33	10.62
$u-u_0$ (mm)	0.65	0.30	0.38	0.40	0.33	0.62
STD (mm)	0.081	0.025	0.023	0.026	0.016	0.074

3.4 System Validation Methods

3.4.1 Mock Seed Implantation in Agar Phantoms

Mock therapy procedures were performed on agar-based tissue-mimicking phantoms to quantify the accuracy of the 3D TRUS system for seed placement, needle guidance and recording the 3D location of the needle using 3D TRUS for both parallel and oblique needle trajectories. The phantom was constructed by adding agar to a 7% by mass glycerol/water solution to produce a speed of sound similar to that of human tissue (1540 m/s).[41] Cellulose (15% by weight) was also added to create acoustic backscattering in US to mimic the appearance of tissue. We used an ultrasound tissue mimicking phantom to determine the feasibility of using the needle positioning device manually to align the needle to the intended trajectory, and to guide the needle to the correct depth using 3D ultrasound. Since this system was designed to use the same imaging equipment and needles currently used in brachytherapy, we do not expect the needle to react any differently in tissue than other methods that utilize a manual needle insertion technique. Therefore, agar was used in place of animals or ex-vivo tissue to provide a 3D record of the experiment as the added variation from the tissue-needle interactions may occlude our ability to measure the targeting error resulting from manual control of this system.

Stainless steel ball bearings of 1 mm diameter were placed in a geodesic configuration centered 60 mm from the surface of the agar block, and 30mm from the center of a hole in the agar, which accommodated the TRUS probe. These ball bearings served as fiducials for coordinate registration between the 3D TRUS and micro-CT images. Since each component (x, y, and z) of target registration error (TRE) is inversely proportional to both the spread of the fiducials about each principle axes and the location of the fiducial centroid, the choice of using a spherical distribution eliminated any orientation biases across phantoms.[42] The positional accuracy of the fiducial centroid was achieved by constructing the phantom in two parts. The geodesic fiducial pattern was cast separately in a spherical mould, which was then supported in the acrylic box (which served as the agar phantom mould) surrounded by agar blocks to hold its position in the center of a cube defied by the planned targets.

The parallel needle plan involved implanting ten 1 mm diameter beads into the phantoms along trajectories that were parallel to the long axis of the TRUS probe. Five of the planned targets were centered in the image forming a line from image left to right in the transverse plane at 10 mm increments and 100 mm below the surface of the agar phantom. The other five targets were also centered in the image 4 cm closer to the probe axis and at a shallower depth of 60 mm. This needle configuration was similar to the needle placement accuracy experiments used by Wei. et al. (2004)[20] and formed a 4x4x4 cube centered 30 mm from the TRUS probe axis to simulate both shallow and deep targets within a prostate. This experiment was repeated four times to give a total of 20 beads in the top row with deep penetration and 20 beads in the bottom row with shallow penetration.

The angled needle plan consisted of implanting nine beads 100 mm behind the surface of the agar block through a common point 50 mm from the probe axis. The intersection of the needle trajectories was positioned approximately 10 mm in front of the surface of the phantom to space the entry points in 1 mm increments and prevent damage to the agar from multiple needle entries through a common point. The angled needle trajectories were positioned both vertically and laterally to the left and right of image center at 5º, 10º and 15º and the experiment was repeated four times to give a total of 36 implanted beads.

To start the procedure, the tracking apparatus was positioned by inserting the TRUS transducer into the agar phantom hole. Each of the preplanned targets was selected randomly and the user aligned the needle guide to the target needle path using the four encoder readouts as a guide. A near real-time 3D image of the needle path was then acquired by the computer using a motorized assembly to continuously rotate the TRUS probe back and forth about its long axis in a narrow path to cover the planned needle track. An updated 2D TRUS image was continuously displayed on the computer interface in a 2D view that was parallel to the needle track illustrating the current needle position and the intended target point within the image (Figure 3.7). Using a 16 gauge brachytherapy needle with a pyramid shaped tip (Nucletron, Veenendaal, The Netherlands), an incision was made on the surface of the agar phantom by inserting the brachytherapy needle approximately 10-20mm into the phantom. The needle was then retracted and a 1mm diameter ball bearing was fixed to the end of the brachytherapy needle sleeve using ultrasound transmission gel (Parker Laboratories, Fairfield, NJ). The bead was then implanted into the phantom using a near real-time 3D TRUS image as a guide to a predetermined depth. When all of the beads were implanted, a 3D TRUS image of the phantom was then acquired to provide a record of the procedure.

The agar phantom was then imaged using an eXplore Locus Ultra Pre-Clinical CT scanner (GE Healthcare, London, ON), which is commonly used for small animal imaging.[43] The high-resolution CT image (isometric voxel dimensions of 0.15 mm^3) served as the reference standard representing the true location of each needle track and bead location. In the CT image, a needle trajectory was evident as an air track left from the insertion of the 16-gauge needle into the agar phantom. The location of a needle track and bead were extracted from a CT image by using a linear regression of selected points along the center of the air track, from the base to the tip located at the center of the implanted bead. The centers of the 1mm fiducial markers surrounding the needle paths were manually selected from corresponding CT and 3D TRUS images to co-register the two coordinate systems.

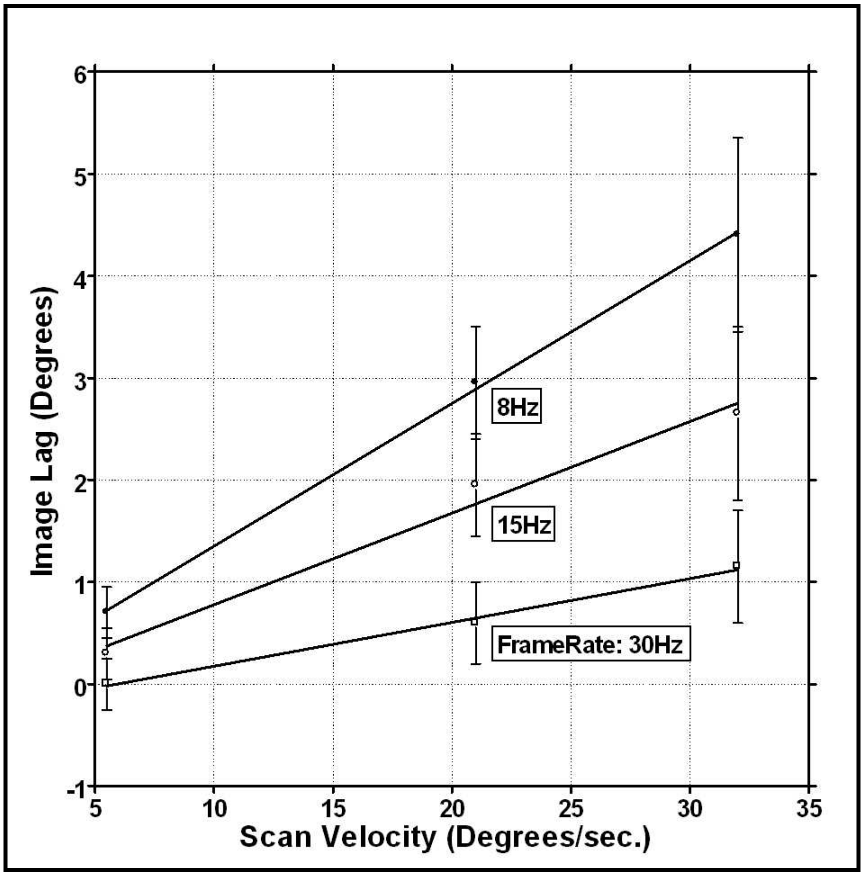

Figure 3.7: Graph showing the image lag (in degrees) as a function of the scan velocity at three different US frame rates (8, 16, and 32 Hz). Image lag is defined as the angular misalignment of the image about the z-axis of the machine coordinate system. The image lag is proportional to the motor speed and inversely to the frame rate. The error bars in the graph represent the standard deviation in the measurements.

3.4.2 Needle targeting error in agar phantoms

A rigid body transformation was then applied to align both the ultrasound and CT images under investigation by solving the orthogonal Procrustes problem.[40] Using this combined image, the system was evaluated for its ability to (a) guide a needle to a 3D target, and (b) record the location of the needle within 3D image following the methods described by Cool et al. (2008).[44] Refering to Figure 3.8, the mean targeting error MTE^{CT} is the mean distance between each identified bead location, a_i^{CT}, in the 3D CT image located at the

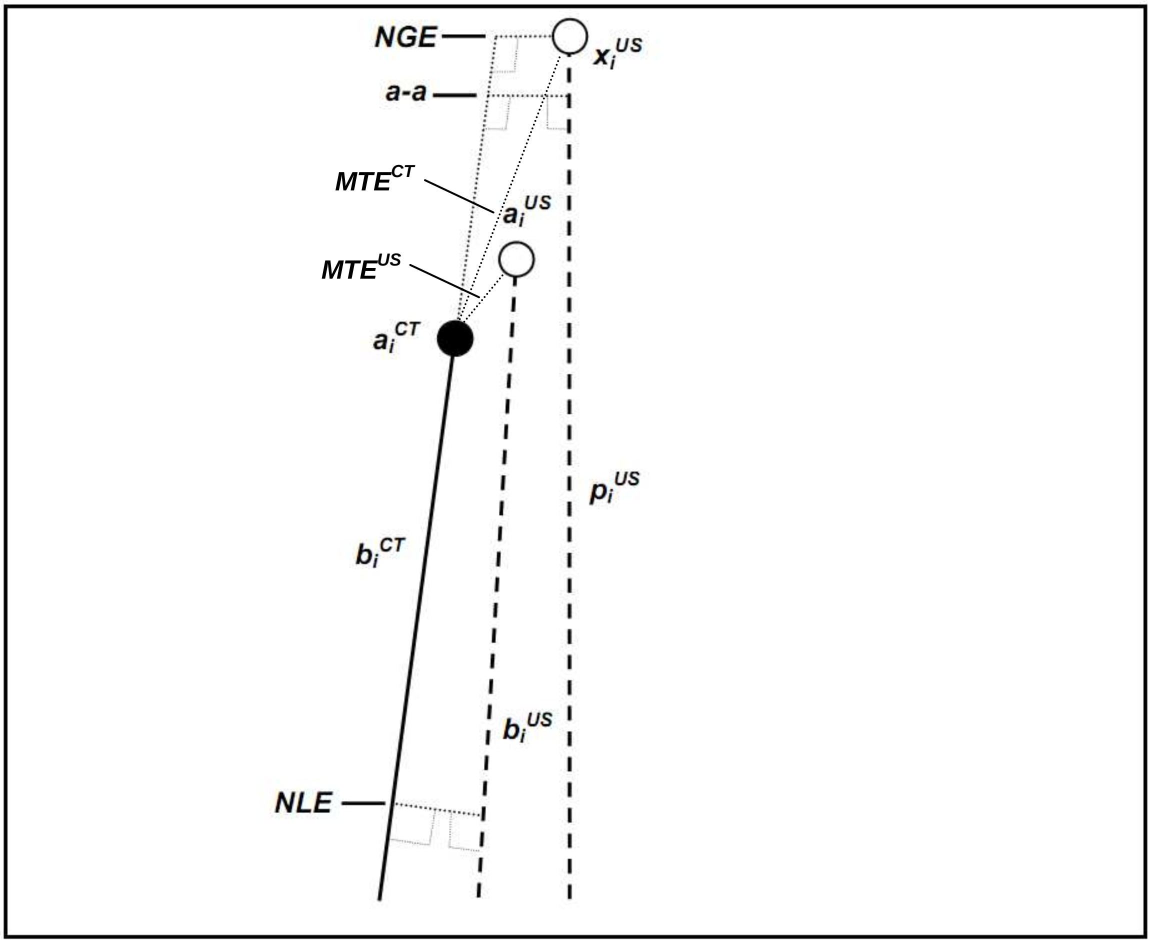

Figure 3.8: Illustration showing the error metrics used to evaluate the user's ability to guide a needle to a 3D target, and record the location of the needle within 3D image. The mean targeting error MTE^{CT} is the mean distance between each identified bead location, a_i^{CT}, in the 3D CT image and associated target location x_i^{US}, which is a virtual point in the ultrasound coordinate frame represented by the open circle. The mean target error MTE^{US} is the mean distance between the each bead location a_i^{US} in the 3D US image and the corresponding target location x_i^{US}. The needle guidance error, *NGE*, is the mean total error associated with the system's ability to guide the needle path to predefined targets. NGE^{θ} is the angle between the needle trajectory identified in the CT image b_i^{CT} and the planned needle path p_i^{US} when projected on to a plane perpendicular to the line *a-a*, which is the shortest distance between the two lines. *NLE* is defined as the minimum distance between the "true" needle axis from CT, b_i^{CT}, and the recorded 3D TRUS needle axis, b_i^{US}. NLE^{θ} is the angle between the needle trajectories when projected on a plane perpendicular to *NLE*.

end of the i^{th} air track b_i^{CT}, and the i^{th} target location x_i^{US}, which is a virtual point in the ultrasound coordinate frame. The mean target error MTE^{US} is the mean distance between the each bead location a_i^{US} in the 3D US image located at the end of each air track b_i^{US} and the corresponding target location x_i^{US}:

$$MTE^{CT} = \frac{\sum_{i=1}^{n} D_{p-p}(x_i^{US}, a_i^{CT})}{n}$$ [1],

$$MTE^{US} = \frac{\sum_{i=1}^{n} D_{p-p}(x_i^{US}, a_i^{US})}{n}$$ [2],

where $D_{p\text{-}p}(\ )$ is a function that determines the 3D distance between a target point, x_i, and the corresponding bead location identified in the CT, a_i^{CT} (or US image a_i^{US}), and n is the number of times the experiment was performed. The registration error between the bead in US and CT is given by the target registration error (TRE):[42]

$$TRE = \sqrt{\frac{\sum_{i=1}^{n} D_{p-p}(a_i^{CT}, a_i^{US})^2}{n}}$$ [3].

The needle guidance error, *NGE*, is the mean total error associated with the system's ability to guide the needle path to predefined targets. This error was quantified for each needle trajectory as the shortest distance between the i^{th} target location x_i^{US}, and the corresponding needle path identified in the 3D CT image b_i^{CT}:

$$NGE = \frac{\sum_{i=1}^{n} D_{p-l}(x_i^{US}, b_i^{CT})}{n}$$ [4],

where $D_{p\text{-}l}(\ )$ is a function that determines the minimum 3D distance between a target point a_i, and the line corresponding to the air track identified in the CT image, b_i^{CT}. NGE^{θ} is the angle between the needle trajectory identified in the CT image b_i^{CT} and the planned needle path p_i^{US} when projected on to a plane perpendicular to the shortest line between b_i^{CT} and p_i^{US} :

$$NGE^{\theta} = \frac{\sum_{i=1}^{n} \theta(p_i^{US}, b_i^{CT})}{n}$$ [5],

where $\theta(u,v)$ is the function that defines the minimum angle between the needle trajectories.

The system's ability to record the needle location in 3D (Needle Localization Error, *NLE*) was quantified using two metrics: *NLE*, and NLE^{θ}. *NLE* is defined as the minimum distance between the "true" needle axis from CT, b_i^{CT}, and the recorded 3D TRUS needle axis, b_i^{US}.

$$NLE = \frac{\sum_{i=1}^{n} D_{l-l}(b_i^{CT}, b_i^{US})}{n} \qquad [6],$$

where $D_{l\text{-}l}(\ )$ measures the minimum distance between two line segments.

NLE^{θ} is the angle between the needle trajectories when projected on a plane perpendicular to *NLE*:

$$NLE^{\theta} = \frac{\sum_{i=1}^{n} \theta(b_i^{CT}, b_i^{US})}{n} \qquad [7]$$

where $\theta(u,v)$ is the function that defines the minimum angle between the vectors b_i^{CT} and b_i^{US}.

3.4.3 Results from needle-guidance experiment

The quantitative results for the bead implant experiment using parallel needle paths to the top and bottom rows were similar but the top row values were generally similar as summarized in Table 3.4. Guidance of the bead to each target had a mean error of MTE^{CT}=1.54±0.49 mm and in CT and MTE^{US}=1.22±0.36 mm in US. The mean needle guidance error was smaller where *NGE*=1.11±0.52 mm and NGE^{θ}=0.97±0.49º. A one-tailed t-test showed that the mean targeting error was statistically significantly less than 5 mm (p=0.001, n=39), which is the smallest tumor considered clinically significant.[45] The needles were accurately localized to 0.58±0.41 mm (*NLE*) and with a mean angulation difference of 1.69±1.38º (NLE^{θ}).

Table 3.4: 3D system accuracy for the parallel needle trajectories based on the error analysis described in section 3.4. Mean targeting error, MTE^{CT} and MTE^{US} (Eq. 2 and 1), needle guidance error, NGE (Eq. 4), and NGE^{θ} (Eq. 5), all evaluate the seed placement and needle targeting accuracy. The localization metrics, NLE and NLE^{θ} (see Eq. 6, and 7) indicate the errors in recording the 3D location of the needle trajectories. All of the values are reported as Mean±STD except for the target registration error (TRE) between CT and US and is quantified by Eq. 3.

Needle Position (mm)	***TRE (mm)***	***System Accuracy***				***Localization Error***	
		MTE^{US} (mm)	*MTE^{CT} (mm)*	*NGE (mm)*	*NGE^{θ} (degrees)*	*NLE (mm)*	*NLE^{θ} (degrees)*
Top row, Deep (0.72)	0.79	1.15±0.37	1.49±0.57	1.05±0.55	0.75±0.36	0.54±0.51	2.64±1.45
Bottom row, Shallow	1.04	1.28±0.37	1.60±0.40	1.15±0.50	1.17±0.51	0.61±0.26	0.74±0.72
Mean	0.91	1.22±0.36	1.54±0.49$^{\#}$	1.11±0.52	0.97±0.49	0.58±0.41	1.69±1.38

The quantitative results for the bead implant experiment using oblique needle paths are summarized in Table 3.5. All of the beads were successfully implanted with exception of the vertical needle path of 15º, where the needle interfered with the TRUS probe to a prohibitive extent. Although it was possible to insert the needle by bending it around the TRUS probe, it was apparent that the needle was damaged from excessive bending as it would not roll freely on the granite block. Navigation of the bead to each target had a maximum targeting error of MTE^{CT}=2.92±0.76 mm in CT and MTE^{US}=2.86±0.72 mm in US at 15º. Although this error is slightly larger than the results for the parallel needle paths, a one-tailed t-test showed the mean targeting error was statistically significantly less than 5 mm (p=0.005, n=7), which is the smallest tumor considered clinically significant.[45] Guidance of the needle to each target had a maximum *NGE*=1.95±0.80 mm and NGE^{θ}=1.4º for all needle trajectories less than 15º. The angled needle paths were accurately localized to a maximum *NLE*=0.36±0.32 mm and with a maximum angulation difference of 1.25±0.90º (NLE^{θ}).

Table 3.5: 3D mechatronic system needle guidance results for the oblique needle trajectories at varying angles from 5 to 15 degrees. Mean targeting error, MTE^{CT} and MTE^{US} (eq. 2 and 1), needle guidance error, NGE (eq. 3), and NGE^{θ} (eq. 4), all determine the seed placement and needle guidance accuracy. The localization metrics NLE , and NLE^{θ} (see eq. 5, and 6), indicate the errors in recording the 3D location of the needle trajectories. All of the values are reported as Mean±STD except for the target registration error (TRE) between CT and US and is quantified by equation 3.

Needle Position (TRE)		*TRE*	*System Accuracy*				*Localization Error*	
			MTE^{US} (mm)	*MTE^{CT} (mm)*	*NGE (mm)*	*NGE^{θ} (degrees)*	*NLE (mm)*	*NLE^{θ} (degrees)*
Vertical	5°	0.70	1.97±0.32	2.22±0.61^{+}	1.45±0.36	0.82±0.07	0.59±0.15	0.76±0.15
	10°	0.91	2.35±0.56	2.49±0.80^{+}	1.23±0.67	0.82±0.33	0.32±0.30	1.25±0.90
	15°	0.64	3.19±0.23	4.02±0.66	3.17±0.28	0.79±0.25	0.36±0.32	0.79±0.24
Lateral	5°	0.72	1.68±0.68	2.06±0.67$^{\#}$	1.17±0.36	1.10±0.38	0.26±0.16	0.51±0.32
	10°	0.69	1.96±0.75	2.10±0.88$^{\#}$	1.20±0.81	1.37±0.40	0.28±0.16	0.86±0.44
	15°	0.68	2.86±0.72	2.92±0.76$^{\#}$	1.95±0.80	1.36±0.22	0.30±0.23	0.59±0.44

3.5 Discussion and Conclusion

There are two factors that contribute to the positioning error of the mechatronic device: the positioning error contributed from each parallelogram linkage, and the alignment error between the needle axis and RCM. The positioning error of each linkage illustrated in Table 3.1 is the result of the accumulation of encoder error and machining tolerances within the parallelogram linkages. This bias can be accounted for by incorporating the calibration tables into the forward and inverse kinematics equations by adding a correction factor, which was estimated using a linear interpolation between the three nearest points within the calibration tables. On the other hand, the alignment error between the needle axis and the machine RCM is the result of the accumulation of machining tolerances within the spherical couplings. Because the calibration procedure for the forward and rear parallelogram linkages was performed with the needle guide parallel to the z-axis of the machine coordinate system, this error becomes more apparent with larger oblique angles as seen in Table 3.2. Since the forward and inverse kinematics equations assume the needle axis is aligned to the forward RCM as a means of solving the equations, this error should be kept to a minimum as a manufacturing constraint to reduce its impact on oblique trajectories.

The string phantom measurements were within 0.4mm of the known string separations measured in the three orthogonal views {(x, y), (x, z), (y, z)}. This suggests that geometrical distortion from transducer misalignment was not significant. A rotational misalignment about the z-axis revealed an image lag, which was caused by the misplacement of the 2D images in the 3D reconstructed image due to the assumption that the motor speed and US processing time is negligible. This results in each captured image being associated with the current encoder position, which is ahead of the angular US image location. Although this error was accounted for by using the string phantom to link the machine and image coordinate system, Figure 3.7 shows that this process would need to be repeated if a different motor speed or US frame rate was used.

In the mock seed implant experiment, the 3D system was able to guide beads along parallel needle paths *in vitro* to predefined targets with an average error of 1.4 mm (MTE^{CT}). This error was primarily due to the relatively large needle guidance error (NGE=1.1 mm, NGE^{θ}=1.0º), which was a result of the registration error, the machine error, and partially due to the operator error in placing the bead at the correct depth using the image as a guide.

For the oblique needle trajectories, all of the beads were successfully implanted with exception of the vertical angulated needle path of 15º, where it was necessary to bend the needle around the TRUS probe resulting in a relatively large bead displacement (MTE^{CT}=4.0 mm, Table 3.5) and needle guidance error (NGE=3.2 mm). This imposes a limit on the planning of oblique needle trajectories as the thin brachytherapy needles are fragile. Guidance of a bead to the other targets resulted in a mean error that varied from MTE^{CT}=2.06±0.67 mm for shallow angles (5º, Table 3.5) to MTE^{CT}=2.92±0.76 mm at 15º. Although these errors are slightly larger than the results for the parallel needle paths, a one-tailed t-test showed that the mean targeting error was statistically significantly less than 5 mm (p=0.005, Table 3.5), which is the smallest tumor considered clinically significant.[45] One component contributing to this error is the needle guidance error, *NGE*, which varied from 1.2 mm at 5 degree angles to 2.0 mm for 15º angles. These errors were additionally influenced by the misalignment of the needle axis with the machine RCM, which increases at larger angles. Although the machine error was a significant component of the mean target error (MTE^{CT}), placement error, the error in placement of the bead along the needle track at an oblique trajectory, was larger (2.2 mm at 15º versus 1.1 mm for parallel trajectories). These values were calculated using equation (8), where the bead guidance error (BGE) was determined from (MTE) and (NGE):

$$BGE = \sqrt{MTE^2 - NGE^2} \qquad [8].$$

This error was likely due to the reduced contrast of the needle in the US image at larger angles, where the needle was nearly invisible leaving only the shadow artifact created by the needle, obscuring layers that were behind it as seen from the transducer line of sight (see Figure 3.9). Since localization of the needle path to each target is independent of the machine positional errors, the needle localization error results were smaller than the system accuracy results, showing that the 3D image was accurately calibrated to the mechatronic device, where NLE<0.6 mm, and NLE^{θ}<1.3º.

For both parallel and oblique needle trajectories, the mean targeting error measured in US (MTE^{US}) was similar to but slightly smaller than the values measured in CT (MTE^{CT}). Since the US image is accurately aligned to the machine coordinate system and the geometric distortions are small, as shown in Table 3.3, 3D US can provide an accurate estimate of the true 3D needle location.

Although these errors are statistically significantly less than the smallest tumour considered clinically significant,[45] this does not guarantee that the deposited radioactive source distribution will not be modified to a prohibitive extent or potentially cause harm to nearby organs. The cause of this problem is well known as the thin bevelled tip brachytherapy needle will often deflect from the preplanned trajectory through the perineum, altering the intended dose pattern and at times requiring multiple needle insertions to correct for the problem.[39] Since the physician is in direct control of both the needle and its trajectory while using our mechatronic system, methods like needle steering[39] could be used to aid the physician in guiding the needle to its intended target while using the 3D US image as a guide. To accomplish this, the physician will need to interact with the mechanism in an intuitive manner in order to successfully steer the needle, which our system can provide by allowing the physician to directly pivot the needle about the front RCM (at the patient’s skin) while advancing and rotating the needle. This highlights the importance of using a near real-time imaging system to help the physician guide the needle as both the needle and prostate can shift during the procedure.

Another important factor determining the success of a brachytherapy procedure is maintaining a uniform distribution of seeds throughout the prostate, without overdosing nearby organs such as the bladder, rectum, urethra and seminal vesicles. Without the use of a template, seeds can be spaced further from the urethra to prevent overdosing the urethra while maintaining coverage at the anterior parts of the prostate. Oblique needles can help here since the needles can be angled to avoid the pubic arch and gain access to the anterior parts of the prostate. Also, not using a template provides more freedom to prevent overdosing the urethra for small prostates where the 5 mm spacing in the fixed template is too coarse.

Current methods used clinically to overcome PAI include either the freehand technique or the use of the manipulation ruler, both of which are highly skill dependant. Under manual control, this system consists of a passive mechanical linkage for guiding, tracking and stabilizing the position of the needle. The stabilization is accomplished by counter-balancing the linkage to maintain the position and orientation of the needle and needle guide even when the physician removes his hand from the device. This permits smooth motion of the needle guide with a light touch of the physician's hand providing the same feel and control as the freehand technique. In addition, the current needle trajectory is also displayed on the ultrasound image, allowing the physician to coordinate the needle position to the image. This interface should not only decrease the implantation time, but also make the procedure less skill dependant as the physician will no longer need to visualize and coordinate the needle to the image, thus potentially reducing the number of times the needle has to be retracted and reinserted.

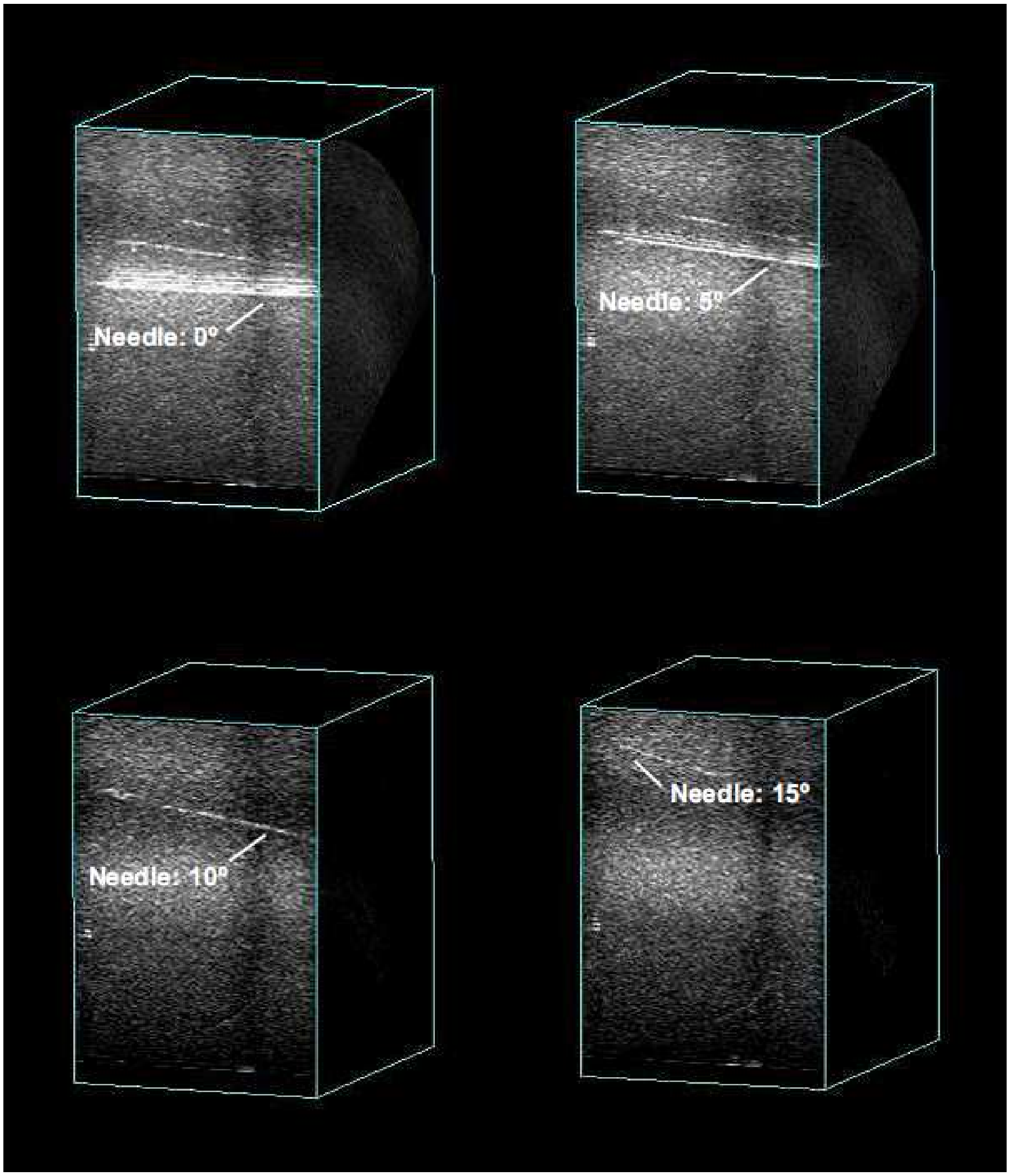

Figure 3.9: 3D images of an agar phantom used in the mock seed implant experiment illustrating the needle at various oblique trajectories from 0º (top left) to 15º (bottom right).

In conclusion, by combining the 3D TRUS imaging system with a dynamically adjustable needle guide, the physician will be able to place the needle trajectory to selected targets in the 3D TRUS image with a mean error that closely matches the ultrasound resolution. This would be beneficial as the physician has complete control of the needle and can safely manoeuvre the needle guide around obstacles like previously placed needles or a TRUS probe. Although this system was tested using a 3D imaging system, this system is also compatible with any 2D system and protocol currently in use. Our future direction will be to clinically validate our prostate therapy system (delivering brachytherapy first, but be able to accommodate other prostate therapy approaches like cryotherapy and laser ablation), in which all aspects of the procedure will be carried out intra-operatively including dosimetry planning, monitoring of prostate changes, dynamic re-planning including oblique trajectories and needle placement verification.

3.6 References

1. Horner M, Ries L, Krapcho M, et al, eds. SEER Cancer Statistics Review, 1975–2006. Bethesda, MD: National Cancer Institute; 2009.

2. Brawer M. K. Prostate-specific antigen. Semin. Surg. Oncol., 18: 3-9, 2000.

3. Kirby RS. Pre-treatment staging of prostate cancer: recent advances and future prospects. *Prostate Cancer Prostatic Dis.* Sep 1997;1(1):2-10.

4. Terris MK, McNeal JE, Stamey TA. Estimation of prostate cancer volume by transrectal ultrasound imaging. *J Urol.* Mar 1992;147(3 Pt 2):855-857.

5. Middleton RG, Thompson IM, Austenfeld MS, et al. Prostate Cancer Clinical Guidelines Panel Summary report on the management of clinically localized prostate cancer. The American Urological Association. *J Urol.* Dec 1995;154(6):2144-2148.

6. Edmundson GK, Yan D, Martinez AA. Intraoperative optimization of needle placement and dwell times for conformal prostate brachytherapy. *Int J Radiat Oncol Biol Phys.* Dec 1 1995;33(5):1257-1263.

7. Stokes SH, Real JD, Adams PW, Clements JC, Wuertzer S, Kan W. Transperineal ultrasound-guided radioactive seed implantation for organ-confined carcinoma of the prostate. *Int J Radiat Oncol Biol Phys.* Jan 15 1997;37(2):337-341.

8. Wallner K, Blasko J, Dattoli M. *Prostate Brachytherapy made Complicated.* Seattle: Smart Medicine Press; 2001.

9. Okaneya T, Nishizawa S, Nakayama T, Kamigaito T, Hashida I, Hosaka N. Permanent prostate brachytherapy for Japanese men: results from initial 100 patients with prostate cancer. *Int J Urol.* Jul 2007;14(7):602-606.

10. Gibbons EP, Smith RP, Beriwal S, Krishna K, Benoit RM. Overcoming pubic arch interference with free-hand needle placement in men undergoing prostate brachytherapy. *Brachytherapy.* Jan-Mar 2009;8(1):74-78.

11. Sejpal SV, Sathiaseelan V, Helenowski IB, et al. Intra-operative pubic arch interference during prostate seed brachytherapy in patients with CT-based pubic arch interference of < or = 1cm. *Radiother Oncol.* May 2009;91(2):249-254.

12. Nag S, Beyer D, Friedland J, Grimm P, Nath R. American Brachytherapy Society (ABS) recommendations for transperineal permanent brachytherapy of prostate cancer. *Int J Radiat Oncol Biol Phys.* Jul 1 1999;44(4):789-799.

13. Bagrodia A, Diblasio CJ, Wake RW, Derweesh IH. Adverse effects of androgen deprivation therapy in prostate cancer: Current management issues. *Indian J Urol.* Apr 2009;25(2):169-176.

14. Moran B. Using the manipulation ruler. Basic and Advanced Techniques in Prostate Brachytherapy, Adam P. Dicker (Editor), Gregory Merrick (Editor), Leonard Gomella (Editor), Richard K. Valicenti (Editor), Frank Waterman (Editor) 2005;363-8.

15. Phee L, Yuen J, Xiao D, et al. Ultrasound guided robotic biopsy of the prostate. *Int J Hum Robot.* Dec 2006;3(4):463-483.

16. Taylor RH, Funda J, Eldridge B, et al. A Telerobotic Assistant for Laparoscopic Surgery. *IEEE Eng Med Biol.* May-Jun 1995;14(3):279-288.

17. Bassan HS, Patel RV, Moallem M. A Novel Manipulator for Percutaneous Needle Insertion: Design and Experimentation. *IEEE-Asme T Mech.* Dec 2009;14(6):746-761.

18. Yousef B, Patel R, Moallem M. A macro-robot manipulator for medical applications. *IEEE Sys Man Cybern.* 2006:530-535.

19. Fichtinger G, Burdette EC, Tanacs A, et al. Robotically assisted prostate brachytherapy with transrectal ultrasound guidance - Phantom experiments. *Brachytherapy.* Jan-Mar 2006;5(1):14-26.

20. Wei Z, Wan G, Gardi L, Mills G, Downey D, Fenster A. Robot-assisted 3D-TRUS guided prostate brachytherapy: system integration and validation. *Med Phys.* Mar 2004;31(3):539-548.

21. Yu Y, Podder TK, Zhang YD, et al. Robotic system for prostate brachytherapy. *Comput Aided Surg.* Nov 2007;12(6):366-370.

22. Hu Y, Podder T, Buzurovic I, Yan K, Ng WS, Yu Y. Hazard analysis of EUCLIDIAN: an image-guided robotic brachytherapy system. *Conf Proc IEEE Eng Med Biol Soc.* 2007;2007:1249-1252.

23. Salcudean SE, Prananta TD, Morris WJ, Spadinger I. A robotic needle guide for prostate brachytherapy. *2008 IEEE International Conference on Robotics and Automation, Vols 1-9.* 2008:2975-2981.

24. Hungr N, Troccaz J, Zemiti N, Tripodi N. Design of an ultrasound-guided robotic brachytherapy needle-insertion system. *Conf Proc IEEE Eng Med Biol Soc.* 2009;2009:250-253.

25. Meltsner MA, Ferrier NJ, Thomadsen BR. Observations on rotating needle insertions using a brachytherapy robot. *Phys Med Biol.* Oct 7 2007;52(19):6027-6037.

26. Fichtinger G, Fiene JP, Kennedy CW, et al. Robotic assistance for ultrasound-guided prostate brachytherapy. *Med Image Anal.* Oct 2008;12(5):535-545.

27. Kettenbach J, Kronreif G, Figl M, et al. Robot-assisted biopsy using computed tomography-guidance: initial results from in vitro tests. *Invest Radiol.* Apr 2005;40(4):219-228.

28. Stoianovici D, Cleary K, Patriciu A, et al. AcuBot: A robot for radiological interventions. *IEEE T Robotic Autom.* Oct 2003;19(5):927-930.

29. Stoianovici D, Song D, Petrisor D, et al. "MRI Stealth" robot for prostate interventions. *Minim Invasive Ther Allied Technol.* 2007;16(4):241-248.

30. Podder TK, Ng WS, Yu Y. Multi-channel robotic system for prostate brachytherapy. *Conf Proc IEEE Eng Med Biol Soc.* 2007;2007:1233-1236.

31. Lagerburg V, Moerland MA, Konings MK, van de Vosse RE, Lagendijk JJW, Battermann JJ. Development of a tapping device: a new needle insertion method for prostate brachytherapy. *Phys Med Biol.* Feb 21 2006;51(4):891-902.

32. Bax J, Gardi L, Montreuil J, Smith D, Fenster A. A compact robotic apparatus and method for 3-D ultrasound guided prostate therapy - Art. No. 65092H. *P Soc Photo-Opt Ins.* 2007;6509:H5092-H5092.

33. Bax J, Cool D, Gardi L, et al. Mechanically assisted 3D ultrasound guided prostate biopsy system. *Med Phys.* Dec 2008;35(12):5397-5410.

34. Bax J, Fenster A, Montreuil J, Gardi L, Smith D, Inventors. Apparatus and method for guiding insertion of a medical tool. US patent Pending 2008.

35. Tong S, Downey DB, Cardinal HN, Fenster A. A three-dimensional ultrasound prostate imaging system. *Ultrasound Med Biol.* 1996;22(6):735-746.

36. Fenster A, Downey DB, Cardinal HN. Three-dimensional ultrasound imaging. *Phys Med Biol.* May 2001;46(5):R67-99.

37. Ding M, Wei Z, Gardi L, Downey DB, Fenster A. Needle and seed segmentation in intra-operative 3D ultrasound-guided prostate brachytherapy. *Ultrasonics.* Dec 22 2006;44 Suppl 1:e331-336.

38. Ding M, Fenster A. A real-time biopsy needle segmentation technique using Hough transform. *Med Phys.* Aug 2003;30(8):2222-2233.

39. Wan G, Wei Z, Gardi L, Downey DB, Fenster A. Brachytherapy needle deflection evaluation and correction. *Med Phys.* Apr 2005;32(4):902-909.

40. Arun KS, Huang TS, Blostein SD. Least-squares fitting of two 3-d point sets. *IEEE Trans Pattern Anal Mach Intell.* May 1987;9(5):698-700.

41. Rickey DW, Picot PA, Christopher DA, Fenster A. A Wall-Less Vessel Phantom for Doppler Ultrasound Studies. *Ultrasound in Medicine and Biology.* 1995;21(9):1163-1176.

42. Fitzpatrick JM, West JB, Maurer CR. Predicting error in rigid-body point-based registration. *Ieee T Med Imaging.* Oct 1998;17(5):694-702.

43. Badea CT, Drangova M, Holdsworth DW, Johnson GA. In vivo small-animal imaging using micro-CT and digital subtraction angiography. *Phys Med Biol.* Oct 7 2008;53(19):R319-R350.

44. Cool D, Sherebrin S, Izawa J, Chin J, Fenster A. Design and evaluation of a 3D transrectal ultrasound prostate biopsy system. *Med Phys.* Oct 2008;35(10):4695-4707.

45. Epstein JI, Sanderson H, Carter HB, Scharfstein DO. Utility of saturation biopsy to predict insignificant cancer at radical prostatectomy. *Urology.* Aug 2005;66(2):356-360.

Chapter 4

4 Micro-CT Geometric Accuracy Phantom for Use with Image-Guided Needle Positioning Systems and Other Quantitative Applications

4.1 Introduction

Volumetric X-ray micro-computed tomography (micro-CT) is an increasingly important tool for research requiring imaging of small specimens or animals.[1] The growing importance of micro-CT is reflected in the exponential growth of publications since the early 1980s on the topic of small animal micro-CT imaging and the availability of a variety of micro-CT scanners from at least a dozen manufacturers.[2] Although often used for qualitative research applications, micro-CT has also developed into a useful tool for a wide range of quantitative applications. Micro-CT has been used for quantitative measurements in small-animal imaging applications such bone volume and roughness,[3] tracking of tumour progression and volume,[4] and the quantification of whole body composition.[5] Micro-CT has been demonstrated in the quantitative assessment of medical devices such as the characterization of ion chambers[6] and measurement of wear in replacement joints.[7] Quantitative information from micro-CT images has also been demonstrated in guiding mechatronic devices to complete preclinical micro-injection procedures.[8, 9] The success and utility of these applications is dependent on the geometric fidelity of images produced by micro-CT scanners. In applications that demand the highest geometric fidelity, such as the characterization of ion chambers[10] or image-guided devices, the ability to characterize the geometric accuracy of micro-CT scanners to a traceable standard ensures the highest quality results.

In-plane geometric inaccuracies of 0.2%[11] and 0.3%[12] have been previously reported for micro-CT scanners. These percentages represent the error in calibration of the micro-CT voxel size. The reported errors correspond to an error of 20 µm to 30 µm per centimeter of distance in an image. Although these errors are relatively small, they can still exert a noticeable negative influence on quantitative results. For instance, mechatronic devices using micro-CT image guidance to complete microinjection procedures may be required to place a needle tip with a positioning error of < 200 µm to reach small targets.[8] The demanding requirements of these mechatronic devices challenge the limits of micro-CT scanners. The previously reported geometric inaccuracies of micro-CT scanners would result in an error of approximately 50 µm, or at least one fourth of the allowable positioning error of the device, when applied over a typical range of motion of 20 mm. Geometric inaccuracies in micro-CT images are not an error source that can be neglected for demanding applications, and they need to be minimized.

Previous efforts have been made to develop quality assurance phantoms to evaluate the geometric accuracy of micro-CT scanners. Perilli et al. developed a phantom consisting of aluminum inserts of known geometry embedded in a cylinder of polymethylmethacrylate to evaluate imaging parameters for trabecular bone imaging applications.[13, 14] The known geometries of the inserts were compared to their geometry in the micro-CT images to evaluate the geometric accuracy of the scanner. However, the geometry of the inserts was never qualified to a traceable standard and the phantom did not offer a method to correct detected geometric inaccuracies in images. Du et al. developed a quality assurance phantom to assess a number of parameters related to image quality, including geometric accuracy.[11] The phantom assessed geometric accuracy by comparing the known distance of five beads to their positions in micro-CT images. However, again, the distances of the bead in the phantom were never qualified to a traceable standard. The phantom also only provides a measurement of in-plane geometric accuracy and not out-of-plane accuracy. Finally, the phantom was large and required a custom scanner bed that precludes it from use in a wide variety of micro-CT models.

In this paper, a compact quality assurance phantom qualified to a traceable standard is presented for routine evaluation of the geometric accuracy of micro-CT scanners. An automated algorithm is described that processes micro-CT images of the phantom to characterize the geometric accuracy of the scanner and calculate correction factors to reduce the geometric error of the images. The phantom and algorithm are used to evaluate the geometric accuracy of five micro-CT scanners representing four different models of micro-CT systems. The calculated correction factors are then applied to measurements of fiducial markers in each of the five scanners to evaluate their ability to improve fiducial localization. The techniques developed in this study allow the micro-CT end user to guarantee the highest level of geometric fidelity and to calibrate images to a traceable standard.

4.2 Methods

4.2.1 Calibration Phantom Construction

A calibration phantom was custom built to evaluate the geometric accuracy of micro-CT scanners. The physical size of the phantom is approximately 45 mm × 25 mm × 40 mm. The small size of the phantom enables it to be easily integrated onto a mechatronic device and allows it to fit within a wide range of micro-CT bore sizes. The calibration phantom contains six fiducial markers, which are 6.35 mm (¼") diameter borosilicate spherical beads (McMaster-Carr, Cleveland, OH). The fiducials are fixed in position using a frame constructed onto a 6.35 mm diameter carbon fiber shaft backbone (McMaster-Carr, Cleveland, OH). Attached to the carbon fiber backbone are three custom-made Delrin plastic clamps. One end of each of the three clamps attaches to the carbon fiber backbone and the other end supports a short length of 6.35 mm diameter carbon fiber shaft. The borosilicate bead fiducials are attached to the short carbon fiber shafts using cyanoacrylate glue (Loctite 4541, Henkel Corp., Düsseldorf, Germany). A micro-CT surface rendering of the completed calibration phantom is provided in Figure 4.1.

Delrin plastic and carbon fiber were selected for frame construction due to their high rigidity and low X-ray attenuation. High rigidity is a key material property since high dimensional stability of bead locations is required to evaluate the geometric accuracy of micro-CT scanners. Drift in bead positions would cause erroneous overestimates of image geometric error. For the frame, low X-ray attenuation is also a key material property to avoid micro-CT imaging artifacts and to ease segmentation and centroiding of the borosilicate beads. The borosilicate beads were selected as fiducials since they possess a precise sphericity of 2.54 µm. The sphericity of each bead was validated to a traceable standard using gauge blocks (Grade B-18, Mitutoyo Canada Inc., Toronto, ON, Canada) and an indicator (Model 24165-10**,** Starrett, Waite Park, MN).

The high sphericity of the beads ensures accuracy in phantom construction and in centroiding the beads in micro-CT images. The phantom design was carefully developed to ensure the phantom design is compact, possesses high dimensional stability and the fiducials can be easily segmented and centroided in micro-CT images.

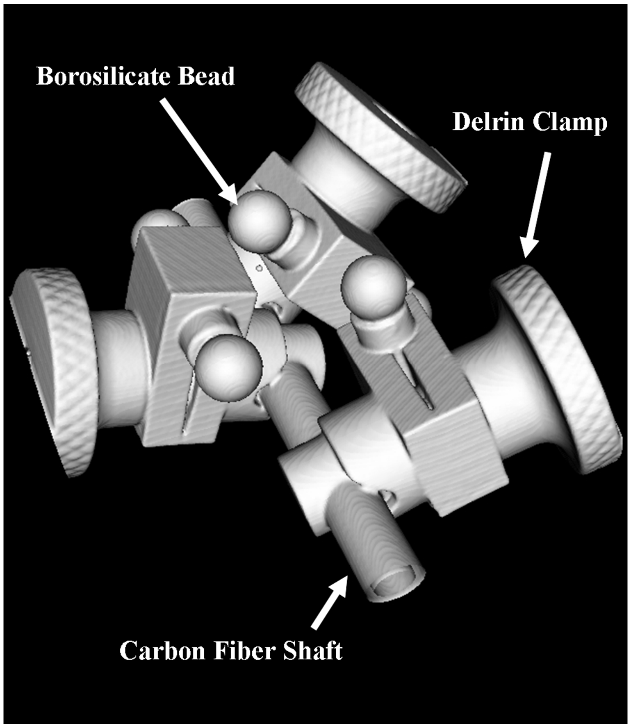

Figure 4.1: Micro-CT surface rendering of the calibration phantom.

4.2.2 Determination of Bead Positions within Calibration Phantom

The calibration phantom was used to evaluate the geometric accuracy of micro-CT scanners by comparing the known positions of beads within the phantom to the position of the beads in a micro-CT image. The dimensional accuracy of the calibration phantom is therefore critical to enable detection and correction of geometric errors of < 1 % in the voxel dimensions of micro-CT scanners. Therefore, a method was developed to measure the bead positions to a known and traceable standard of measurement.

The position of each bead in the phantom was measured using a calibrated XYZ positioning stage (M-462-XYZ-SD Series, Newport, Irvine, CA) with an attached indicator (Model 24165-10**,** Starrett, Waite Park, MN) mounted onto a granite surface plate (Grade B, Starrett, Waite Park, MN). The phantom was suspended above the granite surface plate by clamping the phantom carbon fiber backbone to a V-block (Model 228, Starrett, Wait Park, MN). Gauge blocks (Grade B-18, Mitutoyo Canada Inc., Toronto, ON, Canada) were then stacked onto the granite surface plate. The dimensional accuracy of the gauge blocks is certified to a known and traceable standard of measurement. The height of the stacked gauge blocks was compared to the height of a single bead above the granite surface using the XYZ positioning stage and attached indicator. The height of the gauge blocks was iteratively adjusted until the indicator indicated no difference between the stack height and bead height. The indicator possessed a measurement resolution of 2.54 µm.

The distance measurement process was completed for each of the six fiducial beads. The distance of each bead from the granite surface plate was then measured twice more in two directions orthogonal to the original measurement direction. The orthogonal distances were measured by rotating the V-block on the granite surface plate and repeating the iterative measurement process for each bead. The orthogonality of the V-block was measured by the same XYZ stage and attached indicator to be < 2.54 µm over 2.0 cm of stroke. The phantom and measurement tools are shown in Figure 4.2. Using this method, the three-dimensional position of each bead in the phantom was measured relative to a known and traceable standard of measurement.

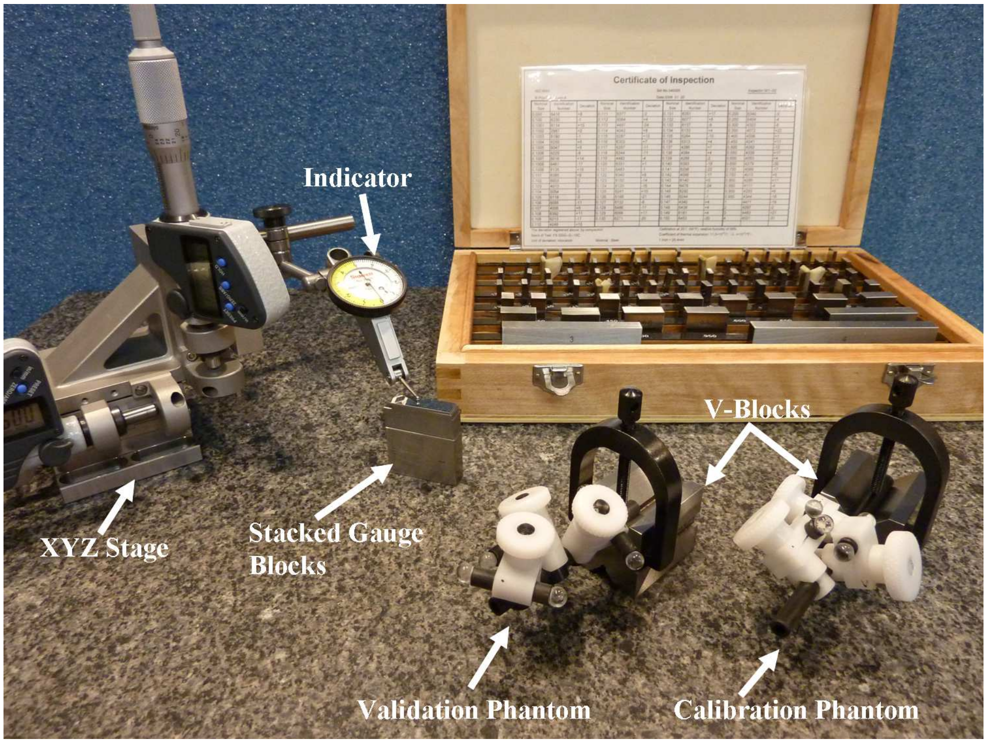

Figure 4.2: Calibration and validation phantom with measurement equipment.

4.2.3 Scanner Selection and Calibration Phantom Imaging

The calibration phantom was used to evaluate the geometric accuracy of five volumetric X-ray micro-CT scanners commercially available from General Electric Healthcare Biosciences (London, ON, Canada). The models of scanner evaluated included two eXplore Ultra Locus scanners and one of each of eXplore speCZT, eXplore CT 120 and eXplore RS. These scanners were selected to represent a range of commercially available micro-CT scanning equipment commonly employed in research laboratories, with a range of voxel spacing (0.05 mm to 0.15 mm) and transaxial field-of-view (70 mm to 150 mm).

A single common calibration phantom was imaged by all five scanners. The calibration phantom was scanned by each scanner five times at the approximate scanner isocenter. Between each scan the phantom was removed from the micro-CT bore and repositioned. For the eXplore Ultra Locus, in addition to five scans at the isocenter, five scans were taken at a position offset from the scanner isocenter by approximately 70 mm, for a total of 10 scans. The phantom was not scanned at a second position in the three remaining scanners since the phantom almost fully occupied these scanners maximum trans-axial field of view. The imaging parameters used for each scanner are summarized in Table 4.1.

Table 4.1: Summary of the micro-CT scan parameters used for imaging of the phantoms.

Scanner	Tube Voltage (kVp)	Tube Current (mA)	Views	View Exposure Time (ms)	Total Scan Time	Nominal Voxel Size (μm)
eXplore Locus Ultra	140	20	1000	16	16 seconds	153.9
eXplore SpecZT	110	32	900	16	5 minutes	49.8
eXplore CT 120	110	32	900	16	5 minutes	49.7
eXplore RS	80	45	900	400	120 minutes	45.4

4.2.4 Geometric Correction Calculation

An automated algorithm was developed using MATLAB (The Mathworks, Inc., Natick, MA) to compare the known position of beads in the phantom to their positions in the micro-CT images. The algorithm determines the position of the phantom’s borosilicate beads in the images by using a multi-step bead localization technique. Beads were first segmented using a threshold-based region growing algorithm. The threshold level was calculated using an iterative algorithm developed in MATLAB to determine the threshold that yielded an average segmented volume of the beads to within 0.1% of their known volume. The center of the segmented bead was then calculated using a squared-intensity-weighted centroiding algorithm. The algorithm used to calculate the bead centroids has an accuracy of < 5% of the nominal image voxel size in localizing 3D centroid positions in simulated images.[15] Since distance is measured between two bead centroids, the error in distance arising from this centroiding error is doubled.

Within the image set of each scanner, the distance of each bead to all other beads in the phantom was measured for a total of 15 distances. The distance in the images from each bead to all other beads was scaled to the known bead distances using the equation:

$$Dist_{Known} = \sqrt{(X_{img}/CF_x)^2 + (Y_{img}/CF_y)^2 + (Z_{img}/CF_z)^2} \qquad [1]$$

where X_{img} , Y_{img} , and Z_{img} are the components of the bead distance in the images along the respective axes of the scanner and CF_x, CF_y, and CF_z are the correction factors required along the respective axes of the scanner to transform the bead distances in the images to the known bead distances. Equation 1 for each of the 15 bead distances was combined to form the system of equations:

$$\begin{bmatrix} X_{img1}^2 & Y_{img1}^2 & Z_{img1}^2 \\ \downarrow & \downarrow & \downarrow \\ X_{img15}^2 & Y_{img15}^2 & Z_{img15}^2 \end{bmatrix} \times \begin{bmatrix} (1/CF_x)^2 \\ (1/CF_y)^2 \\ (1/CF_z)^2 \end{bmatrix} = \begin{bmatrix} Dist_{known1}^2 \\ \downarrow \\ Dist_{known15}^2 \end{bmatrix} \qquad [2]$$

The least-squares solution of Eq. 2 was determined to calculate values for each of the correction factors.

4.2.5 Validation Phantom Construction

A second phantom was constructed to validate the correction factors measured by the calibration phantom. The validation phantom is an independent verification that the calculated correction factors are not unique to the calibration phantom and generally correct images produced by the micro-CT scanner. The validation phantom, like the calibration phantom, contains six 6.35 mm (¼") diameter borosilicate spherical beads acting as fiducial markers (McMaster-Carr, Cleveland, OH). The beads were again secured to a 6.35 mm diameter carbon fiber shaft backbone using Delrin clamps. The positions of the beads in the validation phantom differed from the bead positions in the calibration phantom. Different bead positions were obtained by changing the angle of the Delrin clamps and by adjusting the length of carbon fiber shafts used to mount the beads to a length of 25.4 mm. Once the validation phantom was constructed, the bead positions within the phantom were measured using the method previously described for the calibration phantom. A micro-CT surface rending of the validation phantom is shown in Figure 4.3.

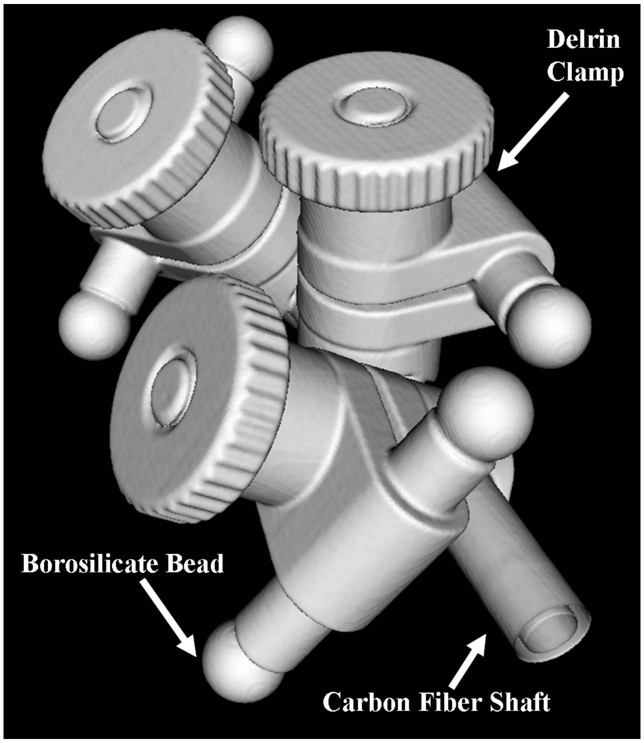

Figure 4.3: Micro-CT surface rendering of the validation phantom.

A rigid-body registration was applied between the measured bead positions of the calibration and validation phantom. The registration was applied to ensure that the bead positions in the validation phantom were truly independent of the calibration phantom. A poor rigid-body registration, as demonstrated by a large fiducial registration error (FRE),[16] would indicate that the validation phantom bead arrangement was different from the calibration phantom arrangement. An FRE of greater than 6.35 mm (or approximately one bead diameter) was assumed to indicate a sufficiently different bead arrangement.

The validation phantom was imaged once at the isocenter of each scanner. Again for the eXplore Ultra Locus, the phantom was imaged at an additional position offset from the isocenter. For each scanner, the same scan parameters summarized in Table 4.1 were used for the validation phantom. The validation phantom beads were segmented and centroided using the algorithm previously described for the calibration phantom. The distances between each bead pair in the validation phantom was calculated with and without applying the correction factors calculated for each scanner using the calibration phantom.

4.2.6 Data Analysis

The sets of calculated correction factors for each scanner were statistically compared using ANOVA and Tukey tests with $p < 0.05$ to determine if any statistically significant differences exist for the correction factors along the x, y and z axes of each scanner. This comparison was performed to determine if the geometric error of the scanners was isotropic or anisotropic in nature. If the correction factors are not significantly different (i.e. indicating an isotropic error), a single averaged correction factor could be used for each axis. For the two eXplore Locus Ultra scanners, pairs of correction factors from the isocenter and offset position for each axis were compared using a two-tailed paired t-test with $p < 0.05$ to determine if any significant difference exists for each respective correction factor at the two positions. If correction factors from the two positions are significantly different, it may indicate that the values of the correction factors are dependent on position within the scanner bore.

The correction factors were also statistically evaluated for their effectiveness in improving the geometric accuracy of micro-CT scanners. The distances between beads within the calibration phantom and the validation phantom were calculated with and without using the correction factors. The error for each of these distances was compared using a two-tailed paired t-test with $p < 0.05$ to determine if the correction factors reduced the error by a statistically significant amount. The distance errors were also qualitatively compared to determine if the differences in error were practically meaningful. Failure to identify a statistically significant and practically meaningful improvement in bead distance errors would indicate that use of the correction factors to improve scanner geometric accuracy is not a useful exercise.

4.3 Results

4.3.1 Correction Factor Values

The average calculated correction factor of each axis for each scanner is summarized in Table 4.2. In addition, an average volumetric correction factor is provided to characterize the correction in voxel volume for each scanner arising from the linear axis correction factors. A correction factor > 1 indicates that distances in the uncorrected micro-CT images overestimated the true dimensions. Generally, geometric errors in-plane along the X and Y axes are larger than out-of-plane errors in the Z direction. In-plane distances tend to be overestimated while out-of-plane distances are underestimated. A statistically significant difference was found between the correction factors in the X ($p = 0.043$ and $p < 0.001$), Y ($p < 0.001$ for both scanners) and Z ($p < 0.001$ for both scanners) axes for the

Table 4.2: Calculated average scanner correction factors of each axis.

Scanner	X-Axis Correction Factor	Y-Axis Correction Factor	Z-Axis Correction Factor	Volumetric Correction Factor
eXplore Locus Ultra Isocenter Scanner One	0.9998 ± 0.00006	1.0009 ± 0.00012	1.0002 ± 0.00021	1.0008 ± 0.00034
eXplore Locus Ultra Offset Scanner One	1.0008 ± 0.00063	0.9968 ± 0.00018	0.9987 ± 0.00040	0.9962 ± 0.00063
eXplore Locus Ultra Isocenter Scanner Two	1.0033 ± 0.00013	0.9981 ± 0.00012	0.9978 ± 0.00014	1.0020 ± 0.00012
eXplore Locus Ultra Offset Scanner Two	1.0022 ± 0.00010	0.9999 ± 0.00009	0.9998 ± 0.00008	0.9993 ± 0.00012
eXplore SpecZT	1.0011 ± 0.00007	1.0008 ± 0.00002	0.9990 ± 0.00004	1.0009 ± 0.00043
eXplore CT 120	1.0027 ± 0.00006	1.0031 ± 0.00103	1.0005 ± 0.00014	1.0064 ± 0.00133
eXplore RS	0.9963 ± 0.00021	0.9965 ± 0.00069	0.9957 ± 0.00025	0.9886 ± 0.00092

two different bore positions of the two eXplore Locus Ultra sccanners. These results suggest that the value of the correction factors varies within the micro-CT bore. The calibration phantom should ideally be placed as close as possible in the bore to the anticipated location of targets.

The results of Tukey tests comparing the correction factors for each scanner are summarized in Table 4.3. Generally, no significant difference was found between the X and Y correction factors for the scanners, indicating a single average correction factor can be used for the in-plane direction. The X and Y correction factors were only found to be significantly different for the two eXplore Locus Ultra scanners. However, for these two scanners the absolute difference between the X and Y factors were quite small, with < 1% difference. In general, the X and Y correction factors were generally significantly different from the Z correction factors. This result suggests the out-of-plane correction factor is unique from the in-plane correction factors.

Table 4.3: Results of Tukey test ($p < 0.05$) to determine if correction factors for each scanner are significantly different for each axis.

Scanner	X & Y	X & Z	Y & Z
eXplore Locus Ultra Isocenter Scanner One	Yes	No	Yes
eXplore Locus Ultra Offset Scanner One	Yes	Yes	No
eXplore Locus Ultra Isocenter Scanner Two	Yes	Yes	Yes
eXplore Locus Ultra Offset Scanner Two	Yes	Yes	Yes
eXplore SpecZT	No	Yes	Yes
eXplore CT 120	No	Yes	Yes
eXplore RS	No	No	Yes

4.3.2 Geometric Correction to Calibration Phantom

The average error in bead distance within the calibration phantom for all sets of images was calculated with and without application of the calculated correction factors. The corrected and uncorrected bead distances are summarized in Table 4.4. Application of the correction factors reduced the error in bead positions for the calibration phantom in four out of five image sets. In nearly all cases the corrected and uncorrected error were found to be significantly different. The p-values for each scanner are also summarized in Table 4.4. The mean difference in corrected and uncorrected errors ranged from negligible to 83 μm in absolute terms or 0 to 0.338 in percent terms.

Table: 4.4: Summary of the mean error in the measured bead distances of the calibration phantom for each scanner. The uncorrected errors and the corrected errors calculated using the appropriate scaling factors is provided. Each error is described with both a mean absolute value in μm and as a percent of the total bead distance. Finally, the p-value of the t-test between the corrected and uncorrected error of each scanner is provided.

Scanner	**Uncorrected Error (μm)**	**Corrected Error (μm)**	**Uncorrected Error (%)**	**Corrected Error (%)**	**p-Value**
eXplore Locus Ultra Isocenter Scanner One	22 ± 2	22 ± 3	0.096 ± 0.013	0.101 ± 0.016	p = 0.03
eXplore Locus Ultra Offset Scanner One	38 ± 3	31 ± 4	0.172 ± 0.014	0.148 ± 0.014	p = 0.002
eXplore Locus Ultra Isocentre Scanner Two	19 ± 1	7 ± 1	0.078± 0.006	0.031± 0.007	p < 0.001
eXplore Locus Ultra Offset Scanner Two	36 ± 1	35 ± 1	0.146± 0.003	0.150± 0.003	p = 0.16
eXplore SpecZT	18 ± 4	11 ± 3	0.080 ± 0.016	0.054 ± 0.014	p < 0.001
Explore CT 120	50 ± 7	7 ± 1	0.200 ± 0.027	0.007 ± 0.001	p = 0.001
eXplore RS	92 ± 6	9 ± 2	0.380 ± 0.027	0.042 ± 0.011	p < 0.001

4.3.3 Bead Arrangement of Calibration Phantom and Validation Phantom

The average distance between beads within the calibration phantom was measured to be 24.14 ± 7.51 mm. Within the validation phantom, the average bead distance was 39.41 ± 12.99 mm. The smallest FRE of the rigid body registration of the measured calibration bead locations to the validation phantom locations was 18.4 ± 6.3 mm, or approximately three fiducial bead diameters. A large FRE indicates that the bead pattern in the validation phantom is unique from the bead pattern within the calibration phantom.

4.3.4 Geometric Correction to Validation Phantom

The average error in bead distance within the validation phantom for all sets of images was calculated with and without application of the calculated correction factors from the calibration phantom. The corrected and uncorrected bead distances are summarized in Table 4.5. The p-values for the two-tailed t-tests between the corrected and uncorrected errors are also summarized in table 4.5. In three scanners with minimal geometric accuracy errors, application of the correction factors slightly increased the geometric errors of the images. However, this increase was not statistically significantly except for the offset position of the second eXplore Locus Ultra scanner. For the two remaining scanners, application of the correction factors significantly improved the geometric accuracy of the scanner.

Table 4.5: Summary of the mean error in the measured bead distances of the validation phantom for each scanner. The uncorrected errors and the corrected errors calculated using the appropriate scaling factors from the calibration phantom are provided. Each error is described with both a mean absolute value in µm and as a percent of the total bead distance. Finally, the p-value of the t-test between the corrected and uncorrected error of each scanner is provided.

Scanner	Uncorrected Error (µm)	Corrected Error (µm)	Uncorrected Error (%)	Corrected Error (%)	p-Value
eXplore Locus Ultra Isocenter Scanner One	37 ± 27	38 ± 26	0.100 ± 0.080	0.101 ± 0.074	p=0.46
eXplore Locus Ultra Offset Scanner One	44 ± 36	54 ± 41	0.132 ±0.138	0.163 ±0.158	p=0.26
eXplore Locus Ultra Isocentre Scanner Two	27 ± 15	29 ± 15	0.077 ± 0.068	0.084 ± 0.056	p=0.69
eXplore Locus Ultra Offset Scanner Two	44 ± 22	80 ± 54	0.132 ± 0.117	0.215 ± 0.145	p= 0.01
eXplore SpecZT	15 ± 10	19 ± 13	0.047 ±0.041	0.049 ±0.033	p=0.35
eXplore CT 120	67 ± 27	22 ± 16	0.168 ± 0.037	0.052 ± 0.025	p<0.001
eXplore RS	148 ± 61	27 ± 19	0.370 ± 0.086	0.074 ± 0.054	p<0.001

4.3.5 Comparison of Validation Phantom Errors

The eXplore CT 120, eXplore speCZT and eXplore RS all yielded images with a voxel size of approximately 50 µm. The corrected and uncorrected errors of these three scanners were compared using ANOVA and Tukey tests with $p < 0.05$ to see if errors were consistent across three scanners with images of the same voxel size. The uncorrected errors of all three scanners were found to be statistically different. However, the corrected errors of all three errors were not found to be statistically different. This indicates scanners of the same voxel size tend to have unique geometric inaccuracies but will possess similar non-unique accuracies when corrected by the phantom. The corrected and uncorrected errors of the two positions of the two eXplore Locus Ultra scanners were also compared using a two-tailed paired t-test. The uncorrected errors of the isocenter (p = 0.29) and offset (p = 0.94) positions were not significantly different. Similarly, the corrected isocenter (p = 0.23) and offset (p = 0.21) positions were also not significantly different.

4.4 Discussion

We have demonstrated the use of a specialized calibration phantom to measure and correct the geometric accuracy of five different micro-CT scanners spanning four model types. The calibration phantom can be used to calculate traceable correction factors that improve the localization of fiducials in micro-CT images whose positions are independent of the initial calibration phantom.

In two of the five scanners tested, calculation and application of the correction factors were found to significantly improve fiducial localization independent of the calibration phantom. For these two scanners, the mean geometric error of the images was reduced from 0.20% and 0.38% to 0.01% and 0.04% respectively. For the three remaining scanners, application of the correction factors slightly increased geometric error of the validation phantom; however, the increase was not statistically significant. Although small in absolute terms, the calibration phantom can provide a significant and meaningful improvement for completing image-guided micro-injection procedures. For the worst-case scanner, the mean error in fiducial localization for the validation phantom was reduced from 0.370% of the bead distance to 0.074% of bead distance. Over a 20 mm travel of a typical small-animal mechatronic device, this represents a reduction of error from 74 µm to 15 µm. An improvement of 59 µm provides a considerable benefit towards achieving a desirable position error > 200 µm for a mechatronic device. In addition, the linear correction factors of each scanner axis will multiply to result in a larger volumetric correction factor. The volumetric correction factor characterizes the change in voxel volume resulting from the calculated correction factors. The greatest volumetric correction occurred for the eXplore RS and was approximately 1.14%. This value indicates the un-calibrated scanner would be expected to underestimate the volume of an object by 1.14 % based on the correction factor values. These results suggest measurement, and if need be, correction of the geometric inaccuracies in micro-CT images is required for image-guided interventions or any other application that demands high geometric fidelity of images.

The small size of the calibration phantom allows it to fit within the bore of a wide range of micro-CT scanner designs and to be easily incorporated into the designs of mechatronic devices. The use of an automated algorithm allows the correction factors to be calculated quickly. The most significant interruption to the work flow of mechatronic micro-injection procedures would be the time required to scan and reconstruct images of the calibration phantom. However, micro-CT mechatronic devices typically require a scan at the start of interventions to register the device with the micro-CT scanner. Measurement and correction of scanner geometric inaccuracies could be incorporated into the registration process of mechatronic devices. Either the scanner is well calibrated and the correction factors provide no significant improvement at the cost of a minimal time increase for registration or best case, application of the correction factors provides a meaningful improvement to target localization and targeting accuracy. In either case, the end user is assured that localization errors resulting from geometric errors have been minimized and will not affect the success of their interventions. The application of correction factors can provide a major improvement in targeting accuracy with minimal additional cost in time or resources and should be incorporated into the design of any micro-CT guided mechatronic device.

Statistical analysis of the correction factors suggests the geometric inaccuracy of micro-CT scanners is slightly anisotropic in nature. Although the anisotropy was statistically significant, it was extremely small. The largest percent difference between the mean scaling factors of an axis of a scanner was approximately 0.5% for the isocenter of the second eXplore Locus Ultra scanner. The X and Y correction factors were generally not significantly different from each other but were generally significantly different from the Z correction factor. These results are not surprising. In the scanners tested, the same X-ray detector pixel spacing is used for measurement of the in-plane direction along the x and y axes but not along the z axis. These results suggest a single averaged value of the X and Y correction factors can be used along these axes. When exceptions existed for this trend, the absolute difference between these two correction factors remained quite small (< 0.5 %), suggesting an average correction factor can still be used. Between the isocenter and offset positions of the two eXplore Locus Ultra scanners a significant difference in correction factors was found along all three axes. These results suggest the geometric accuracy of micro-CT scanners may vary with location in the bore. The calibration phantom should therefore be placed as close to targets as possible.

Interesting inferences can be made from the calculated corrected and uncorrected errors across the micro-CT scanners. The eXplore CT 120, eXplore speCZT and eXplore RS all yielded images with an isotropic voxel size of approximately 50 µm. The eXplore speCZT had a small geometric error indicating it was already well-calibrated for geometric accuracy, whereas the eXplore CT 120 and eXplore RS possessed correctable initial geometric errors. A Tukey test found these three scanners to have statistically significant difference in uncorrected errors. However, the corrected errors of these three scanners were not significantly different and are all approximately the same. These results suggest use of the calibration phantom can correct the geometric accuracy of poorly calibrated micro-CT scanners to correspond with the accuracy of an already well calibrated scanner of equivalent voxel size. Similarly, both eXplore Locus Ultra scanners were well-calibrated and possessed a similar small geometric error. Between these two scanners, no significant difference was found between the uncorrected and corrected errors. The eXplore Locus Ultra results again suggest scanners of the same voxel size will possess similar geometric errors when calibrated.

For comparison of results, previous studies to quantify the geometric accuracy of micro-CT scanners have been limited. Furthermore, none of these previous studies offered methods to correct geometric inaccuracies. However, previous studies have measured the in-plane geometric error of both the eXplore Locus Ultra and eXplore CT 120. Du et al. reported a 0.2% error for the eXplore Locus Ultra. This is comparable to the mean errors of 0.10 ± 0.01 % and 0.08 ± 0.01 % detected by our calibration phantom at the isocenter and 0.17 ± 0.01 % and 0.15 ± 0.01 % detected offset from the isocenter.

Bahri et al. reported a 0.3% error for the eXplore CT 120, which is comparable to the averaged error of 0.20 ± 0.03 % detected using our calibration phantom. Our phantom found both the eXplore Locus Ultra and eXplore CT 120 to undersize voxels when compared to the manufacture’s specifications, which is consistent with the findings of both Du et al. and Bahri et al.. The results reported in this paper appear in line with these previous results.

4.5 Conclusion

We have developed a traceable calibration phantom and a technique to evaluate the geometric accuracy of micro-CT scanners. The geometric errors detected by this new phantom are in-line with previous errors reported using non-traceable phantom designs. In two of the five scanners evaluated using the new phantom design, statistically significant correction factors were derived to correct the scanner geometric accuracy. However, for many applications, the impact of these correction factors would be small. These results suggest that non-traceable phantom designs are sufficient for the geometric calibration of micro-CT scanners for the majority of applications. Use of a traceable calibration phantom may be useful for applications demanding the highest geometric fidelity of images, such as small animal image-guided interventions or the characterization of medical devices. The calibration phantom is an easily implemented assurance to micro-CT end users that the geometric fidelity of their images has been calibrated against a traceable standard of measurement.

4.6 References

1. Badea CT, Drangova M, Holdsworth DW, Johnson GA. In vivo small-animal imaging using micro-CT and digital subtraction angiography. *Phys Med Biol.* Oct 7 2008;53(19):R319-350.

2. Schambach SJ, Bag S, Schilling L, Groden C, Brockmann MA. Application of micro-CT in small animal imaging. *Methods.* Jan 2010;50(1):2-13.

3. Silva MD, Savinainen A, Kapadia R, et al. Quantitative analysis of micro-CT imaging and histopathological signatures of experimental arthritis in rats. *Mol Imaging.* Oct 2004;3(4):312-318.

4. Namati E, Thiesse J, Sieren JC, Ross A, Hoffman EA, McLennan G. Longitudinal assessment of lung cancer progression in the mouse using in vivo micro-CT imaging. *Med Phys.* Sep 2010;37(9):4793-4805.

5. Granton PV, Norley CJ, Umoh J, et al. Rapid in vivo whole body composition of rats using cone beam micro-CT. *J Appl Physiol.* Oct 2010;109(4):1162-1169.

6. McNiven AL, Umoh J, Kron T, Holdsworth DW, Battista JJ. Ionization chamber volume determination and quality assurance using micro-CT imaging. *Phys Med Biol.* Sep 21 2008;53(18):5029-5043.

7. Teeter MG, Naudie DD, McErlain DD, et al. In vitro quantification of wear in tibial inserts using microcomputed tomography. *Clin Orthop Relat Res.* Jan 2011;469(1):107-112.

8. Nicolau SA, Mendoza-Burgos L, Soler L, Mutter D, Marescaux J. In vivo evaluation of a guidance system for computer assisted robotized needle insertion devoted to small animals. *Medical Imaging and Augmented Reality, Proceedings.* 2008;5128:241-250.

9. Waspe AC, McErlain DD, Pitelka V, Holdsworth DW, Lacefield JC, Fenster A. Integration and evaluation of a needle-positioning robot with volumetric microcomputed tomography image guidance for small animal stereotactic interventions. *Med Phys.* Apr 2010;37(4):1647-1659.

10. Ross CK. Comments on 'Ionization chamber volume determination and quality assurance using micro-CT imaging'. *Phys Med Biol.* Mar 2009;54(6):L23-L27.

11. Du LY, Umoh J, Nikolov HN, Pollmann SI, Lee TY, Holdsworth DW. A quality assurance phantom for the performance evaluation of volumetric micro-CT systems. *Phys Med Biol.* Dec 7 2007;52(23):7087-7108.

12. Perilli E, Baruffaldi F, Bisi MC, Cristofolini L, Cappello A. A physical phantom for the calibration of three-dimensional X-ray microtomography examination. *J Microsc.* May 2006;222(Pt 2):124-134.

13. Bahri MA, Warnock G, Plenevaux A, Choquet P, Constantinesco A, Salmon E, Luxen A, Seret A. Performance of the General Electric eXplore CT 120 micro-CT using the vmCT phantom. *Nucl. Instr. and Meth A*, in press, 2010.

14. Stoico R, Tassani S, Perilli E, Baruffaldi F, Viceconti M. Quality control protocol for in vitro micro-computed tomography. *J Microsc.* May 2010;238(2):162-172.

15. Patwardhan A. Subpixel position measurement using 1D, 2D and 3D centroid algorithms with emphasis on applications in confocal microscopy. *J Microsc-Oxford.* Jun 1997;186:246-257.

16. Fitzpatrick JM, West JB, Maurer CR. Predicting error in rigid-body point-based registration. *IEEE T Med Imaging.* Oct 1998;17(5):694-702.

Chapter 5

5 3D Image-Guided Robotic Needle Positioning System for Small Animal Interventions

5.1 Introduction

Clinical medical robotics is a mature field and dozens of clinical robotic systems have been developed for use in a wide range of interventional applications.[1] Today, use of medical robotics is increasingly becoming part of routine procedures for example, the da Vinci robot by Intuitive Surgical for radical prostatectomy.[2] This growing use and importance of medical robotic systems is a stark contrast to the state of robotics for use with small animals in preclinical research. A particular preclinical application, that could greatly benefit from the use of robotics is the development of an image-guided robotic system for needle interventions. Although a number of systems have been developed for image-guided clinical needle interventions[3] no such systems are in use for routine preclinical use. Rather, sub-optimal non-robotic and non-image-guided techniques remain the norm for small animal needle interventions. Techniques typically used for small animal needle interventions require surgical exposure of targets,[4-7] percutaneous injections through the skin[4, 8] or stereotactic devices.[9] Exposure of the subjects to surgery suffers from associated surgical mortality and morbidity, which may confound research results. Both percutaneous and surgical techniques are ultimately highly dependent on the ability of a human operator to correctly place a needle, and they suffer from problems of accuracy and repeatability. Stereotactic devices are limited to interventions within the skull and are limited by the accuracy of anatomic atlases and localization of external landmarks. In comparison, the current methods typically used for small animal needle interventions are relatively unsophisticated in comparison to clinical methods.

Imaging technology has outperformed robotics in the development of specialized small-animal systems for preclinical research. Analogous small-animal imaging systems have been developed for all the major clinical imaging modalities including computed tomography (CT), magnetic resonance (MR), positron emission tomography (PET), single-photon emission computed tomography (SPECT) and ultrasound. These small-animal imaging systems have achieved popular use and are considered to have greatly contributed to preclinical research.[10] CT imaging developed for use with small-animals, commonly referred to as micro-CT, is a particular imaging modality of interest. Micro-CT scanners are available from at least a dozen manufacturers[11] with typical voxel sizes ranging from 5 μm to 450 μm and trans-axial fields of view ranging from 1 to 20 cm.[12, 13]

To ameliorate small animal needle interventions, a number of previous efforts have been made to integrate robotic devices with micro-CT imaging systems to perform image-guided needle interventions.[14-17] In addition, several devices not explicitly intended for imaging-guidance have also been developed for small needle interventions and could be potentially integrated with micro-CT imaging.[18, 19] The development of these systems combines the accurate and non-invasive target localization of imaging with the positioning accuracy and repeatability of robotic systems. The design requirements these devices must satisfy are demanding. A needle positioning error of < 200 μm may be required to successfully complete small animal needle interventions.[17] Furthermore, the design of these devices must be extremely compact to allow them to be fully integrated into the small bores of micro-CT imaging systems.

Five previous efforts for potential small animal micro-CT robotic needle intervention systems have been identified. Unfortunately, none of these systems are ideal. The system developed by Waspe et al.[17] is the most sophisticated and best characterized of these devices. The system was successfully integrated with a micro-CT scanner and achieved a mean targeting error of 154 ± 113 μm in a tissue mimicking phantom. The system was also able to successfully inject tungsten beads into a rat brain. However, the system was too large to fit within a micro-CT bore and required transport of the animal to the robot workspace following imaging. The system also suffered from variations in targeting accuracy as evidenced by the large standard deviation in targeting error. The four remaining systems also suffer from a number of drawbacks. The three systems developed by Kanzides et al.,[14] Hwang et al .[18] and Ramrath et al.[19] all lack a technique to register the robotic devices with a micro-CT imaging system. The accuracy of these three systems was only evaluated in air rather than in tissue mimicking phantoms. Ramrath et al. achieved an impressive mean positioning accuracy of 32 μm; however, the robot is based on a stereotactic device and is limited to interventions in the skull. Kanzides et al. and Hwang et al. achieved poorer mean targeting accuracies of 0.4 mm and 2 mm respectively. The fourth system, developed by Nicolau et al.[15], did not have its overall targeting accuracy characterized, but the authors demonstrated its ability to localize the needle tip to within 0.7mm. None of the aforementioned authors evaluated the ability of their robot to operate within a micro-CT bore.

This paper presents the design of a micro-CT guided small-animal robotic needle-positioning system and demonstrates its ability to perform needle interventions within the bore of the scanner with a targeting accuracy of < 200 μm. The robotic system implements a spherical linkage design, based on the miniaturization of previous clinical systems used for prostate[20] and breast biopsy[21]. The spherical linkages of the robot are designed to create a remote center of motion (RCM).[22] In order to simplify the robotic design and maintain a small targeting error, a novel implementation of the RCM is used in the system. The positioning error of the robotic system is quantified using targeting experiments in tissue-mimicking phantoms. *In vivo* experiments were performed to test the robotic system's ability to direct a needle to a specified target in a xenograft mouse model and to assist with tumour interstitial fluid pressure (IFP) under image guidance.

5.2 Methods

5.2.1 Mechatronic System Design

5.2.1.1 Kinematic Frame Design

High rigidity is the critical factor in the success of a kinematic frame design used for high targeting accuracy. The rigidity of the kinematic frame can be most easily improved by miniaturizing the size of the mechanism. Decreasing the size of the frame by half would increase its rigidity by eight times. In addition, a smaller frame will also allow the robotic system to operate within a micro-CT bore and complete interventions without the need to relocate the animal. Not requiring relocation of the animal during interventions reduces opportunities for target motion and improves targeting accuracy. The kinematic frame design must therefore be as compact as possible.

The use of a robot architecture based on a fixed remote center of motion (RCM) is best suited for completing a specific task in a confined workspace.[1] The RCM architecture, is well established within clinical robotic systems.[22] In an RCM-based robot architecture all of the rotational axes of the robot intersect at a common point in 3D space. This architecture allows for higher angular mobility in a confined space such as a scanner bore. An RCM design also has the added advantage of allowing needle translation and orientation to be decoupled when positioning the needle for interventions. The decoupling of translation and orientation no longer makes it necessary to simultaneously control multiple degrees of freedom during the most delicate part of procedures: needle insertion.

A comparative analysis was performed to determine the RCM architecture best suited for the kinematic frame. The designs considered were the double parallelogram linkage,[17] the goniometric arc[19] and the spherical linkage[18, 20]. The double-parallelogram design was found to be unsuitable for this application because of its size and number of components required. The goniometric arc is a simpler design than the double-parallelogram. However, it is difficult to manufacture a linear bearing from CT-compatible materials to support the tool in a goniometric arc design. The ferrous materials typically used in most linear bearings will generate streak artifacts because of high attenuation and non-ferric CT-compatible materials typically lack rigidity, which results in bearing deflection and friction. The spherical linkage was found to be better than the other two options due to its simplicity of design. The spherical linkage design also allows for ease in adjustability and calibration to create a precise RCM independent of the manufacturing tolerances in each part of the linkage. The RCM adjustment is accomplished by splitting the base link (Figure 5.1) into two parts to control the orientation of each hinged connection in the linkage. The orientation of the hinged connections can then be calibrated to intersect at the RCM. A spherical linkage was selected for the kinematic frame of the system due to its simplicity and ability to achieve a precise RCM.

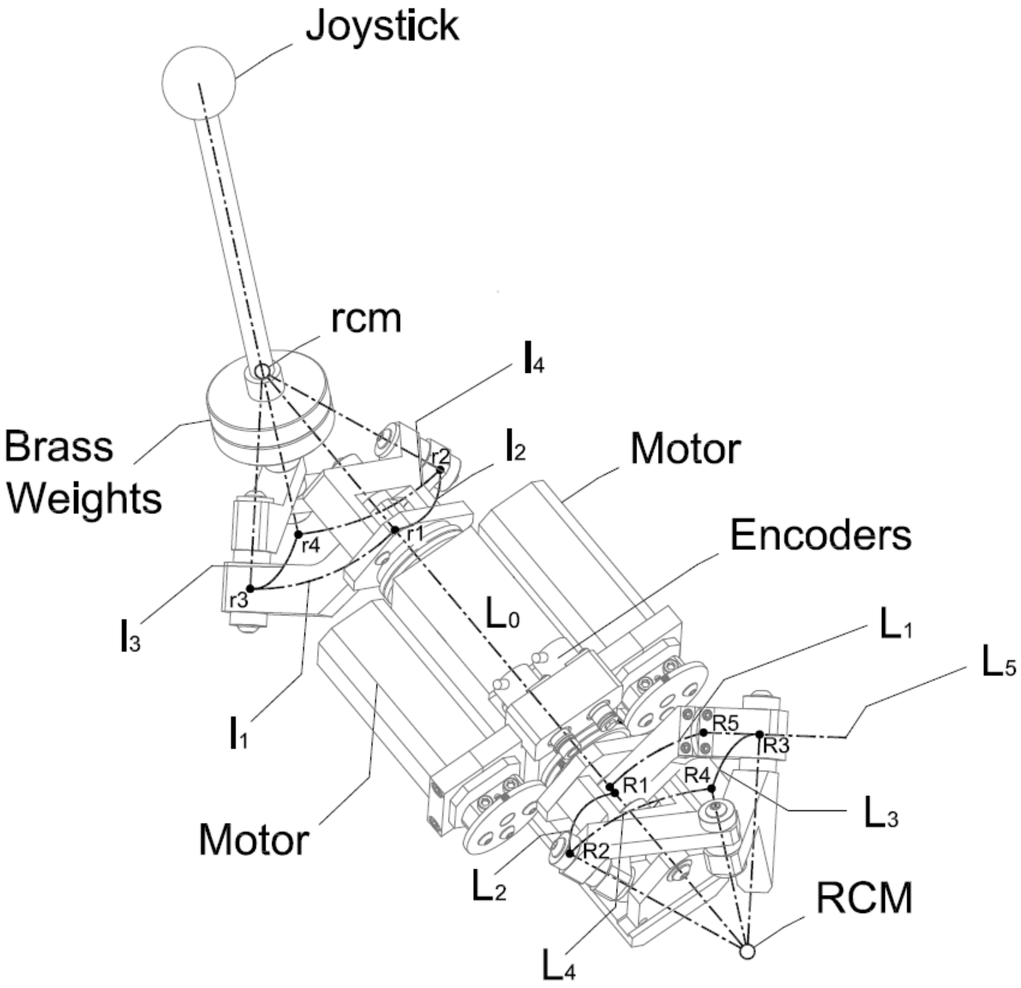

Figure 5.1: A schematic representation of the proposed RCM linkage design, which consists of two parts: a forward (labeled L_1 through L_5) and a rear spherical linkage (labeled l_1-l_4). The forward spherical linkage consists of five links (L_1-L_5) supporting the needle driver and five hinged connections (R_1-R_5) pinned to the base (L_0). The rear linkage is a mirror image of the forward linkage and consists of four linkage elements (l_1-l_5) and four hinged connections (r_1-r_4). The extra pinned connection (R_5) in the forward assembly is used to adjust the axis of each pinned connection (R_3 and R_4) in the base link (L_1 and L_5) to create a precise RCM. The linkage functions as a pantograph to constrain the rear linkage to counterbalance the forward linkage and payload using the brass weights attached to the rear spherical linkage. The two encoders are mounted to the base (L_0), and record the angle of each rotational axis. The needle is mounted to the link L_3 and its axis is aligned along the rotational axis R_5. The spherical linkages can be manipulated using either motors or through manual manipulation of a handle mounted to the rear spherical linkage. The axis of each hinged connection in the spherical linkages converges to a common point in space to form a remote center of motion: (RCM) at the forward spherical linkage and (rcm) at the rear linkage

5.2.1.2 Mechatronic System Description

The mechatronic system contains a total of six degrees of freedom. Two degrees of freedom are contained within the systems spherical linkages, which form two rotational axes: roll and pitch. The rotational axes control needle orientation during interventions. Three degrees of freedom are contained in a custom-built 3-axis xyz linear stage, which supports the spherical linkage (Figure 5.2). The linear stage controls needle translation during interventions. The stage provides 3 cm of stroke along the x and y axes and 1.5 cm along the z axis, with an accuracy 2.54 µm in each axis. The position of the stage along each axis is tracked using three optical encoders. Finally, the system consists of a one degree of freedom linear needle driver. The needle driver is used to insert and retract the needle during interventions. Both the mouse bed and robotic system are secured directly to the couch of the micro-CT scanner (Figure 5.2). The entire system is compact enough to operate entirely within the micro-CT bore.

The spherical linkage assembly consists of two parts: a forward and a rear linkage (Figure 5.1). The forward and rear linkages are coupled together through an elongated shaft assembly. The shaft assembly and associated linkage functions as a pantograph to allow the rear linkage to counterbalance the forward linkage and payload. The forward spherical linkage contains an encoder (RM22SC001 2B30F1C00, Renishaw, Gloucestershire, U.K.) for each of the two rotational axes. The two encoders are mounted to the base of the spherical linkage and record the angle of each rotational axis. The encoders allow for real-time monitoring and display of each rotational axes' angle. The spherical linkages can be manipulated using either motors or manual manipulation of a joystick mounted to the rear spherical linkage. The axis of each hinged connection in the spherical linkage converges to a common point in space to form an RCM. The angle between each hinged connection in the spherical linkage defines the size and shape of the operating envelope of the kinematics frame. The base link (Figure 5.1, L_1) defines the reference axis of the rotational coordinate system, which is fixed at the RCM. The encoders mounted on the robot base are used to measure the relative angles between the two successive linkages (Figure 5.1, links: L_1 and L_2) and between the links L_1 and base respectively.

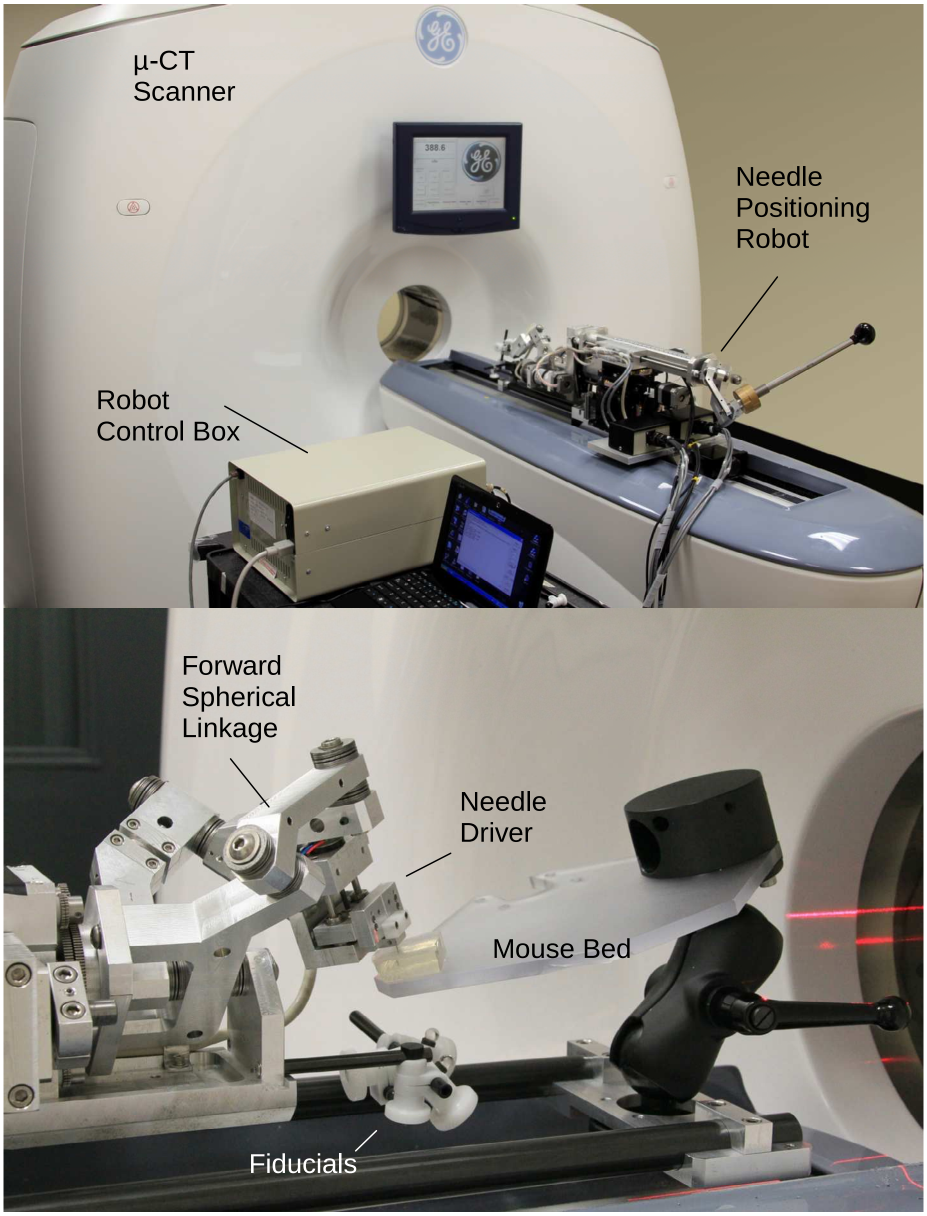

Figure 5.2: (Top) Photograph of the robotic apparatus mounted on the CT scanner animal couch and control system. The mechatronic apparatus consists of an XYZ linear stage that supports the spherical linkage. (Bottom) Photograph of the forward spherical linkage and attached needle driver. The needle driver is mounted such that the axis of the needle intersects the RCM of the spherical linkage. The mouse bed is attached to a double ball joint, which in turn is clamped to the animal couch via a pair of hollow aluminum rails giving a total of six degrees of freedom. The fiducials mounted to the aluminum shaft below the mouse bed are used to register the robot to the CT scanner. This registration will account and correct for the variability introduced when the robot is reattached to the micro-CT.

The forward spherical linkage consists of six links and five hinged connections supporting the needle driver. The rear linkage is a mirror image of the forward linkage and consists of five linkage elements and four hinged connections. The extra pinned connection in the forward assembly is used to adjust the axis of each pinned connection in the base link to create a precise RCM. Figure 5.1 shows a schematic representation of the RCM linkage design.

To determine the stability of the RCM, a precision tooling ball (6.35mm diameter, part 29011, Jergens Inc., Cleveland, OH) was attached to the linkage and aligned to the RCM. The tooling ball displacement throughout the spherical linkages' full range of motion was measured using a calibrated xyz stage (M-462, Newport Corp., Irvine, CA) and attached indicator (Model 25164-10, The L.S. Starrett Company, Waite Park, MN). The measured tooling ball deviation was < 12.5 μm along the x, y and z axis.

The motorized needle driver is mounted to the forward spherical linkage to insert and retract the needle (Figure 5.2). The needle driver is mounted such that the axis of the needle intersects the RCM of the spherical linkage. The robot implements the RCM in a unique fashion compared to previous designs for small animal interventions. The RCM of the system is positioned at the target location within the animal, using the 3-axis xyz linear stage. Next, the needle driver inserts the needle to the RCM location, which also corresponds with the target. This is a clear divergence from previous robotic designs where the RCM is typically placed on the skin surface. The RCM is positioned at the target rather then the skin to improve targeting accuracy through simplification of the needle driver design. The needle driver is not required to position the needle tip at a range of depths. Rather, the needle driver only needs to position the needle tip in either an inserted or retracted position. The use of a hard stop to control the needle's inserted position eliminates the need for encoders to track the driver position. As part of the robot calibration procedure, the needle is adjusted to locate the inserted needle tip position at the RCM of the robot's linkages.

The electronics of the robot are divided into two separate control systems: one system for the xyz stage and one system for the spherical linkage and needle driver. The spherical linkage and needle driver are driven by stepper motors controlled by a multi-axis dual-loop controller (MAXNet, Pro-Dex Oregon Micro Systems, Oregon, WA) and stepper motor drivers (BSD-01v2, Interinar Electronics, Tampa, FL). The xyz stage is powered by three stepper motors coupled to lead screws. The stepper motors are controlled by a multi-axis controller with integrated stepper motor drivers (DMC2133 with SDM-20242, Galil Motion Controls, Rocklin, CA). Each axis of the xyz stage contains a linear encoder, which feeds into the multi-axis controller. Custom closed-loop software on the controller monitors the encoders to compare the target position of each axis against its desired position. Both control systems are interfaced to a host PC via an ethernet hub. Custom software on the host PC sends programs and commands to each of the controllers. The user enters the desired position and orientation of the needle into the PC. The software then uses appropriate inverse kinematic equations to calculate the appropriate commands to send to each controller.

5.2.2 Robot Calibration

5.2.2.1 Coordinate System Calibration

The coordinate system of the robot was calibrated to ensure accurate control of the robot position. The coordinate system of the robot is aligned to the three axes of the xyz linear stage and tracks the position of the device's RCM. The RCM position was calibrated by repositioning the xyz linear stage at 7.5 mm increments along each axis covering a total range of ±15.0 mm, ±15.0 mm and ±7.5 mm. At each position, the encoder count for each of the xyz linear stage’s three axes was recorded using a depth gauge (Model 2776S, Mitutyo Canada, Toronto, ON) mounted onto a calibrated manual xyz stage (M-462, Newport Corp., Irvine, CA). The encoder step size for the xyz linear stage was calculated by averaging the measurements along each axis. The flatness, straightness and perpendicularity of each axis of the XYZ linear stage were also verified using a granite surface plate (Grade B-18, The L.S. Starrett Company, Waite Park. MN), indicator (Model 25164-10, The L.S. Starrett Company, Waite Park, MN) and the same calibrated manual xyz stage used earlier to determine the stability of the RCM. Flatness was evaluated by running the indicator along the surface of the stage for each of the three translational axes and recording any deviations. Straightness was evaluated by placing the indicator onto a surface perpendicular to a translational axis. The stage was then advanced a known distance along the axis and this distance compared to the distance measured by the indicator. The straightness measurement was completed three times;

once for each of the translational axes. The perpendicularity was evaluated by placing the indicator against surfaces parallel to a translational axis. The stage was then advanced along the axis and the indicator recorded for any motion. The deviation of the flatness, straightness and perpendicularity was ≤ 1.81 µm, ≤ 0.77 µm and ≤ 74.4 µrad respectively. These values were all measured over 20 mm of stroke.

The angular orientation of each of the two arms in the forward spherical linkages was also calibrated. The robotic system was first placed onto a granite surface plate, which served as a reference plane. Each of the two arms was independently orientated so that one arm was in a plane perpendicular and one arm was in a plane parallel to the granite surface. Each arm was adjusted to within 2.5 µm of the perpendicular or parallel plane using the same calibrated manual xyz stage and indicator as earlier. The encoder values of the two encoders in the spherical linkage were recorded with the arms in this orientation. The two arms were then rotated 90° once. The encoder values of the second orientation were recorded giving the step size and absolute reference of the encoder home position.

5.2.2.2 Optical Needle Tip Calibration to RCM

To complete an intervention, the RCM of the robot is translated to correspond with the localized position of the target. It is therefore of the utmost importance that the needle tip reaches the RCM when it is at the inserted position. Thus, a method to accurately calibrate the needle tip to the RCM is critical to the success of the robotic system. Waspe et al. previously developed a method to evaluate the RCM calibration of a needle in a robotic system for small animal interventions.[17] The method involved photographing the needle tip using a high-resolution macro lens. The camera was fixed in two planes perpendicular to each of the robot's rotational axes. In each plane, a 23-gauge needle was photographed at predetermined angles throughout the respective axes' full range of motion. In each photograph, the needle was then segmented and its center line calculated. Using the center lines, the location of the RCM was calculated by determining the center of rotation of the needle axes. The calibration error was determined by calculating the distance of the needle axes from the RCM point. Unfortunately, this calibration method is limited given our robotic system RCM implementation. The method by Waspe et al. only accounts for the location of the needle axis and not the needle tip. The needle axis may travel very closely to the RCM but the needle tip may be much further from the RCM depending upon its insertion depth. Thus, the needle may miss the target even through the reported calibration error was quite small. To avoid this problem, the calibration method of Waspe et al. *w*as modified to account for the needle tip position.

Calibration of the robot was again completed using a CCD camera (EOS-1D Mark IV, Canon Canada Inc., Mississauga, ON) and a high-resolution macro lens (MP-E 65 mm f/2.8 1-5x, Canon Canada Inc., Mississauga, ON). The pixel size of the images captured using this camera and lens was approximated to be 1.0 µm. A length of 27 gauge drill stock (Model 3009A239, Mcmaster-Carr, Aurora, OH) sharpened to form a conical tip was mounted onto the needle driver. The insertion depth of the needle was adjusted using a set-screw on the needle driver. The set-screw was iteratively adjusted until the magnitude of tip motion in both rotational axes was minimized in the camera viewfinder. The needle was then photographed in two planes perpendicular to each of the rotational axes. For each plane the needle was photograph five times at approximately equally spaced angular positions. In the pitch axis the needle was photographed over a range of 60°. In the roll axis the needle was photographed over a range of 120°.

Once all the photographs had been acquired, the needle tip was segmented in each image using a semi-automated algorithm developed in MATLAB (The Mathworks Inc., Natick, MA). A Sobel edge detector was first applied to the needle tip images. The identified edge points from the Sobel edge detector, which followed the outer edge of the needle tip, were detected based on a user initialization. A linear least squares regression was applied to the detected points to determine the lines of best fit for both of the two edges of the needle tip. The bisector of the two lines of best fit was then calculated. The needle tip location was finally determined by calculating the intersection of the bisector with the detected points of the needle edge. This process was repeated for each photograph to yield a set of tip positions for each of the planes. The calibration error in each plane was then calculated by determining the total range of movement of the needle tip over the full range of motion in the two rotational axes.

5.2.2.3 Calibration Fixture Needle Tip Calibration to RCM

A calibration fixture was introduced to simplify the needle tip calibration process. The fixture consists of a Delrin plastic block with a flatness verified to within 25.4 µm (Figure 5.3). The calibration fixture was itself verified to ensure its top surface matched the RCM position. The fixture was mounted to the robot using two 6.35 mm diameter aluminum shafts (Figure 5.3). The shafts were machined to have an approximate 200 µm eccentricity in their diameter. By rotating the aluminum shaft, the top surface of the calibration fixture can be adjusted upwards and downwards to match the RCM location. The correct height of the block was determined by mounting the fixture to the robot and advancing the needle driver to the fully inserted position. A needle was then placed into the loosened needle holder of the driver. The needle was slowly lowered in the holder until its tip was at the surface of the Delrin block. The needle tip was identified as being at the block surface by lightly sliding a 25.4 µm steel shim back and fourth while lowering the needle. The needle tip caught the shim and no longer allowed it to slide freely when in contact with the needle tip. The needle holder was then tightened to fix the inserted needle tip to correspond with the block surface. The calibration block was then detached from the robot and the needle tip observed using the viewfinder of the camera and macro lens. This process underwent several iterations of calibration fixture adjustment until needle motion was minimized in the camera viewfinder. With needle motion minimized, the eccentric shaft was fixed with a set-screw to maintain the appropriate calibration fixture position. The calibration fixture can then be mounted to the robot and used to calibrate the needle tip as needed.

The calibration fixture reduces the time required to complete needle calibration. Ccalibrating the needle with a camera requires an iterative process of adjusting the needle insertion depth every time the needle is calibrated. Iterative calibration is time consuming and requires approximately 30 minutes to complete. On the other hand, the calibration fixture requires only one iterative calibration of the fixture itself. Once the fixture is calibrated, it can be mounted to the robot and used to calibrate the needle tip in less than five minutes. The results of the calibration using the fixture were validated using the camera and macro lens. The needle was again imaged at five approximately equally spaced positions in planes perpendicular to the roll and pitch axes. The needle tips were then localized in each of the photographs using the previously described technique. The calibration error was calculated by determining the total range of movement of the needle tip in each plane. The calibration results of the calibration fixture were compared to the iterative optical calibration results to determine the difference in the accuracy of the two methods.

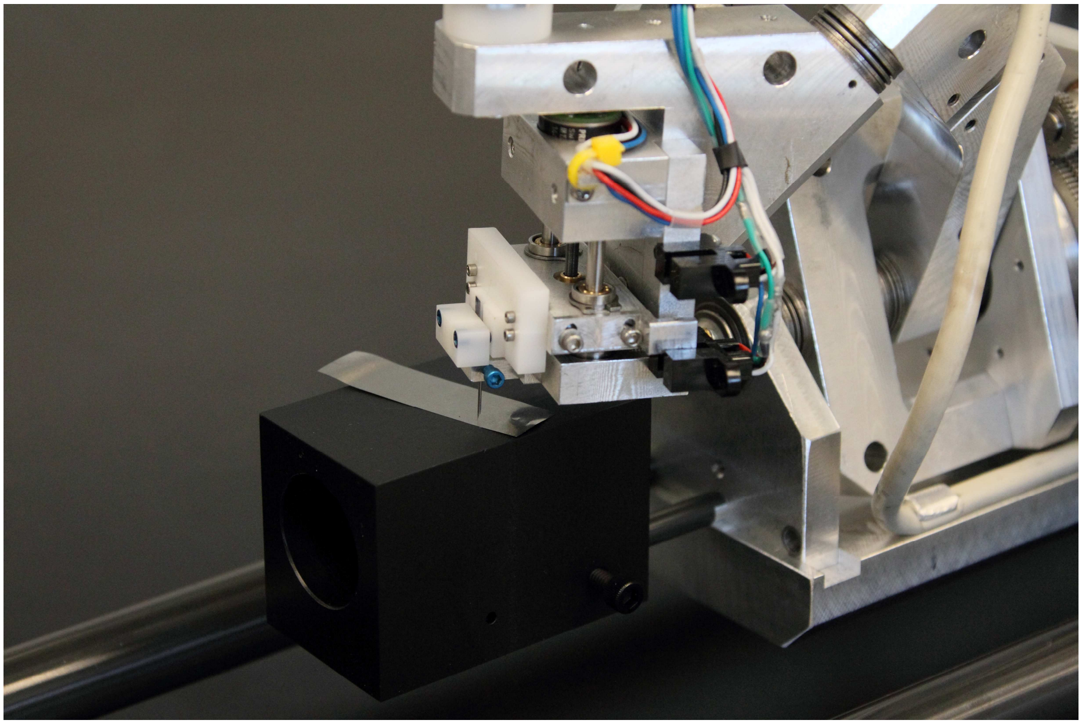

Figure 5.3: Photograph of the calibration fixture used to set the needle tip position at the RCM when the needle driver is in its forward position. The fixture consists of a Delrin plastic block that is mounted to the robot via two aluminum shafts, one attached to the block and one attached to the robot (same shaft supporting the fiducials visible in Figure 5.2). The needle height was set by slowly lowering the loosened needle until its tip was at the surface of the shim on top of the Delrin block.

The repeatability of the needle driver was characterized to ensure the stability of the needle tip calibration. The needle tip will quickly become un-calibrated if the needle driver does not consistently and reproducibly place the needle tip to the correct depth, which corresponds with the RCM. To characterize the needle driver repeatability, the needle orientation was adjusted to be fully upright using the spherical linkage encoders.

The needle was then inserted and retracted nine times while maintaining a constant orientation. Each time the needle was inserted, it was photographed using the high-resolution macro lens. The location of the tip was calculated in each of the nine photographs using the needle tip localization technique described during RCM calibration. The repeatability was characterized by determining the standard deviation of the needle tip position in the photographs.

5.2.3 Robot to micro-CT Robot Registration

5.2.3.1 Registration Process

A two-stage registration process was developed to register the coordinate system of the robot to the micro-CT scanner (eXplore Ultra Locus, General Electric Healthcare Biosciences London, ON, Canada). The two-stage registration was developed to achieve a balance between a high quality registration and the time requirements of an end user to complete a pre-clinical intervention. Completion of the primary first step of the registration requires that a removable 6.35 mm borosilicate fiducial bead (McMaster-Carr, Cleveland, OH) be mounted onto the device at the RCM. In addition, an array of six more borosilicate bead secondary fiducials was mounted onto the robot below the animal bed (fiducial array visible in Figure 5.2). With the RCM fiducial bead attached, the robot was positioned at four different locations within the micro-CT bore, and a CT image was obtained each time. Using registration software developed in MATLAB (The Mathworks Inc., Natick, MA), the rigid body transformation between the two sets of coordinates was calculated by comparing the position of the RCM fiducial in robot coordinates to its position in each of the four images. This primary registration can be used alone to guide to the robot to targets in micro-CT images. However, if the robotic system is removed and then reattached to the micro-CT bed, this primary registration is no longer valid due to variability in robot reattachment.[16] Unfortunately, repeating the primary registration each time the robot is reattached to the micro-CT to complete an intervention is time consuming and laborious. To avoid constant repetition of the primary registration a secondary registration was developed.

The secondary registration takes advantage of the six borosilicate secondary fiducials attached to the robot below the animal bed (Figure 5.2). During primary registration, these six fiducials are imaged along with the RCM fiducial bead. One of the scans acquired for the primary registration is of the robot at its home position. To complete the secondary registration, the reattached robot and six secondary fiducials are imaged with the robot at its home position. The registration software is then used to calculate the rigid body transformation using the six secondary fiducial positions in the primary registration home scan and the secondary fiducial positions in the secondary registration home scan. This secondary registration will account for and correct the variability introduced when the robot is reattached to the micro-CT scanner. A target in the micro-CT images can then be localized in robot coordinates by applying both registrations. Through the secondary registration, the end user is only required to acquire one image at the initiation of an intervention, rather then four. Furthermore, imaging of the fiducials for secondary registration can be simultaneously acquired while imaging the small animal, to localize targets. Since the small animal must always be imaged, the secondary registration does not increase the total number of scans required and allows for the primary registration to be reused across multiple interventions. Unfortunately, use of the secondary registration will also reduce overall targeting accuracy since two registration errors, from the primary and secondary, will be combined. The primary registration can be used by itself to improve targeting accuracy; however, this will be at the expense of increasing total registration time. Use of the combined registration reduces time for procedures at the expense of accuracy. The end-user must determine which registration process will best suit their application needs.

5.2.3.2 Registration Software

The fiducial bead mounted onto the robot RCM was segmented and its centroid was determined in each of the four images acquired for the primary registration. Segmentation was accomplished through a threshold based region-growing. The center of the segmented RCM fiducial was then calculated using a squared-intensity-weighted centroiding. The centroiding algorithm used was found in simulated images to have an error of < 5% of the image voxel size in localizing 3D centroids.[23] The centroided RCM fiducial positions were then rigidly registered to their homologous robot coordinates using a least squares algorithm.[24] The results of the primary registration represented the translation and rotation required to align the coordinate system of the micro-CT scanner with the robotic system.

The secondary registration first required that during the primary registration, with the robot at its home position, the centroids of the six secondary fiducial beads are determined using the technique previously described. During the secondary registration, again with the robot at its home position, these six secondary fiducials are reimaged and their centroids determined. The two sets of centroids are then registered using a rigid body transformation. This secondary registration represents the transformation required to realign the robot axes at the time of the intervention with the robot axes at the time of the primary registration. The errors of the primary, secondary and combined registration were characterized by calculation of the fiducial registration error (FRE) and target registration error (TRE).[25] The TRE of the primary registration was calculated by acquiring five additional images, not used in the registration, of the RCM fiducial at positions in the robot's full range of motion. The secondary and combined TREs were calculated by attaching and reattaching the robot to the micro-CT scanner bed five times with the RCM fiducial still attached. In each image, five of the six secondary fiducials were used to calculate the secondary registration. The sixth secondary fiducial in each of the five images was used to calculate the secondary TRE. The combined TRE in these five images was calculated using the position of the RCM fiducial in the images following robot reattachment to the scanner bed.

5.2.4 Robot Targeting Accuracy

5.2.4.1 Targeting Accuracy Phantom Design

Tissue-mimicking phantoms were used to quantify the targeting accuracy of the robotic device. The phantoms consist of a 15% by weight gelatin solution (Porcine Skin Type A, Sigma-Aldrich, St. Louis, MO) that forms a cross-linked matrix.[26]

5.2.4.2 Targeting Accuracy Experiment

Two separate sets of targeting experiments were completed. The first set used the combined registration process to guide the robot to targets in tissue-mimicking phantoms. The second set used only the primary registration to guide the robot. For each set, the targeting phantom was first secured to the phantom holder of the robotic device and the robot inserted into the bore of the eXplore Locus Ultra micro-CT scanner. The phantom was then imaged using a 16 second anatomical scan at 140 kVp and 20 mAs. The image was reconstructed to yield an image with 153.9 µm isotropic voxel size (example shown in Figure 5.4). The image of the phantom was then visualized within MATLAB. Ten image voxel coordinates within the phantom were manually localized and selected as target positions. For each set, the location of each of the 10 target voxel coordinates within robot coordinates was calculated using either a combined registration or a primary only registration. For each target, the robot RCM was placed at the target location, the needle inserted and an image acquired. Throughout the targeting experiments, the needle angulation remained constant, at approximately 90° in the roll axis and 45° in the pitch. Needle angulation was maintained constant to allow targeting accuracy to be quantified independently of angle.

For each acquired image, the distance of the needle from target voxel coordinates was determined by first segmenting the inserted needle using a threshold-based region growing algorithm. The center line of the needle in the image was estimated using principal components analysis (PCA) to fit a 3D line to the segmented needle. The targeting accuracy was quantified by calculating the distance of each 3D fitted line to the target voxel. The distance of the line to the target voxel represents the accumulation of error from a number of sources including robot positioning error, registration error, needle calibration error and needle deflection.

5.2.4.3 Needle Angulation Accuracy

We used a gelatin phantom to evaluate the variation in needle positioning over the full range of needle angulation. The gelatin phantom was placed onto the animal bed of the robot and the robot was then oriented in seven different positions (see Table 5.1) covering the angular range of the robot motion. At each orientation the needle was inserted into the gelatin phantom and imaged by the micro-CT scanner. In each image, the needle center-line was calculated using the same technique previously described. Ideally, all seven center-lines should intersect at a common point in space (i.e., the RCM) if no variation in needle positioning is present with angulation. An iterative solution was used to calculate the point in space with the smallest sum of squares distance from each of the centerlines. The variation in needle positioning over the full range of needle angulation was then quantified by calculating the distance of each center-line to the point of best fit.

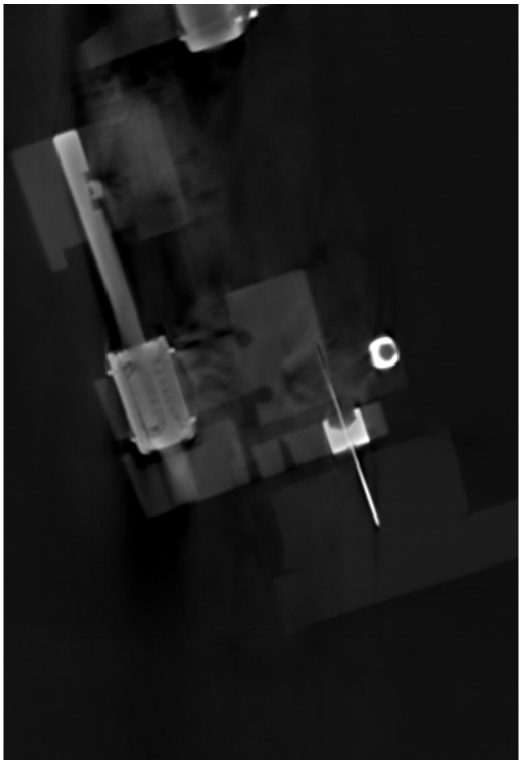

Figure 5.4: View of reconstructed CT scan used for the needle targeting experiment. For each target, the robot RCM was placed at the target location, the needle inserted and an image acquired. For each acquired image, the distance of the needle from target voxel coordinates was determined by first segmenting the inserted needle using a threshold-based region growing algorithm. The center line of the needle in the image was estimated using principal components analysis (PCA) to fit a 3D line to the segmented needle.

5.2.5 Preclinical Application

All *in vivo* imaging was performed under a protocol approved by the University Health Network Animal Care and Use Committee. Measurements were performed in two female SCID mice, each bearing a single subcutaneous human cervix carcinoma tumour (ME180). A tumour was established in the first mouse by suturing a 2 to 3 mm^3 tumour fragment, along with a 1.5 mm radio-opaque pellet (Beekley Co., Bristol, CT), into the dorsal subcutaneous tissue. A tumour was established in the second mouse by suturing a 2–3 mm^3 tumour fragment into the subcutaneous tissue of the hind limb. The experiment was performed once the tumours had reached approximately 1 cm in diameter. The mice were anesthetized using a 2% by volume isoflurane-oxygen mixture, the hair removed from their tumours' areas, and they were immobilized in a supine position with their front and back paws taped to a custom-built mouse platform mounted on the robot. The mice were imaged using a standard anatomical imaging protocol consisting of a 16 second scan with an 80 kVp and 60 mAs. The images were reconstructed to yield a 153.9 µm isotropic voxel size.

The mouse bearing the dorsal tumour with the implanted radio-opaque pellet was used to evaluate the robot's ability to perform image-guided needle placement *in vivo*. Similar to *in vitro* experiments, a 23-gauge needle was mounted on the needle driver. The tumour was immobilized by taping it onto a plastic block and surrounding it with pieces of rigid foam. A pre-needle insertion CT scan was performed to visualize the radio-opaque pellet. The robot RCM was placed at the centre of mass (CM) of the radio-opaque pellet and the needle was inserted. A post-needle insertion scan was acquired to confirm successful contact with the target. This process was repeated for three angles of insertion chosen randomly, and the distance between the needle tip and surface of the radio-opaque pellet measured.

Interstitial fluid pressure (IFP) measurements were performed in the mouse bearing the hind limb subcutaneous tumour, using the wick-in-needle technique.[27] Measurements were made using a 23-gauge needle containing both a front and side port connected to a pressure transducer (Model P23XL, Harvard Apparatus, Canada), which in turn was connected to a data acquisition system (PowerLab 4/35 with LabChart Pro, ADInstruments Pty Ltd., USA) through 50 cm of PE20 polyethylene tubing (Becton Dickinson, Franklin Lakes, NJ, USA). The entire system was flushed with a heparin sulphate/saline solution (1:10). A pre-needle insertion scan was performed, the tumour indentified, and a position chosen such that the side port of the needle would be inside the tumour volume, while the front port would be in healthy tissue. IFP measurements were made as the needle was inserted, and maintained for 30 sec after reaching the target location. A post-needle injection scan was performed to confirm the location of the needle inside the tumour. The needle was then retracted by approximately 3 mm while continuously monitoring IFP. The two positions were chosen to demonstrate the importance of correct needle placement on stable IFP measurements.

5.3 Results

Table 5.1 provides a summary of the results obtained for each of the experiments described in the methods.

5.3.1 Robot Calibration

5.3.1.1.1 Optical Needle Tip Calibration Error to RCM

The RCM calibration error represents the range of motion of the needle tip as the robot's rotational axes are moved through its full range of motion. In the roll plane, the RCM calibration error range was found to be Δ_x= 43 µm and Δ_y= 28 µm, where the x and yaxis represent the horizontal and vertical axis orientated perpendicular to the z axis which represents the long axis of the CT bore. In the pitch direction the RCM calibration error was Δ_y=69 µm and Δ_z= 30 µm. Added in quadrature the total errors were $\text{Error}_{\text{Roll}}$=51 µm and $\text{Error}_{\text{Pitch}}$= 75 µm. The maximum calibration error is expected to occur at the extremes of the rotational axes. Figure 5.5 displays a composite photo of the calibration photos and the segmented needle tip locations.

5.3.1.2 Calibration Fixture Needle Tip Calibration Error to RCM

RCM calibration was also completed using a precision calibration block. In the roll plane, the RCM calibration error was Δ_x=36 µm Δ_y=70 µm. In the pitch plane the RCM

Table 5.1: Summary of the results obtained for each experiment.

		Error *(μm)*
A.1 Optical Needle Tip Calibration Error to RCM		
	Roll plane	
	Δ_x	43
	Δ_y	28
	Pitch plane	
	Δ_y	69
	Δ_z	30
A.2 Fixture Based Needle Tip Calibration Error to RCM		
	Roll plane	
	Δ_x	36
	Δ_y	7
	Roll plane	
	Δ_y	36
	Δ_z	7
A.3 Needle Driver Repeatability		
	σ_{needle}	9
B Robot Registration		
	Primary	
	$FRE_{primary}$	21
	$TRE_{primary}$	31
	Secondary	
	$FRE_{secondary}$	70
	$TRE_{secondary}$	79
	Combined	
	$TRE_{combined}$	139
C Robot Positioning Accuracy		
Primary Registration Positioning Accuracy		
	$Total_{error}$	131 ± 25
Combined Registration Positioning Accuracy		
	$Total_{error}$	206 ± 20
C.3 Needle Angulation Accuracy		
	σ_{angle} (< 50°)	72± 62
	σ_{angle} (< 30°)	51± 31

calibration error was Δ_y=11 µm and Δ_z=5 µm. Added in quadrature the total errors were $Error_{Roll}$=75 µm and $Error_{Pitch}$= 12 µm.

5.3.1.3 Needle Driver Repeatability

The needle driver must consistently position the needle tip at the same location in space following repeated insertions and retractions. Significant variations in needle positioning by the needle driver will reduce the ability of the system to maintain calibration. Needle driver repeatability is the standard deviation of needle depth in multiple insertion procedures. The needle driver repeatability was found to be σ_{needle}=±9 µm.

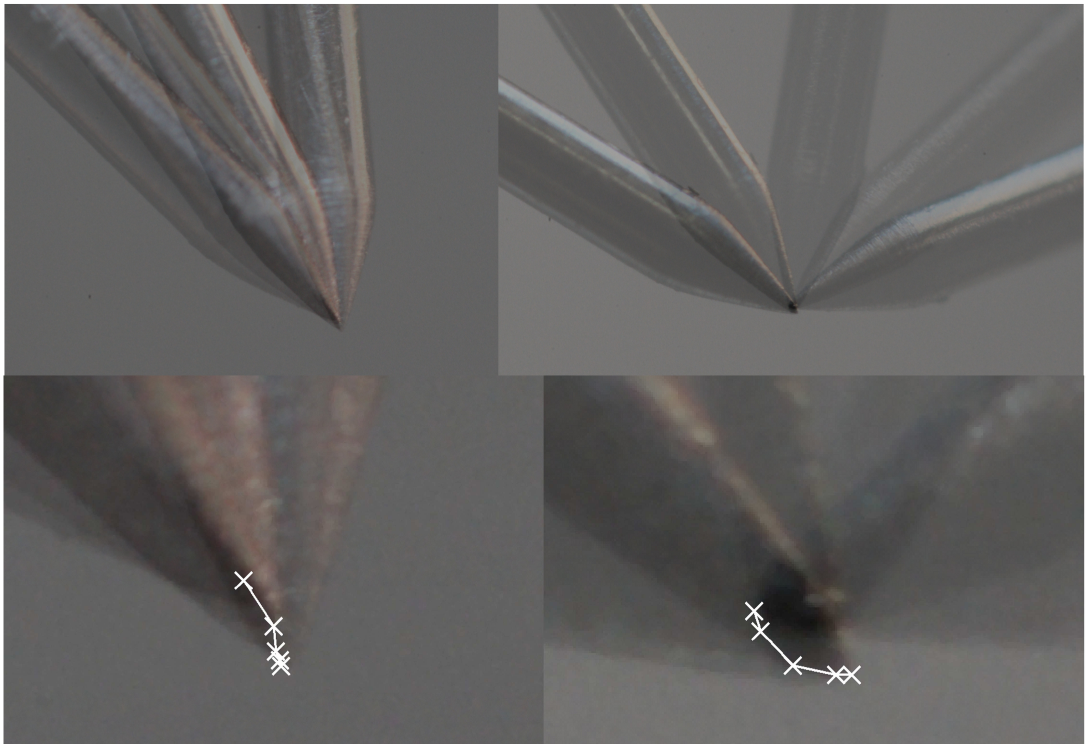

Figure 5.5: Composite photographs of the calibration photos showing the pitch (top left) and roll (top right) of the needle throughout its full range of motion. The bottom two photographs show close-up views of the segmented needle tip locations in the pitch (bottom left) and roll (bottom right) directions.

5.3.1.4 Robot to Micro-CT Robot Registration

The primary robot registration is the transformation required to convert the micro-CT scanner coordinate system to the robot coordinate system, and was calculated using the location of the fiducial bead at the RCM of the robot. The fiducial localization and registration errors were found to be $FRE_{primary}$= 21 ± 6 µm and $TRE_{primary}$= 31 ± 12 µm.

The secondary robot registration is the transformation required to relate the robot coordinate system at the time of an intervention to the time of the primary registration, and was calculated using fiducials fixed to the robot frame. The fiducial localization and registration errors were found to be $FRE_{secondary}= 70 \pm 25$ µm and $TRE_{secondary}= 79 \pm 14$ µm.

The combined registration is the combined transformations performed in the primary and secondary registrations. The combined registration error represents the total error of the complete registration process. Since the combined registration itself has no fiducials, there is no fiducial registration error to report. For the combined registration the $TRE_{combined}=139 \pm 63$ µm.

5.3.2 Robot Positioning Accuracy

5.3.2.1 Combined Registration Positioning Accuracy

The needle positioning accuracy is the distance of the segmented needle track in the gelatin phantom from the target pixel in a micro-CT image. The targeting experiments were completed with the rotational axes of the robot approximately constant: with the needle pose at 90° in the roll plane and 45° to the CT bore in the pitch plane. The calculated mean targeting errors along the three images axes were: $X_{error}=194 \pm 16$ µm, $Y_{error}=33 \pm 17$ µm and $Z_{error}=57 \pm 19$ µm. The total mean error of the needle position was $Total_{error}= 206 \pm 20$ µm. An ANOVA test ($p = 0.05$) found a significant difference between the mean targeting errors of each axis. A Tukey test ($p = 0.05$) found the errors of all axes to be significantly different from each other.

5.3.2.2 Primary Registration Positioning Accuracy

A second set of targeting experiments were completed using only the primary registration. The calculated mean targeting errors along the three images axes were $X_{error}=119 \pm 22$ µm, $Y_{error}=19 \pm 10$ µm and $Z_{error}=46 \pm 24$ µm. The total mean error of the needle position was $Total_{error}= 131 \pm 25$ µm. An ANOVA test ($p = 0.05$) found a significant difference in the mean targeting errors of each axis. A Tukey test ($p = 0.05$) found the errors of all axes to be significantly different from each other.

Table 5.2: Summary of needle angulations used to test needle deflection at different angles of attack. The variables α and β represent the angle of the primary and secondary crank measured by the encoders. The angle of attack represents the angle between the needle axis and the normal vector to the surface of the phantom.

Scan	α°	β°	Angle of attack (degrees)	Error (μm)
1	45	135	11	34
2	25	155	14	51
3	25	115	21	24
4	66	155	21	110
5	-5	114	30	34
6	60	178	25	56
7	105	172	50	189

5.3.2.3 Needle Angulation Accuracy

The consistency of needle accuracy was evaluated by inserting the needle multiple times to the same position in space at varying angles of attack (10 to 50 degrees). The results for these experiments are given in Table 5.2, and show that the average normal distance from each axis to the fixed target was determined to be $\text{Error}_{\text{angle}} = 72\pm62$ μm.

5.3.2.4 Preclinical Application

The experimental setup used in each of the small animal experiments is shown in Figure 5.6. The robot was used to target a radio-opaque pellet implanted in a subcutaneous dorsal tumour under image guidance. Post-needle insertion CT projection images showed that the needle was successfully delivered to the target (Figure 5.8). Measurement of the distance between the needle tip and the surface of the pellet was difficult due to partial volume effects and beam hardening artifacts caused by the radio-opaque pellet and steel needle. The measured distance between the needle tip and pellet surface was 0.41±0.12 mm. The CM of the radio-opaque pellet shifted 0.85±0.28 mm relative to its pre-needle insertion position. A real time CT scan of the final needle placement showed that the shift in pellet position was due to contact with the needle as well as tissue deformation during needle insertion.

Robot-guided IFP measurements were made at two locations in the subcutaneous hind limb tumour. In the first location the post-needle insertion CT scan demonstrated that the front port of the needle was straddling the boundary between tumour and healthy tissue, and the side port was in the centre of the tumour (Figure 5.7a). The needle was then retracted 3 mm and a CT scan showed that both the front and side ports of the needle were inside the tumour volume (Figure 5.7b). The accuracy and stability of the wick-in-needle technique requires that both ports of the needle are exposed to a similar external pressure. If the pressure at one port is substantially lower than the other, fluid flow is directed out of the IFP system and a decreasing pressure is measured. Region III of Figure 5.7c demonstrates this effect. When the needle was retracted to the second position shown in Figure 5.7b, the IFP measurement stabilized (Figure 5.7b, region IV). This highlights the important of using an accurate position system under image guidance to perform reliable IFP measurements.

The robot was used to target a radio-opaque pellet implanted in a subcutaneous dorsal tumour under image guidance. Post needle insertion CT projection images showed that the needle was successfully delivered to the target (Figure 5.8). Measurement of the distance between the needle tip and the surface of the pellet was difficult due partial volume effects and beam hardening artifacts caused by the radio-opaque pellet and steel needle. The measured distance between the needle tip and pellet surface was 0.41±0.12 mm. The CM of the radio-opaque pellet shifted 0.85±0.28 mm relative to its pre-needle insertion position. A real time cine-CT scan of the last needle placement showed that the shift in pellet position was due to contact with the needle as well as tissue deformation during needle insertion.

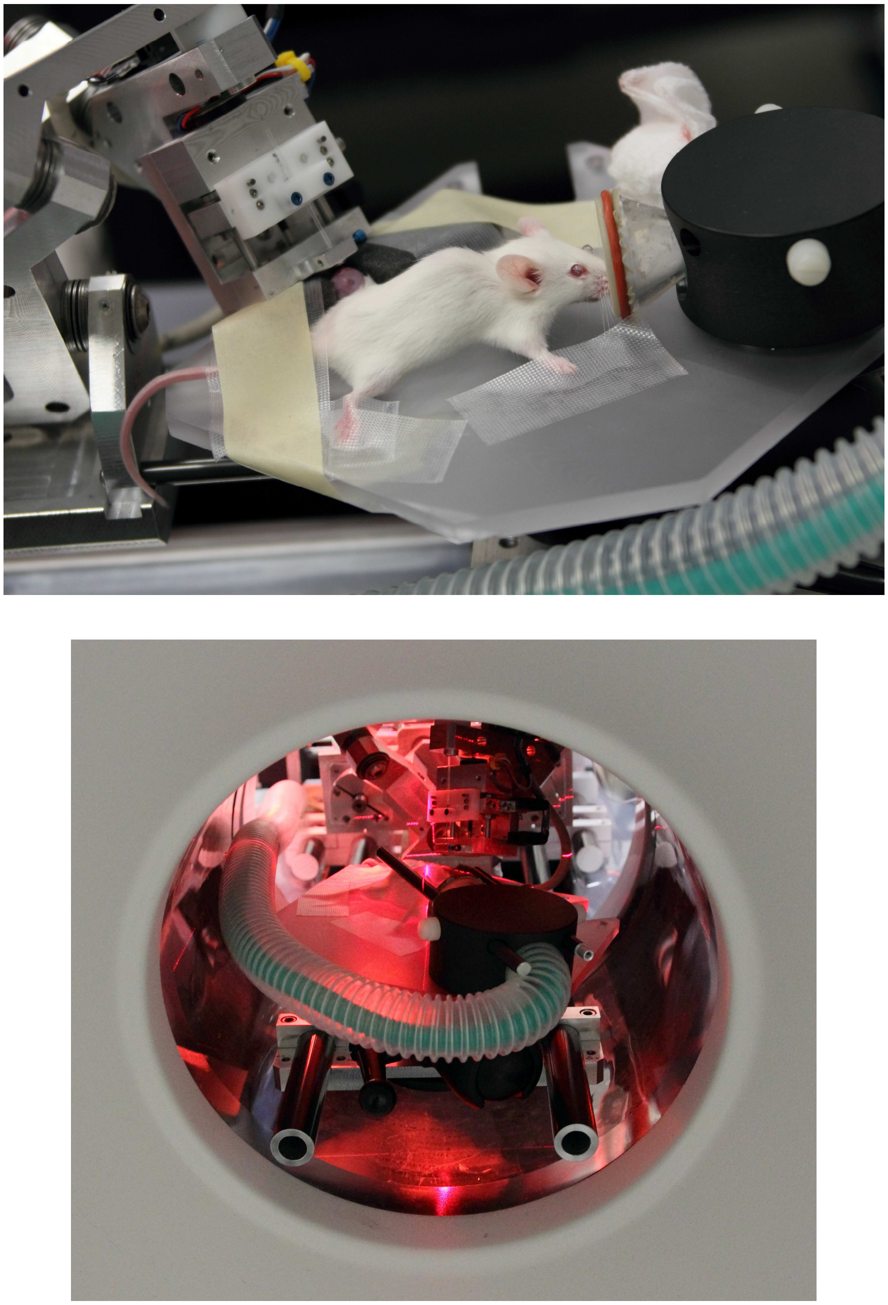

Figure 5.6: Photograph of the experimental setup used for the animal interventions **(a, top)** outside, and **(b, bottom)** inside of the bore of the CT scanner. The only part of the apparatus that resides inside the scanner is the mouse bed and part of the needle driver, to minimize artifacts in the image.

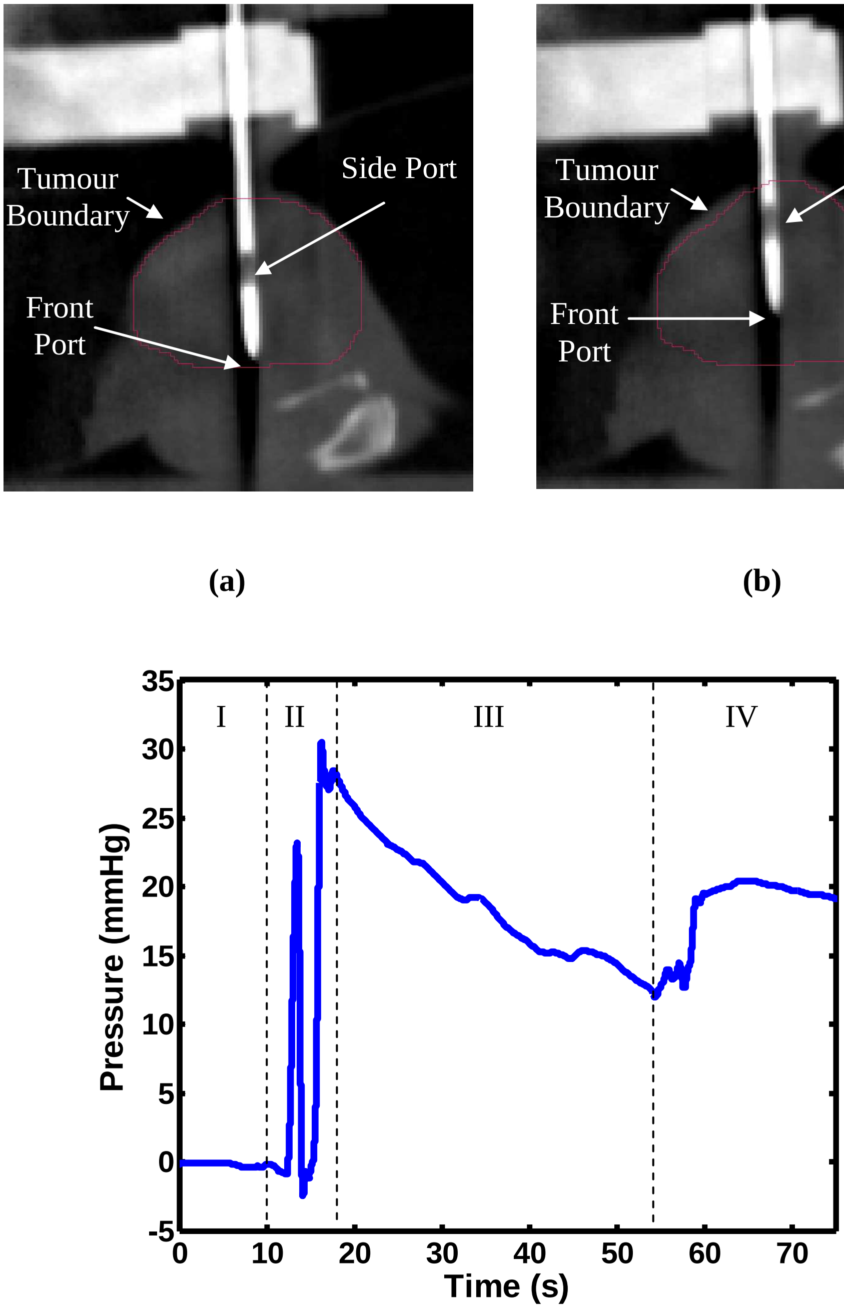

(c)

Figure 5.7: Wick-in-needle measurements of IFP demonstrating the importance of needle placement for stable and accurate results. **(a)** The front port of the IFP needle is straddling the tumour boundary (outline), while the side port is in the centre. **(b)** Both the front and side ports are within the tumour boundary (outline). **(c)** Results of IFP measurements showing (I) the pre-needle insertion baseline (II) the signal as the needle is inserted; (III) the measured IFP at the position shown in **(a)**; and (IV) the measured IFP at the position shown in **(b)**.

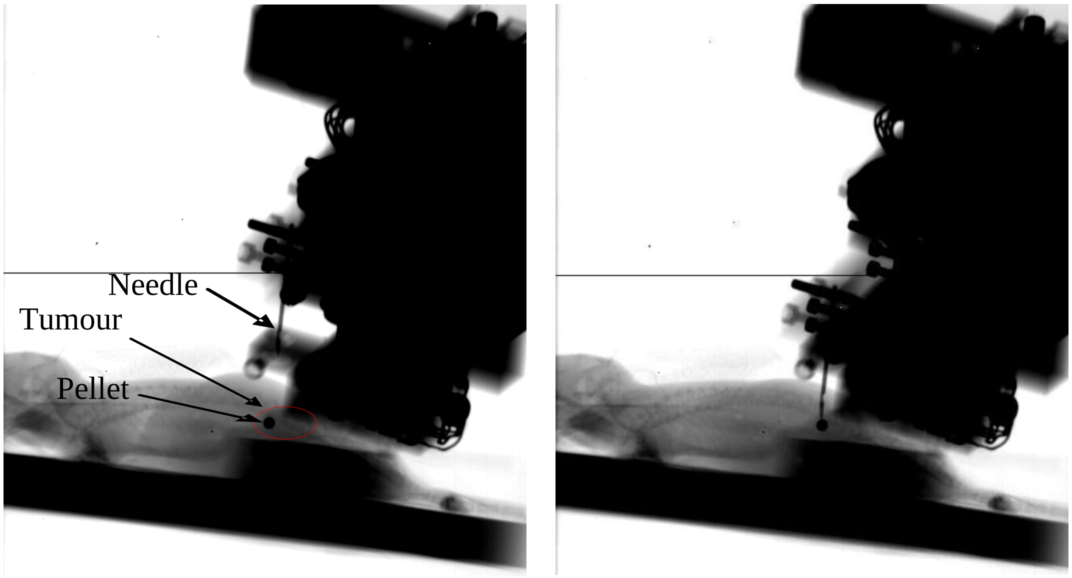

Figure 5.8: Projection views obtained from two sequential CT scans that demonstrate the ability to perform image guided needle placement in vivo. **(a, left)** A pre-needle insertion image highlighting the location of the needle, the tumour (red outline), and the radio-opaque pellet (fiducial). **(b, right)** A post-needle insertion image showing the needle making contact with the radio-opaque pellet.

5.4.1 Robot Calibration

During the initial setup of the robot linkages, the RCM of the robot was found to remain relatively fixed in space with a maximum deviation of 12.5 μm. As a result, the calibrated needle tip would be expected to track a path corresponding closely to the surface of a sphere when the robot is adjusted through its full range of motion. The center of the sphere is the RCM position and the radius of the sphere is the needle calibration error. The calibration error is quantified by measuring the range of pixels the needle travels along each axis in each plane. As shown in Figure 5.5, the Δ_x and Δ_z errors should be equal and the two Δ_y errors should both be equal to half this value. Furthermore, the segmented needle tips in both planes should form a circular path. However, this is not true for the obtained results. A number of sources of error exist in the methods used, causing the measured calibration error to deviate from this ideal case. First, the use of photography to validate the calibration results in a three-dimensional path being projected onto a two-dimensional plane. Errors in positioning the camera truly perpendicular to each of the rotational axes will result in the needle paths failing to track a circular path. Secondly, to measure the radius of the sphere, the needle tip must track a path of at least 90 degrees or greater. In the roll axis, the needle traveled approximately 120 degrees allowing the sphere to be correctly characterized. In the pitch direction, the robot's range of motion is limited to approximately 60 degrees. The track measured in the pitch axis travels a smaller sector of the sphere compared to the roll axis. The errors measured in the pitch axis will inherently underestimate the calibration error. The roll axis results therefore are a better characterization of the needle calibration errors.

The calibration results demonstrated that the roll axis has the largest error, as expected. However, for the optical calibration, the pitch axis contains the largest errors even though the pitch error should be inherently less. The likely cause of this aberration is deflection in the shaft of needle itself. Deflections inherent to any needle will result in overestimates of calibration error as the distance traveled by the needle will be amplified by deflection. Depending on how the needle is mounted, this error may occur in the roll plane, the pitch plane or some combination of the two. Two different needles were used for the optical calibration and the fixture calibration. The needle selected for the optical calibration likely deflected in the pitch direction, resulting in an unexpectedly large pitch calibration error. Needle deflection along with the previously discussed sources of error cause the calibration results to deviate from their expected results.

The radius of the calibration error sphere, or the true calibration error, is shrouded behind a number of other unavoidable error sources. However, an estimate of the independent needle tip calibration error can be distilled from reported results. As discussed, the pitch axis lacks sufficient range of motion to accurately estimate the sphere radius. An estimate must therefore come from the roll results. Two potential cases exist for the roll results: either needle deflection occurred in the roll plane or deflection did not occur in the roll plane. If no deflection errors exist in the roll plane, the Δ_y measured in the roll direction should be approximately half Δ_x. This case is true for the optical calibration results. The radius of the calibration error sphere is therefore approximately equal to the mean of Δ_y and half of Δ_x or 25 um. If deflection did occur, the relationship between Δx

and Δ_y no longer holds true. For the fixture calibration, deflection is evident with Δ_y much larger then Δ_x. In the deflection case, the most reasonable estimate of the sphere radius is half of Δ_x. Δ_x is the most reasonable estimate since it corresponds with the calibrated needle axis. For the calibration fixture, the radius can be estimated to be approximately 18 um. The expected standard deviation of both calibration errors is the needle driver repeatability of 9.1 um.

The two estimates of the calibration errors for the optical method and fixture method are extremely close and less than one standard deviation apart. The results suggest that the calibration obtained using these two methods are equivalent. However, calibration can be completed much faster using the fixture rather than the iterative optical method. Therefore, the calibration fixture should be the preferred method of completing calibration.

5.4.2 Robot Registration

For the primary registration (robot coordinates to fiducial bead centroids in micro-CT images), the robot coordinates are measured with high accuracy using a calibrated XYZ positioning stage with a measurement resolution of 0.1 µm. However, the secondary registration is a registration of fiducial bead centroids from two different micro-CT images. The secondary registration therefore has the centroiding error in both sets of coordinates whereas the primary only possesses the error in one coordinate set. The secondary registration would therefore be expected to have twice the fiducial centroiding error of the primary registration. However, the mean TRE of the secondary registration is approximately 2.5 times larger than the TRE of the primary registration. This suggests that much of the TRE arises from fiducial localization error (FLE) in the centroiding of fiducials in the micro-CT images. The registration errors would therefore be expected to be reduced if using a scanner with higher resolution.

Either the primary registration alone or the combined registration can be used to guide the robotic device for interventions. Use of the primary registration would be expected to result in much higher targeting accuracy with greater repeatability than the combined registration. The combined registration contains the accumulation of many more error sources then the primary registration. The combined registration contains errors from both the primary and secondary registrations along with errors resulting from attaching and detaching the robot from the micro-CT scanner bed. As a result, the primary registration offers the advantage of nearly a fifth of the TRE of the combined registration and a much smaller standard deviation. Unfortunately, the primary registration is more time-consuming then the combined registration. Four scans are required to complete the primary registration and they must be repeated every time the robotic system is removed from the scanner bed. In contrast, the combined registration can be completed with a single image, which can be acquired simultaneously with imaging of the small animal. Depending on the application, the end user must determine the ideal balance between time requirements and accuracy.

Waspe et al.[16] is the only other method developed to register a robotic system with a micro-CT imaging system. The reported FRE and TRE of the registration process were 96 µm and 210 µm respectively. Both the primary and combined registrations offer a reduction in error over this method.

5.4.3 Robot Positioning Accuracy

The 153.9 µm micro-CT voxel size is relatively large in relation to the desired needle targeting accuracy of 200 µm. Therefore, in order to be able to use the micro-CT to meaningfully quantify targeting error, a technique capable of sub-voxel accuracy is required. Unfortunately, the needle tip cannot be localized to sub-voxel accuracy. Rather, to achieve the desired measurement accuracy, the needle must be segmented and a line of best fit calculated to determine the needle axis in the micro-CT image. The metric used to calculate targeting accuracy is the shortest distance of the needle axis to the target. Unfortunately, this metric does not provide any information about the error in needle depth or its associated variability. Furthermore, the reported errors were measured at a constant angle and do not account for variation in targeting accuracy due to needle angulation. The reported targeting errors therefore underestimate the true targeting error. The targeting errors can be corrected to better represent the true targeting error by using the errors measured during needle calibration and needle angulation testing, which do account for these other factors. Since these errors are all independent, their means and standard deviations can be added in quadrature to estimate the true targeting error.

The RCM deviation is known to be a maximum of 12.5 µm through the robot's full range of motion. In comparison, the mean error from the point of best for the robot angulation testing was 72± 62 µm. Therefore, the variation in angular targeting accuracy is largely not the result of mechanical errors. Rather, this error would largely be due to needle tip calibration error and needle deflection in the tissue-mimicking phantom. Error resulting from needle tip calibration error is constant and should remain near constant with respect to needle angulation. The large standard deviation observed in needle angulation accuracy is likely the result of needle deflection. As shown in Table 5.2**,** the error was the smallest for angles of attack less than 30° from the normal. For these small angles the mean error was 51 ± 31 µm. The error tended to increase with larger angles of attack. For the example illustrated in Figure 5.9, for the maximum angle tested of 50° the error increased to 188 µm. These results are not surprising: the larger the angle of attack, the more obliquely the needle penetrated the phantom surface and the greater the proportion of the needle within the phantom. Both of these conditions are conducive to needle deflection. Targeting error increases with the angle of attack of the robot is largely the result of needle deflection.

A source of error typically neglected in the literature is the rearward deflection of the robot itself during needle insertion. This error is neither accounted for in the robot targeting error or calibration error. The robot deflection is the result of the entire machine shifting due to reactionary forces acting on the needle driver as it advances the needle through the tissue. To determine the magnitude of this deflection in our design, a brass weight, which exerted 10 N of force, was mounted to the robot RCM. The deflection of the robot with the brass weight was measured using an indicator to be 151 µm. However, the needle driver is capable of delivering a maximum force of 2 N, which corresponds with a rearward robot deflection of 30 µm. This illustrates the need to make the robot as rigid as possible. Although our system is suitable for inserting needles into soft tissue, the rigidity of this device would need to be improved for applications like drilling into harder materials like bone.

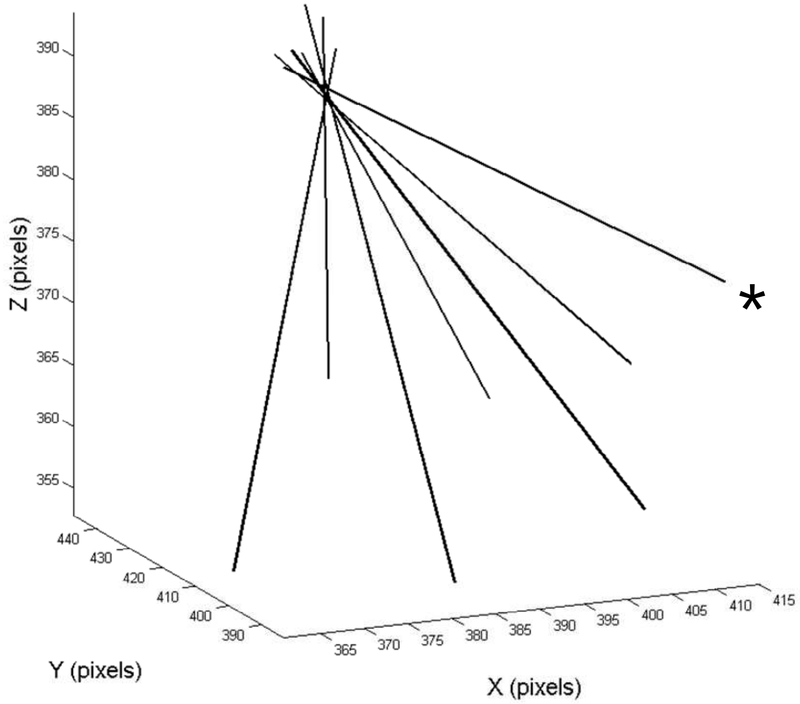

Figure 5.9: A composite image of the needle tracks from the needle angulation accuracy experiment (section 5.2.4.3). All of the needle tracks, with the exception of one track, approached the target point with an angle of attack (from the normal) of less than 30 degrees. The one track labeled as (*) illustrates an exaggerated needle deflection with the needle approaching the target at 50 degrees from the normal, where the needle is perpendicular to the phantom surface.

Combining the measured targeting error with the tip calibration error and angulation error, the resultant targeting errors for both the primary and combined registration techniques would be 142 ± 41 µm and 213 ± 38 µm. Including the presence of a 2 N axial load, the targeting errors would be 149 ± 41 µm and 218 ± 38 µm. These estimates of targeting error are better representative of the true targeting error of the robotic system. Even with the inclusion of additional error sources, the targeting accuracy of the robot is approximately equal to the imaging voxel size of 153.9 µm. This targeting accuracy makes the robot potentially useful for targeting small vessels with a high degree of confidence. Although the secondary registration reduces the time requirements of interventions, the targeting accuracy is greater than the image voxel size.

This method would be useful for targeting larger structures like the left or right ventricle of a mouse's heart or a large tumour. Since the variability in targeting is relatively low in comparison to the mean error, the targeting accuracy could be further improved to achieve finer targeting accuracies using micro-CT scanners with smaller voxel sizes. One approach to improve the targeting accuracy is introduced by Ramrath *et* al. to measure the magnitude and direction of needle misalignment using a high-resolution camera.[19] An appropriate correction can then be applied when positioning the needle to reduce error from needle misalignment.

5.4.4 Preclinical Application

Under image guidance, the robot was able to successfully target a 23G needle to a 1.5 mm radio-opaque pellet implanted in a subcutaneous tumour. Tissue deformation was observed during the initial penetration and retraction of the needle, and could potentially result in missing the intended *in vivo* target. While the effect of tissue deformation was negligible in our ability to target a 1.5 mm radio-opaque pellet, it likely worsens with smaller targets and with proximity of the target to the skin (where the observed tissue deformation was the largest). Using real-time image guidance it may be possible to reduce, if not eliminate, the effect of tissue deformation.

The wick-in-needle technique requires proper placement of the needle for reliable IFP measurements in small tumours. Both the front and side ports of the IFP needle must be inside the tumour volume, which becomes difficult in small animal tumours with diameters between 5 and 10 mm. The average distance between the front and side port of our IFP needle was approximately 5 mm. Therefore, a great deal of uncertainty in manually placing the IFP needle in mouse tumours smaller than 10 mm is expected. For example, we have found that performing repeated manual needle placement in an intra-muscular ME180 tumour 7 mm in diameter results in IFP values that differ by a factor of five. In this study, we have shown that the robotic position system in combination with image guidance provides an accurate method to guide needle placement, and reliably perform IFP measurements. Additionally, the design of the robot allows for spatial mapping of IFP over the tumour volume and is an application we plan to explore in the future.

5.5 Conclusion

The design of a micro-CT guided needle positioning system for small animal intervention has been presented. The system has been developed to achieve a mean targeting error of less than 200 µm while maintaining a high degree of user friendliness. The robot is compact enough to operate within the micro-CT bore. Small animals can be imaged and the intervention performed without transporting the animal from one workspace to another. Not requiring transport of the animal reduces opportunities for targets to shift from their localized position in the image and simplifies the workflow of interventions. An improved method of needle calibration is presented that better characterizes the calibration using the position of the needle tip in photographs, rather than the needle axis. A calibration fixture was also introduced that dramatically reduces the time requirements of calibration while maintaining calibration accuracy. Two registration modes have been developed to correspond the robot coordinate system with the coordinate system of the micro-CT scanner. The two registration modes offer a balance between the time required to complete a registration and the overall registration accuracy. The development of slow high accuracy and fast low accuracy registration modes provides the user with a degree of flexibility in selecting a registration mode best suited for their application. The errors of the high accuracy primary registration were $FRE_{primary} = 21 \pm 6$ µm and $TRE_{primary} = 31 \pm 12$ µm. The error in the low accuracy combined registration was $TRE_{combined} = 139 \pm 63$ µm. Both registration modes are therefore suitable for small animal needle interventions. The targeting accuracy of the robotic system was then characterized using targeting experiments in tissue-mimicking gelatin phantoms. The results of the targeting experiments were combined with the known calibration and needle deflection errors to provide a more meaningful measure of the needle positioning accuracy of the system. The combined targeting errors of the system were 149 ± 41 µm and 218 ± 38 µm using the primary and combined registrations respectively. Finally, pilot *in vivo* experiments were completed to demonstrate the performance of the system in a biomedical application.

5.6 References

1. Taylor RH, Stoianovici D. Medical robotics in computer-integrated surgery. *IEEE T Robotic Autom.* Oct 2003;19(5):765-781.

2. Stitzenberg KB, Wong YN, Nielsen ME, Egleston BL, Uzzo RG. Trends in radical prostatectomy: centralization, robotics, and access to urologic cancer care. *Cancer.* Jun 29 2011.

3. Cleary K, Melzer A, Watson V, Kronreif G, Stoianovici D. Interventional robotic systems: applications and technology state-of-the-art. *Minim Invasive Ther Allied Technol.* 2006;15(2):101-113.

4. de la Cueva T, Naranjo A, de la Cueva E, Rubio D. Refinement of intrathymic injection in mice. *Lab Anim (NY).* May 2007;36(5):27-32.

5. El-Ghamari M, Bergmann F, Schmied BM, Weitz J, Ulrich A. Islet cells contribute to pancreatic carcinogenesis in an animal model. *Pancreas.* Mar 2011;40(2):242-246.

6. Springer ML, Sievers RE, Viswanathan MN, et al. Closed-chest cell injections into mouse myocardium guided by high-resolution echocardiography. *Am J Physiol-Heart C.* Sep 2005;289(3):H1307-H1314.

7. Li Q, Li BS, Wang XW, et al. Overexpression of insulin-like growth factor-1 in mice protects from myocyte death after infarction, attenuating ventricular dilation, wall stress, and cardiac hypertrophy. *J Clin Invest.* Oct 15 1997;100(8):1991-1999.

8. Blair-Handon R, Mueller K, Hoogstraten-Miller S. An alternative method for intrathymic injections in mice. *Lab Animal.* Aug 2010;39(8):248-252.

9. Horsley V, Clarke RH. The structure and function of the cerebellum examined by a new method. *Brain.* 1908;31(1):45–124

10. Kagadis GC, Loudos G, Katsanos K, Langer SG, Nikiforidis GC. In vivo small animal imaging: current status and future prospects. *Med Phys.* Dec 2010;37(12):6421-6442.

11. Schambach SJ, Bag S, Schilling L, Groden C, Brockmann MA. Application of micro-CT in small animal imaging. *Methods.* Jan 2010;50(1):2-13.

12. Bartling SH, Stiller W, Semmler W, Kiessling F. Small animal computed tomography Imaging. *Curr Med Imaging Rev.* Feb 2007;3(1):45-59.

13. Badea CT, Drangova M, Holdsworth DW, Johnson GA. In vivo small-animal imaging using micro-CT and digital subtraction angiography. *Phys Med Biol.* Oct 7 2008;53(19):R319-R350.

14. Kazanzides P, Chang JH, Iordachita I, Li J, Ling CC, Fichtinger G. Development of an image-guided robot for small animal research. *Comput Aided Surg.* Nov 2007;12(6):357-365.

15. Nicolau SA, Mendoza-Burgos L, Soler L, Mutter D, Marescaux J. In vivo evaluation of a guidance system for computer assisted robotized needle insertion devoted to small animals. *Medical Imaging and Augmented Reality, Proceedings.* 2008;5128:241-250.

16. Waspe AC, McErlain DD, Pitelka V, Holdsworth DW, Lacefield JC, Fenster A. Integration and evaluation of a needle-positioning robot with volumetric microcomputed tomography image guidance for small animal stereotactic interventions. *Med Phys.* Apr 2010;37(4):1647-1659.

17. Waspe AC, Cakiroglu HJ, Lacefield JC, Fenster A. Design, calibration and evaluation of a robotic needle-positioning system for small animal imaging applications. *Phys Med Biol.* Apr 7 2007;52(7):1863-1878.

18. Hwang MJ, Bebek O, Liang F, Fei BW, Cavusoglu MC. Kinematic Calibration of a Parallel Robot for Small Animal Biopsies. *2009 IEEE-RSJ International Conference on Intelligent Robots and Systems.* 2009:4104-4109.

19. Ramrath L, Hofmann UG, Schweikard A. A robotic assistant for stereotactic neurosurgery on small animals. *Int J Med Robot Comp.* Dec 2008;4(4):295-303.

20. Bax J, Cool D, Gardi L, et al. Mechanically assisted 3D ultrasound guided prostate biopsy system. *Med Phys.* Dec 2008;35(12):5397-5410.

21. Ma K, Kornecki A, Bax J, Mundt Y, Fenster A. Development and validation of a new guidance device for lateral approach stereotactic breast biopsy. *Med Phys.* Jun 2009;36(6):2118-2129.

22. Taylor RH, Funda J, Eldridge B, et al. A Telerobotic Assistant for Laparoscopic Surgery. *Ieee Eng Med Biol.* May-Jun 1995;14(3):279-288.

23. Patwardhan A. Subpixel position measurement using 1D, 2D and 3D centroid algorithms with emphasis on applications in confocal microscopy. *J Microsc-Oxford.* Jun 1997;186:246-257.

24. Arun KS, Huang TS, Blostein SD. Least-squares fitting of two 3-d point sets. *IEEE Trans Pattern Anal Mach Intell.* May 1987;9(5):698-700.

25. Fitzpatrick JM, West JB, Maurer CR, Jr. Predicting error in rigid-body point-based registration. *IEEE Trans Med Imaging.* Oct 1998;17(5):694-702.

26. Ryan LK, Foster FS. Tissue equivalent vessel phantoms for intravascular ultrasound. *Ultrasound Med Biol.* 1997;23(2):261-273.

27. Fadnes HO, Reed RK, Aukland K. Interstitial fluid pressure in rats measured with a modified wick technique. *Microvasc Res.* Jul 1977;14(1):27-36.

Chapter 6

6 Summary and Future Work

6.1 6.1 Summary of thesis:

The purpose of the work in this thesis was to develop image-guided needle positioning systems to increase the accuracy and repeatability of needle interventions in a variety of clinical applications. Each project involved not only designing a mechatronic system for the application, but also interfacing and co-registering each system with various clinical US probes and a micro-CT small animal imaging system. The specific technical developments, registration methods, and validation of each system are summarized below.

6.1.1 A 3D Ultrasound-guided prostate biopsy system

In Chapter 2, we developed a 3D TRUS-guided biopsy system, which can make use of any manufacturer's end-fire TRUS probe that records and displays the 3D locations of biopsy cores.[1, 2] It is composed of a 3D TRUS imaging subsystem and a passive mechanical arm with a fixed remote center-of-motion positioned near the tip of the TRUS probe. The RCM is intended to minimize prostate motion during reorientation of the probe when aiming at different targets in the biopsy plan. The stabilization of the TRUS probe and associated linkage is accomplished using a mechanical spring-loaded counter-balancing system that maintains the position and orientation of the probe even when the physician removes his hand from the handle.[3] This permits smooth motion of the transducer with a light touch of the physician's hand.

To calibrate and register the system to the 3D US image, the device was constrained into a known pose with the US transducer aligned to the RCM of the device. This provided a link between the encoder readout to the pose of the linkage, and also provided a means to register the first 2D US image in the 3D reconstruction linking the image to the device kinematics.

By adding 3D information to the prostate biopsy procedure, our system should improve the recording procedure as well as the physician’s ability to accurately guide the biopsy needle to selected targets. This would be beneficial in cases where the patient was diagnosed on biopsy to have atypical small acinar proliferation (ASAP) and requires the physician to rebiopsy the same area. Using the 3D TRUS image, the physician was able to observe the patient’s prostate in views currently not possible in 2D procedures. Overall, our 3D system should result in prostate biopsy procedures that are stereotactic and more reproducible, which may lead to higher cancer detection rates and improve the yield on repeat biopsy.

Finally, integration of our system into the current prostate biopsy procedure requires minimal physician retraining as procedural workflow is maintained. By adhering to the imaging tools and protocols of current biopsy procedures, clinical integration of our 3D system should be cost effective.

6.1.2 A 3D ultrasound-guided prostate therapy system

In Chapter 3, we developed a mechanical assisted prostate therapy system, that facilitates the physician in performing transperineal prostate therapy procedures, in which the needle can be positioned (*i.e.*, ready for insertion) manually with improved accuracy and flexibility, and the needle insertion into the prostate is done manually by the physician.[4, 5] Our approach to the problem differs from the prior approaches in that many of the benefits of a robotic system (accuracy and improved needle coverage) can be realized with the option to control the needle location and trajectory (including oblique) manually.

The device was calibrated by constraining the linkage into a known orientation providing a fixed link between the encoder readout and kinematics. To register the image to the system, a string phantom was fixed to a known position on the device, which was in turn submerged into a tank of glycerol and water solution to create a registration image.

Combining 3D TRUS imaging system with a dynamically adjustable needle guide, the physician will be able to place the needle trajectory to selected targets in the

3D TRUS image with a mean error that closely matches the ultrasound resolution. This would be beneficial as the physician has complete control of the needle and can safely manoeuvre the needle guide around obstacles like previously placed needles or a TRUS probe. Although this system was tested using a 3D imaging system, this system is also compatible with any 2D system and protocol currently in use. Our future direction will be to clinically validate our prostate therapy system (delivering brachytherapy first, but able to accommodate other prostate therapy approaches like cryotherapy and laser ablation), in which all aspects of the procedure will be carried out intra-operatively including dosimetry planning, monitoring of prostate changes, dynamic re-planning including oblique trajectories and needle placement verification.

6.1.3 A 3D micro-CT-guided needle positioning system for small animal research

Preclinical micro-injection procedures in various research applications are particularly dependent on the accuracy of mechatronic devices, such as micro-CT systems, used to guide needle insertion into soft tissues of the animal.[6] A foundation of these interventions is the ability to accurately localize the position of targets and fiducial markers in space using micro-CT images. A mechatronic device with near-perfect positioning accuracy will always miss a target if guided to the wrong position in space due to image distortion. Therefore, the geometric accuracy of micro-CT scanners is fundamentally important for the successful completion of interventions by micro-CT guided mechatronic needle positioning systems.

Chapter 4 describes the development and testing of a traceable calibration phantom and technique to evaluate the geometric accuracy of five different micro-CT scanners, representing four scanner models. The geometric errors detected within micro-CT images by this study are not immediately obvious but could be serious in an application (such as a micro-CT guided small animal intervention) that may require targeting accuracies of less than 200 μm.[7] Use of this calibration phantom should therefore be considered for any application that demands high geometric fidelity in images.[8]

In chapter 5, the design of a micro-CT guided needle positioning system for small animal intervention has been presented. The system has been developed to achieve a mean targeting error of less than 200 µm while maintaining a high degree of user friendliness. In addition, the robot is compact enough to operate within the micro-CT bore. Small animals can be imaged and the intervention performed without transporting the animal from one workspace to another. Not requiring transport of the animal reduces opportunities for targets to shift from their localized position in the image and simplifies the workflow of interventions. In addition, performing the intervention within the bore of the scanner will allow techniques that employ near-real-time imaging. For example, the GE Locus Ultra scanner is capable of acquiring volumetric frame rates as high as 1Hz .[9]

An improved method of needle calibration is presented that better characterizes the calibration using the position of the needle tip in photographs rather the needle axis. A calibration fixture was also introduced, which significantly reduces the time requirements of calibrating the needle depth while maintaining calibration accuracy. Two registration modes have been developed to link the robot coordinate system with the coordinate system of the micro-CT scanner. The two registration modes offer a balance between the time required to complete a registration and the overall registration accuracy. The development of slow high accuracy and fast low accuracy registration modes provides the user with a degree of flexibility in selecting a registration mode best suited for their application.

The targeting accuracy of the robotic system was then characterized using targeting experiments in tissue-mimicking gelatin phantoms. The results of the targeting experiments were combined with the known calibration and needle deflection errors to provide a more meaningful measure of the needle positioning accuracy of the system. Finally, pilot *in vivo* experiments were completed to demonstrate the performance of the system in a biomedical application.

6.2 Future Work

Innovations relevant to Chapter 2 of this thesis resulted in the filing of two patents included in Appendices A, and B and the licensing of the system to Eigen (Grass Valley, CA) where the clinical prototype system presented here has been developed into a commercial product (see Figure 6.1).[10] In addition, the series of phantom experiments provided sufficient validation of the system to begin clinical trials in collaboration with University Hospital, London, ON; Dr. Cesare Romagnoli. The device has been approved by Health Canada for use on human subjects and a number of clinical studies have been approved by The University of Western Ontario Ethics Board for Health Sciences Research Involving Human Subjects (HSREB) (see Appendix D). The purpose of this trial was to:

1. Validate a novel adaptation of a 2D TRUS probe for producing 3D images of biopsy data,
2. Determine the ability of the system to record the 3D location of biopsy cores removed from the prostate during the procedure.

Figure 6.1: Photograph of the Atremis prostate biopsy tracking system by Eigen (Grass Valley, CA).

With the help from Dr. Romagnoli, the system has undergone a number of improvements to help to translate the initial prototype into a potentially useful clinical tool. Improvements to the mechanical design allowed us to substantially reduce the mass and associated inertia of the linkage, thus making it easier for the physician to maneuver the TRUS probe. The new system illustrated in Figure 6.2 uses a single spring-loaded counterbalance assembly in place of the original spring-counterweight combination presented in Chapter 2. The new spring counterbalance provides two degrees of adjustment to account for both the magnitude and orientation of the payload, which consists of the TRUS probe and connecting arm. Once set, the spring-loaded counterbalance will completely support the payload without further adjustment and with minimal loss of manipulative transparency regardless of the linkage pose or presence of the TRUS probe and/or attached biopsy gun.

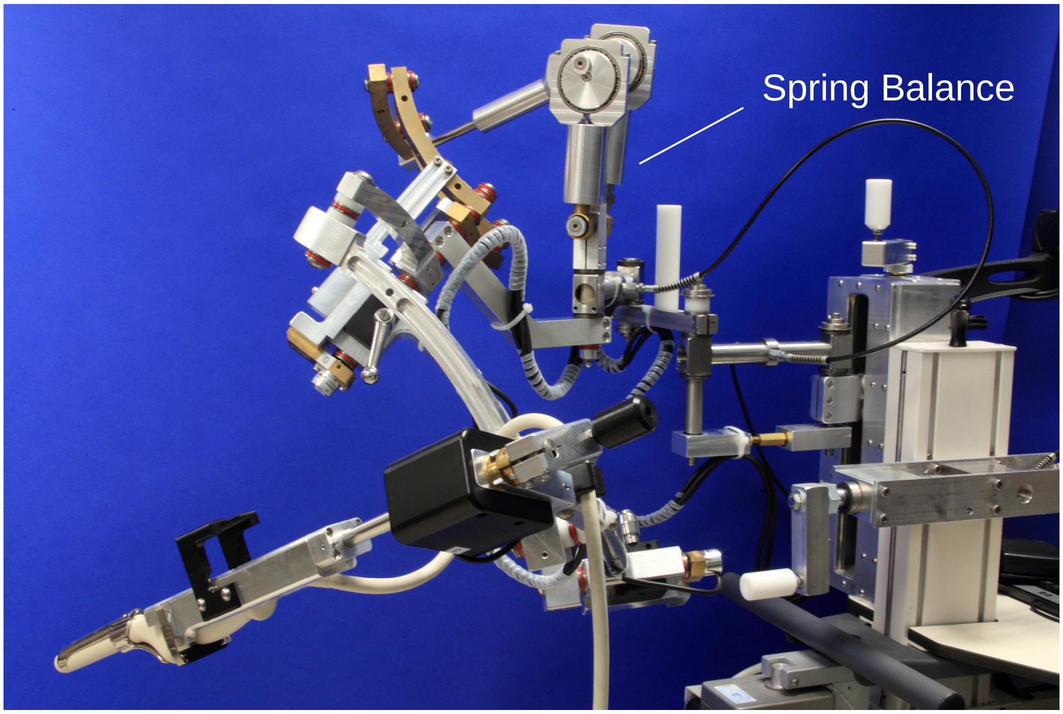

Figure 6.2: Photograph of the clinical prototype mechanical tracking system for prostate biopsy. A single spring-loaded counterbalance assembly is used in place of the original spring-counterweight combination presented in Chapter 2.

Additional research questions related to this project that have been undertaken include Determining a) the intra- [11] and b) inter-session registration accuracy of patient 3D ultrasound scans,[12] and c) the study of prostate motion due to the firing of the biopsy gun during the procedure.[13] In addition, a clinical study is currently being undertaken to determine the feasibility of using the mechanical system to guide the biopsy needle using preoperative MRI images.

Innovations relevant to Chapter 3 of this thesis resulted in the filing of a patent included in Appendix C and the licensing of the technology to Eigen (Grass Valley, CA) where the clinical prototype system presented here is currently being developed into a commercial product. With the help from Dr. David D'Souza and Dr. Nikhilesh Patil, the system has undergone some improvements to prepare the device for an upcoming clinical evaluation. The new device, as shown in Figure 6.3, consists of a right-and left-hand needle guide to increase its flexibility and eliminate the counterweights used in the prototype presented in Chapter 3. In addition, the motorized 3D US mover was also redesigned to reduce both the size and weight of the mechatronic system, allowing it to be adapted to any clinical stabilizer used for prostate brachytherapy.

The clinical investigation will be in collaboration with the London Regional Cancer Center, London, ON. The system has been approved by Health Canada for use on human subjects and a clinical study has been approved by The University of Western Ontario Ethics Board: HSREB (see Appendix E). The purpose of this trial is to:

1. Determine the improvement to treatment delivery using 3D imaging,
2. Determine the effectiveness of the intra-operative delivery compensation for prostate movement using the system,
3. Determine if 3D US imaging can be used in place of a combination of 2D US and CT imaging, and
4. Determine whether delivery can be improved using the flexibility of the mechatronic device.

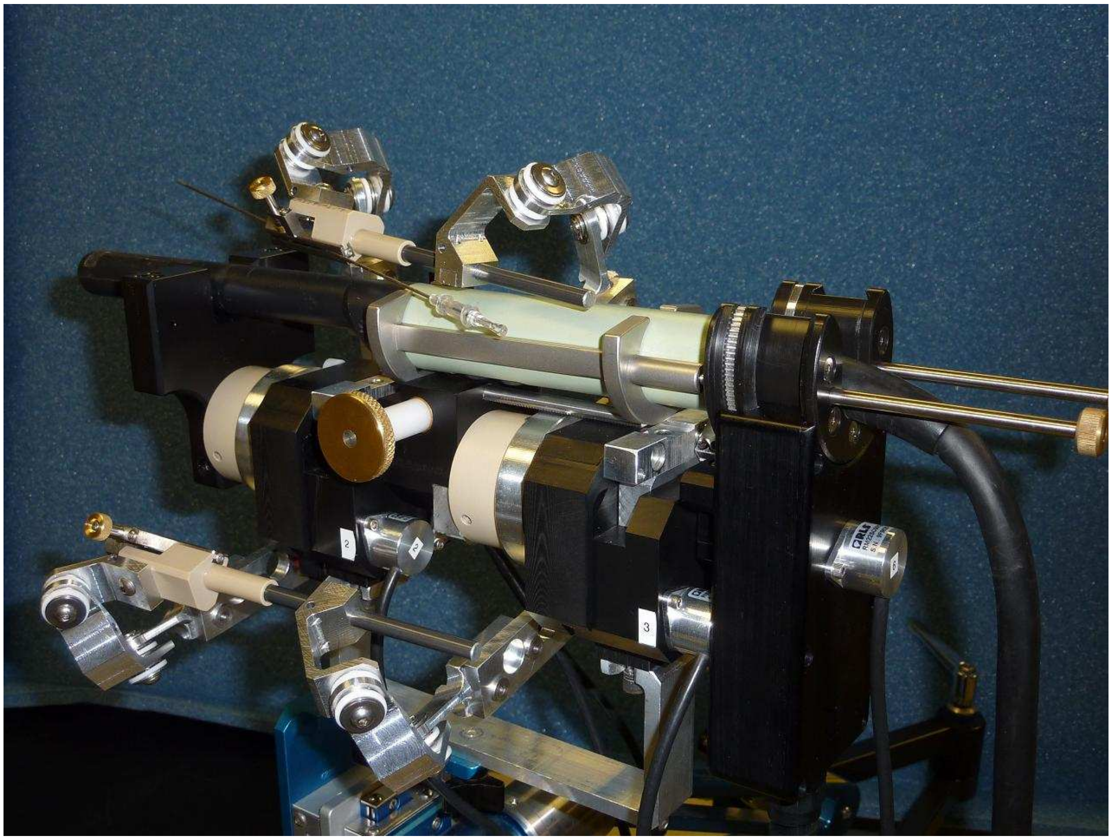

Figure 6.3: Photograph of the clinical prototype system for ultrasound guided prostate therapy. The new device consists of a right-and left-hand needle guide to increase its flexibility and eliminate the counterweights used in the prototype presented in Chapter 3.

With respect to the small animal system introduced in Chapters 4 and 5, the series of phantom experiments and pilot animal studies provided sufficient validation to use the system for a number of preclinical research projects ranging from needle-guided interventions to image reconstruction. An initial preclinical investigation using the system will be in collaboration with the STTARR Pre-clinical Core at Princess Margaret Hospital, Toronto, ON. In addition, this system, including the device, phantom and validation method developed for this project, can also be adapted to any small imaging CT scanner with fields of view ranging from 1 to 20 cm. Since there is no method in the literature to calibrate a micro-CT scanner to a traceable standard, the phantom design can be potentially useful for any research project that uses the CT as a means of quantitative measurement.[8]

6.3 Conclusion

In addressing each objective of this thesis, a number of novel mechanical designs incorporating an RCM design with varying degrees of freedom have been presented. Each of these designs can be deployed in a variety of imaging modalities and clinical applications, ranging from preclinical to human interventions, with an accuracy of control in the millimeter to sub-millimeter range. In addition, a low inertia spring balance was designed to carry larger payloads, and can be adapted to any robot architecture as a means to improve safety. In addition, the spring-loaded counterbalance can also be modified to provide tremor reduction or inertia negation by adding a simple electromechanical feedback circuit or velocity control by combining the springs with hydraulic dampers to form a hydro-mechanical feedback loop.

6.4 References

1. Bax J, Cool D, Gardi L, et al. Mechanically assisted 3D ultrasound guided prostate biopsy system. *Med Phys.* Dec 2008;35(12):5397-5410.

2. Bax J, Cool D, Gardi L, Fenster A, Inventors. Apparatus for guiding a medical tool. US Patent Pending. Sept 17, 2009, 2009.

3. Bax J, Fenster A, Inventors. Counterbalance Assembly. US Patent Pending. Dec. 23, 2010, 2010.

4. Bax J, Smith D, Bartha L, et al. A compact mechatronic system for 3D ultrasound guided prostate interventions. *Med Phys.* Feb 2011;38(2):1055-1069.

5. Bax J, Fenster A, Montreuil J, Gardi L, Smith D, Inventors. Apparatus and method for guiding insertion of a medical tool. US Patent Pending 2008.

6. Waspe AC, Cakiroglu HJ, Lacefield JC, Fenster A. Design, calibration and evaluation of a robotic needle-positioning system for small animal imaging applications. *Phys Med Biol.* Apr 7 2007;52(7):1863-1878.

7. Waspe AC, McErlain DD, Pitelka V, Holdsworth DW, Lacefield JC, Fenster A. Integration and evaluation of a needle-positioning robot with volumetric microcomputed tomography image guidance for small animal stereotactic interventions. *Med Phys.* Apr 2010;37(4):1647-1659.

8. Ross CK. Comments on 'Ionization chamber volume determination and quality assurance using micro-CT imaging'. *Phys Med Biol.* Mar 2009;54(6):L23-L27.

9. Du LY, Umoh J, Nikolov HN, Pollmann SI, Lee TY, Holdsworth DW. A quality assurance phantom for the performance evaluation of volumetric micro-CT systems. *Phys Med Biol.* Dec 7 2007;52(23):7087-7108.

10. Natarajan S, Marks LS, Margolis DJA, et al. Clinical application of a 3D ultrasound-guided prostate biopsy system. *Urol Oncol-Semin Ori.* May-Jun 2011;29(3):334-342.

11. Karnik VV, Fenster A, Bax J, et al. Assessment of image registration accuracy in three-dimensional transrectal ultrasound guided prostate biopsy. *Med Phys.* Feb 2010;37(2):802-813.

12. Karnik VV, Fenster A, Bax J, Romagnoli C, Ward AD. Evaluation of intersession 3D-TRUS to 3D-TRUS image registration for repeat prostate biopsies. *Med Phys.* Apr 2011;38(4):1832-1843.

13. De Silva T, Fenster A, Bax J, et al. Quantification of prostate deformation due to needle insertion during TRUS-guided biopsy: Comparison of hand-held and mechanically stabilized systems. *Med Phys.* Mar 2011;38(3):1718-1731.

Appendices

Appendix A (Patent application): Apparatus for guiding a medical tool

US 20090234369A1

(19) **United States**

(12) **Patent Application Publication** (10) **Pub. No.: US 2009/0234369 A1**

Bax et al. (43) **Pub. Date: Sep. 17, 2009**

(54) **APPARATUS FOR GUIDING A MEDICAL TOOL**

(75) Inventors: **Jeffrey Bax**, London (CA); **Derek Cool**, London (CA); **Lori Gardi**, London (CA); **Aaron Fenster**, London (CA)

(73) Assignee: **ROBARTS RESEARCH INSTITUTE**, London, Ontario (CA)

(21) Appl. No.: **12/303,415**

(22) PCT Filed: **Jun. 19, 2007**

(86) PCT No.: **PCT/CA2007/001076**

§ 371 (c)(1),
(2), (4) Date: **Feb. 9, 2009**

Related U.S. Application Data

(60) Provisional application No. 60/814,539, filed on Jun. 19, 2006.

Publication Classification

(51) **Int. Cl.**
A61B 19/00 (2006.01)

(52) **U.S. Cl.** **606/130**

(57) **ABSTRACT**

There is provided a guide apparatus for orienting a medical tool relative to and through a remote fulcrum or remote center of motion. The guide apparatus may comprise: at least one crank arm comprising at least a portion of a first hinged coupling for hinged coupling to a stabilizer; at least one link arm comprising at least a portion of a second hinged coupling for hinged coupling to the crank arm at a location spaced from the first hinged coupling; a tool holder for supporting a medical tool on the link arm at a location spaced from the first hinged coupling; wherein the rotational axes of the first and second hinged couplings intersect to define a remote fulcrum. The guide apparatus may be configured to be an open-loop spherical chain or a closed-loop spherical chain.

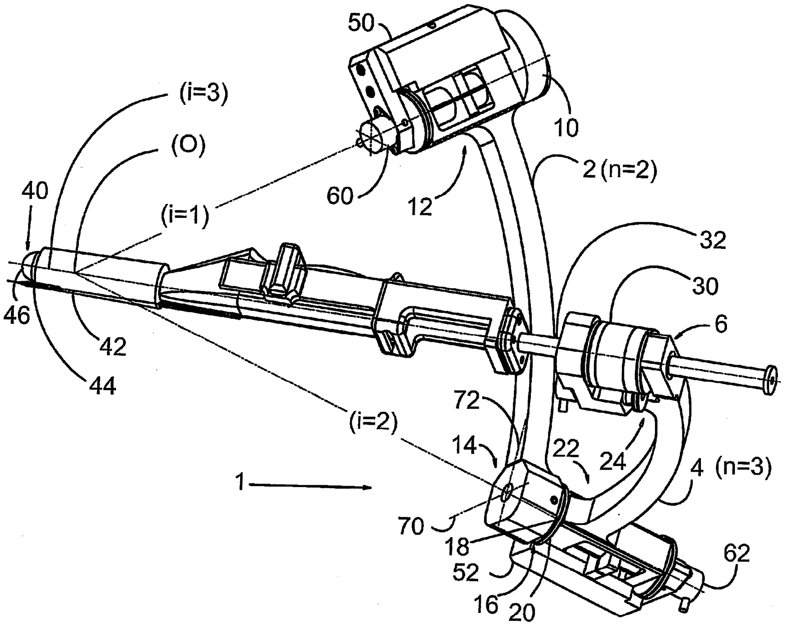

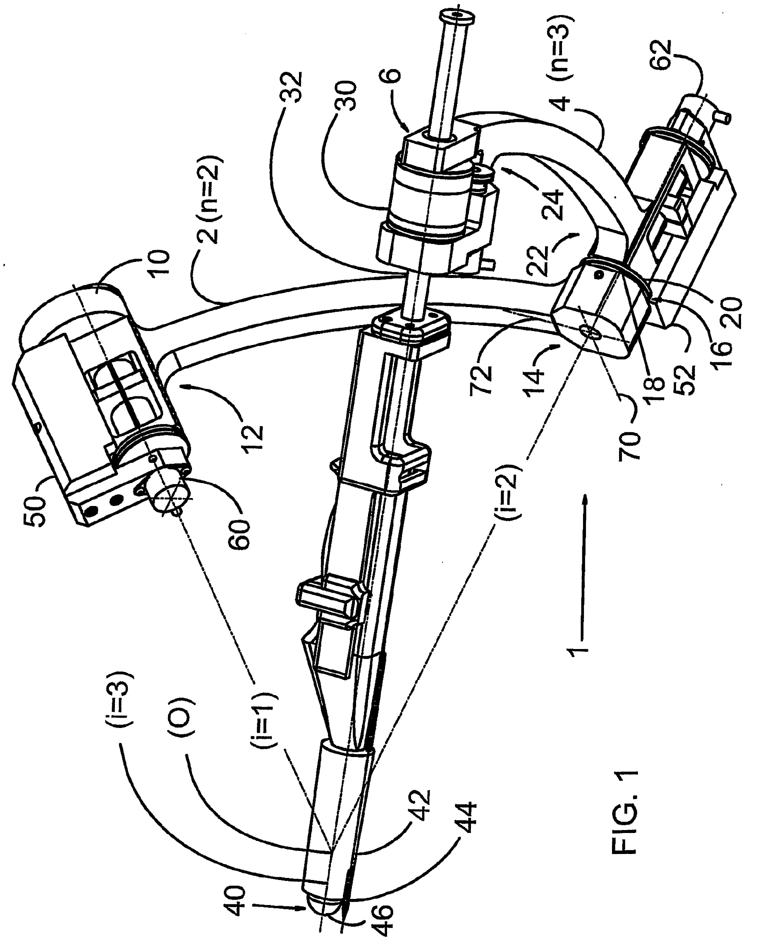
32
30
6
4 (n=3)
62
2 (n=2)
10
24
22
20
16
52
18
70
14
72
12
50
60
(i=2)
1
(i=3)
(O)
(i=1)
42
44
40
46

FIG. 1

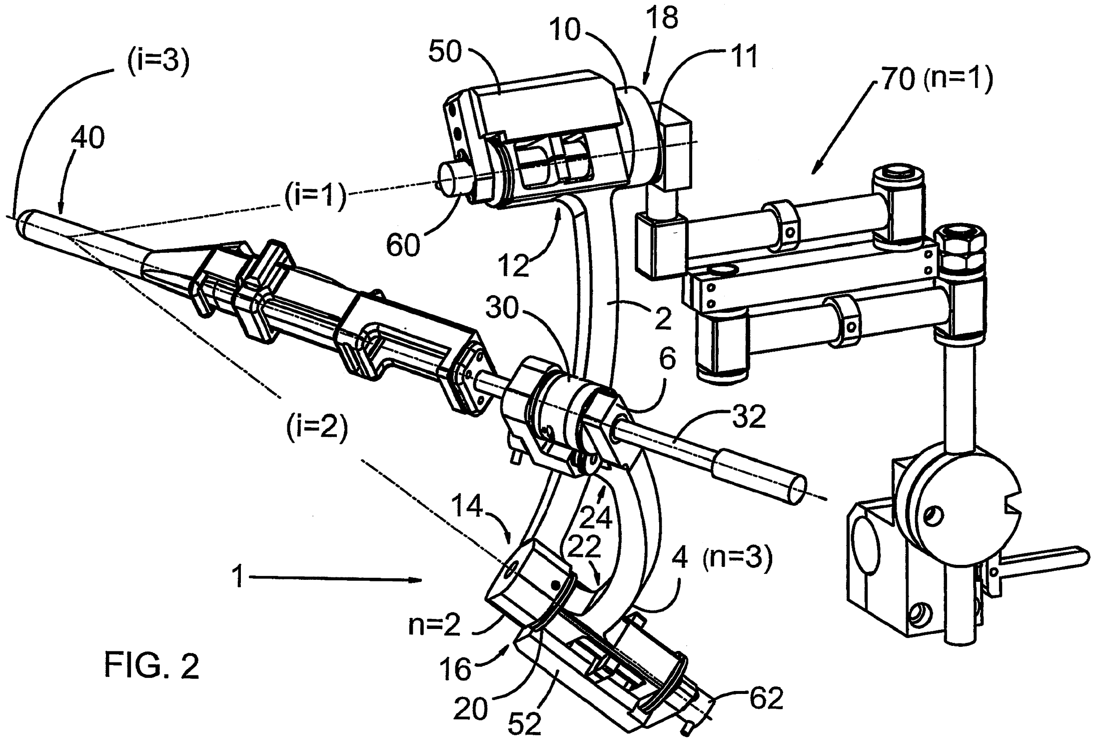
(i=3)
40
50
10
18
11
70 (n=1)
(i=1)
60
12
30
2
6
32
(i=2)
14
24
22
4 (n=3)
1
n=2
16
20
52
62

FIG. 2

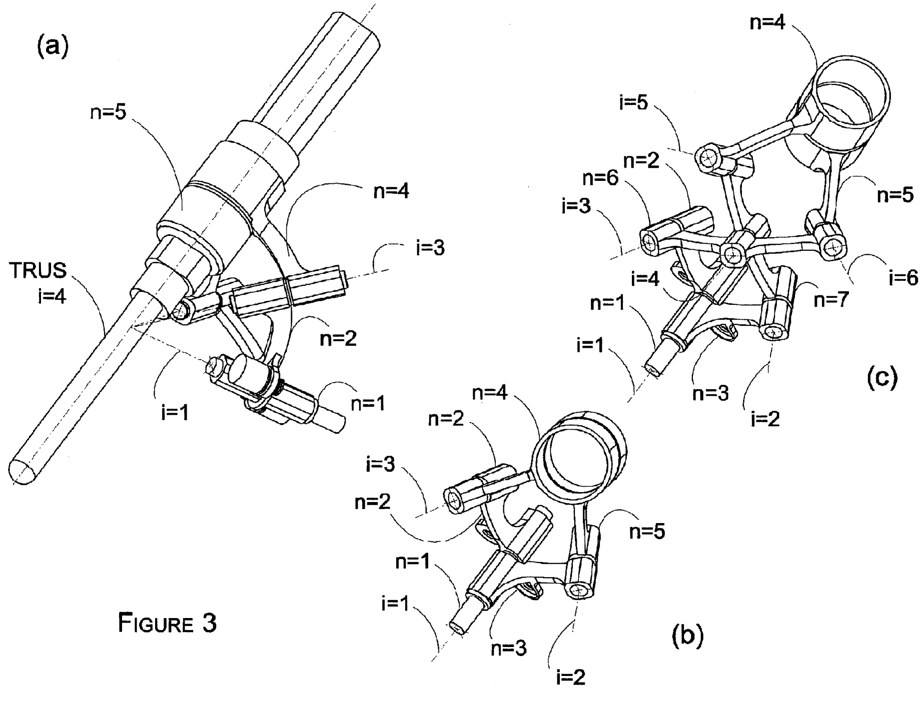
(a)
n=5
n=4
TRUS
i=4
i=3
n=2
i=1
n=1
(b)
n=4
n=2
i=3
n=2
n=5
n=1
i=1
n=3
i=2
(c)
n=4
i=5
n=2
n=6
i=3
n=5
i=4
n=1
i=6
n=7
i=1
n=3
i=2

FIGURE 3

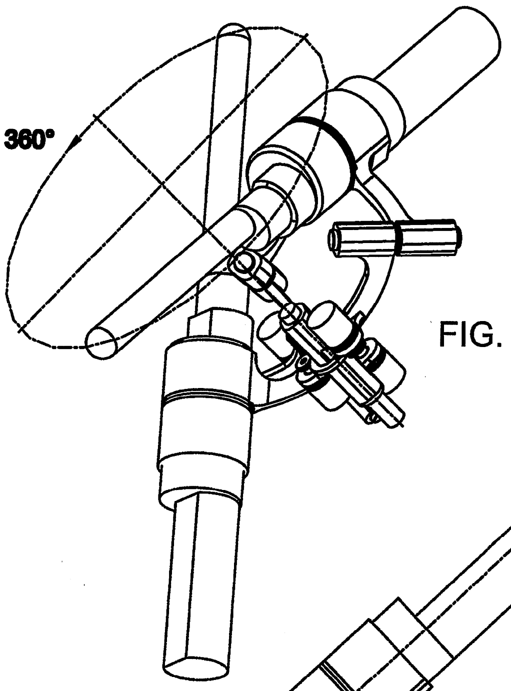

FIG. 4(a)

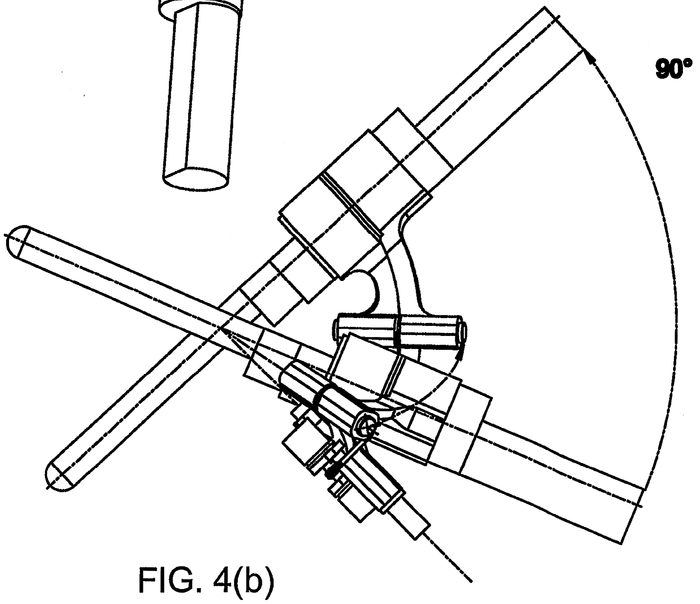

FIG. 4(b)

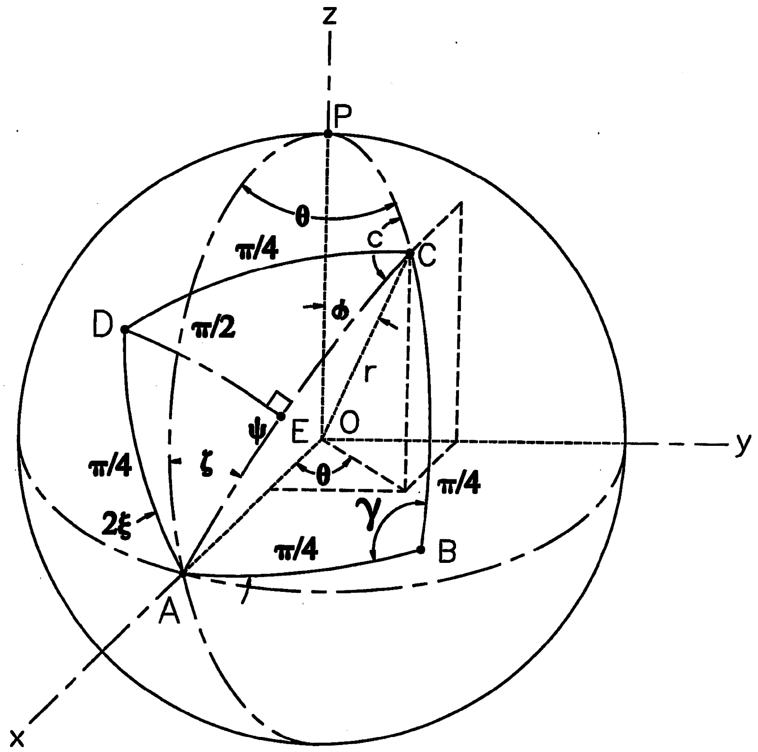

FIG. 5

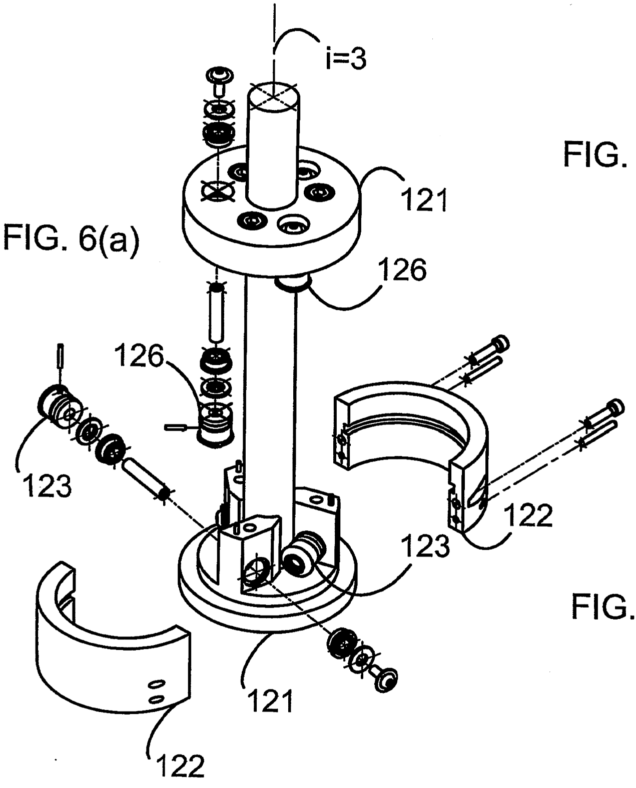

FIG. 6(a)

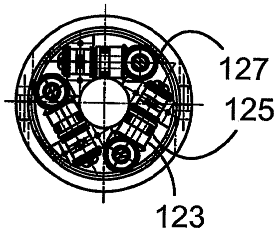

FIG. 6(c)

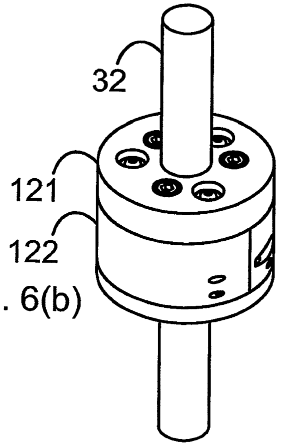

FIG. 6(b)

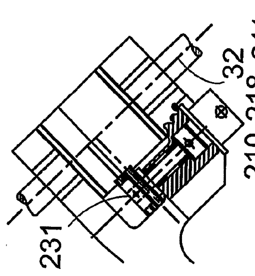

FIG. 7(a)

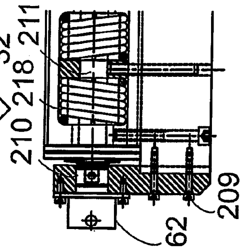

FIG. 7(b)

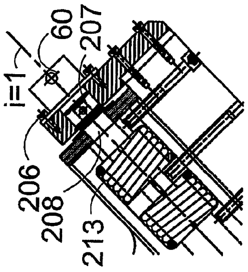

FIG. 7(c)

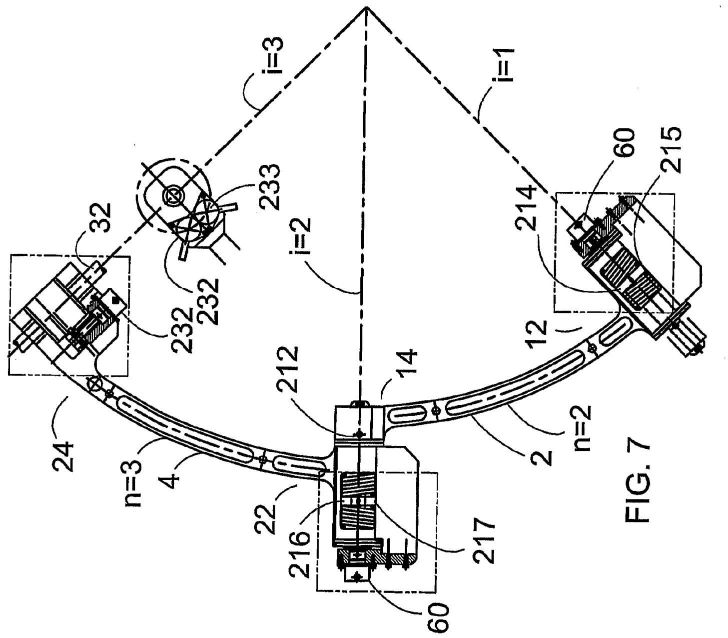

FIG. 7

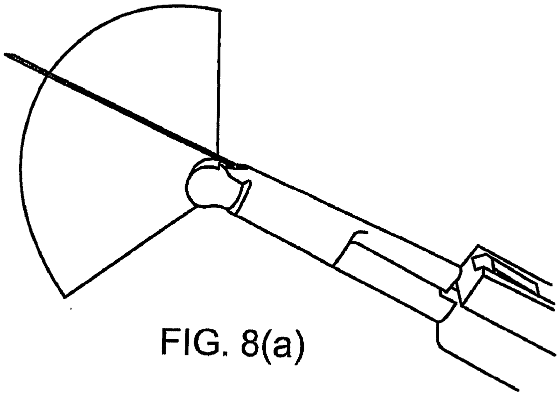

FIG. 8(a)

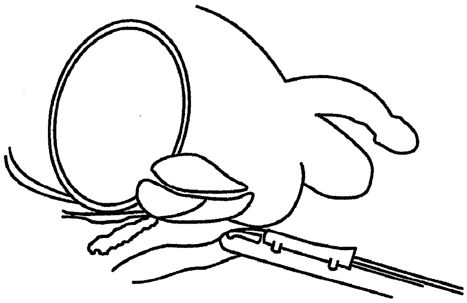

FIG. 8(b)

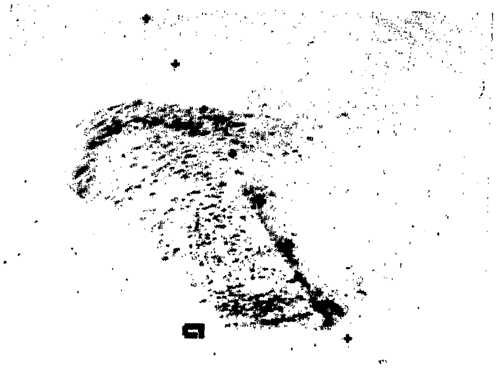

FIG. 8(c)

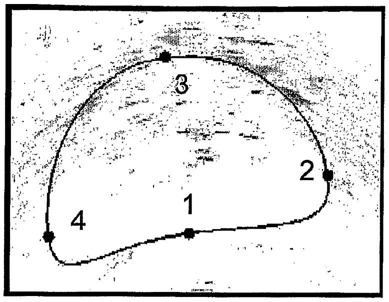

FIG. 9(a)

FIG. 9(b)

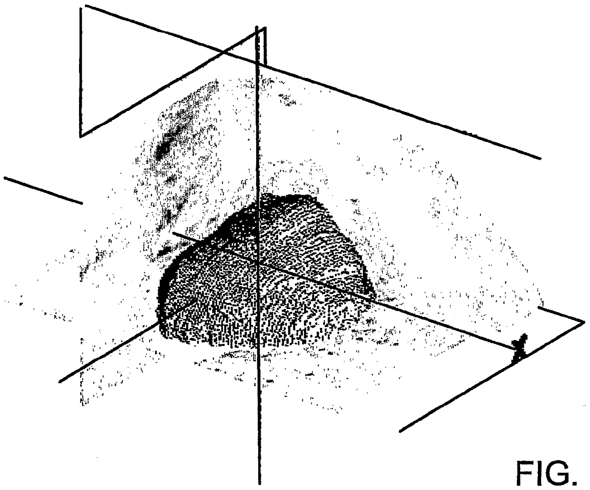

FIG. 9(c)

APPARATUS FOR GUIDING A MEDICAL TOOL

CROSS-REFERENCE TO RELATED APPLICATIONS

[0001] This application claims the benefit of U.S. Patent Application Ser. No. 60/814,539 filed on Jun. 19, 2006, the content of which is incorporated herein by reference.

FIELD OF THE INVENTION

[0002] The present invention relates generally to medical devices and, more particularly, to an apparatus for guiding a medical tool.

BACKGROUND OF THE INVENTION

[0003] Apparatus for guiding medical tools have been shown to be of valuable assistance in various medical procedures, for example, manipulation of surgical tools, manipulation of cameras or sensors, biopsy, etc. An apparatus for guiding a medical tool usually also improves reproducibility compared to free-hand medical procedures, for example, surgical or biopsy procedures.

[0004] These apparatus typically have one or more degrees of freedom and may be manually driven in that the one or more degrees of freedom may be equipped with a brake with motive force being provided by a human practitioner, or may be automated in that at least one degree of freedom is driven by a computer controlled actuator.

[0005] A medical tool often needs to be oriented about a point in, on, or in proximity to a patient's body. However, having the main body of an apparatus that supports the tool located too proximal to the patient's body may be disadvantageous, since the supporting apparatus may, for example, interfere with the view of or access to the patient by the practitioner. An apparatus which can orient a tool about a remote fulcrum or remote center of motion can avoid such disadvantages.

[0006] The use of an apparatus that orients a tool about a remote center of motion is known in robotics as described, for example, in U.S. Pat. Nos. 5,397,323, 5,515,478, 5,630,431, 5,817,084, 5,907,664, 6,047,610, 6,246,200, and 7,021,173. U.S. Pat. No. 5,397,323 to Taylor et al. discloses the remote center of motion principle in surgical robots with a first axis of rotation pointing into the remote center of motion, and a second axis materialized by a parallelogram mechanism implemented by two coupled parallel linkages of rigid bars and cylindrical joints. The two axes of the remote center of motion are orthogonal, and the mechanism operated around an upright initial (zero) direction.

[0007] Unfortunately, the parallelogram structure of Taylor et al. and other conventional parallelogram mechanisms is bulky, making it difficult to position with respect to a patient's body and in some cases forcing a patient to assume an uncomfortable or unconventional position. Therefore, there is a need for an alternative apparatus for guiding medical tools.

[0008] It is an object of an aspect of the present invention to provide a novel apparatus for guiding a medical tool.

SUMMARY OF THE INVENTION

[0009] In an aspect, there is provided an apparatus for guiding a medical tool, comprising:

- **[0010]** at least one crank arm comprising at least a portion of a first hinged coupling for hinged coupling to a stabilizer;
- **[0011]** at least one link arm comprising at least a portion of a second hinged coupling for hinged coupling to the crank arm at a location spaced from the first hinged coupling;
- **[0012]** a tool holder for supporting a medical tool on the link arm at a location spaced from the first hinged coupling;
- **[0013]** wherein the rotational axes of the first and second hinged couplings intersect to define a remote fulcrum.

BRIEF DESCRIPTION OF THE DRAWINGS

[0014] Embodiments will now be described, by way of example only, with reference to the attached Figures, wherein:

[0015] FIG. **1** is a front perspective view of a 3-element guide apparatus for guiding a transrectal ultrasound (TRUS) probe and biopsy needle with 'n' representing linkage elements, and 'i' representing hinged coupling axes;

[0016] FIG. **2** is a front perspective view of the 3-element guide apparatus of FIG. **1** attached to a multijointed stabilizer, which in turn may be attached to an operating room bed or fixture with 'n' representing linkage elements, and 'i' representing hinged coupling axes;

[0017] FIGS. **3**(*a*) and (*b*) illustrate a 5-element, and (*c*) a 7-element closed loop spherical linkage with additional linkage elements used to provide additional support for the TRUS probe; 'n' representing connection elements, and 'i' representing hinge joint axes;

[0018] FIG. **4** is a schematic of 2 rotational motions within the 5-element guide apparatus of FIG. **3**(*a*);

[0019] FIG. **5** is an illustration of the spherical coordinate reference frame used to define the forward kinematics between the primary alignment axis (base) and tertiary alignment axis (probe tip);

[0020] FIG. **6**(*a*) is an exploded isometric view of the differential gear train used to decouple the rotation and linear travel of the TRUS about the tertiary alignment axis; FIG. **6**(*b*) is an isometric view of the differential gear train; FIG. **6**(*c*) is a top cross-sectional view of the differential train illustrating how the central shaft is coupled to the base and outer ring;

[0021] FIG. **7** is an illustration of the top view of the guide apparatus of FIG. **1** laid open on a surface showing the layout of the arcuate arms, braking sub-assembly, and encoders;

[0022] FIG. **8**(*a*) is an illustration of a trans-rectal ultrasound (TRUS) transducer with an attached biopsy guides showing an 18-gauge biopsy needle constrained within the imaging plane of the 2D US beam; FIG. **8**(*b*) shows a schematic diagram of the TRUS transducer, biopsy needle and guide in the rectum during a prostate biopsy; FIG. **8**(*c*) is an illustration of a TRUS image of the prostate with a biopsy needle (arrow) in the inner gland;

[0023] FIG. **9** shows steps of a 2D and 3D prostate segmentation algorithm; (a) the user initializes the algorithm by placing 4 points on the boundary to generate an initial contour; (b) deformable dynamic contour approach is used to refine the initial contour until it matches the prostate boundary; (c) the contour is propagated to adjacent 2D slices of the 3D TRUS image and refined; the process is repeated until the complete prostate is segmented as shown.

DETAILED DESCRIPTION OF THE EMBODIMENTS

[0024] A guide apparatus can be useful for guiding a medical tool in 3D space. A guide apparatus may comprise one or more rotational degrees of freedom and an adaptable cradle for coupling a medical tool. Using this guide apparatus, physicians can maneuver a medical tool to a desired 3D position and orientation.

[0025] The guide apparatus is capable of producing a remote fulcrum and can be configured to constrain movement of a medical tool relative to the remote fulcrum. The constrained movements produced by the guide apparatus are consistent with movements produced by a user during a conventional surgical procedure. When the instrument is manipulated manually, the guide apparatus will passively follow the user's movements while still maintaining orientation of a medical tool relative to a fixed remote fulcrum that may be positioned to coincide with a restricted entrance point of a patient's body, for example a rectum or any surgical incision. Since the guide apparatus constrains the orientation of a medical tool relative to and through a fixed point in space, a user's movements are reproduced at a scaled down rate (minimized through the remote fulcrum) that allows for a level of precision that was thought to only be possible with robotic assisted machines. This improves the ability of a user to accurately target a point of interest within a patient's body.

[0026] FIG. **1** shows an example of a guide apparatus **1** that may be used for 3D orientation of a medical tool relative to and through a fixed point in space, a remote fulcrum. The guide apparatus comprises two linkage elements or arms, a crank **2** and a link **4**. The crank **2** and the link **4** may be of any size, or shape that allows for the remote fulcrum **0**.

[0027] The linkage elements may be hingedly coupled to form positioning elements. In FIG. **1** the crank **2** and link **4** both have an arcuate structure having a central angle of about 45 degrees. The crank has a first end **12** and a second end **14**. The link also has first and second ends **22**, **24**. When the guide apparatus is in use the first end **12** of the crank is hingedly coupled to a base or stabilizer. The first end **12** may comprise a full hinged coupling (not shown) that is attached to a member that is rigidly fixed to the base or stabilizer. Alternatively, the first end **12** may comprise a portion of a hinged coupling **10** with the remainder of the hinged coupling being provided by the base or stabilizer. The second end **14** of the crank forms a hinged coupling **16** with the first end **22** of the link. The second end **14** of the crank comprises a portion **18** of the hinged coupling **16**, while the first end **22** of the link comprises the remaining portion **20** of the hinged coupling **16**. The second end **24** of the link is coupled to a tool holder **6**. The tool holder may be in the form of an adaptable cradle for securing a shaft **32** that may be used to actuate a medical tool **40**.

[0028] FIGS. **1** and **2** show a medical tool **40** and a shaft **32** for actuating the medical tool. The shaft may be used to actuate longitudinal and/or rotational or angular motion of medical tool **40** relative to the tertiary alignment axis; longitudinal or linear motion along the axis provides one degree of freedom, while rotational or angular motion about the axis provides another degree of freedom. The shaft **32** passes through a cylindrical joint provided by tool holder **6**. The shaft **32** may be coupled directly to the medical tool **40**, or may be coupled to a sleeve or any other convenient structure for receiving the medical tool **40**. The medical tool **40** shown in FIG. **1** is a combination of a transrectal ultrasound (TRUS) transducer **46**, a biopsy needle **44** and a needle guide **42**.

[0029] A remote fulcrum **0** produced by the guide apparatus **1** is shown in FIGS. **1** and **2**. As shown in FIG. **2** the remote fulcrum **0** is formed at an intersection of the rotational axis (i=1) of the first hinged coupling formed between the first end **12** of the crank and the base or stabilizer **70** and the rotational axis (i=2) of the second hinged coupling formed between the second end **14** of the crank and the first end **22** of the link. When the guide apparatus is in use and is coupled to the medical tool **40** the axis (i=3) of the medical tool **40** passes through the remote fulcrum. In certain examples, the axes of the medical tool **40** and its shaft actuator **32** are collinear and both pass through the remote fulcrum.

[0030] The guide apparatus may be equipped with further components as desired to aid in the orientation or tracking of a medical tool, for example, without limitation, brakes for locking a hinged coupling, encoders for measuring rotational angles of a hinged coupling, counterweights and/or spring balances to offset the mass of the system, computer controlled actuators for automating rotation of a hinged coupling, additional linkage arms or the use of linkage arms having an adjustable arcuate structure. Further components that may be incorporated into the guide apparatus will be apparent to the skilled person, and suitable combinations of optional components will also be apparent depending on the particular medical tool and the particular use of the guide apparatus.

[0031] One example of an optional component that may be included in a guide apparatus is a rotational encoder. As seen in FIGS. **1** and **2**, a first rotational encoder **60** that may be mounted to the first end **12** of the crank **2**, while a second rotational encoder **62** may be mounted to the first end **22** of the link **4**.

[0032] As another example of an optional component, counterweight **52** is mounted to the link arm to offset the mass of a medical tool and associated hardware supporting it; while counterweight **50** is mounted to the crank arm to offset the mass of the crank arm, counterweight **52**, and the link arm. The counterweights may be replaced or used in conjunction with a spring balance to offset the mass of the system.

[0033] As yet another example of an optional component, a braking mechanism may be mounted within the crank and/or the link to inhibit motion of linkage elements relative to each other. In one example, a spring clutch may be mounted within the first end **12** of the crank arm to prevent or inhibit motion of the crank relative to the stabilizer or base fixture. The spring clutch (shown in FIG. **9**) may be comprised of two brake pads, in which at least one of the brake pads is affixed to the first end **12** of the crank, and at least one torsion spring is wrapped around the pair of brake pads.

[0034] As still another example of an optional component, a guide apparatus may be equipped with motors (not shown), for example servo motors that may be controlled by a computer to automate the motion of various linkage elements. In a particular example, each hinged coupling independently may be controlled by a servo motor.

[0035] As a further example of an optional component, a guide apparatus with an adjustable remote fulcrum may be produced by incorporating linkage arms having an adjustable arcuate structure (not shown). To make the remote fulcrum adjustable, an additional two hinged couplings can be integrated into the guide apparatus shown in FIG. **1**. The first additional hinged coupling can be located between **12** and **14** of the first crank with its axis of rotation being parallel to the axis **70**. By adjusting the angle between **12** and **14**, the point of intersection between i=**1** and i=**2** can be changed. In order to maintain the remote fulcrum, a second additional hinged coupling on link **4**, between **22** and **24** with its axis of rotation parallel to the axis **72**, can be used to adjust the intersection point between i=**2** and i=**3** to coincide with the previous adjustment. This optional component is particularly useful to adjust the remote fulcrum for different medical tools and/or different uses, or to account for manufacturing tolerances in the device. Typically, the remote fulcrum of the guide apparatus would be adjusted prior to a surgical procedure, set in place, and then maintained in a fixed position throughout the procedure. A planar coupling can be used in place of the first additional hinged coupling between **12** and **14** if the planar connection is parallel to the plane formed by the axis i=**2** and **72**. A planar coupling can be used in place of the second additional hinged coupling between **22** and **24** if the planar connection is parallel to the plane formed by the axis i=**2** and **70**.

[0036] An even further example of an optional component are further linkage elements, for example a second crank arm and a second link arm. While the guide apparatus has so far been described as comprising two linkage elements, FIGS. **3** and **4** show that the guide apparatus can be configured two comprise further linkage elements and be converted from an open-loop spherical chain to a closed-loop spherical chain. For example, to reduce inertia effects from the use of two arcuate linkage elements in an open-loop spherical chain, 2 or 4 additional linkage arms (FIG. **3**) may be integrated into the design and form a closed-loop spherical chain. The closed chain design can dampen the inertia effects present in the open chain design illustrated in (FIG. **1**). This would be useful for applications where improved sensitivity is required for finer adjustments (e.g. small animal interventions), or the guide apparatus is supporting relatively large payloads (e.g. the addition of motors to automate the motion of the guide apparatus under the control of a computer). Additional linkage elements (FIG. **3**) may also be useful for supporting a number of different medical tools of varying sizes and weights. The closed-loop spherical chain is more capable of supporting unbalanced loads from the additional support provided by the additional linkage illustrated in (**3***b*) and (**3***c*). As can be seen in FIG. **3***a-c*, the tool holder can be constructed as two separate portions that are independently linked to the link arms. The ring portions may be free of each other and may be aligned by a shaft passing through the rings. The ring portions may also be rotatably coupled to each other.

[0037] When the guide apparatus is manipulated manually, the closed kinematics frame will follow the user's hand movements with minimal resistance. Accordingly, any number of different paths of motion may be achieved by the guide apparatus. Two paths of motion that are intuitive to most user's are illustrated in FIGS. (**4***a*) and (**4***b*). As illustrated in FIG. (**4***a*), the apparatus can revolve about the base alignment axis of a hinged coupling between the first end of the crank and the base or stabilizer. This rotation becomes more apparent as the angle between the medical tool axis and the base alignment axis increases. There is also a natural tendency for many user's to change the angle between the medical tool axis and the base alignment axis as this produces a side-to-side motion of the medical tool about the remote fulcrum point of the guide apparatus. As shown in FIG. **4***b*, as each of the cranks rotates away from one another, the opposing inertial forces, which are generated within the linkage, will direct the medical tool along a path which is perpendicular to the path of motion previously described for FIG. **4***a*. Therefore, the additional two linkage elements are useful as they reduce the effect of inertial influence in comparison to a corresponding open-loop chain design. User's are able to recreate the intuitive paths of motion shown in FIGS. **4***a* and **4***b* with reduced veer or drag due to inertial forces of a heavy medical tool.

[0038] Various configurations of linkage arms or hinged coupling are readily available to the skilled person. For example, the crank arm **2** and the link arm **4** may be of any size, or shape that allows for a configuration of the guide apparatus that produces a remote fulcrum **0**. The crank and the link may be of equal length, the crank may be longer than the link, or the crank may be shorter than the link. The crank and the link may be the same or different in terms of rigidity or flexibility. The crank and the link will typically be arcuate, and the crank and the link may be the same or different in terms of arcuate structure. The arcuate structure may have any suitable central angle for maintaining a remote fulcrum. For example, an arcuate crank or an arcuate link may each independently have a central angle of about 10, 20, 30, 40, 50, 60, 70, 80, 90, 100,120,130,140,150,160,170,180,190, or 200 degrees, or any suitable angle therebetween. Typically, the central angle will be less than 360, 330, 300, 270, 240, 210, 180,150,120, 90, 60, or 30 degrees, or less than any angle therebetween.

[0039] Hinged couplings do not need to be placed at the end of linkage elements. For example, the first end of the crank arm may extend beyond the first hinged coupling, As another example, the second end of the crank arm and/or the first end of the link arm may extend beyond the second hinged coupling. The link arm is coupled to the crank arm at a second hinged coupling sufficiently spaced from the first hinged coupling to achieve two positioning elements and such that their rotational axes can define a remote fulcrum.

[0040] Still further optional features will be apparent to the skilled person.

[0041] While the guide apparatus **1** shown in FIGS. **1** and **2** has so far been described in terms of structural features, a guide apparatus may also be described in terms of its axial components and planes defined by the axial components. The guide apparatus typically comprises a primary (or base) alignment axis (i=**1**); a secondary alignment axis (i=**2**) that intersects the base alignment axis at a remote fulcrum point **0** and at a fixed angle to the base alignment axis, defining a first plane that represents a first positioning element; a tertiary alignment axis (i=**3**) which intersects the base and secondary alignment axes forming a fixed angle between the secondary and tertiary axes, and defining a second plane that represents a second positioning element; and, the first, and second positioning elements are separately adjustable in order to provide a pre-determined and/or angular relationship between the base and tertiary alignment axes. The first, and second positioning elements are separately adjustable to allow for 3D orientation of the tertiary alignment axis through the remote fulcrum.

[0042] As seen in FIGS. **1** and **2**, the crank **2** of the guide apparatus is parallel to the first plane defined by the intersection of a base alignment axis (i=**1**) and a secondary alignment axis (i=**2**), while the link **4** is parallel to the second plane defined by the intersection a secondary alignment axis (i=2) and a tertiary alignment axis (i=3).

[0043] The first and/or second positioning elements may be manually, automatically or both manually and automatically adjustable. The first and second positioning elements provide for adjustment of the distance between the primary alignment axis (i=1) and the tertiary alignment axis (i=3) by adjusting the polar position of the first and second positioning elements. As seen in FIGS. **1** and **2**, adjustment of the angular displacement between the primary and tertiary alignment axis may comprise a link arm having a first end **22** hingedly coupled to a second end **14** of a crank arm where its first end **12** may be hingedly coupled to a grounded fixture or stabilizer **70** shown in FIG. **2**. The second end **24** of the link arm may comprise a cylindrical joint to which medical tool(s) **40** may be coupled. Typically, the base, secondary and tertiary axes of the revolute hinged couplings and cylindrical joints of the crank and link converge to a remote fulcrum point **0**, thereby forming an open-loop spherical chain.

Kinematics Equations of Motion

[0044] The guide apparatus may be considered as a coordinated spherical linkage assembly, which comprises two hinged couplings and three linkage elements. The axis of each hinged coupling converges to a common point to produce a remote fulcrum. The linkage assembly is a compound spherical joint with two degrees of freedom (DOF), as defined by the Kutzbach criterion:

$$DoF(n,\ j) = l(n-1) + \sum_{i=1}^{j} (p_i - 1)(f_i - 1) \qquad [1]$$

where:

[0045] 'n' represents the total number of connected elements and 'j' is total number of lower pair joints in the mechanism. For a single joint, 'i', the relative mobility of the joint and the number of elements connected to it are given by 'f_i' and 'p_i', respectively. The mobility of each linkage element relative to each other is quantified by 'I'.

[0046] Equation 1 is useful for analyzing a complex linkage to quantify its mobility and/or to determine the degrees of freedom provided by the linkage.

[0047] The first hinged coupling defines the reference axis of the coordinate system and is fixed to the multi-jointed stabilizer that may be attached to an exam room bed (or fixture). Because each linkage element is constrained to pivot about a common point (ie., the remote fulcrum), the mobility of one linkage element, I, is constrained to three degrees of rotation. The angular size and length of each element in the linkage assembly defines the size and shape of the operating envelope of the kinematics frame.

[0048] The spherical linkage assembly supports a medical tool and its associated supporting elements through a tool holder so that the longitudinal axis of the medical tool is collinear with the tertiary alignment axis (i=3). The angular position of the axis of the medical tool, relative to the base alignment axis, is determined by measuring the angle between the base and secondary alignment axes. As shown in FIG. **1**, shaft **32** with a sleeve may be coupled to a cylindrical joint provided by the tool holder, with the sleeve adapted to receive the medical tool **40**. The cylindrical joint allows the shaft, sleeve and medical tool, to pivot and slide freely along the axis of the tertiary alignment axis, providing an additional two DOF as the probe penetration and relative rotational angle to the supporting frame are defined.

[0049] The following equations represent the forward kinematics equations of motion for the open-loop linkage:

$$\tan\frac{1}{2}(\theta + c) = \cos\frac{1}{2}\left(\psi - \frac{\pi}{2}\right)\sec\frac{1}{2}\left(\psi + \frac{\pi}{2}\right)\cot\frac{1}{2}\zeta \qquad [2]$$

$$\tan\frac{1}{2}(\theta - c) = \sin\frac{1}{2}\left(\psi - \frac{\pi}{2}\right)\csc\frac{1}{2}\left(\psi + \frac{\pi}{2}\right)\cot\frac{1}{2}\zeta \qquad [3]$$

$$\tan\frac{1}{2}\varphi = \tan\frac{1}{2}\left(\psi - \frac{\pi}{2}\right)\sin(\theta + c)\csc(\theta - c) \qquad [4]$$

$$\tan\frac{1}{2}\psi = \cos\xi \qquad [5]$$

$$\tan\frac{1}{2}(\gamma + \xi) = \cos\frac{1}{2}\left(\psi - \frac{\pi}{4}\right)\sec\frac{1}{2}\left(\psi + \frac{\pi}{4}\right)\cot\frac{1}{2}\xi \qquad [6]$$

$$\tan\frac{1}{2}(\gamma - \xi) = \sin\frac{1}{2}\left(\psi - \frac{\pi}{4}\right)\csc\frac{1}{2}\left(\psi + \frac{\pi}{4}\right)\cot\frac{1}{2}\xi; \qquad [7]$$

or Equation 2 to 5 and

[0050]

$$\cot\frac{1}{2}\xi = 1/\sqrt{2}\tan\gamma. \qquad [7a]$$

[0051] Equations 2, 3 and 4 were derived by applying the Napier analogies to spherical triangle APC (FIG. **5**), and Equation 5 was determined by solving the right spherical triangle ABE. Applying the Napier analogies to spherical triangle ABC, gives Equations 6 and 7. Equation 7a is derived by solving the right spherical triangle ABE.

[0052] Equations 2-7 are useful to calculate the orientation of the medical tool in 3D space relative to the remote fulcrum based on encoder positions in the open-loop chain design. Alternatively, replacing Equation 6 and 7 with 7a, Equations 2-5 and 7a are useful to calculate the orientation of the medical tool in 3D space relative to the remote fulcrum based on encoder positions in the open-loop chain design. For, corresponding calculations for the closed-loop chain design can be performed using Equations 2 to 5.

[0053] The position vector, r defining the 3D position of the medical tool relative to its fulcrum is defined as:

$$\vec{r} = \begin{bmatrix} x \\ y \\ z \end{bmatrix} = \begin{bmatrix} r\cos\theta\sin\varphi \\ r\sin\theta\sin\varphi \\ r\cos\varphi \end{bmatrix}. \qquad [8]$$

(see Figure 5)

[0054] Equation 8 is useful for coordinate transformation from a spherical coordinate system (which references angles as with Equations 2-5 or Equations 2-7 or Equations 2-5 and 7a) into a Cartesian coordinate system (x,y,z) with the origin being a remote fulcrum **0**.

[0055] The encoders **60**, **62** mounted to the hinged couplings (FIG. **2**, i=**1**, **2**) are used to measure the angles (ξ+ζ) and γ, respectively.

[0056] In order to uniquely define the orientations of the medical tool about the remote fulcrum, as defined by the vector r (FIG. **5**), information about any two of the three possible angles (gamma (angle ABC), xi (angle CAB), and zeta (angle PAC) designated as γ, ξ, and ζ, respectively) measured by the encoders at the hinged couplings is needed to solve the forward kinematics equations.

[0057] In one example, the position of each arm (AB and BC in FIG. **5**) in the linkage is determined by measuring the spherical angles at each of the hinged couplings A and B, respectively. The encoder mounted at 'A' would measure the angle (ξ+ζ), and the encoder mounted at the second hinged coupling 'B' would be used to measure the angle between the two arms (γ). Equation 6 and 7 or Equation 7a can be used to decouple the values for (ξ) and (ζ), required to solve the Equations 2-5.

[0058] In an alternate example, where an additional two arms are incorporated to produce a closed-loop chain design (FIG. **3**), the encoder mounted at point B, can also be mounted at points D or A. If the second encoder were mounted at coupling 'D', the analysis described in the previous paragraph would be used since the encoder provides the same information. However, if both of the encoders were mounted at point 'A', each encoder would be used to measure the angle of rotation of link AD and AB about the x-axis (FIG. **5**). The encoder mounted on arm AD would measure (ζ−ξ), and the encoder mounted on arm AB would measure (ξ+ζ). This would provide enough information to solve Equations 2-5 without the need for Equations 6 and 7 or Equation 7a. Since the encoders can be mounted in different configurations, Equations 2-5 can be used to optimize the encoder placement for a particular application. This is because the encoder sensitivity to movement is different for each of the cases described above.

[0059] Degrees of freedom of the guide apparatus may be provided by hinged coupling of linkage elements. Additional degrees of freedom may be provided depending on the medical tool and its associated hardware and actuator. For example, FIG. **1** shows a medical tool **40** and a shaft **32** for actuating the medical tool, with the medical tool axis and the shaft axis being collinear with the tertiary alignment axis (i=**3**). The shaft may be used to actuate longitudinal and/or rotational or angular motion of medical tool **40** relative to the tertiary alignment axis; longitudinal or linear motion along the axis provides one degree of freedom, while rotational or angular motion about the axis provides another degree of freedom. The shaft may be equipped with a lockable collar to prevent linear motion of a medical tool during a procedure. The shaft **32** passes through a cylindrical joint provided by tool holder **6** and is coupled to a differential gear train **30** that is housed within tool holder **6**. The differential gear train may be used to decouple degrees of freedom, for example linear and angular motion about an axis. Furthermore, the differential gear train may be equipped with or coupled to encoders to measure each decoupled degree of freedom.

[0060] As illustrated in FIG. **1**, a differential gear mechanism **30** housed within tool holder **6**, mechanically decouples two degrees-of-freedom provided by the shaft and its coupling to the tool holder. These degree of freedoms represent the linear and the angular orientations, respectively of the shaft **32** and its associated medical tool about a longitudinal axis.

[0061] Referring to FIG. **6**, an example of a differential gear train is illustrated. The differential gear train comprises of three basic components:

[0062] Base Drum (**121**)

[0063] Planetary Gear Train (**123** and **126**)

[0064] Outer Ring (**122**).

[0065] Referring to FIGS. **6** and **7**, the angular and linear displacement of a medical tool about the tertiary alignment axis is measured using two rotary (rotational) encoders (FIG. **7**: **232**, **233**), by measuring the angular displacement of the base drum (FIG. **6**:**121**) and outer (**122**) rings respectively. Three miter gears **123**, whose axis are perpendicular to the tertiary alignment axis, are connected to the shaft **32** by a friction wheel **125**. In an alternate embodiment, a spur gear meshing with a rack embedded within a splined shaft would be used in place of the friction wheel **125**. Meshing with the inner gears **123**, are a set of three matching miter gears **126** pivotally attached to the inner ring **121**, and axis of rotation parallel to the tertiary alignment axis, transfers the linear displacement of the shaft to a rotational movement that is aligned with the longitudinal axis of the shaft. The three miter gears **126** attached to the base drum **121**, engages with the inner diameter of the outer ring **122** by means of a friction wheel **127**. In an alternate embodiment, a spur gear meshing with an internal gear mounted to the inner ring would be used in place of the friction wheel **127**.

Rotational Motion of the Differential Gear Mechanism

[0066] The base drum, which has an outer diameter (D=1.75 inches), is mechanically coupled to the shaft **32** (see FIG. **7**) and to one of the two encoders having a friction-wheel (see **231** in FIG. **7**, which has a diameter, dencoder=1.0 inches). As shown in Equation 9, the ratio of the drum diameter, D, to the friction wheel diameter of the encoder, $d_{encoder}$, determines the error reduction ratio between the encoder and the positional accuracy of the medical tool ($\mu_{reduction}$).

$$\mu_{reduction} = \frac{D}{d_{encoder}} \qquad [9]$$

$$\mu_{reduction} = 1.8$$

[0067] As shown in Equation [10], the ratio of the encoder accuracy, $\delta_{encoder}$,(Renishaw 2006) to the error reduction ratio, Preduction, defines the accuracy of the rotational motion for the shaft **32** (δ_{shaft}).

$$\delta_{shaft} = \frac{\delta_{encoder}}{\mu_{reduction}} \qquad [10]$$

$$\delta_{shaft} = \pm 0.29^\circ$$

Linear Motion Using a Differential Gear Mechanism

[0068] The planetary gear train **123**, **126**, which comprises three pairs of miter gears, converts the longitudinal or linear movement of the shaft (i.e. penetration of the shaft along its axis into a subject's body) to a rotational motion of the outer ring (see **122** in FIG. **6**).

[0069] As the shaft **32** is displaced 1.0 inches along the longitudinal direction, the 1:1 ratio of the miter gears (Berg M72N-72-S) produces a displacement of 1.0 inches along the inner diameter of the outer ring (see Item **122** in FIG. **6**). As shown in Equation [11], this movement results in an angular displacement of the outer ring:

$$\Delta D_{angular} = \frac{1.0''}{\pi \cdot d} \cdot 360°, \qquad [11]$$

$$\text{where } d = 1.387 \text{ inches}$$

$$\Delta D_{angular} = 82.618°$$

[0070] Because the friction wheel of the encoder, (dencoder=1.0 inches), is coupled to the outside diameter of the outer ring (D=1.75), the accuracy of the encoder (Renishaw 2006) is minimized (see Equation [9]). Equation [9] is combined with the results of Equation [11] in order to obtain the encoder sensitivity for the penetration of the shaft and its associated medical tool, $\delta_{penetration}$:

$$\delta_{penetration} = \frac{\pm 0.5°}{\Delta D_{angular} \cdot \mu_{reduction}} \cdot 1.0'' \qquad [12]$$

[0071] As mentioned above, the guide apparatus may be equipped with optional components as desired to aid in the orientation or tracking of a medical tool, for example, without limitation, brakes for locking a hinged coupling, encoders for measuring rotational angles of a hinged coupling, counterweights and/or spring balances to offset the mass of the system, computer controlled actuators for automating rotation of a hinged coupling, or additional linkage arms. Further components that may be incorporated into the guide apparatus will be apparent to the skilled person, and suitable combinations of optional components will also be apparent depending on the particular medical tool and the particular use of the guide apparatus.

[0072] Particular examples of encoders, counterweights and braking mechanisms are now described.

[0073] Referring to FIG. **7**, to determine the spatial orientation of the tertiary alignment axis to the base alignment axis, two rotational encoders **60**, **62** mounted to a first end **12** of the crank **2**, and a first end **22** of the link **4** are used to measure the polar rotation of the crank arm relative to the base fixture, and the relative angles between the crank arm and the link arm. To measure the angle between the base fixture and the crank arm, a rotational encoder **60**, mounted to a first end **12** of the crank by fasteners **206** measures the relative angular orientation of the encoder magnet **207** fixed to the shaft **208**, which is in turn is rigidly mounted to a fixture or stabilizer. To measure the angle between the crank arm and the link arm, an angular encoder **62** mounted to a first end **22** of the link by fasteners **209** measures the relative angular orientation of the encoder magnet **210** fixed to the shaft **211**, which is in turn is rigidly mounted to the second end **14** of the crank by pin **212**.

[0074] Referring to FIG. **1**, to dynamically balance the guide apparatus, counterweights may be affixed to the crank arm and/or the link arm. The counter weight **52** mounted to the first end **22** of the link is in place to offset the mass of a medical tool and associated hardware supporting it; while counterweight **50** mounted to the first end **12** of the crank is in place to offset the mass of the crank arm, counterweight **52**, and the link arm. In an alternate embodiment, the counterweights may be replaced or used in conjunction with a spring balance to offset the mass of the system.

[0075] Referring to FIG. **7**, a first end **12** of the crank arm comprises a spring clutch to prevent movement of the crank about the attached base fixture or stabilizer. The spring clutch comprised of two brake pads (**214** and **215**) in which at least one of the brake pads is affixed to the first end **12** of the crank, and at least one torsion spring **213** is wrapped around the pair of brake pads. When the torsion spring is in its relaxed state, the inner diameter of the spring must be smaller than the outer diameter of the brake pads. When the torsion spring(s) are mounted onto the brake pads, the force of the spring causes the pads to collapse onto the shaft, which in turn is rigidly fixed to the stabilizer or fixture. The frictional force generated by this clamping action prevents the crank arm from rotating about the primary alignment axis.

[0076] Referring again to FIG. **7**, the second positioning element **250** includes a spring clutch integrated into a first end **22** of the link arm to prevent movement of the link arm about the secondary alignment axis. The spring clutch comprised of two brake pads (**216** and **217**) in which at least one of the brake pads is affixed to the first end **22** of the link arm, and at least one torsion spring **218** wrapped around the pair of brake pads. When the torsion spring is in its relaxed state, the inner diameter of the spring must be smaller than the outer diameter of the brake pads. When the torsion spring(s) are mounted onto the brake pads, the force of the spring causes the pads to collapse onto the shaft, which in turn is pinned to the first positioning means. The frictional force generated by this clamping action prevents the link arm from rotating about the secondary alignment axis.

[0077] As will be recognized by the skilled person, the guide apparatus may be used for different medical applications using a variety of medical tools. In one particular example, a guide apparatus may be used as a 3D mechanically tracked transrectal ultrasound (TRUS) prostate biopsy system.

[0078] Definitive diagnoses of prostate cancer are typically determined from the histological assessments of tissue samples drawn from the prostate during biopsy procedures. Most biopsies are performed by a physician using a transrectal ultrasound probe (FIG. **8***a, b*) which uses a needle guide attached to the probe in order to constrain an 18 gauge needle so that it is always visible in the 2D US image (FIG. **8***c*). Each biopsy core is identified separately as to its location. As a result, so the pathologists can report the extent and the grade of the cancer. Depending on the pathological results of a biopsy procedure, urologists must either avoid the previously targeted biopsy sites or target those locations directly. Therefore, it is important to know exactly where the initial sample was taken in order to target more relevant tissue if the pathologist requests a repeat biopsy.

[0079] Currently, physicians are limited to using 2D transrectal ultrasound for guiding a biopsy needle into the prostate. Since 2D ultrasound images do not provide any spatial information about the location of the biopsy sample, it is difficult for physicians to plan repeat biopsy procedures.

[0080] A guide apparatus forms part of an effective mechanical 3D biopsy system that addresses the limitations of current 2D biopsy procedures, and minimizes the cost and retraining the physician must acquire. The biopsy system consists of a 4 degree-of-freedom guide aparatus comprising an adaptable cradle that supports a commercially available trans-rectal ultrasound transducer. Using this apparatus, physicians can maneuver an ultrasound transducer while a tracking system records the 3D position and orientation of the biopsy needle in real-time.

[0081] This approach involves the use of a device composed of two mechanisms (FIGS. **1**, **2**):

- **[0082]** a. an articulated multi-jointed stabilizer (FIG. **2**), and
- **[0083]** b. the guide apparatus shown in FIG. **1** having a TRUS transducer **46**, a needle guide **42**, and biopsy needle **44**.

[0084] The end-firing TRUS transducer (with the biopsy needle guide in place (**42**, FIG. **1**) is mounted to the guide apparatus in a manner where the TRUS transducer is actuated by shaft **32** for rotational and linear movement along the longitudinal axis of the TRUS transducer. This will allow the physician to insert the TRUS transducer through the restricted opening of the patient's rectum and to rotate it in order to acquire a 3D image of the prostate. In certain examples, the multi-jointed stabilizer does not contain angle sensing encoders. However, the guide apparatus comprises angle sensing encoders mounted to each joint in order to measure the angle between the arms as well as the rotational and longitudinal motion of the shaft **32** and its associated medical tool **40**, in this case the TRUS transducer **46**, a needle guide **42**, and biopsy needle **44**. Information from the encoders is transmitted to a computer for further processing. This arrangement will allow the computer to determine not only the relative position of the transducer but also the needle relative to remote fulcrum **0**.

[0085] In use, the TRUS transducer is mounted into the guide apparatus such that the tip of the probe is initially set to the remote fulcrum point of the guide apparatus. The multi-jointed stabilizer is unlocked and the physician manipulates the transducer (the fulcrum of the guide apparatus), to the patients rectal sphincter. The stabilizer mechanism is then locked and the probe is inserted into the patient's rectum. The physician (or a motor) rotates the probe about its longitudinal axis to acquire a 3D TRUS image of the prostate. The prostate is then segmented using a manual semi-automated segmentation algorithm. An example of prostate segmentation is shown in FIG. **9**. Further information (e.g, functional, anatomical or probability image), if available, is registered to the 3D TRUS image and displayed as an overlay on the computer screen (FIG. **9**). After the target in the 3D TRUS image is chosen using the US image as a guide, one or more linkage elements of the guide apparatus are then unlocked using a separate braking system then the one used to lock the stabilizer. The transducer is then free to allow the physician to move it to a new location while the TRUS probe and needle position is tracked by the encoders and associated software. At the same time, the needle trajectory is continuously displayed as a graphic overlay in the 3D TRUS image. When the needle path intersects the chosen target, the linkage elements of the guide apparatus are locked in place and a biopsy is performed in real time using 2D US guidance. The biopsy location is then recorded in 3D from the tracker orientation, and the system is ready for the next biopsy. After the needle is withdrawn, a 3D image may be obtained to determine if there is any movement or swelling of the prostate.

[0086] Biopsies are typically performed with a thin, 18-guage needle mounted on a spring-loaded gun connected to the ultrasound ("US") probe, forcing the needle to stay in the imaging plane so that it is always visible in the US image. The location of each core is registered, so that the pathologist can report the extent and grade of the cancer. This is especially important if the histological result is equivocal and the pathologist requests a repeat biopsy. It is, therefore, important to know from what exact location the=sample was obtained in order to target more relevant tissue if a repeat biopsy is performed.

[0087] FIG. **8** shows a TRUS with an attached biopsy guide that holds a needle. The needle extends into the plane of the TRUS image so that it is continuously visible therein.

[0088] While the method of performing biopsy has been described with specificity to manual biopsy needle insertion using a template, other types of biopsy needle insertion methods will occur to those of skill in the art. For example, insertion and/or alignment of the biopsy needle can be performed in a number of manners. In one embodiment, a robotic assembly is used to control the alignment and insertion of the biopsy needle. In another embodiment, a computer is used to control the needle guide in order to control the alignment of the biopsy needle, but still permits manual control of its insertion. In still another embodiment, via a robot or can be computer-controlled.

[0089] In a further embodiment, an end-firing US transducer can be coupled to a magnetic tracking device that provides position information to the computer. In this manner, 2D images with position and orientation measurements are simultaneously acquired using a free-hand magnetically tracked approach and are then reconstructed into 3D TRUS images in real-time. A free-hand magnetically or optically tracked scanning approach is used to allow the user to manipulate the transducer freely, and record the position and orientation of the transducer in space. The magnetic tracking approach is based on a small 6 degree-of-freedom magnetic field sensor (receiver) mounted on the TRUS transducer, and a transmitter is placed near the patient to produces a spatially varying magnetic field. The small sensor measures the three components of the local magnetic field strength, and these are used to calculate the TRUS transducer's position and orientation, which are then used in the 3D reconstruction algorithm.

[0090] In still yet another embodiment, markers can be attached to the TRUS transducer and a camera tracks movement of the markers in order to determine the position and orientation of the TRUS transducer.

[0091] The above-described embodiments are intended to be examples and alterations and modifications may be effected thereto, by those of skill in the art, without departing from the scope of the invention which is defined by the claims appended hereto.

1. An apparatus for guiding a medical tool, comprising:

at least one crank arm comprising at least a portion of a first hinged coupling for hinged coupling to a stabilizer;

at least one link arm comprising at least a portion of a second hinged coupling for hinged coupling to the crank arm at a location spaced from the first hinged coupling;

a tool holder for supporting a medical tool on the link arm at a location spaced from the first hinged coupling;

wherein the rotational axes of the first and second hinged couplings intersect to define a remote fulcrum.

2. The guide apparatus of claim **1**, further comprising a brake for inhibiting rotational motion of the first hinged coupling.

3. The guide apparatus of claim **1**, further comprising a brake for inhibiting rotational motion of the second hinged coupling.

4. The guide apparatus of claim **1**, further comprising a first brake carried by the crank arm and actuable to inhibit rotational motion of the first hinged coupling; and

a second brake carried by the link arm and actuable to inhibit rotational motion of the second hinged coupling.

5. The guide apparatus of claim **1**, further comprising a rotational encoder for sensing rotational motion of the first hinged coupling.

6. The guide apparatus of claim **1**, further comprising a rotational encoder for sensing rotational motion of the second hinged coupling.

7. The guide apparatus of claim **1**, further comprising a first rotational encoder carried by the crank arm for sensing rotational motion of the first hinged coupling; and a second rotational encoder carried by the link arm for sensing rotational motion of the second hinged coupling.

8. The guide apparatus of claim **1**, further comprising a motor for controlling rotational motion of the first hinged coupling.

9. The guide apparatus of claim **1**, further comprising a motor for controlling rotational motion of the second hinged coupling.

10. The guide apparatus of claim **1**, further comprising a first motor carried by the crank arm actuable to control rotational motion of the first hinged coupling; and a second motor carried by the link arm actuable to control rotational motion of the second hinged coupling.

11. The guide apparatus of claim **1**, further comprising a counterweight or a spring balance for offsetting mass of the crank arm and the link arm.

12. The guide apparatus of claim **1**, further comprising a counterweight or a spring balance carried by the link arm adjacent to the second hinged coupling.

13. The guide apparatus of claim **1**, further comprising a counterweight or a spring balance carried by the crank arm adjacent to the first hinged coupling; and a counterweight or a spring balance carried by the link arm adjacent to the second hinged coupling.

14. The guide apparatus of claim **1**, wherein the tool holder axis passes through the remote fulcrum thereby forming an open-loop spherical chain.

15. The guide apparatus of claim **1**, further comprising a shaft, for actuating a medical tool, coupled to a cylindrical joint of the tool holder.

16. The guide apparatus of claim **15**, wherein the shaft axis passes through the remote fulcrum thereby forming an open-loop spherical chain.

17. The guide apparatus of claim **1**, further comprising:

a second crank arm coupled to the first hinged coupling; and

a second link arm coupled to the tool holder; and

a third hinged coupling for hinged coupling of the second crank arm and the second link arm at a location spaced from the first hinged coupling and the tool holder.

18. The guide apparatus of claim **17**, wherein the tool holder comprises two rings each independently coupled to the link arms.

19. The guide apparatus of claim **1**, further comprising a medical tool.

20. The guide apparatus of claim **19**, further comprising a counterweight for offsetting the mass of the medical tool.

21. The guide apparatus of claim **19**, wherein the axis of the medical tool passes through the remote fulcrum.

22. The guide apparatus of claim **19**, wherein the medical tool is an ultrasound transducer.

23. The guide apparatus of claim **1**, further comprising a shaft, for actuating a medical tool, coupled to a cylindrical joint of the tool holder and coupled to a differential gear train housed within the tool holder.

24. The guide apparatus of claim **23**, further comprising first and second rotational encoders housed within the tool holder, for measuring angular displacement of a base drum and outer ring, respectively, of the differential gear train.

25. The guide apparatus of claim **1**, wherein the crank arm and the link arm are each of an arcuate shape having a central angle of less than 90 degrees.

26. The guide apparatus of claim **1**, further comprising:

a second crank arm coupled to the first hinged coupling; and

a link arm assembly acting between each crank arm and the tool holder, each link arm assembly comprising at least two hingedly coupled link arms.

* * * * *

Appendix B (Patent application): Counterbalance Assembly

US 20100319164A1

(19) **United States**
(12) **Patent Application Publication**
Bax et al.

(10) **Pub. No.: US 2010/0319164 A1**
(43) **Pub. Date: Dec. 23, 2010**

(54) **COUNTERBALANCE ASSEMBLY**

(76) Inventors: **Jeffrey Bax**, London (CA); **Aaron Fenster**, London (CA)

Correspondence Address:

(21) Appl. No.: **12/680,102**

(22) PCT Filed: **Sep. 26, 2008**

(86) PCT No.: **PCT/CA2008/001716**

§ 371 (c)(1),
(2), (4) Date: **Aug. 20, 2010**

Related U.S. Application Data

(60) Provisional application No. 60/975,514, filed on Sep. 26, 2007.

Publication Classification

(51) **Int. Cl.**

F16F 15/28	(2006.01)
B25J 18/00	(2006.01)
B25J 19/00	(2006.01)
B66C 23/72	(2006.01)

(52) **U.S. Cl.** **16/401**; 901/48

(57) **ABSTRACT**

There is provided a mechanical arm assembly comprising: an arm rotatable about a pivot, a first force generating device for maintaining the arm at a datum, a second force generating device for compensating for the first generating device to maintain the arm in positions other than the datum.

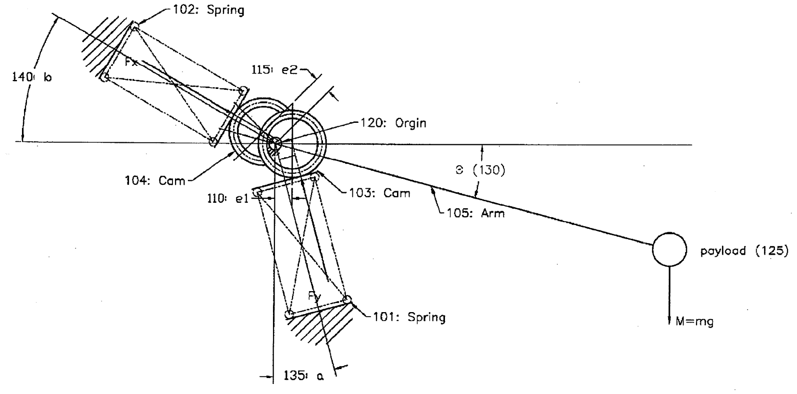

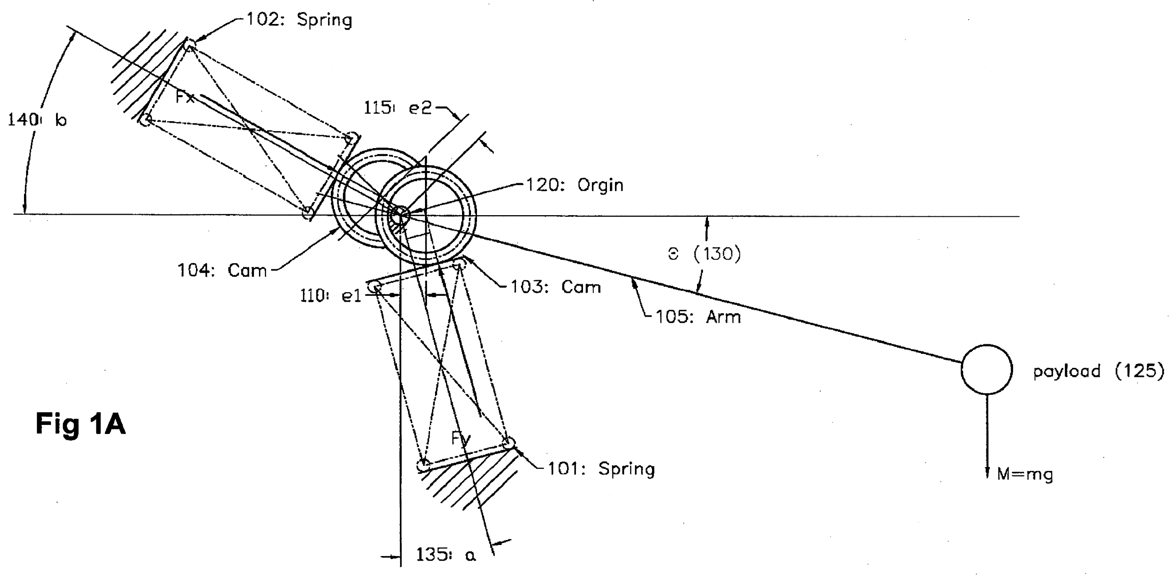
102: Spring
140: b
115: e2
120: Orgin
Fx
104: Cam
110: e1
103: Cam
Θ (130)
105: Arm
payload (125)
M=mg
Fy
101: Spring
135: a

Fig 1A

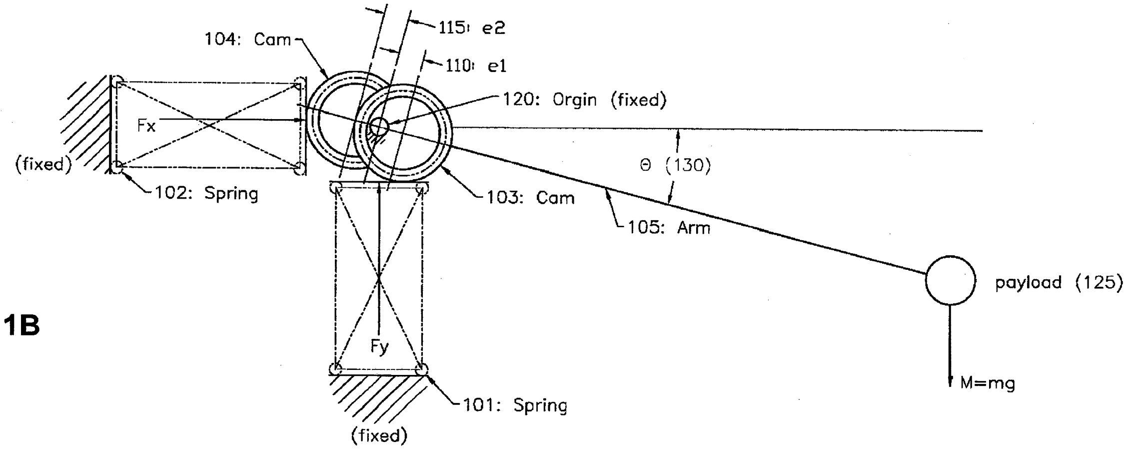
104: Cam
115: e2
110: e1
120: Orgin (fixed)
Fx
(fixed)
102: Spring
Θ (130)
103: Cam
105: Arm
payload (125)
Fy
M=mg
101: Spring
(fixed)

Fig 1B

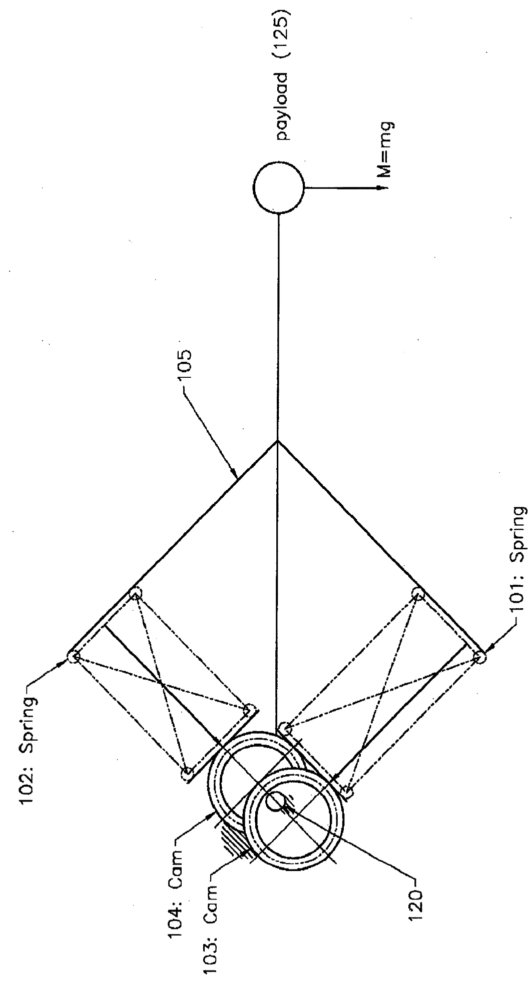

Fig 1C

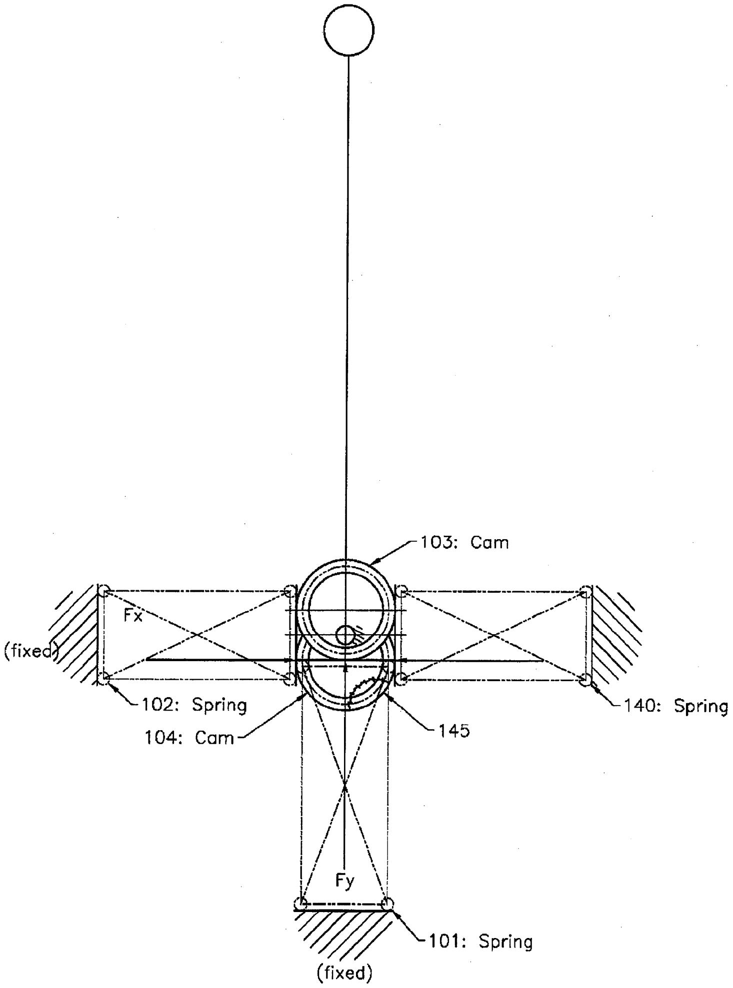
103: Cam
Fx
(fixed)
102: Spring
104: Cam
145
140: Spring
Fy
101: Spring
(fixed)

Fig 1D

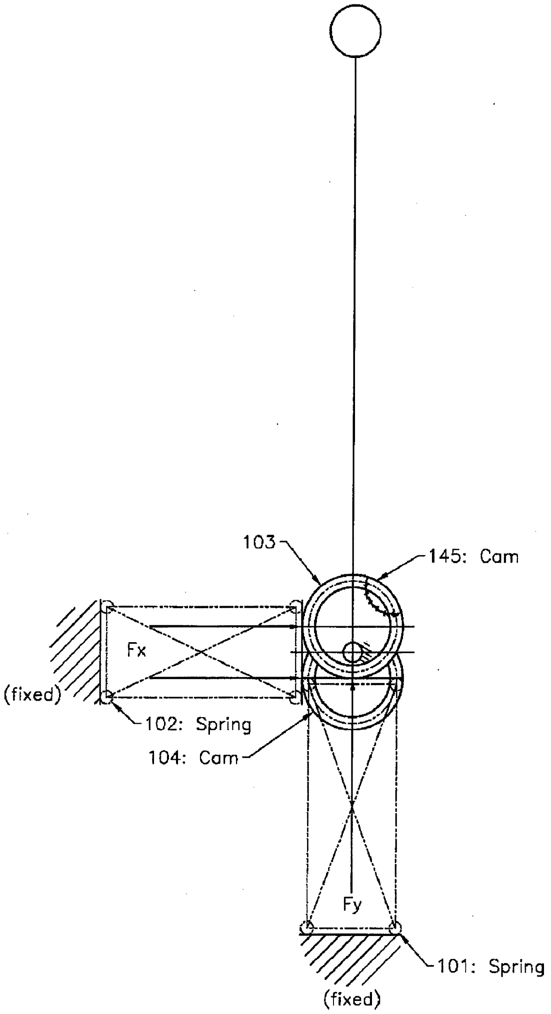

Fig 1E

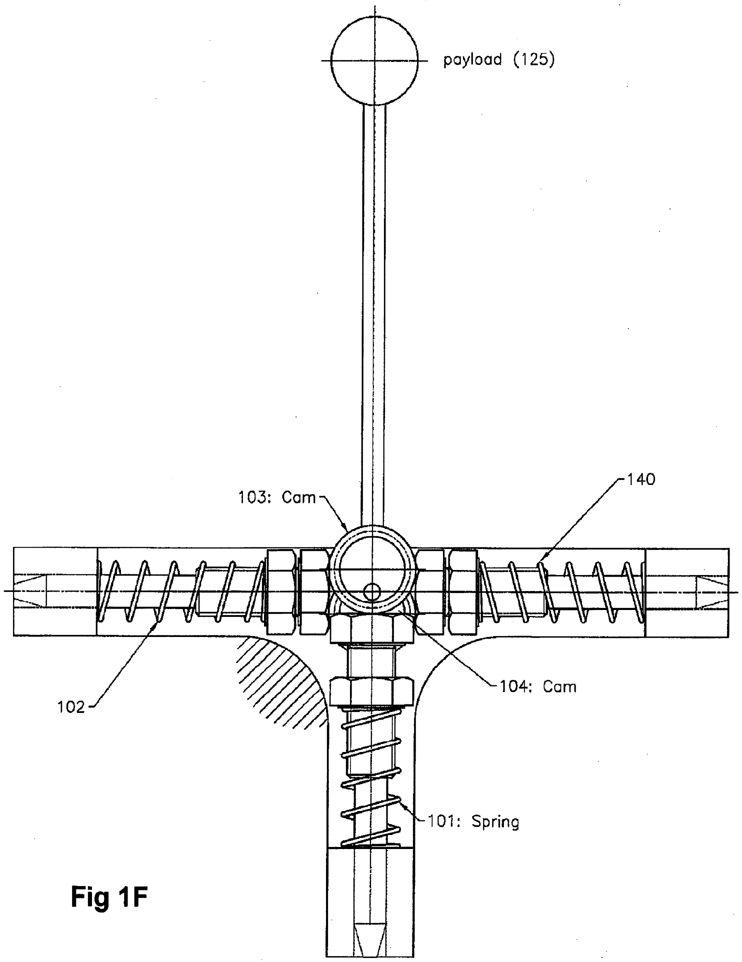

Fig 1F

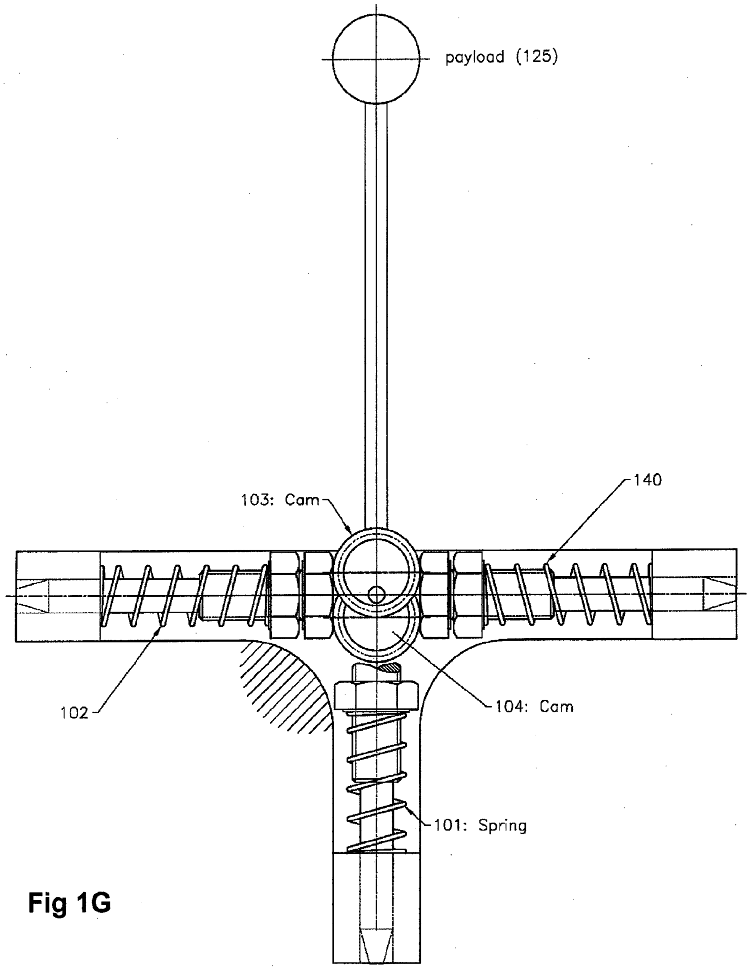

Fig 1G

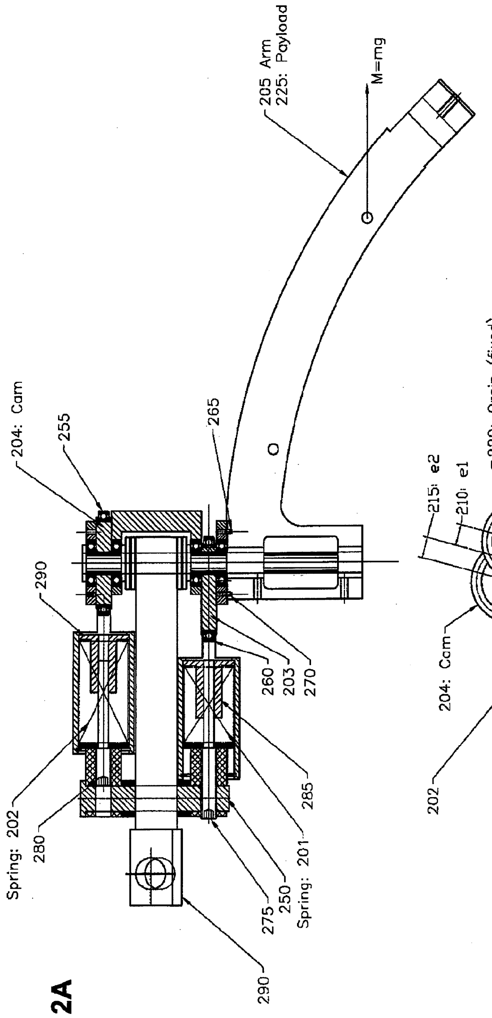
205 Arm
225: Payload
M=mg
O
204: Cam
255
265
290
260
203
270
285
Spring: 202
280
275
250
Spring: 201
290

Fig 2A

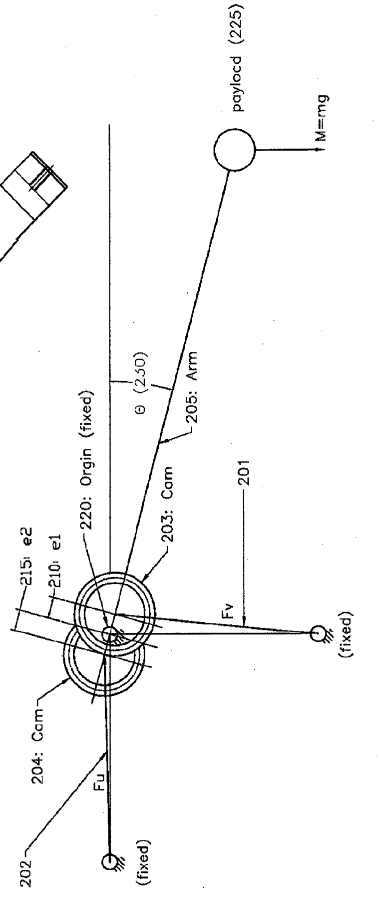
payload (225)
M=mg
Θ (230)
205: Arm
220: Orgin (fixed)
203: Cam
201
215: e2
210: e1
Fv
(fixed)
204: Cam
Fu
202
(fixed)

Fig 2B

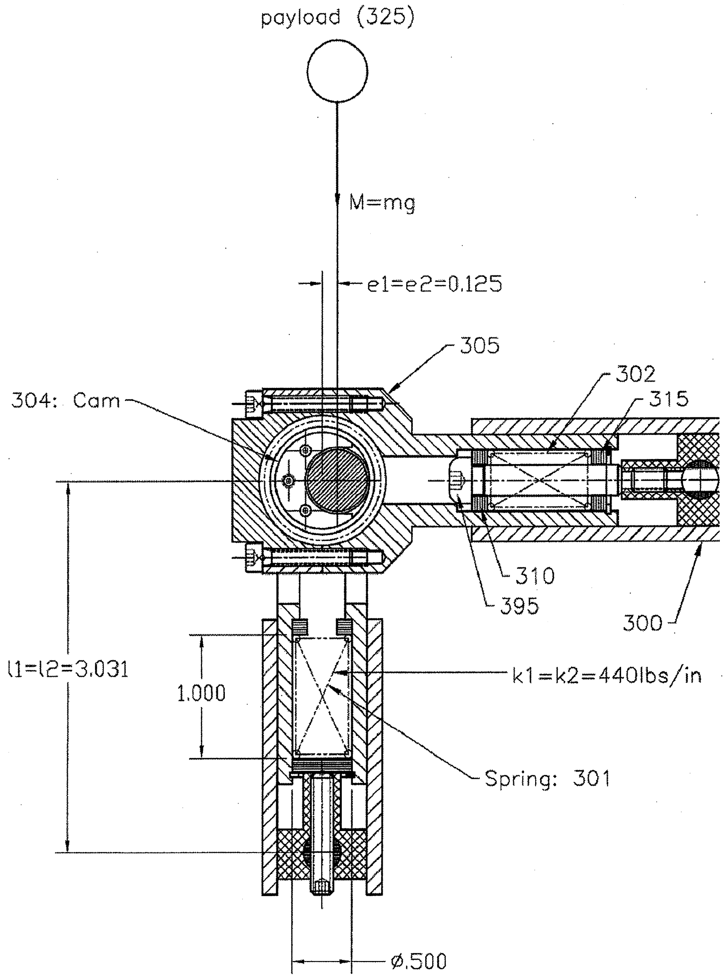
payload (325)
M=mg
e1=e2=0.125
305
302
315
304: Cam
310
395
300
l1=l2=3.031
1.000
k1=k2=440lbs/in
Spring: 301
ø.500

Fig 3

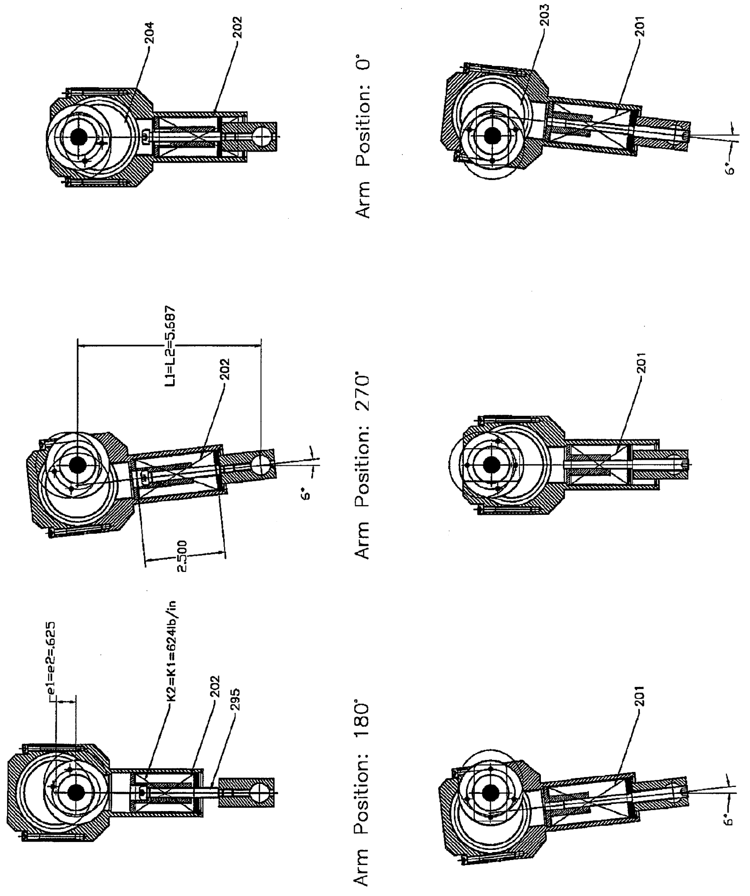
e1=e2=.625
K2=K1=624lb/in
202
295
Arm Position: 180°
201
6°
L1=L2=5.587
202
2.500
6°
Arm Position: 270°
201
204
202
Arm Position: 0°
203
201
6°

Fig 4

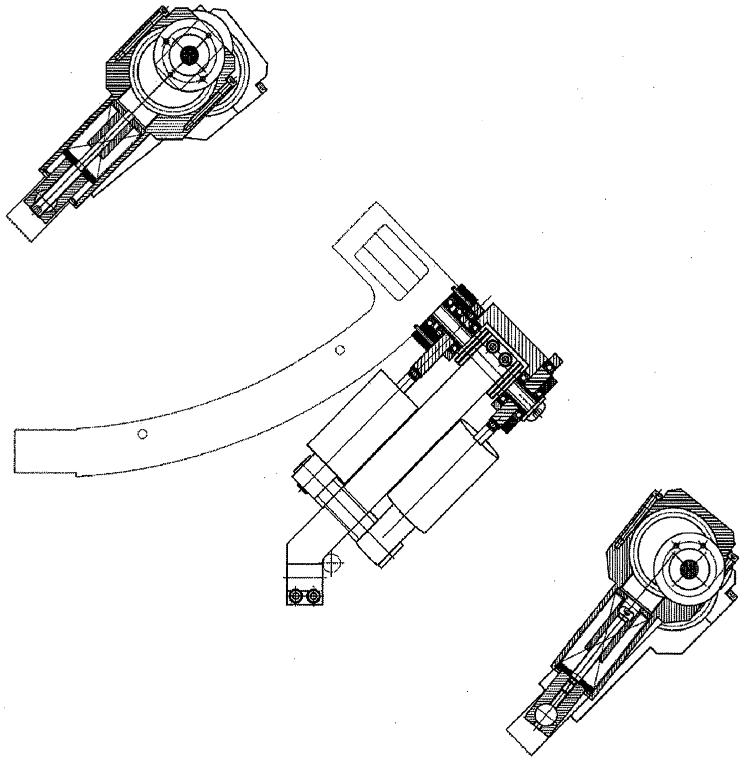

Fig 5

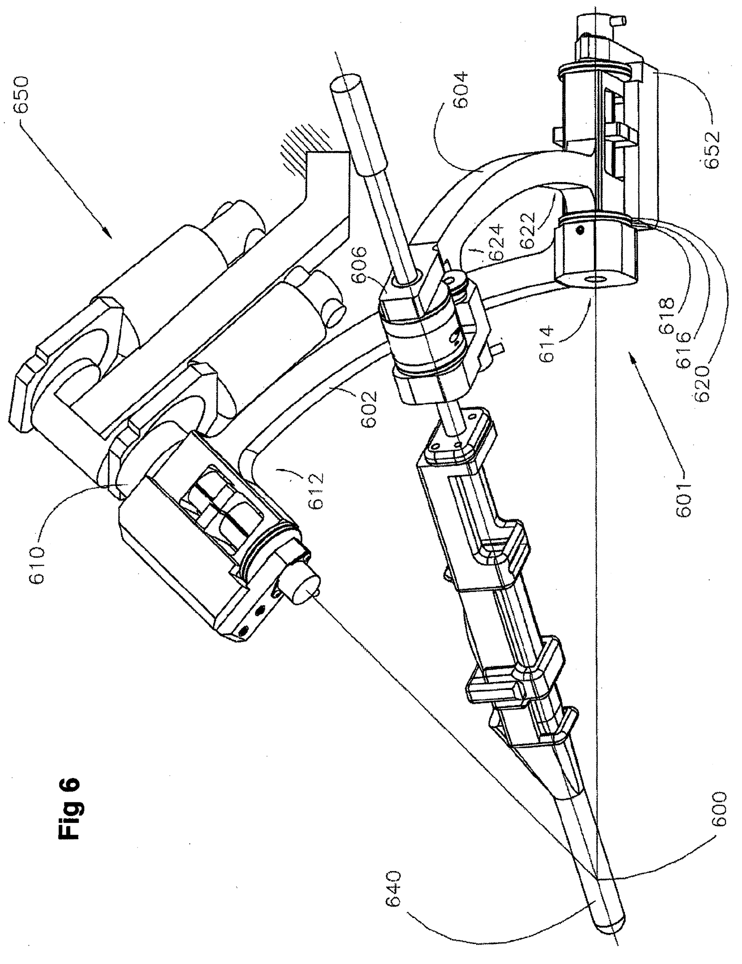

Fig 6

COUNTERBALANCE ASSEMBLY

FIELD OF THE INVENTION

[0001] The present invention relates generally to counterbalances and, more particularly, to a counterbalance for a joint of a mechanical arm.

BACKGROUND OF THE INVENTION

[0002] Apparatus comprising a mechanical arm that can hold and guide a payload have been shown to be of valuable assistance in various industrial procedures or medical procedures, for example, manipulation of tools, manipulation of cameras or sensors, etc.

[0003] These apparatus typically have one or more degrees of freedom and may be manually driven in that the one or more degrees of freedom may be equipped with a brake with motive force being provided by a human user, or may be automated in that at least one degree of freedom is driven by a computer controlled actuator.

[0004] A balancing mechanism may be used to counteract the force of gravity for hinged and/or articulated arm. Elimination or reduction of the effects of gravity allow the use of smaller power sources, gears and/or less effort exerted by a manual user. This is desirable from a cost standpoint and allows for a more compact design which, in turn, allows greater accessibility to the workspace.

[0005] Several counterbalancing mechanisms have been previously disclosed, for example, U.S. Pat. No. 4,756,204, U.S. Pat. No. 4,546,233, or U.S. Pat. No. 4,500,251.

[0006] Balancing mechanisms used on articulated arms and hinge mechanisms include counterweights. However, the use of counterweights can result in added mass and increase in arm inertia.

[0007] A tension spring or passive pneumatic balancer may be used for balancing within a small angle or within a single quadrant (i.e. from a horizontal to vertically upward orientation). However, conventional tension springs typically do not adequately balance the gravitational load. Also, it is inherent in most spring balancing methods that complete balance is possible only for one or two configurations of the arm and spring combination. As the robot arm moves away from that configuration in either of two possible directions, an unbalance is generated. Thus, a danger of this mechanism may be drifting or falling under the force of gravity when actuation is removed or reduced. Therefore, such mechanisms are usually provided with brakes to alleviate the potential danger, or are overbalanced against gravity.

[0008] Compression springs operating on small moment arms may overcome an angular limitation problem and offer better balance over the entire range of travel of the robot's arm. However, the problem of drift or falling under gravity also exists with compression springs.

[0009] It is an object of an aspect of the present invention to provide a counterbalance assembly for a joint of a mechanical arm.

SUMMARY OF THE INVENTION

[0010] In an aspect, there is provided a counterbalance assembly for a joint of a mechanical arm comprising:

[0011] a first force generating device;

[0012] a second force generating device;

[0013] the first and second force generating devices interacting with at least first and second cams, respectively;

[0014] the first and second cams fixed eccentrically relative to the pivot of a joint;

[0015] and the relationship of the first spring to the second spring and the first cam to the second cam being preserved throughout rotation of the joint.

[0016] In another aspect, there is provided a mechanical arm assembly comprising:

[0017] an arm rotatable about a pivot,

[0018] a first force generating device for maintaining the arm at a datum,

[0019] a second force generating device for compensating for the first generating device to maintain the arm in positions other than the datum.

BRIEF DESCRIPTION OF THE DRAWINGS

[0020] Embodiments will now be described, by way of example only, with reference to the attached Figures, wherein:

[0021] FIG. **1***a* illustrates a dual spring counterbalance assembly at a joint of a mechanical arm using springs that are fixed to a ground and cams set eccentrically relative to the pivot of the joint;

[0022] FIG. **1***b* illustrates a variant of the counterbalance assembly shown in FIG. **1***a* with a different orientation of springs and cams;

[0023] FIG. **1***c* illustrates a dual spring counterbalance assembly having springs attached to the payload arm;

[0024] FIG. **1***d* illustrates a triple spring counterbalance assembly with an additional spring and an additional cam being added to the counterbalance assembly shown in FIG. **1***b;*

[0025] FIG. **1***e* illustrates a simplified variant of the counterbalance assembly shown in FIG. **1***d* with removal of a spring resulting in two springs interacting with three cams;

[0026] FIG. **1***f* illustrates a mechanical arm of the counterbalance assembly shown in FIG. **1***d*; spring/cam relationship in a spring balance mechanism for a mechanical arm;

[0027] FIG. **1***g* is the same as FIG. **1***f* except that the bolt head extension of a spring is cut away to more clearly show two cams;

[0028] FIG. **2***a* illustrates a cross-sectional view of a dual spring counterbalance assembly showing springs coupled to cams set eccentrically relative to a pivot of a joint;

[0029] FIG. **2***b* is a schematic diagram illustrating the geometric relationship between each spring-cam assembly shown in FIG. **2***a;*

[0030] FIG. **3** illustrates a cross-sectional view of a mechanical arm comprising a variant of the spring balance mechanism shown in FIG. **2**;

[0031] FIG. **4** illustrates the phase relationship between springs and cams in various configurations of mechanical arm rotation;

[0032] FIG. **5** illustrates a variant to the design presented in FIG. **3**; and

[0033] FIG. **6** illustrates an example of a medical guide apparatus that can comprise the spring balance mechanism shown in FIG. **1**.

DETAILED DESCRIPTION

[0034] FIGS. **1***a* to **1***e* are schematic illustrations of spring counterbalance assemblies which show the geometric relationship of spring and cams. Referring to FIG. **1***a* and **1***b*, the spring counterbalance assembly comprises two compression springs (**101**, **102**), each of which are fixed at the base (or grounded fixture) and the other end(s) are connected to eccentric circular cams (**103**, **104**) by a yoke (not shown), such that each cam is free to rotate about the fulcrum or pivot (**120**) of a joint, and the springs are free to compress (or stretch). The springs may be adjustable. Cam **103** is eccentrically set relative to the pivot (**120**) of a joint by a distance equal to **e1** (**110**), and cam **104** is eccentrically set relative to the pivot (**120**) of the joint by a distance of **e2** (**115**).

[0035] Spring (**101**) interacts only with cam (**103**), and spring (**102**) interacts with cam (**104**). Both of the cams are in turn pinned to the lever/arm (**105**) that supports the payload (**125**). The compressive (or tensile) force exerted by each spring results in a net torque being exerted about the pivot (**120**) of the lever supporting the load.

[0036] FIGS. **1***a* and **1***b* schematically illustrate different orientations of springs and cams in a counterbalance assembly designed to fully support the weight of a payload about a hinged connection which is connected to a ground or stable fixture. The base of each spring is anchored to the ground (or fixture) while the lever/arm (**105**), pinned to the cams (**103**, **104**) is free to rotate about the pivot (**120**) of a joint of a mechanical arm. The ability to establish equilibrium of torque relative to pivot (**120**) is not limited to specific spring-cam orientations shown in FIGS. **1***a* and **1***b* as will be apparent from equilibrium equations provided below.

[0037] In FIG. **1***a* the relationship between spring (**101**) and cam (**103**) to the lever/arm supporting the load is orientated such that the line joining the pivot (**120**) and e1 (**110**) is not coincident with the line joining the pivot (**120**) to the center of gravity of the payload (**125**), which includes mass of the lever/arm (**105**). In an example of an alternate orientation shown in FIG. **1***b* the relationship between spring (**101**) and cam (**103**) to the lever/arm supporting the load is orientated such that the line joining the pivot (**120**) and e1 (**110**) is coincident with the line joining the pivot (**120**) to the center of gravity of the payload (**125**), which includes mass of the lever/arm (**105**). In both FIGS. **1***a* and **1***b* the orientation of the spring/cam relationship is preserved throughout rotation. Thus, if the cam is in a desired position with respect to the pivot, that will define the orientation of the spring in space. If the spring is in a desired position in space, that will define the position of the cam with respect to the pivot.

[0038] In the configuration shown in FIG. **1***b*, the orientation of the cam to the lever/arm constrains spring (**101**) to a vertical position. If the eccentric point is in between the pivot/fulcrum and center of gravity as shown in FIG. **1***b*, spring (**101**) will exert a compressive force in its current configuration to offset the payload when the arm is horizontal (theta (**130**)=0 degrees). If the pivot/fulcrum is in between eccentric point and center of gravity (not shown), spring (**101**) will exert a tensile force to offset the weight of the payload. The user can initially set spring (**101**) such that its initial compression offsets the mass of the payload, for example when the arm is in the horizontal position (ie, when the cam **103** is 90 degrees out of phase with spring **101**). The pre-compression of spring (**101**) will typically be set with the arm (**105**) in the horizontal position since the torque exerted by the arm is greatest at this point. However, pre-compression may also be set with the arm being above or below horizontal by extrapolation.

[0039] In FIG. **1***b*, the relationship between spring (**102**) and cam (**104**) to the lever/arm supporting the load is orientated such that the line joining the pivot (**120**) and e1 (**10**) is coincident with the line joining the pivot (**120**) to the center of gravity of the payload (**125**), which includes mass of the lever/arm (**105**). The orientation of the cam to the lever constrains spring (**102**) to a horizontal position. If the eccentric point is in between the pivot and center of gravity (not shown), spring (**102**) will exert a tensile force in its current configuration to offset the linear change in force of spring (**101**). If the pivot (**120**) is in between eccentric point and center of gravity as shown in FIG. **1***b*, spring (**102**) will exert a compressive force. In the specific example shown in FIG. **1***b*, spring (**102**) is not adjustable, and is set by design such that the spring exerts no load on cam (**104**) when the arm (**105**) is in a vertical orientation (90 or 270 degrees relative to a Cartesian coordinate system where 0 degree corresponds to the positive X axis).

[0040] Still referring to FIG. **1***b*, the relationship between each cam-spring pair is such that each cam is 180 degrees out of phase with each other (pivot (**120**) is in-between the eccentric points (**110**) and (**115**)). In this configuration, each of the springs is constrained to be 90 degrees out of phase with each other (perpendicular). The relationship created from the constrained relationship between each spring/cam pair is the torque exerted by spring (**101**) leads spring (**102**) by 90 degrees.

[0041] In an alternate embodiment, each spring/cam pair can be rotated about the pivot (**120**) to any position (for example, springs are aligned, 0 or 180 degrees) as long as the relationship between the cam and corresponding spring is maintained.

[0042] Thus, the ability to establish equilibrium relative to pivot (**120**) is not limited to specific spring-cam orientations shown in FIGS. **1***a* and **1***b* as will also be apparent from equilibrium equations provided in the following paragraphs.

[0043] Alternatives to FIGS. **1***a* and **1***b* are shown in FIGS. **1***c*-**1***e*. FIG. **1***c* is an alternate embodiment of the mechanism illustrated in FIGS. **1***a* and **1***b* where the springs are attached to the arm (**105**) and the cams are attached to the ground (or fixture). FIG. **1***d* adds an additional spring (**140**) and cam (**145**) to the spring/cam relationships shown in FIGS. **1***a* and **1***b* and thus eliminates the need for spring (**102**) to exert both compressive and tensile loads. Spring (**102**) as shown in FIGS. **1***a* and **1***b* when coupled by a yoke to cam (**104**) can be required to exert both tensile and compressive loads. Addition of spring (**140**) and cam (**145**) shown under the cutaway portion of cam (**104**) in FIG. **1***d*, allows the use of compression springs (**102** and **140**) that abut their respective cams (**104** and **145**) and exert only compressive loads. FIG. **1***e* shows a further simplification of the assembly illustrated in FIG. **1***d* with spring **102** interacting with both cams (**145** and **104**). Cam **145** is shown under the cutaway of cam (**103**). The assembly design shown in FIG. **1***d* allows for the use of compression spring (**102**) to abut cams and only exert a compressive load, while removing the need for spring (**140**). The assembly shown in FIG. **1***e* can be even further simplified by setting spring (**102**) to interact with both cams (**103** and **104**), thus removing the need for spring (**140**) and cam (**145**). FIGS. **1***f* and **1***g* show the assembly design of FIG. **1***d* as implemented on a mechanical arm.

[0044] The following is a description of the equilibrium equations that govern the geometric spring/cam relationships shown in FIG. **1***a*-**1***e*. The force friction has been omitted from this analysis as it has no bearing on the equilibrium equations when the machine is at rest. Friction can be used as an advantage to construct inexpensive mechanisms that behave in a similar manner to the case illustrated in FIG. **1** but do not fully balance the load. The sum of all the frictional forces between every moving part within the mechanism would prevent drift.

[0045] Referring to FIG. **1***a*, equilibrium about the pivot (**120**) is established when the net torque is zero, i.e.:

$$T_g+T_x+T_y=0 \quad (1),$$

where Tg is the unbalanced torque due to the payload (**125**), and the unbalanced torque produced from spring (**101**) and (**102**) are Tx and Ty respectively. The unbalanced torque produced by the weight is the product of the gravitational force due to the payload M, and the shortest distance between the force vector (M=mg) and the point (**120**):

$$T_g=Mr\cos(\theta) \quad (2).$$

The net torque of spring (**101**) about (**120**) is equal to the sum of the torque produced from the compression of the spring due to the arm displacement (**130**) and the pre-compression of the spring when the arm is horizontal (**130**: θ=0), and is given by:

$$T_y=-(K_y e_1\sin(\theta)+K_y\Delta y)(e_1\cos(\theta)) \quad (3),$$

where Ky is the spring rate of (**101**), and Δy is the displacement of the spring from rest when the arm is horizontal. The net torque produced from spring (**102**) is given by:

$$T_x=K_x e_2^2\cos(\theta)\sin(\theta) \quad (4),$$

where Kx is the spring rate of (**102**) and is uncompressed when the arm is in a vertical orientation (up or down). Substituting equations (2-4) into 1 gives the following:

$$Mr\cos(\theta)-K_y\Delta y e_1\cos(\theta)+K_x e_2^2\cos(\theta)\sin(\theta)-K_y e_1^2\sin(\theta)\cos(\theta)=0 \quad (5).$$

Equation 5 is equal to zero and independent of the angle θ, and the spring-cam orientations (**135**: a) and (**140**: b) under the following conditions:

$$Mr=K_y\Delta y e_1 \quad (6),$$

$$K_x e_2^2=K_y e_1^2 \quad (7).$$

Equation 6 provides that spring (**101**) pre-compression is set to counterbalance the payload (**125**) at the arm position within the desired rotation where the torque exerted is greatest, typically when the arm is horizontal. Equation 7 provides the physical constraints which govern the relationship of each spring cam pair.

[0046] Equation 5 can be expanded and written in the following form:

$$Mr\cos(\theta)-(K_{ya}\Delta y_a e_{1a}+K_{yb}\Delta y_b e_{1b}+\dots)\cos(\theta)+(K_{xa}e_{2a}^2+K_{xb}e_{2b}^2+\dots)\cos(\theta)\sin(\theta)-(K_{ya}e_{1a}^2+K_{yb}e_{1b}^2+\dots)\sin(\theta)\cos(\theta)=0 \quad (8).$$

Equation 8 is equal to zero and independent of the angle θ, and the spring-cam orientations (a:**135**) and (b:**140**) under the following conditions:

$$Mr=K_{ya}\Delta y_a e_{1a}+K_{yb}\Delta y_b e_{1b}+\dots \quad (9),$$

$$K_{xa}e_{2a}^2+K_{xb}e_{2b}^2+\dots=K_{ya}e_{1a}^2+K_{yb}e_{1b}^2+\dots \quad (10).$$

[0047] From equations 9 and 10, the following illustrative embodiments are apparent:

- **[0048]** The spring (**101**), and cam (**103**) can be replaced with multiple spring and cam assemblies.
- **[0049]** If ($e_{1a}^2=e_{1b}^2=\dots$), and ($K_{ya}=K_{yb}=\dots$) then the spring (**101**) can be replaced by multiple springs acting against the cam (**103**).
- **[0050]** The spring (**102**), and cam (**104**) can be replaced with multiple spring and cam assemblies.
- **[0051]** If ($e_{2a}^2=e_{2b}^2=\dots$), and ($K_{xa}=K_{xb}=\dots$) then the spring (**102**) can be replaced by multiple springs acting against the cam (**104**).
- **[0052]** If multiple springs are used in place of (**101**), then each spring can be preloaded a different amount to offset the payload when the arm is horizontal.

[0053] Now referring to FIG. **1***c*, an alternate embodiment of the mechanism illustrated in FIGS. **1***a* and **1***b* is shown where the springs are attached to the arm (**105**) and the cams are attached to the ground (or fixture). Consistent with the embodiments shown in FIGS. **1***a* and **1***b*, in FIG. **1***c* equilibrium about the pivot (**120**) is established when the net torque is zero, i.e.:

$$T_g+T_x+T_y=0 \quad (1),$$

where Tg is the unbalanced torque due to the payload (**125**), and the unbalanced torque produced from spring (**101**) and (**102**) are Tx and Ty respectively. The unbalanced torque produced by the weight is the product of the gravitational force due to the payload M, and the shortest distance between the force vector (M=mg) and the point (**120**):

$$T_g=Mr\cos(\theta) \quad (2).$$

The net torque of spring (**101**) about (**120**) is equal to the sum of the torque produced from the compression of the spring due to the arm displacement (**130**) and the pre-compression of the spring when the arm is horizontal (**130**: θ=0), and is given by:

$$\begin{aligned} T_y &= (K_y e_1\sin(\theta+\pi)+K_y\Delta_y)(e_1\cos(\theta+\pi)), && \text{(11a)}\\ &= (-K_y e_1\sin(\theta)+K_y\Delta_y)(-e_1\cos(\theta)), && \text{(11b)} \end{aligned}$$

where Ky is the spring rate of (**101**), and Δy is the displacement of the spring from rest when the arm is horizontal. This spring force is equal and opposite of the spring in FIG. **1***a*, and the cams are 180 degrees out of phase to the cam arrangement in FIG. **1***a*.

The net torque produced from spring (**102**) is given by:

$$T_x=-K_x e_2^2\cos(\theta+\pi)\sin(\theta+\pi) \quad (12a),$$

$$T_x=-K_x e_2^2\cos(\theta)\sin(\theta) \quad (12b),$$

where Kx is the spring rate of (**102**) and is uncompressed when the arm is in a vertical orientation (up or down).

Substituting equations (2), (11) and (12) into (1) gives the following:

$$Mr\cos(\theta)-K_y\Delta y e_1\cos(\theta)-K_x e_2^2\cos(\theta)\sin(\theta)+K_y e_1^2\sin(\theta)\cos(\theta)=0 \quad (13).$$

Equation (13) is equivalent to equation (5).

[0054] In FIGS. **1***a*-**1***e* when the illustrated mechanism is in balance, the torque exerted by the payload is equal and opposite to the torque exerted by the springs, regardless of the angular orientation of the arm (**105**). As illustrated in equation (7), this condition is met when the product of **e1** squared and Ky is equal to the product of e2 squared and Kx. If **e1** and **e2** are equal, then both springs must have the same spring rate (Kx=Ky).

[0055] If tension springs are used in place of compression springs in FIG. **1***a*, then placing the payload on the opposite side of the pivot (or rotating both cams 180 degrees), equilibrium about the pivot (**120**) is established when the net torque is zero, i.e.:

$$-T_g-T_x-T_y=0 \quad (1),$$

where −Tg is the unbalanced torque due to the payload (**125**), on the opposite side of the fulcrum illustrated in FIG. **1***a*, and the unbalanced torque produced from tension spring (**101**) and (**102**) are −Tx and −Ty respectively. The unbalanced torque produced by the weight is the product of the gravitational force due to the payload M, and the shortest distance between the vector (M) and the point (**120**):

$$-T_g=-Mr\cos(\theta) \quad (2).$$

The net torque of spring (**101**) about (**120**) is equal to the sum of the torque produced from the extension of the spring due to the arm displacement (**130**) and the pre-tension of the spring when the arm is horizontal (**130**: θ=0), and is given by:

$$T_y=+(K_ye_1\sin(\theta)+K_y\Delta y)(e_1\cos(\theta)) \quad (3),$$

where Ky is the spring rate of (**101**), and Δy is the displacement of the spring from rest when the arm is horizontal. The net torque produced from spring (**102**) is given by:

$$T_x=-K_xe_2^2\cos(\theta)\sin(\theta) \quad (4),$$

where Kx is the spring rate of (**102**) and is uncompressed when the arm is in a vertical orientation (up or down). Substituting equations (2-4) into 1 gives the following:

$$-Mr\cos(\theta)+K_y\Delta ye_1\cos(\theta)-K_xe_2^2\cos(\theta)\sin(\theta)+K_ye_1^2\sin(\theta)\cos(\theta)=0 \quad (5).$$

Since this is equation 5, then it becomes apparent that tension springs can be used as a replacement for compression springs

[0056] Now referring to FIG. **2***a*, an alternate embodiment is illustrated, where both of the compression springs are pivotally attached (**250**) at the base (or grounded fixture) and the other ends are fixed to the cams by a hinged connection (roller bearings **255** and **260**). This mechanism exerts its torque through the pins (**265**) and (**270**) to the arm (**205**) supporting the payload (**225**).

[0057] The section view of this assembly illustrates that spring (**201**) and (**202**) can only exert compressive loads on the cams. Spring (**201**) is compressed between the adjustment screw (**275**) attached to the base (**290**) and the bushing (**285**), resulting in a compressive load on cam (**203**). Spring (**202**) is compressed in a similar manner between adjustment screw (**280**) and bushing (**290**) to exert compressive loads on cam (**204**). As a result this variation is capable of fully supporting the weight of the payload to a maximum of ±90 degrees from its rest position. The rest position of the arm is in the horizontal position (not shown in FIG. **2***a*).

[0058] Adjustment screw (**275**) is used to set the pre-compression load on spring (**201**) to support the weight of the payload when the arm is in the horizontal position (preload=Mr). Adjustment screw is set such that the spring (**202**) exerts no load on cam (**204**) when the arm (**205**) is in a vertical orientation (illustrated in FIG. **2***a*).

[0059] FIG. **2***b* is a schematic diagram illustrating the geometric relationship between each spring/cam pair shown in FIG. **2***a*.

[0060] Equilibrium equations will now be described with reference to FIG. **2***b*. In FIG. **2***b*, equilibrium about the pivot (**220**) is established when the net torque is zero, i.e.:

$$T_g+T_u+T_v=0 \quad (14),$$

where Tg is the unbalanced torque due to the payload (**225**), and the unbalanced torque produced from spring (**201**) and (**202**) are Tu and Tv respectively. The unbalanced torque produced by the weight is the product of the gravitational force due to the payload M, and the shortest distance between the force vector (M=mg) and the point (**220**):

$$T_g=Mr\cos(\theta) \quad (2).$$

The net torque of spring (**201**) about (**220**) is equal to the sum of the torque produced from the compression of the spring due to the arm displacement (**230**) and the pre-compression of the spring when the arm is horizontal (**230**: θ=0), and is given by:

$$T_v=K_ye_1\cos(\theta-a_1)[(l_1^2+e_1^2)^{1/2}-(l_1^2-2e_1l_1\sin(\theta)+e_1^2)^{1/2}+K_y\Delta y) \quad (15),$$

where Ky is the spring rate of (**201**), and Δy is the displacement of the spring from rest when the arm is horizontal and l_1 and l_2 is the distance between the pivot (**220**) and a pivot (**250**) where the springs **201** and **202**, respectively, are coupled to the ground (or fixture). The net torque produced from spring (**202**) is given by:

$$T_u=K_xe_2\cos(\theta-a_2)[(l_2^2+e_2^2)^{1/2}-(l_2^2-2e_2l_2\cos(\theta)+e_2^2)^{1/2}) \quad (16),$$

where Kx is the spring rate of (**202**). If l_1>>e_1 and l_2>>e_2, then equation (14) can be reduced to equation (5) or (13) as the directions of the force vectors Fu and Fv become horizontal and vertical respectively in the limit as $l_1,l_2\rightarrow\infty$.

[0061] FIG. **3** illustrates a variation to the design presented in FIG. **2**. A shoulder bolt (**395**) was integrated into the previous design to allow compression spring (**302**) to exert both compressive and tensile loads on cam (**304**). This assembly was designed to support a payload exerting a maximum torque of 27.5 in-lb. This device can support the payload to a maximum of ±180 degrees from the horizontal rest position of the arm.

[0062] When the housing (**305**) supporting the cam (**304**) is moved away from the base (**300**), the spring in turn is trapped between the head of the shoulder bolt (or washer **310**) attached to the base (**300**) and washer **315** (attached to housing **305**). Thus, the compression of the spring (**302**) is converted into a tensile load that is in turn exerted on cam **304**.

[0063] Alternately, if the housing (**305**) is displaced toward the base (**300**), the compression spring (**302**) is now trapped between washer **310** (now fixed to the housing **305** instead of the shoulder bolt **395** previously described) and the base **300** (and washer **315**). Thus, the compression spring is now exerting a compressive load on cam **304**.

[0064] FIG. **4** illustrates the phase relationship between springs **201** and **202** of the counterbalance assembly shown in FIG. **2** with the addition of a shoulder bolt (**295**). The shoulder bolt (**295**) in this design allows the mechanism to apply both compressive and tensile loads to the cam (**204**). Since the maximum spring compression is not equal to the maximum spring tension, this system will support 97.5% of the payload through its full range of motion. However, if the shoulder bolt were applied to both springs **1** and **2** in the embodiment illustrated in FIG. **2**, substantially all of the load but not 100% would be supported through a full 360 degrees of rotation. If the shoulder bolt were applied to both springs **101** and **102** in the embodiment illustrated in FIG. **1***a* or **1***b*, substantially all of the load, and up to 100% would be supported through a full

360 degrees of rotation. As 'l_1' and 'l_2' approach infinity then the embodiment shown in FIG. **2** becomes equivalent to FIG. **1***a* or **1***b*.

[0065] FIG. **4** shows a side view of the springs **201** and **202** illustrating the phase relationship between each spring-cam pair for various arm rotations, with rotational positions stated in relation to a Cartesian coordinate system with 0 degree corresponding to positive X axis. This device was designed to support a payload exerting a maximum torque of 200 in-lb:

[0066] Arm at 180 degrees (left column): In this orientation, the preload of spring (**201**: bottom left) is set to exert a torque to balance the payload. The spring (**202**) does not exert an unbalanced torque in this rotational position.

[0067] Arm at 270 degrees (center column): Spring (**201**: bottom center) does not exert an unbalanced torque in this configuration. Spring (**202**: top center) is relaxed and does not exert an unbalanced torque to the arm. Since the payload is directly over the pivot, the system is in equilibrium.

[0068] Arm at 0 degrees (right column): In this arm rotational position, the preload of spring (**201**: bottom right) is set exert a torque to balance the payload. The spring (**202**) does not exert an unbalanced torque in this arm position.

[0069] FIG. **5**: illustrates an alternate variation to the design presented in FIG. **3**. The spring cam pair(s) illustrated in FIG. **3** were rotated to align both springs in a vertical orientation. However, the relationship between the cam and corresponding spring is still maintained. This design modification supports 97.5% of the load to a maximum of ±90 degrees from its rest position. The rest position of the arm is in the vertical position.

[0070] While the Figures show counterbalance assemblies for a joint of a mechanical arm where the assembly comprises two or three springs, the skilled person having the benefit of reviewing the Figures will recognize that the counterbalance assemblies need not be restricted to spring balance mechanisms and will further recognize equivalent counterbalance assemblies.

[0071] While springs have been used in the Figures it will be recognized that any force generating device may be used in the counterbalance assembly described herein. A force generating device refers to any structure or device which provides resistance to compressive or tensile forces in response to linear deflection imposed thereon. More specifically, any structure or device that exhibits resistance to linear compression or tension along a longitudinal axis thereof may be useful as a force generating device. Thus, a force generating device includes a longitudinal axis along which linear forces shall be imposed as a result of rotational movement of a mechanical arm. The force generating device interacts with a cam to converts rotational movement of the arm into linear deflection of the force generating device. An example of a force generating device is a spring-like device. A spring-like device is any device or structure that acts like a compression or tension spring in providing resistance to a linear compression and/or tension along a longitudinal axis. An example of a spring-like device is a unit of rubber or other resilient material, or a hydraulic or pneumatic pressurized cylinder any one of which may be used in an equivalent manner to a compression or tension spring by providing resistance to a linear force along a longitudinal axis. Another example of a spring-like device is a spring, such as a compression spring or a tension spring. Compression springs is an example of a low cost force generating device that may be utilized to provide a simplified arrangement within the counterbalance assembly. A compression spring includes a longitudinal axis along which linear compressive forces may be imposed as a result of rotational movement of a mechanical arm. Examples of compression springs include relatively standard die springs as commonly available in the industry. The exact number and size of such springs used in the counterbalance assembly described herein can vary depending upon the counterbalance torque desired, the size of the robotic arm involved, and the like, as will be recognized by the skilled person. The force generating device may be adjustable such that the resistive force provided by the force generating device may be increased or decreased to allow for variation in mechanical arms.

[0072] A force generating device will interact with at least one cam in the counterbalance assemblies described herein. A cam is a general term pertaining to a component that rotates or reciprocates to create a prescribed motion in an interacting element, which is often termed the follower. In the context of the counterbalance assembly described herein, a cam may be any structure or device that is set relative to a pivot of a joint, to exert a variable motion on a interacting portion of a force generating device as a function of the rotation of the joint. More specifically, a cam refers to any structure or device that can convert rotational movement of a mechanical arm into a linear movement parallel to a longitudinal axis of a force generating device. A cam is typically set eccentrically relative to a pivot of a joint of the mechanical arm. A cam may be mounted within the circumference of a joint. Alternatively, a cam need not be mounted entirely within the circumference of a joint, and may readily be set outside the circumference of a joint where full rotation is unnecessary or where physical collision or interference of mechanical components is not a concern, for example as may be the case for large industrial robotic arms. One example of a cam is an eccentric bearing. Another example of a cam is a lever extending from the joint that can interact with a force generating device. Cams can be varied shape so as impart a desired linear deflection of the force generating device.

[0073] Any technique for achieving an interaction of a cam to its follower known in the art may be used to achieve interaction of a force generating device and a cam in the counterbalance assembly described herein. The Figures show various alternatives of a spring interacting with a cam. For example, FIGS. **1***d*-**1***g* show various alternatives of a spring abutting a cam. As another example, FIG. **2** shows a spring hingedly coupled to an eccentric bearing. As yet another example, FIGS. **1***a*-**1***c* show a spring coupled to a cam through a yoke. Each of the examples described in the Figures may be used to achieve an interaction between a force generating device and a cam. Still other forms of coupling using slots, pegs or other techniques known in the art can be used to achieve the interaction of a force generating device and a cam. Interaction as used herein contemplates a force generating device abutting or engaging a cam, and a force generating device being linked or coupled to a cam.

[0074] The counterbalance assembly has been structurally shown in the Figures using at least two springs with each spring interacting with at least one cam that is mounted eccentrically relative to a pivot of a joint of a mechanical arm. Functionally, the spring/cam relationships can be divided into first and second groups. The purpose of each group is to generate torque. The torque generated by the first and second groups together allows the counterbalance assembly to maintain an equilibrium of torque exerted on a joint throughout the desired rotation of the joint. The torque provided by the first group is used to counteract the torque exerted by the mechanical arm and its associated payload at a rotational position, typically horizontal, where torque exerted by the arm is greatest. The torque provided by the second group is to counteract the linear change in force exerted by the first group. For example, the linear change in force due to linear displacement of springs in the first group when the arm is above horizontal results in the torque exerted by the mechanical arm being greater than the torque exerted by spring/cam pairs in the first group causing the arm to drift back to horizontal. In contrast, the linear change in force due to linear displacement of springs in the first group when the arm is below horizontal results in the torque exerted by the mechanical arm being less than the torque exerted by spring/cam pairs in the first group causing the arm to drift back to horizontal. The torque provided by the second group can maintain equilibrium when the arm is below and above the horizontal. Thus, the torque provided by the second group compensates for the first group to maintain the arm in positions other than the horizontal. The horizontal is the rest position or datum.

[0075] Using the specific example shown in FIG. **2** for illustration only, the purpose of spring **201** is to offset for the weight of the payload. To account for its weight, the initial compression of the spring is set with an adjustment screw (for example, item **275**, FIG. **2**) such that the torque exerted by the spring through the cam is equal to the counter torque resulting from the weight of the payload. The purpose of the second spring is to offset for the linear change in force with compression of the first spring.

[0076] For example, the pre-compression load of spring **201** may be set with the arm in a rotational position, typically horizontal, where the arm exerts its greatest torque. Thus, the torque exerted by spring **201** maintains the system in equilibrium with the arm in the horizontal position. This arm position is the datum or rest position. When the arm is displaced from its horizontal position when with the pre-compression load of spring **201** set, the lever will return to its initial rest position (horizontal) without spring **202** present due to change in force exerted by the spring **201** due to linear displacement of the spring. With spring **202** in place, when the arm is displaced from the horizontal, the change in force applied by spring **201** is counteracted by spring **202**. The result is the lever will not return to its initial equilibrium position defined by spring **201**. With the addition of spring **202**, its equilibrium position is no longer related to orientation (**230**) of the lever/arm.

[0077] Counterbalance assemblies described herein may maintain equilibrium of torque for an unlimited degree of rotation. Torque equilibrium may be maintained for arm rotations greater than 1 degree, 45 degrees, 90 degrees, 135 degrees, 180 degrees, 225 degrees, 270 degrees, 315 degrees, 360 degrees, and even greater, in both positive and negative directions.

[0078] Counterbalance assemblies described herein may be used for one or more than one joint in a mechanical arm.

[0079] The following relationship as described with reference to FIG. **1***b* holds true for the counterbalance assemblies shown throughout the Figures. Pre-compression of a first spring to counteract torque of a mechanical arm is set for an arm position which exerts its greatest torque, ie horizontal in FIG. **1***b*. With the arm in this position, the line between the pivot (**120**) and the center of eccentric cam (**103**) is substantially perpendicular to the longitudinal axis of spring **101**. At this same arm position, the line between the pivot (**120**) and the center of eccentric cam (**104**) is substantially parallel to the longitudinal axis of spring **102**. In certain examples, with the arm in this position, the line between the pivot (**120**) and the center of eccentric cam (**103**) is perpendicular to the longitudinal axis of spring **101**, and the line between the pivot (**120**) and the center of eccentric cam (**104**) is substantially parallel to the longitudinal axis of spring **102**.

[0080] Counterbalance assemblies, for example spring balance assemblies, described herein may be used in conjunction with further components as desired to aid in the orientation of mechanical arms, for example, without limitation, brakes for locking a hinged arm, encoders for measuring rotational angles of a hinged coupling, counterweights and/or other balances to offset the mass of the system, computer controlled actuators for automating actuation of a hinged coupling. Further components that may be incorporated into the mechanical arm will be apparent to the skilled person, and suitable combinations of optional components will also be apparent depending on the particular mechanical arm and the particular use of the mechanical arm.

[0081] As one example of an optional component, a counterweight may be mounted to the arm to offset the mass of a payload and/or mass of one or more elements of an articulated arm. Although the counterbalance mechanism described herein can eliminate the need for counterweights, counterweights may, if desired, be used in conjunction to offset the mass of the system.

[0082] As yet another example of an optional component, a braking mechanism may be mounted within the mechanical arm to inhibit or stop motion of arm elements relative to each other.

[0083] As still another example of an optional component, the mechanical arm may be equipped with motors (not shown), for example servo motors that may be controlled by a computer to automate the motion of various linkage elements. The counterbalance mechanism described herein reduces the force required by motors to actuate the mechanical arm.

[0084] As another example of an optional component, in embodiments where springs are used in a counterbalance assembly the compression or tension of one or more springs is adjustable.

[0085] Still further optional features will be apparent to the skilled person.

[0086] The spring balance mechanism may be used in conjunction with many different types of mechanical arms, for example, arms having industrial or medical uses.

[0087] A specific illustrative example of a mechanical arm where the counterbalance assembly may be used is a guide apparatus **601** that may be used for 3D orientation of a medical tool relative to and through a fixed point in space, a remote fulcrum (FIG. **6**). The guide apparatus comprises two linkage elements, a crank **602** and a link **604**. The crank **602** and the link **604** may be of any size, or shape that allows for the remote fulcrum **600**.

[0088] The linkage elements may be hingedly coupled to form positioning elements. In FIG. **6** the crank **602** and link **604** both have an arcuate structure having a central angle of about 45 degrees. The crank has a first end **612** and a second end **614**. The link also has first and second ends **622**, **624**.

When the guide apparatus is in use the first end **612** of the crank is hingedly coupled to a base or stabilizer. The first end **612** may comprise a full hinged coupling that is attached to a member that is rigidly fixed to the base or ground arm.

[0089] Alternatively, the first end **612** may comprise a portion of a hinged coupling **610** with the remainder of the hinged coupling being provided by the base or stabilizer. The second end **614** of the crank forms a hinged coupling **616** with the first end **622** of the link. The second end **614** of the crank comprises a portion **618** of the hinged coupling **616**, while the first end **622** of the link comprises the remaining portion **620** of the hinged coupling **616**. The second end **624** of the link is coupled to a tool holder **606**. The tool holder may be in the form of an adaptable cradle for securing a shaft **632** that may be used to actuate a medical tool **640**. The spring balance assembly **650** is provided for the joint between first end **612** and the base or ground arm. A counterweight **652** is provided to offset the weight of the payload. However, if desired counterweight **652** may be replaced with a spring balance assembly.

[0090] The above-described embodiments are intended to be examples and alterations and modifications may be effected thereto, by those of skill in the art, without departing from the scope of the invention which is defined by the claims appended hereto.

1. A counterbalance assembly for a joint of a mechanical arm comprising:

a first force generating device;
a second force generating device;
the first and second force generating devices interacting with at least first and second cams, respectively;
the first and second cams fixed eccentrically relative to the pivot of a joint; and
the relationship of the first spring to the second spring and the first cam to the second cam being preserved throughout rotation of the joint.

2. The counterbalance assembly of claim **1**, wherein the compression of the first force generating device is adjustable.

3. The counterbalance assembly of claim **2**, wherein compression of the first force generating device is adjustable such that a torque exerted by the first force generating device offsets the torque of the mechanical arm, when the arm is in a position to exert its greatest torque about the joint.

4. The counterbalance assembly of claim **1**, wherein the compression of the second force generating device is adjustable.

5. The counterbalance assembly of claim **1**, wherein the longitudinal axis of the first force generating device is substantially perpendicular to the line extending between the pivot and the center of the first cam, and the longitudinal axis of the second force generating device is substantially parallel to the line extending between the pivot and the center of the second cam, when the arm is in a position to exert its greatest torque about the joint.

6. The counterbalance assembly of claim **1**, wherein the first force generating device applies a compressive load to the first cam.

7. The counterbalance assembly of claim **1**, wherein the second force generating device applies a compressive load to the second cam.

8. The counterbalance assembly of claim **1**, wherein the first force generating device applies a compressive load to the first cam and the second force generating device applies a compressive load to the second cam.

9. The counterbalance assembly of claim **1**, wherein the second force generating device applies a compressive load or a tensile load to the second cam depending on the rotational position of the joint.

10. The counterbalance assembly of claim **1**, wherein at least one of the first and second cams is set within The circumference of the joint.

11. The counterbalance assembly of claim **1**, wherein at least one of the first and second cams is set outside the circumference of the joint.

12. The counterbalance-assembly of claim **1**, wherein the first force generating device at least offsets the weight of a payload of the mechanical arm, when the arm is in a position to exert its greatest torque about the joint.

13. The counterbalance assembly of claim **12**, wherein the second force generating device offsets the linear change in force of the first force generating device.

14. The counterbalance assembly of claim **1**, wherein the first and second force generating devices abut first and second cams, respectively.

15. The counterbalance assembly of claim **1**, wherein the first and second force generating devices are coupled to first and second cams, respectively.

16. The counterbalance assembly of claim **1**, further comprising a third force generating device.

17. The counterbalance assembly of claim **16**, wherein the third force generating device interacts with the second cam.

18. The counterbalance assembly of claim **16**, wherein the third force generating device interacts with the first cam.

19. The counterbalance assembly of claim **1**, further comprising a third cam that interacts with the third force generating device.

20. The counterbalance assembly of claim **1**, further comprising a fourth force generating device.

21. The counterbalance assembly of claim **1**, wherein the first and second force generating devices are spring-like devices.

22. The counterbalance assembly of claim **21**, wherein the product of the spring rate of the first spring-like device and the square of the distance between the center of the first cam and the pivot is substantially equal to the product of the spring rate of the second spring-like device and the square of the distance between the center of the second cam and the pivot.

23. The counterbalance assembly of claim **22**, wherein the spring rate of the first spring-like device is substantially equal to the spring rate of the second spring-like device.

24. The counterbalance assembly of claim **21**, wherein at least one of the first and second spring-like devices is a compression spring.

25. The counterbalance assembly of claim **21**, wherein at least one of the first and second spring-like devices is a tension spring.

26-54. (canceled)

* * * * *

Appendix C (Patent application): Apparatus and Method for guiding Insertion of a Medical Tool

US 20080004481A1

(19) **United States**

(12) **Patent Application Publication** (10) **Pub. No.: US 2008/0004481 A1**

Bax et al. (43) **Pub. Date: Jan. 3, 2008**

(54) **APPARATUS AND METHOD FOR GUIDING INSERTION OF A MEDICAL TOOL**

(76) Inventors: **Jeffrey Bax**, London (CA); **Aaron Fenster**, London (CA); **Jacques Montreuil**, London (CA); **Lori Gardi**, London (CA); **David Martin Smith**, London (CA)

Correspondence Address:

(21) Appl. No.: **11/427,121**

(22) Filed: **Jun. 28, 2006**

Publication Classification

(51) **Int. Cl.**
A61M 36/00 (2006.01)

(52) **U.S. Cl.** **600/7**

(57) **ABSTRACT**

An apparatus and method for the insertion of a medical tool, for example a needle, within the human body. The apparatus and method are particularly useful in prostate brachytherapy and in prostate biopsy. The apparatus comprises a telescoping guide universally coupled to a first and second positioning means that are used to automatically and/or manually position the guide at a desired needle insertion trajectory. Automatic positioning of the guide is accomplished with reference to three-dimensional transrectal ultrasound images that can also be used to show needle insertion in real-time. The apparatus may be manually positioned in the approximate insertion trajectory and then a computer interconnected with the apparatus may be used to achieve the final trajectory based upon the ultrasound images. The apparatus is particularly useful in cases where multiple needles are to be inserted into a small target area and in cases where pubic arch interference prevents direct access to the target area.

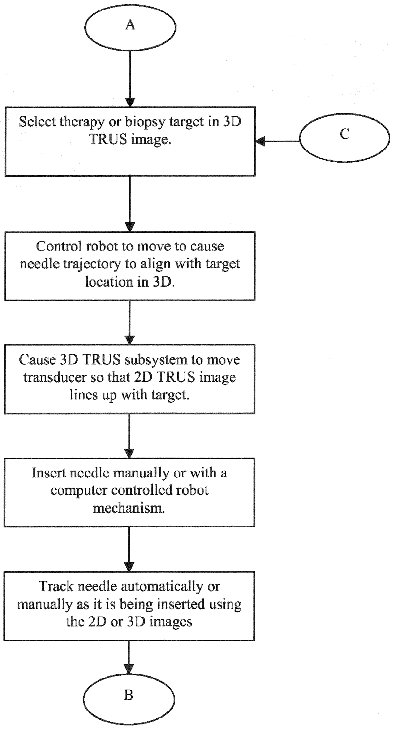

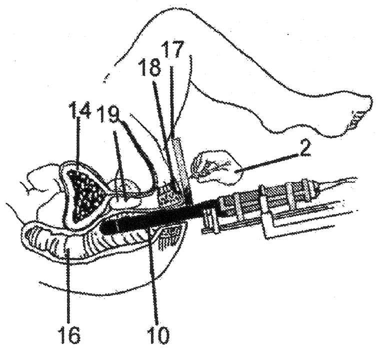

Fig. 1a

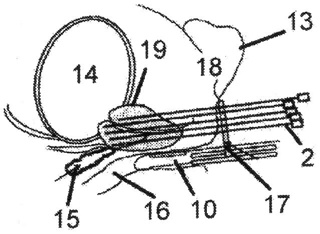

Fig. 1b

Fig. 2a

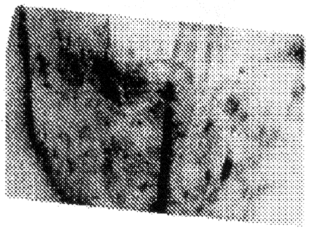

Fig. 2b

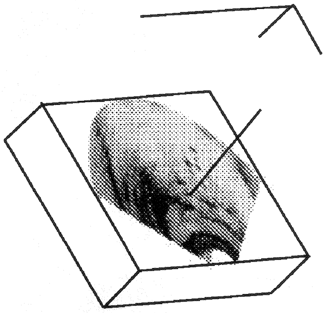

Fig. 2c

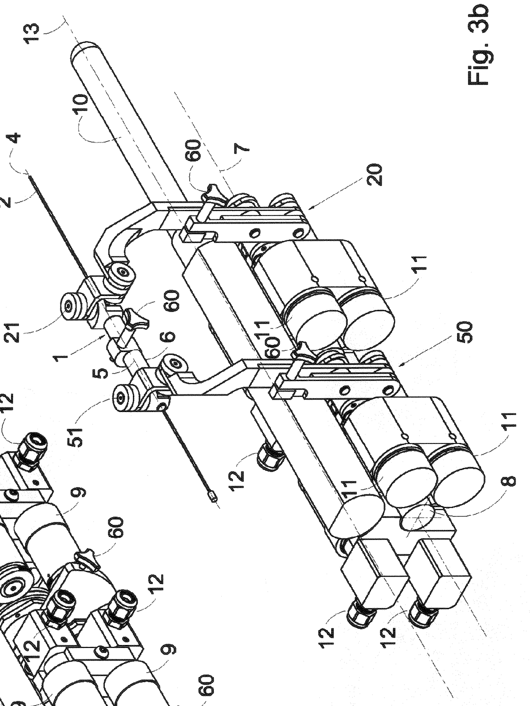
13
10
4
2
60
7
20
21
60
1
6
5
51
11
11
60
50
11
11
12
8
12
12

Fig. 3b

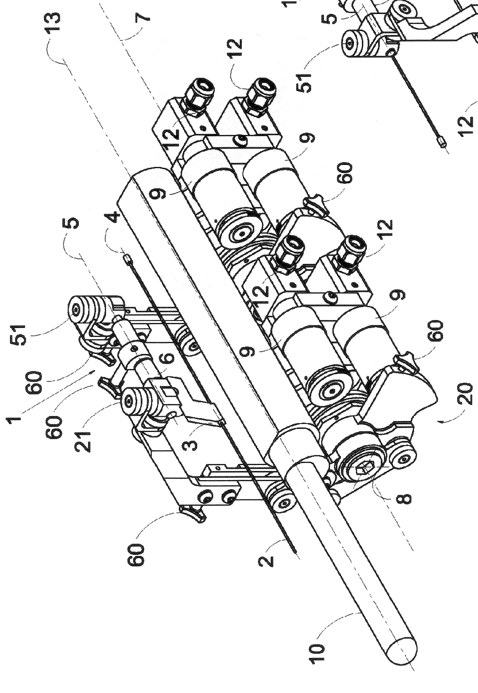
13
7
12
12
12
9
9
60
12
5
4
12
9
9
60
51
60
6
1
60
21
3
20
8
60
2
10

Fig. 3a

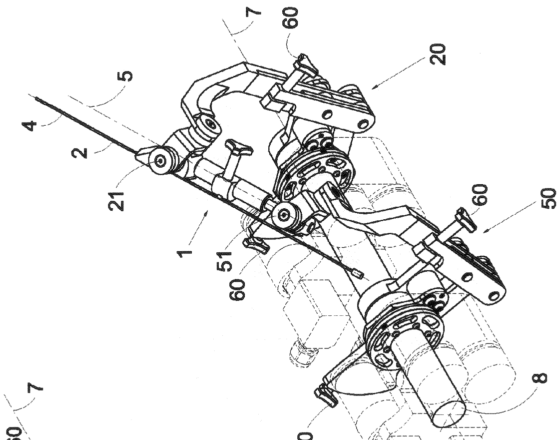

Fig. 4b

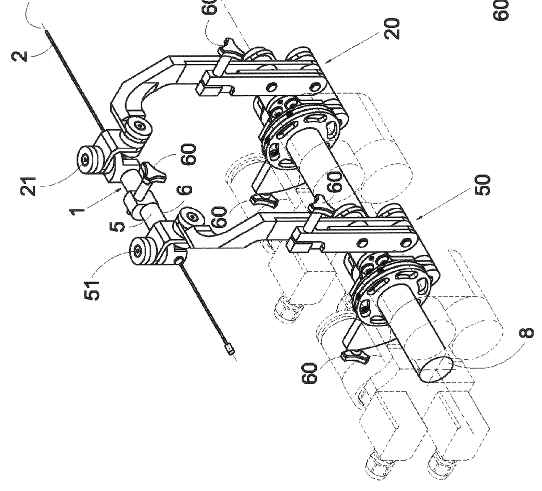

Fig. 4a

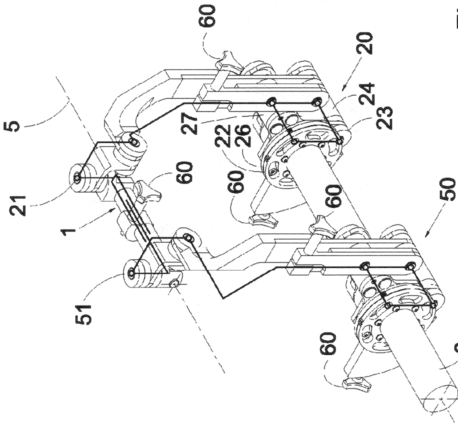
5
21
1
51
60
60
60
60
60
60
27
22
26
24
23
20
50
8

Fig. 5a

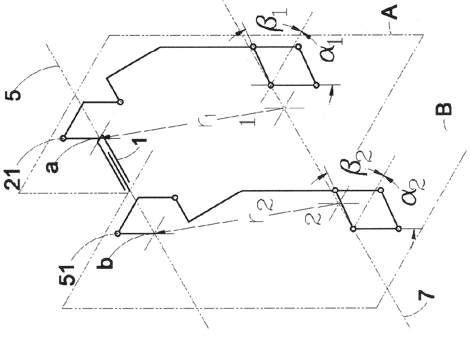
5
21
a
1
51
b
r_1
1
r_2
2
β_1
α_1
A
B
β_2
α_2
7

Fig. 5b

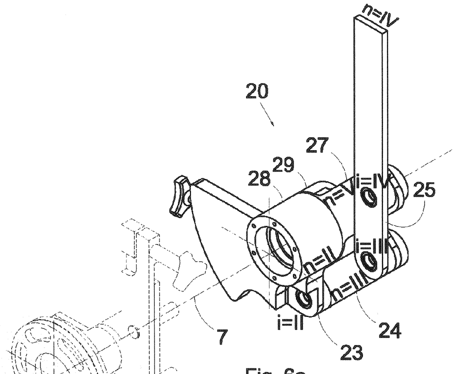

Fig. 6a

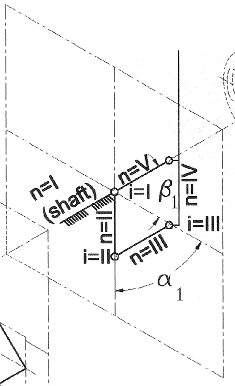

Fig. 6b

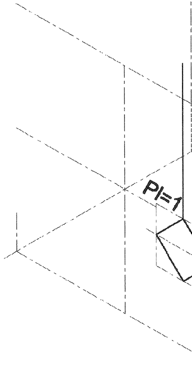

Fig. 6c

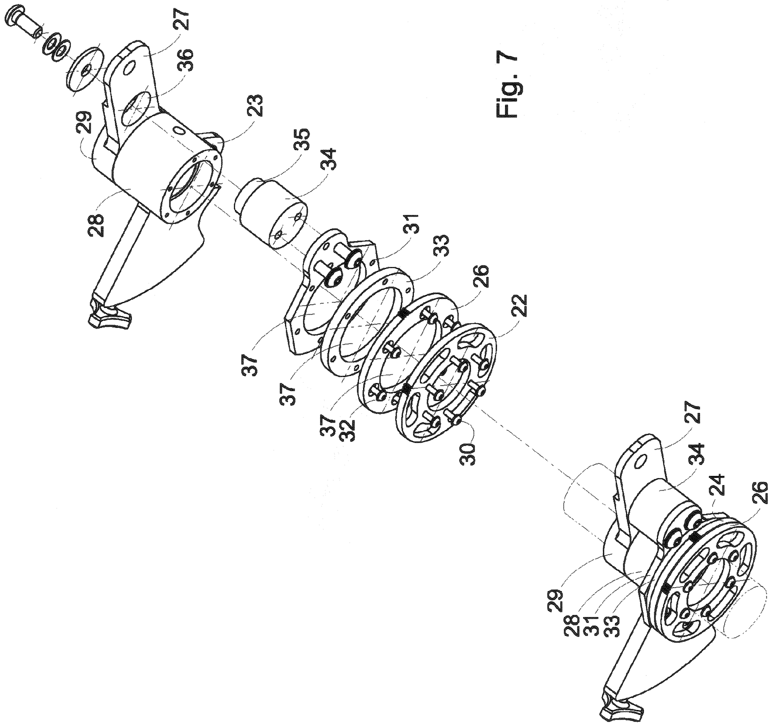

Fig. 7

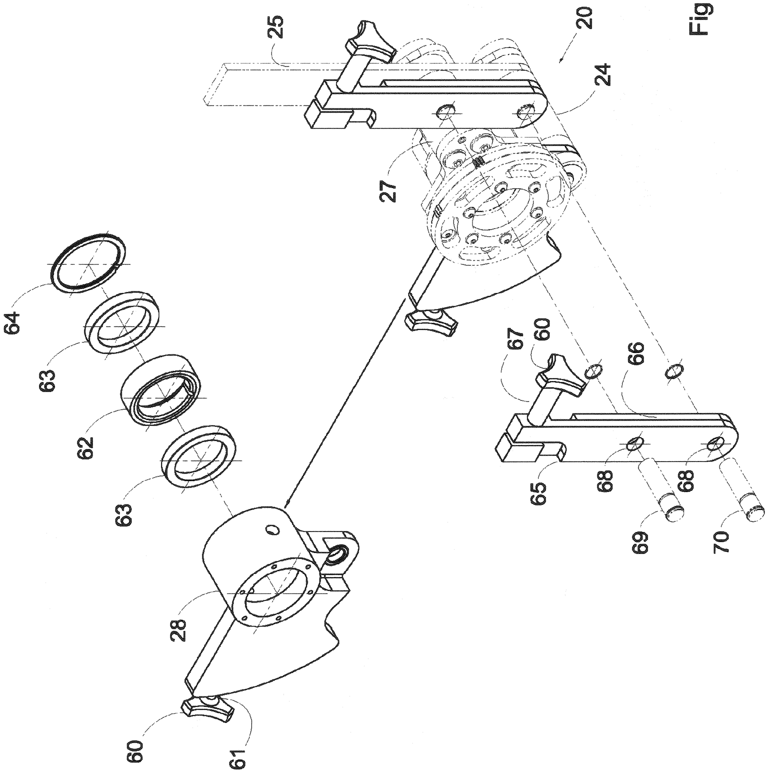

Fig. 8a

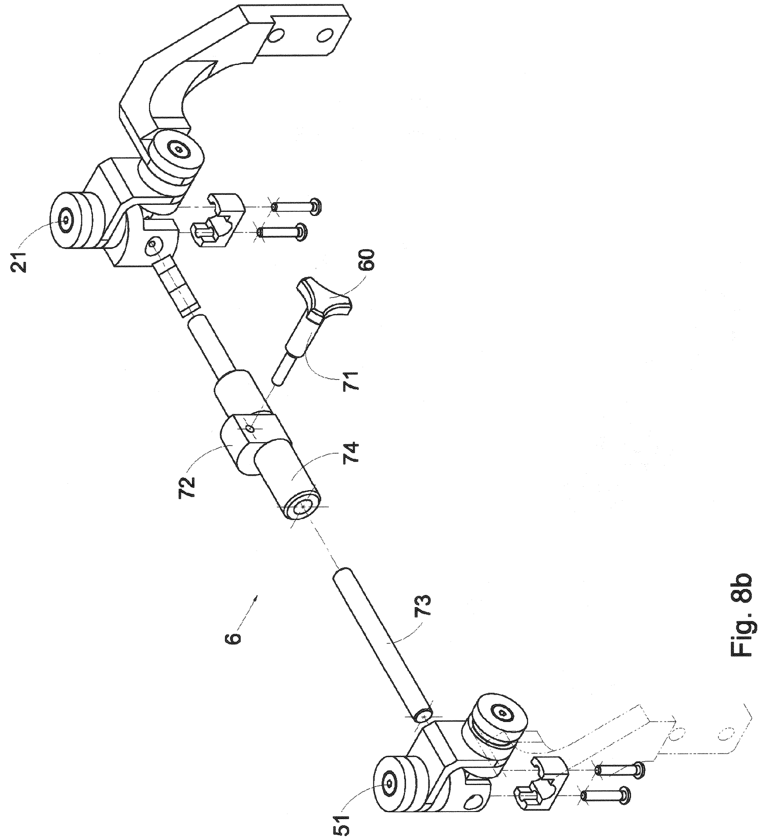

Fig. 8b

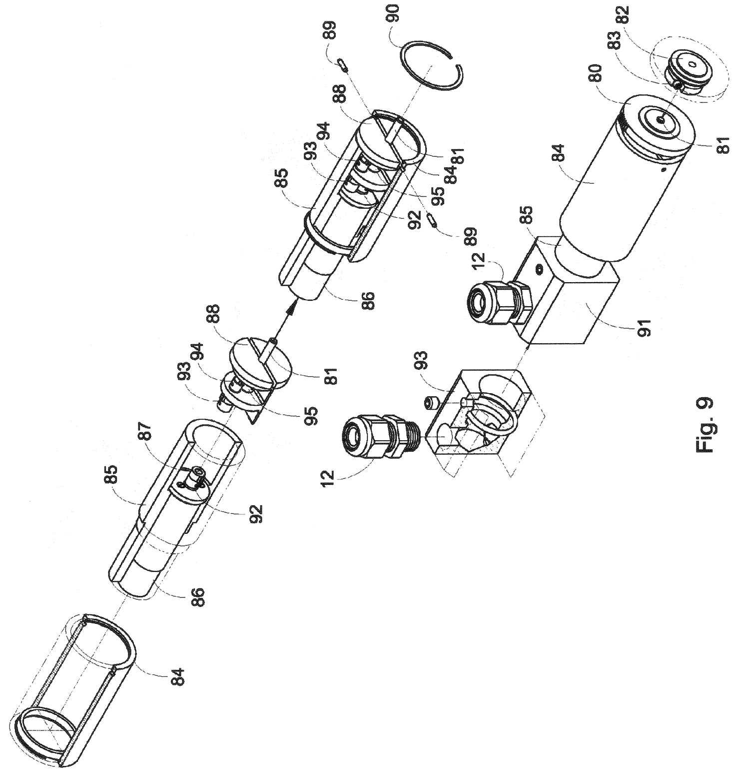
89
90
88
94
93
85
84
81
95
92
89
86
82
83
80
84
81
85
12
91
88
94
93
81
95
87
85
93
12
92
86
84

Fig. 9

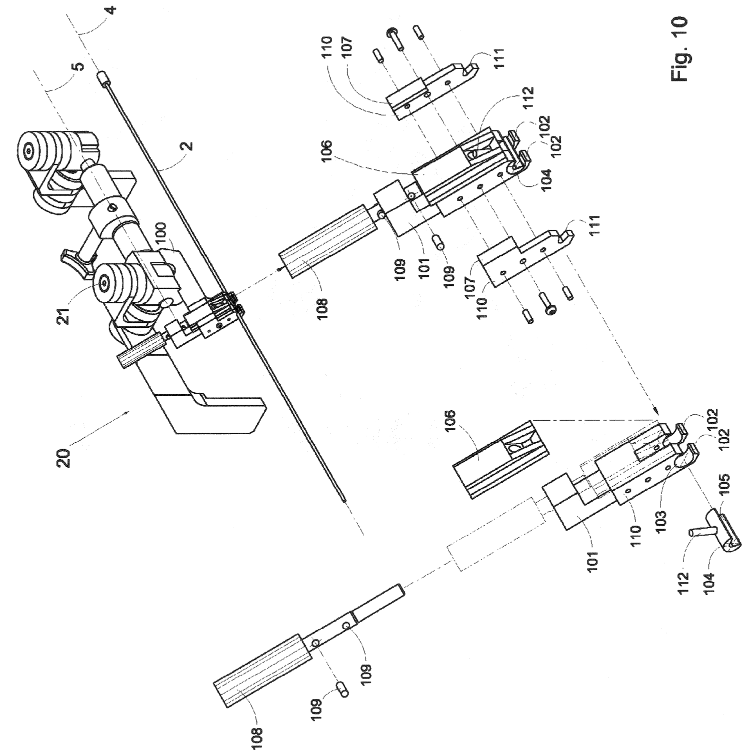
20
21
100
2
5
4
106
110
107
111
112
102
102
104
108
109
101
109
107
110
111
106
102
102
105
101
110
103
112
104
108
109
109

Fig. 10

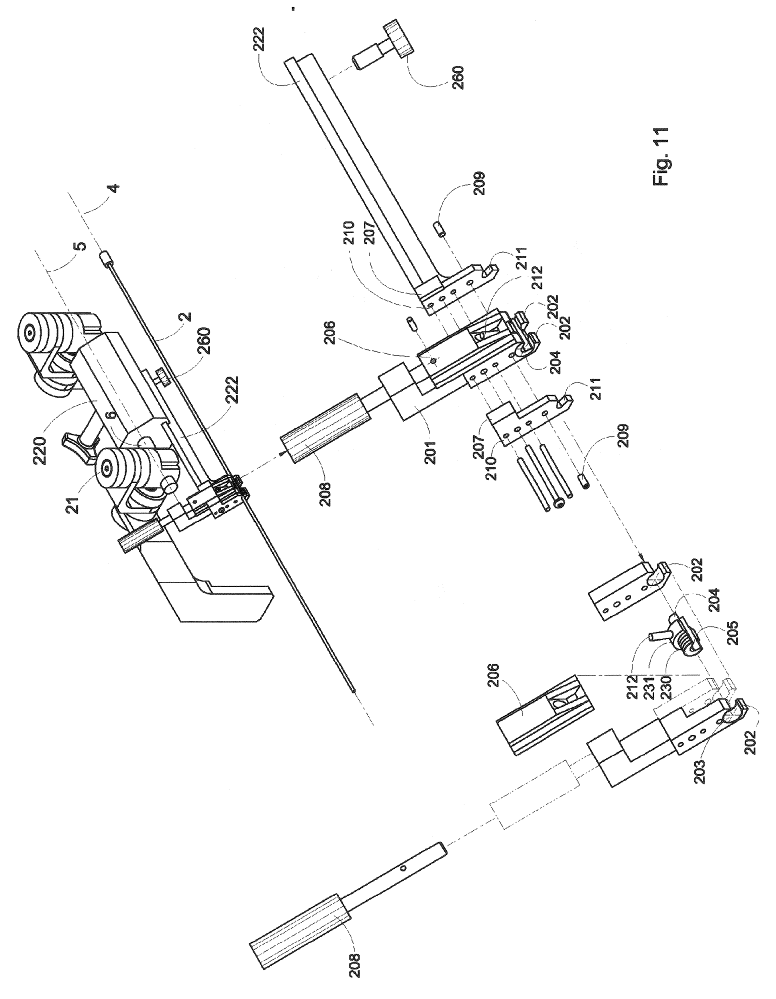
222
260
209
210
207
211
212
202
202
206
204
201
208
207
210
211
209
4
5
2
260
222
220
6
21
202
204
205
212
231
230
206
203
202
208

Fig. 11

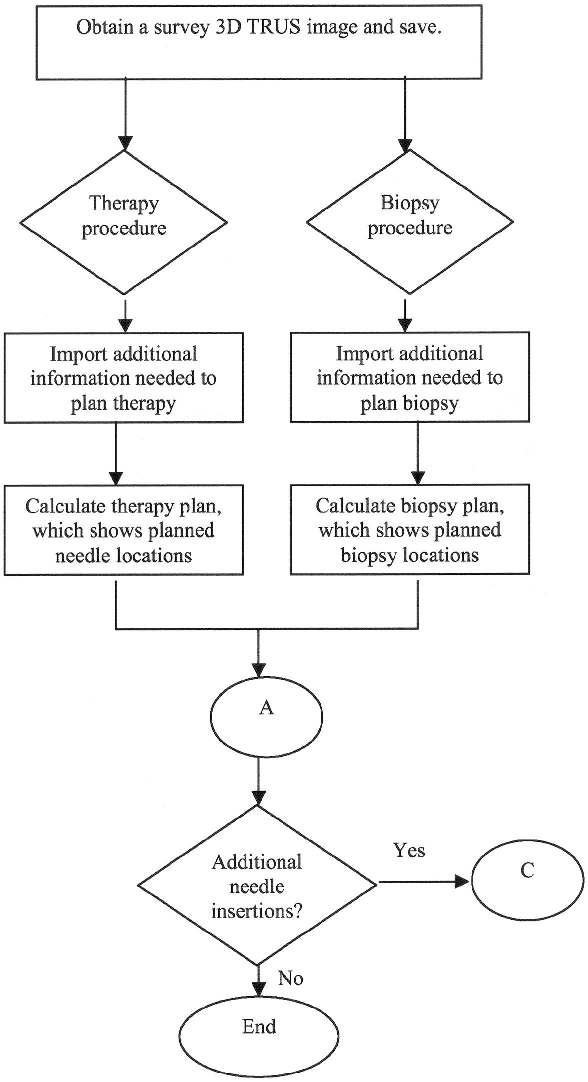
Obtain a survey 3D TRUS image and save.
Therapy procedure
Biopsy procedure
Import additional information needed to plan therapy
Import additional information needed to plan biopsy
Calculate therapy plan, which shows planned needle locations
Calculate biopsy plan, which shows planned biopsy locations
A
Additional needle insertions?
Yes
C
No
End

Fig. 12

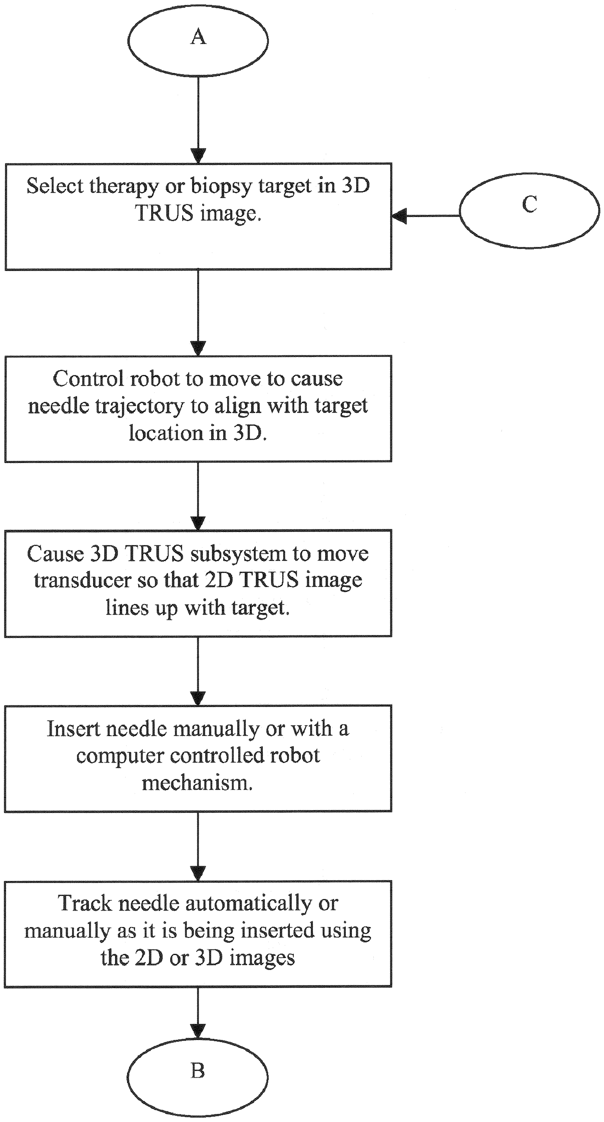
A
Select therapy or biopsy target in 3D TRUS image.
C
Control robot to move to cause needle trajectory to align with target location in 3D.
Cause 3D TRUS subsystem to move transducer so that 2D TRUS image lines up with target.
Insert needle manually or with a computer controlled robot mechanism.
Track needle automatically or manually as it is being inserted using the 2D or 3D images
B

Fig. 13

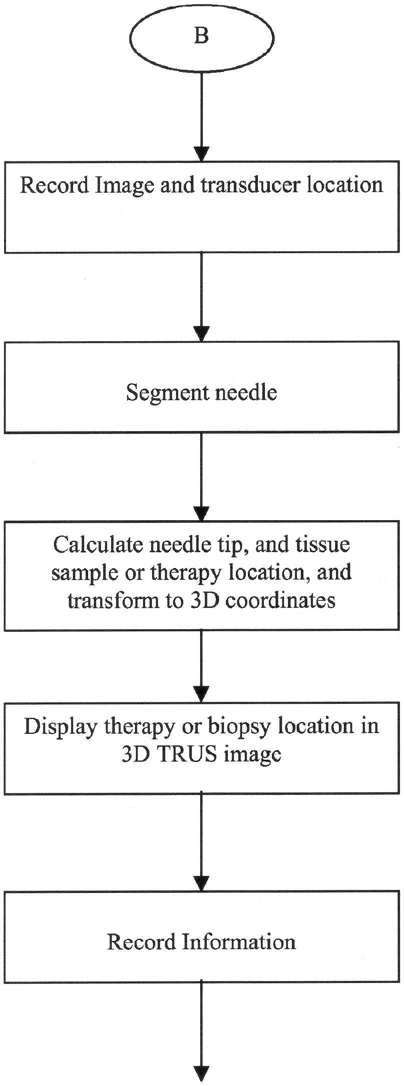
B
Record Image and transducer location
Segment needle
Calculate needle tip, and tissue sample or therapy location, and transform to 3D coordinates
Display therapy or biopsy location in 3D TRUS image
Record Information

Fig. 14

APPARATUS AND METHOD FOR GUIDING INSERTION OF A MEDICAL TOOL

FIELD OF THE INVENTION

[0001] The invention relates to the guiding of medical tools for insertion within the body of an animal. More particularly, the invention relates to an apparatus and method for positioning a guide for use in manually inserting a medical tool, such as a needle, within a human body at a particular angle in three-dimensional space, usually determined with reference to a medical image of an interior of the body. The guide may be automatically positioned by a computer and/or manually positioned. The apparatus and method are particularly useful as an aid in needle placement during the treatment of prostate cancer by brachytherapy or during prostate biopsy procedures.

BACKGROUND

[0002] There are a number of medical procedures where it is desirable to insert a tool within a human body to a precise position based upon medical imagery. An example of such a procedure is prostate brachytherapy, where radioactive seeds are implanted within a cancerous prostate using a long needle that is inserted into the prostate from outside the body. Ultrasound images are used to determine the location and size of the prostate and a plate having a rectangular array of regularly spaced holes is used as a guide in inserting the needle at approximately the right location. An ultrasound transducer inserted within the rectum is sometimes used to provide real-time imagery as an aid in locating the prostate. This approach relies considerably upon the surgeon's skill in locating the prostate and is not particularly accurate in terms of seed placement.

[0003] Recent advances in ultrasound imaging equipment and techniques have allowed increasingly sophisticated models of the prostate to be produced. One such advancement is three-dimensional ultrasound imaging, which allows a three-dimensional model of the prostate to be assembled from a series of two-dimensional images. Accurate targeting of seed placement based upon these three-dimensional models can dramatically increase the efficacy of brachytherapy and therefore improve the survival of prostate cancer patients. However, limitations in the array-based needle guidance technique make it difficult if not impossible to accurately place the seeds in their target location. This is especially true in advanced prostate cancer cases, where enlargement of the prostate often causes a significant portion of the target area to be occluded by the pelvic arch.

[0004] It would be desirable to have an apparatus for accurately positioning a needle guide in three-dimensional space that allows the needle to be accurately inserted into the prostate at an angle that clears the pelvic arch and allows seeds to be precisely placed in their target location. To further improve the accuracy of seed placement, it would be desirable to have the guide positioning apparatus interfaced with a computer that automatically adjusts the position of the guide to the optimal location for placing each seed based upon analysis of an ultrasound image. Real-time feedback of ultrasound imagery to the computer would also be desirable in that it would allow the computer to make micro adjustments to the needle guide position in order to accurately place the seeds. Since many patients and surgeon's are wary of robotic surgical procedures, it is desirable that the needle guide simply position the needle for manual insertion by the surgeon and that the apparatus has sufficient override functionality to allow the surgeon to manually adjust the guide position without damaging the apparatus or endangering the patient.

[0005] U.S. Pat. No. 6,659,956, entitled "Medical Instrument Positioner", describes a stage for a medical instrument that could include an ultrasound probe. The patent describes a method for translating a medical device along the axis of the stage. It does not describe the placement or use of a needle or other invasive medical device. U.S. Pat. No. 5,931,786, entitled "Ultrasound Probe Support and Stepping Device", is similar to U.S. Pat. No. 6,659,956, but also includes rotation of an ultrasound probe in addition to translation. This device also has a template mount for needle insertion. No means is disclosed for guiding a needle to an intended target within the body.

[0006] U.S. Pat. No. 6,544,176, entitled "Computer Guided Cryosurgery", describes a cryosurgery procedure involving a method for acquiring medical images, use of a computer system to plan appropriate placement of cryoprobes, placement of the probes using a template, and image-feedback on the appropriateness of the placement. This patent makes no reference to a means for guiding placement of medical tools and relies solely on a static template.

[0007] U.S. Pat. No. 5,494,039, entitled "Biopsy Needle Guide and Method for Use in Prostate Cryosurgery", describes a cryosurgery placement technique wherein a needle guide is manually adjusted to a desired position, a needle is inserted, and the cryoprobe is inserted thereafter. This device can only be used manually. The angle of the needle is fixed relative to the probe axis, and thus cannot be adjusted in three-dimensional space to reach an occluded target within the human body.

[0008] U.S. Pat. No. 4,899,756, entitled "Articulating Needle Guide for Ultrasound Imaging and Method of Using the Same", describes a fully manual needle guide for use with a surface ultrasound transducer. U.S. Pat. No. 6,695,786, entitled "Guide and Position Monitor for Invasive Medical Instrument", expands on U.S. Pat. No. 4,899,756 by including position encoding devices. However, the devices disclosed in these documents are neither automatically operable, nor compatible with trans-rectal ultrasound probes.

[0009] The publication, Gabor Fightinger; Everette C. Burdette; Attila Tanacs; Alexandru Patriciu; Dumitru Mazilu; Louis L. Whitcomb; Dan Stoianovici; "Robotically assisted prostate brachytherapy with transrectal ultrasound guidance—Phantom experiments", *Brachytherapy* 5 (2006) pp. 14-26, describes two robots for assisting in trans-rectal ultrasound guided prostate brachytherapy. The first robot described has inordinate flexibility of movement; the robot's operating envelope can extend into the patient, creating significant risk, and requiring a complex control system with complicated redundancy. This robot requires significant calibration, since the motive part of the robot is decoupled from the imaging device. It also consists of only a single positioning means, which limits the degrees of freedom that are selectively available in choosing a desired insertion angle. The second robot can position a needle, but has no mechanism to allow release of the needle once it is inserted. Furthermore, the structural supports of the robot's stage mechanism inhibit the inclusion of any kind of needle release mechanism. Since most brachytherapy procedures require the insertion of multiple needles, this makes the robot essentially un-useable in a clinic setting. This robot cannot be manually controlled, and the design also prohibits sterilization, a necessity for surgery or invasive therapy.

[0010] Prior art needle guides have suffered from limited positional accuracy, do not allow needle release for multiple needle placement and/or are either only manually adjustable or only robotically adjustable. The need therefore exists for an improved apparatus and method for guiding insertion of a medical tool, preferably in a manner permitting both manual and automatic position adjustment.

SUMMARY OF THE INVENTION

[0011] According to an aspect of the present invention, there is provided an apparatus for the three-dimensional positioning of a guide for manual insertion of a medical tool within a body, the apparatus comprising: an alignment axis; a guide axis aligned with the guide; a first plane orthogonal to the alignment axis; a second plane orthogonal to the alignment axis and parallel to the first plane, the second plane spaced apart from the first plane along the alignment axis; a first positioning means for positioning a first guide point on the first plane, the guide axis passing through the first guide point; a second positioning means for positioning a second guide point on the second plane, the guide axis passing through the second guide point; and, the first and second positioning means separately adjustable in order to provide a pre-determined angular relationship between the guide axis and the alignment axis.

[0012] According to another aspect of the present invention, there is provided an apparatus for the three-dimensional positioning of a guide for manual insertion of a medical tool within a body, the apparatus comprising: at least one positioning means attached to the guide; at least one motor connected to each positioning means, the motor comprising: an armature; a gear shaft connected with the armature through a set of enmeshed gears; a manual adjustment knob connected with the gear shaft; a slip clutch connecting the gear shaft and the positioning means; and, the manual adjustment knob rotatable to manually adjust the positioning means while the motor is in operation without overdriving the motor.

[0013] According to yet another aspect of the present invention, there is provided a method of positioning a guide for manual insertion of a medical tool within a body, the method comprising: obtaining a medical image of an interior of the body; providing the medical image to a computer in a digital form; determining with the computer a desired angle for manual insertion of the tool based upon analysis of the image; and, automatically positioning the guide at the desired angle using instructions provided by the computer to a motorized guide positioning apparatus.

[0014] The first and/or second positioning means may be manually, automatically, or both manually and automatically adjustable. The first and/or second positioning means may comprise a means of adjusting the distance between the first guide point and the alignment axis and a means of adjusting the polar position of the first guide point on the first plane by rotating a first gear about a first rotation axis parallel to or collinear with the alignment axis. The means of adjusting the distance between the first guide point and the alignment axis may comprise: a first link member having a first end pivotally attached to a first crank member of the first gear and having a second end; a second gear spaced apart from the first gear along the alignment axis and rotatable about a second rotation axis parallel to or collinear with the alignment axis; a second link member having a first end pivotally attached to a second crank member of the second gear and having a second end pivotally attached to the first link member between its first and second ends at a link pivot point; and, the first and second gears rotatable to adjust the distance between the first guide point and the alignment axis. In one embodiment, the first link member and the second crank member are parallel and the first crank member and second link member are parallel, thereby forming a parallelogram linkage, with the first and second rotation axes being collinear. The second end of the first link member may comprise a universal joint or a spherical joint for connecting the guide means with the first link member.

[0015] The first and/or second positioning means may comprise a first locking means to selectively prevent movement of the second link member relative to the first link member about the link pivot point. The first and/or second positioning means may comprise a second locking means to selectively prevent movement of at least the first or second gear about its respective rotation axis. The guide may telescope between the first and second guide points and the guide may be lockable to selectively prevent telescoping. The first and second locking means and the lockable guide may co-operate to prevent movement of the first and/or second positioning means once a desired angle of tool insertion has been established. The guide may further include release means operable to release the tool from the guide without adjusting the position of the tool or the apparatus. This may be used, for example, to allow the tool to be removed from the apparatus without adjusting the position of the guide.

[0016] The angular relationship between the guide axis and the alignment means may be determined with reference to a medical image of an interior of the body. The medical image may comprise an ultrasound image and the apparatus may include means to facilitate the taking of real-time ultrasound images, for example an ultrasound transducer for insertion into the body along the axis of alignment. The ultrasound image may comprise a three-dimensional ultrasound image. The apparatus may further comprise one or more motors connected to the first and/or second positioning means and a computer interconnection means. The computer interconnection means may comprise a digital data connection or an analog connection for providing signals to the motor(s) for use in automatically adjusting the position of the guide. The position of the guide may be adjusted based upon feedback provided by real-time ultrasound images and/or other medical images.

[0017] The armature of the motor may be eccentric relative to the gear shaft and the set of enmeshed gears may comprise at least two eccentrically mounted gears. The apparatus may comprise a position encoder for determining the rotational position of the gear shaft and this rotational position may be fed back to the computer for use in determining any adjustments required in attaining the desired angle of insertion. The motor is designed such that the apparatus may be manually adjusted while the motor is in operation without backdriving or overdriving the motor. This advantageously permits the apparatus to be coarsely adjusted by a surgeon into the approximate position to facilitate proper alignment and/or allows a fine adjustment to be made by the surgeon using the manual adjustment knob, thereby giving the surgeon more control over the procedure. The manual adjustment feature also provides a safety override in the event of failure of the apparatus.

BRIEF DESCRIPTION OF THE DRAWINGS

[0018] Having summarized the invention, preferred embodiments thereof will now be described with reference to the accompanying drawings, in which:

[0019] FIG. **1***a* is an illustration of a prior art needle insertion apparatus;

[0020] FIG. **1***b* is another illustration of the prior art needle insertion apparatus of FIG. **1** *a;*

[0021] FIG. **2***a* is an ultrasound image showing needle insertion in saggital view during a prostate brachytherapy procedure;

[0022] FIG. **2***b* is an ultrasound image showing needle insertion in coronal view during a prostate brachytherapy procedure;

[0023] FIG. **2***c* is an ultrasound image showing needle insertion in transverse view with the needle projected during a prostate brachytherapy procedure;

[0024] FIG. **3***a* is a front perspective view of an embodiment of the apparatus of the present invention;

[0025] FIG. **3***b* is a rear perspective view of the embodiment of FIG. **3***a;*

[0026] FIG. **4***a* is a partial rear perspective view of the embodiment of FIG. **3***a* in a first position;

[0027] FIG. **4***b* is a partial rear perspective view of the embodiment of FIG. **3***a* in a second position;

[0028] FIG. **5***a* is a partial rear perspective view of the embodiment of FIG. **3***a*, overlaid with a schematic illustration of the pivot points in the positioning means;

[0029] FIG. **5***b* is a kinematic diagram of the embodiment of FIG. **3***a*, illustrating the reference geometry;

[0030] FIG. **6***a* is an exploded rear perspective view of the first positioning means of the embodiment of FIG. **3***a;*

[0031] FIG. **6***b* is a kinematics diagram corresponding to FIG. **6***a;*

[0032] FIG. **6***c* is another kinematics diagram corresponding to FIG. **6***a;*

[0033] FIG. **7** is an exploded rear perspective view of a portion of the first positioning means of the embodiment of FIG. **3***a;*

[0034] FIG. **8***a* is an exploded rear perspective view of the first positioning means of the embodiment of FIG. **3***a*, illustrating the locking means;

[0035] FIG. **8***b* is an exploded rear perspective view of the telescoping guide of the embodiment of FIG. **3***a*, further illustrating the locking means;

[0036] FIG. **9** is an exploded perspective view of an embodiment of a motor for use in the present invention;

[0037] FIG. **10** is an exploded perspective view of an embodiment of a needle release mechanism for use in the present invention;

[0038] FIG. **11** is an exploded perspective view of another embodiment of a needle release mechanism for use in the present invention;

[0039] FIG. **12** is a flowchart illustrating a method of use of the apparatus according to the present invention;

[0040] FIG. **13** is a continuation of the flowchart of FIG. **12**; and,

[0041] FIG. **14** is a further continuation of the flowchart of FIG. **12**.

DETAILED DESCRIPTION

[0042] Referring to FIGS. **1***a* and **1***b*, during prostate brachytherapy a needle **2** used for the implantation of radioactive seeds is inserted into the prostate **19** through the perineum **18** of a supine patient. Also shown are the rectum **16**, seminal vesicle **15**, bladder **14**, and scrotum **13**. An ultrasound transducer **10** is inserted trans-rectally to provide real-time images of the needle **2** during insertion. Preferably, the ultrasound transducer **10** comprises a side firing linear array transducer coupled to a rotational mover for creating three-dimensional (3-D) trans-rectal ultrasound (TRUS) images. In creating the 3-D TRUS images, the mover rotates the transducer about its longitudinal axis in 1° increments through a 100° arc to generate a fan-shaped scan. As the transducer is rotated, two-dimensional (2-D) images are digitized by a frame grabber and stored in computer memory for reconstruction into a 3-D image immediately following acquisition. Exemplary images are provided in FIGS. **2***a*, **2***b* and **2***c*. The generation of 3-D ultrasound images is further described in U.S. Pat. Nos. 5,842,473 and 5,964,707, which are hereby incorporated by reference.

[0043] A needle template **17** comprising a rectangular array of uniformly spaced apart holes is provided in a spatially fixed relationship to the ultrasound transducer **10**. By selecting an appropriate hole in the template **17**, one or more needles **2** may be inserted into the prostate **19** using the ultrasound imagery as a guide. This prior art method relies to a certain extent upon trial and error to achieve proper needle placement. Since it is often necessary to insert more than one needle, the angle of needle insertion must be selected to prevent interference between successive needles; the needle template **17** is inherently limited in the angles that can be attempted and it is difficult to achieve proper seed placement at extreme angles. Furthermore, in many cases the pubic arch occludes a portion of the prostate and relatively extreme angles are needed to place seeds behind the arch. For these reasons and others, the prior art needle placement method using a fixed template **17** has certain surgical limitations.

[0044] Referring to FIGS. **3***a*, **3***b*, **4***a* and **4***b*, a positionable guide apparatus according to the present invention comprises a telescoping guide **1** for insertion of a tool into a body (not shown). In the embodiment shown, the tool is a needle **2** for the implantation of radioactive seeds during prostate brachytherapy. A needle holder **3** having an aperture complementary to the needle diameter depends from the guide **1**. A needle axis **4** passes through the aperture and is parallel to and offset from a guide axis **5** passing through the telescoping portion **6** of the guide **1**. The guide **1** is suspended from a first positioning mechanism **20** and a second positioning mechanism **50** by means of a pair of hook joints **21** and **51**. When the first and second positioning means **20**, **50** are differentially moved, the hook joints (also known as universal joints) allow the guide **1** and, by definition, the guide axis **5** to be adjusted to any desired angular orientation in three dimensional space relative to an alignment axis **7** aligned with a central shaft **8**. Since the needle axis **4** is parallel with the guide axis **5**, it is accordingly also adjusted to the desired angle. A plurality of motors **9** are mounted on the central shaft **8** and are provided to facilitate automatic adjustment of the first and second positioning means **20**, **50**

under instruction of a computer (not shown) electrically connected with the apparatus. A position encoder **11** is mounted to the shaft **8** and provided in association with each motor **9** to feed back the rotational position of the motor to the computer. The central shaft **8** provides a fixed reference for all movements of the apparatus and can be used to secure the apparatus to a surgical table or other operating room fixture.

[0045] A transrectal ultrasound transducer **10** may optionally and preferably be provided for use in taking real-time images of the prostate during insertion of the needle **2**. The transrectal transducer **10** is preferably mounted to the central shaft **8** with an insertion axis **13** that is parallel to or coaxial with the alignment axis **7** to simplify calculation of the desired angle of tool insertion with reference to the centerline of the images being taken. The images are preferably fed back to the computer or computer system that is being used to automatically control the position of the guide means so that any changes required to the angle of insertion based upon the images may be readily implemented.

[0046] It should be noted that the entire apparatus is designed to be sterilizable in compliance with applicable medical device regulations; accordingly, all electrical connections are provided via conduits attached to the apparatus through fluid tight fittings **12** selected for compatibility with a variety of commonly known sterilization fluids and conditions.

[0047] At least one locking knob **60** is provided on each of the guide **1**, the first positioning means **20** and the second positioning means **50**. These locking knobs **60** may be rotated in order to selectively prevent their associated mechanism from moving after a desired tool insertion angle has been set. Choosing a desired combination of locking knobs **60** allows the surgeon a number of degrees of freedom in adjusting or selectively preventing the movement of the apparatus, for example to minimize the potential for inadvertent misalignment of the guide means after a desired angle has been set. The function of the locking knobs **60** in conjunction with their associated locking means will be further described hereinafter.

[0048] Referring to FIGS. **5***a* and **5***b*, a first plane A is provided orthogonal to the alignment axis **7** and a second plane B is provided orthogonal to the alignment axis **7** spaced apart from and parallel to the first plane. A first guide point, denoted as a, is located on the guide axis **5** at a position corresponding to the first positioning means **20** and a second guide point, denoted as b, is located on the guide axis at a position corresponding to the second positioning means **50**. The first and second positioning means **20**, **50** each comprise a means of adjusting the polar position of their respective guide points a, b on their respective planes A, B by rotation about the alignment axis **7**, as well as a means of adjusting the distance between the guide points a, b and the alignment axis **7**. In the embodiment shown, these two means are provided together in a parallelogram linkage, which will be further described hereinafter. The guide points a, b are located at the center of the hook joints **21**, **51** and the guide **1** is permitted to telescope between the guide points. As the first and second positioning means **20**, **50** are operated to adjust the location of the guide points a, b on their respective planes, the hook joints **21**, **51** and telescoping guide **1** enable the guide axis **5** to adopt a corresponding angular orientation with reference to the alignment axis **7**. A desired angle of tool insertion can therefore be attained by calculating the corresponding positions of the guide points a, b on the planes A, B in a polar co-ordinate system.

[0049] Referring additionally to FIGS. **6***a*, **6***b* and **7**, the parallelogram linkage of the first positioning means **20** comprises a first gear **22** with a first hub **28** rotationally mounted to the central shaft **8** concentric with the alignment axis **7** attached thereto by means of fasteners **30**. The center of rotation of the hub **28** about the alignment axis **7** is denoted schematically as i=1. The first hub **28** includes a first crank member **23** extending therefrom and having a first end of a first link **24** pivotally attached thereto at a point radially spaced apart from the alignment axis **7**; this point is denoted schematically as i=2. A second end of the first link **24** is pivotally attached to a first end of a second link **25** at a point denoted schematically as i=3.

[0050] A second gear **26** is attached to a stand-off bushing **31** by means of fasteners **32**. A spacer **33** is sandwiched between the second gear **26** and the stand-off bushing **31**. The second gear **26**, spacer **33** and stand-off bushing **31** all have concentrically aligned interior apertures **37** of sufficient diameter to fit over a posterior portion of the first hub **28** and are permitted to rotate relative to the first hub **28**. A posterior end of a stand-off **34** is attached to the stand-off bushing **31** such that the stand-off **34** is spaced apart from the shaft **8** and parallel thereto. The stand-off **34** comprises an anterior end **35** having a reduced diameter that is fitted within a complementary aperture **36** of a second crank member **27**. The second crank member **27** extends outwardly from a second hub **29** that is rotationally mounted to the central shaft **8** concentric with the alignment axis **7**. Rotation of the second gear **26** about the posterior portion of the first hub **28** causes the stand-off bushing **31** to co-rotate, which in turn causes the stand-off **34** to orbit about the shaft **8** and act upon the second crank member **27**, thereby inducing co-rotation of the hub **29** about the alignment axis **7**.

[0051] The second crank member **27** is pivotally attached to the second link **25** at a link pivot point, denoted schematically as i=4, that is radially spaced apart from the alignment axis **7** and located on the second link **25** between its first end and a second end. The second end of the second link **25** extends in a generally upward direction and is connected either directly or indirectly to the hook joint **21**. In the embodiment shown, a parallelogram linkage is formed by two sets of parallel members; the first link **24** and the second crank member **27** are parallel, along with the first crank member **23** and the second link **25**. It will be understood by persons skilled in the art that these members need not necessarily be parallel to achieve the function of a parallelogram linkage.

[0052] Returning briefly to FIG. **5***b*, the angle α_1 is the rotational angle of the first gear **22** defined between the first crank member **23** and a fixed reference perpendicular to the alignment axis **7**, whereas the angle β_1 is the rotational angle of the second gear **26** defined between the second crank member **27** and the same fixed reference. The distance between the first guide point a and the alignment axis **7** is defined by r_1 and the angle between r_1 and the fixed reference is depicted as θ_1. Rotation of the first and second gears **22**, **26** causes adjustment of the angles α_1 and β_1, resulting in “opening” or “closing” of the parallelogram linkage, and may be used to adjust the position of the first guide point a on the first plane A. Depending on the degree of counter or co-rotation of the first and second gears, this change in position may relate to the rotational position of the guide point a (a change in the angle θ_1), the distance between the guide point a and the axis of alignment (a change in r_1), or both simultaneously. For example, co-rotation of the first and second gears **22**, **26** by the same amount causes the sum of the angles α_1 and β_1 to remain constant; this results in a change in θ_1 without adjusting r_1. The second positioning means **50** functions in a similar manner to the first positioning means **20**.

[0053] Referring now to FIGS. **6*b*** and **6*c***, the simplified kinematics' model illustrated in FIG. **6*b*** shows a symbolic representation of the linkage and the nature of its interconnections, which can be simplified further by reducing all of the components into higher-order subassemblies. Applying the Kutzbach criterion:

$$l(n-1)+\sum_{i=1}^{j}(p_i-1)(f_i-l)$$

to the pinned parallelogram schematic reveals that this linkage can be reduced to a non-parametric planar joint of mobility **2**, where n is the total number of elements connected, f_i is the mobility of the joint and l is the mobility one link can have relative to the other. Since this is a planar linkage, each component can have a total of 3-degrees of freedom.

[0054] Reconstructing the kinematics' chain from the spatial components derived in the previous expression generates the simplified closed chain in FIG. **6*c***, where the planar joint P_L (Pl) has replaced the pinned parallelogram. Applying the Kutzbach criterion to the spatial linkage gives a total system mobility of **4**. In this case, the variable l in the spatial system has a total of 6 degrees of freedom.

[0055] The non-parametric model in FIGS. **6*b*** and **6*c*** reveals that the mobility of the system is unaffected by the type of joint represented by P_L (Pl). This element can represent a spherical linkage, or any other type of assembly with mobility **2**, to produce a variation on the parallelogram linkage. The length of each link can be dimensioned to suit an application where the operating envelope needs to be altered. The links and/or cranks need not necessarily be straight, but could be curved, bent, or any other shape.

[0056] All of the apparatus' functions are mechanically coordinated in such a manner where the mobility can be systematically reduced to zero degrees of freedom. Once the needle guide is in the desired position, the degree of freedom can be reduced to zero, thus making the device rigid. At this stage, the needle can be confidently inserted without concern that the apparatus will move. Five mechanical brakes are integrated into the design of the system to constrain each of its decoupled movements, allowing this progressive reduction in degrees of freedom. These brakes include a concentric ring brake and a parallel brake on each of the first and second positioning means **20**, **50** and a guide brake on the telescoping guide **1**, all of which will be further described hereinafter.

[0057] Referring to FIG. **8*a***, the front positioning means **20** includes a concentric ring brake integrated with the first hub **28**. The concentric ring brake comprises a locking knob **60** attached to a clamping screw **61** that exerts pressure upon a split ring **62** that resides inside the first hub **28** between bearings **63**. A snap ring **64** located within a recessed groove (not shown) retains the bearings **63** and split ring **62** within the first hub **28**. Rotating the locking knob **60** to tighten the clamping screw **61** causes the split ring **62** to collapse upon the base shaft **8**. The frictional force generated by this clamping action prevents rotation of the first hub **28** (and hence, the first gear **22**) about the alignment axis **7**; the angle α_1 therefore remains constant. However, the second gear **26** and its associated hub **29** are still permitted to rotate and the angle β_1 can still be adjusted. Application of the concentric ring brake therefore constrains the first positioning means **20** to function as a four-bar linkage. This constraint applies equally to manual or automatic adjustment and the motor **9** associated with the first gear **22** is prevented from operating while the motor associated with the second gear **26** is able to function in the normal manner.

[0058] The front positioning means **20** further includes a parallel brake comprising a first brake plate **65**, a second brake plate **66**, a locking knob **60** and a scissor screw **67**. Each brake plate **65**, **66** includes a pair of spaced apart apertures **68** for receiving first and second linkage pivot pins **69**, **70**. The first linkage pivot pin **69** is used to connect the second crank member **27** to the second link **25** at i=4 and the second linkage pivot pin **70** is used to connect the first link **24** to the second link **25** at i=3. The first linkage pivot pin **69** is secured to the second crank member **27** and the second linkage pivot pin **70** is secured to the first link **24**, while the second link **25** is permitted to pivot about the linkage pins **69**, **70** during movement of the first positioning means **20**. When the parallel brake is installed, the apertures **68** of the two plates are aligned and the brake plates **65**, **66** abut one another. Rotating the locking knob **60** to tighten the scissor screw **67** urges the plates to rotate in opposite directions about the linkage pivot pin **70**, creating a shearing action against the linkage pivot pin **69** that prevents it from rotating; this in turn constrains the parallelogram linkage such that the relative positions of the link and crank members is fixed and the sum of the angles α_1 and β_1 remains constant. When the parallel brake is engaged, the parallelogram linkage is constrained such that the first and second gears **22**, **26** are only able to rotate in unison (at the same speed and in the same direction) about the alignment axis **7**; consequently, only the angle θ_1 is permitted to change, without variation of r_1. This constraint applies equally to manual or automatic adjustment of the apparatus. When both the parallel brake and the concentric ring brake are applied, the first positioning means **20** is locked and the position of the first guide point a on the first plane A is fixed.

[0059] When the first positioning means **20** is locked, the second positioning means **50** may be able to move freely, partially constrained or fully constrained. Re-positioning of the second guide point b on the second plane B allows the trajectory of the needle **2** to be adjusted and is useful in maneuvering the needle around obstacles observed on the ultrasound image. Many surgeons prefer to conduct these trajectory adjustments manually, but they could also be completed automatically through operation of the motors **9** associated with the second positioning means **50** under instruction of the computer associated with the apparatus. Once the desired trajectory has been established, both the first and second positioning means **20**, **50** are normally locked to fix the trajectory and permit insertion of the needle **2** along the desired path without inadvertently misaligning the apparatus. Locking of the first and second positioning means **20**, **50** is also useful in the event of a failure in one or more of the motors **9** to ensure that no adverse outcomes result from any re-alignment of needle trajectory.

[0060] Referring to FIG. **8***b*, the telescoping guide brake comprises a locking knob **60** connected to a guide screw **71**. Rotation of the locking knob **60** causes the end of the guide screw **71** to tighten a concentric ring claim **72** that frictionally engages the circumference of an inner portion **73** of the telescoping guide **6** that is located within a complementary outer portion **74**. This restricts relative movement between the inner portion **73** and the outer portion **74** and prevents telescoping of the guide **1**.

[0061] Application of the telescoping guide brake prevents relative movement of the guide points a, b on their respective planes and constrains the first and second positioning means **20**, **50** to move in unison. This is particularly useful when both of the parallel brakes are engaged, as the first and second positioning means **20**, **50** are then constrained to rotate in unison about the alignment axis **7**. Once a desired trajectory has been established, application of the parallel brakes and guide brake allows the apparatus to be pivoted out of position, for example to replace a given needle with another type of needle or to continue with the procedure in the event of an electrical failure, without affecting the pre-established trajectory. Application of the telescoping brake by itself is also useful in regulating the speed of all of the motors **9** during the final stages of establishing a desired trajectory.

[0062] In manually adjusting the apparatus, the potential exists to move the first and/or second positioning means **20**, **50** out of synchronization with the rotational position of the motor(s) **9** and to damage the motor(s) through overdriving or backdriving. These problems are addressed in the present invention through certain design features that allow the apparatus to be both manually and automatically adjusted, even while the motor(s) are in operation. The ability to manually adjust the apparatus is important from a surgical point of view, in that it allows the surgeon to intervene either to complete the procedure in the event of an electrical failure of the apparatus and permits the surgeon to make both coarse and fine adjustments during a procedure. Coarse adjustments are useful in moving the apparatus to the approximate desired position, with final positioning being determined either by the computer or manually by the surgeon with reference to the ultrasound image using the fine adjustment knobs.

[0063] To enable the computer to synchronize the rotational position of a given motor **9** with the actual position of the first or second positioning means **20**, **50**, the apparatus employs a separate position encoder **11** in association with that motor's respective gear. For example, manual adjustment of the first positioning means **20** causes the first and/or second gears **22**, **26** to rotate; the amount of rotation is tracked by the position encoder **11** associated with that gear and is fed back to the computer. Since the motors **9** only operate if instructed to do so by the computer, the rotational position of the motor associated with a particular gear is also continuously tracked with reference to an initial physical calibration. By comparing the rotational position of a particular gear with the rotational position of its respective motor, the computer is able to synchronize the motor with the actual position of the positioning means so that further automatic adjustments to the location of the guide point on its respective plane produce the desired result. To further ensure positional accuracy, the motors **9** may each be equipped with another internal position encoder that feeds back the rotational position of the motor to the computer. This redundant motor position feedback helps ensure synchronization of the motor with the positioning means, even in the event of a software glitch or temporary power interruption to the computer system.

[0064] Referring to FIG. **9**, each motor **9** comprises a drive gear **80** for engagement with a complementary gear of the first or second positioning means, for example, the first or second gears **22**, **26**. The drive gear **80** is connected with a drive shaft **81** of the motor via an adjustable slip clutch mechanism **82**. Tightening the adjustment nut **83** of the slip clutch mechanism **82** increases the concentric clamping friction between the slip clutch mechanism and the drive shaft **81**. Normally, the drive shaft **81** and drive gear **80** are coupled through the slip clutch **82** and rotate together in unison; however, forces applied to either the drive shaft **81** or the drive gear **80** that exceed the pre-set clamping friction cause decoupling, resulting in independent rotation of the two. Excessive forces may arise through interference between the positioning means and a physical obstacle (for example, another piece of equipment or a body part) or through aggressive manual re-positioning of the apparatus. The slip clutch is a safety mechanism that prevents damage to the apparatus, particularly as a first line of defence in preventing backdriving or overdriving of the motor **9**, and reduces the likelihood of injury to patients or people operating the apparatus.

[0065] Each motor further comprises a drive housing **85** containing a sealed motor unit **86** having an armature **87** extending outwardly therefrom into an interior of the drive housing. A gear drive insert **88** is also inserted within the drive housing **85** and supports an unbalanced differential drive train which will be further described hereinafter. A fine adjustment knob **84** is placed over the drive housing **85** and the gear drive insert **88** is keyed thereto by means of pins **89**. A snap ring **90** resides within a circumferential interior groove of the fine adjustment knob **84** and abuts the exterior face of the gear drive insert **88** to retain the fine adjustment knob in position. The drive shaft **81** extends outwardly from the gear drive insert **88** and is permitted to rotate relative thereto upon operation of the motor unit **86**.

[0066] The motor unit **86** has a high resistance to externally induced rotation of the armature **87**; in effect, the motor unit **86** is locked when not in operation, preventing backdriving during coarse manual adjustment. Similarly, the high resistance to external induced rotation prevents overdriving while the motor is in operation, permitting fine manual adjustment to take place concurrently with automatic adjustment if so desired. This resistance to rotation can be imparted either electrically, mechanically, or both. For example, the motor unit **86** may comprise a DC motor with a large internal magnetic coupling force that prevents undesired external rotation of the armature **87**. In other embodiments, the motor unit **86** may comprise a stepping motor with similar features. The motor unit **86** may include a large internal gear ratio to mechanically amplify its resistance to rotation of the armature **87**. In one embodiment, the internal gear ratio is from 300:1 to 900:1, preferably from 500:1 to 700:1, more preferably about 600:1. It is desirable the motor chosen for the motor unit **86** permits quantifiable rotation of the armature **87** so that an exact movement of the positioning means may be achieved under computer instruction. The motor unit **87** is sealed and resides within a sealed motor base **91** equipped with fluid tight connections **12** for conduits containing electrical power and/or positional signals. This permits the entire apparatus to be sterilized without damaging its electrical components.

[0067] Although the high resistance of the motor unit **86** to externally induced rotation is useful in preventing damage to the motor, it would also prevent rotation of the fine adjustment knob **84** if directly coupled to the armature **87**. In order to permit manual adjustment to occur, the fine adjustment knob **84** is connected to the armature **87** through an unbalanced differential drive train. The unbalanced differential drive train comprises a set of at least four drive gears. The armature **87** is equipped with a first drive gear **92** enmeshed with a second drive gear **93**. The second drive gear **93** is located on a common shaft with a third drive gear **94** that is enmeshed with a fourth drive gear **95** mounted on the drive shaft **81**. The gear ratio of the differential drive train between the first drive gear **92** and the fourth drive gear **95** is preferably greater than one, more preferably greater than two, so that a rotation of the armature **87** translates into only a partial rotation of the drive shaft **81**. For example, in one embodiment, the first drive gear **92** has twelve teeth, the second drive gear **93** has sixteen teeth (gear ratio 1:0.75=4:3), the third drive gear **94** has twelve teeth and the fourth drive gear **95** has sixteen teeth (gear ratio 1:0.75=4:3), producing an overall gear ratio of 16:9=1.78. In another embodiment, the first drive gear **92** has twelve teeth, the second drive gear **93** has twenty teeth (gear ratio 1:0.6=5:3), the third drive gear **94** has twelve teeth and the fourth drive gear **95** has twenty teeth (gear ratio 1:0.6=5:3), producing an overall gear ratio of 25:9=2.78.

[0068] During manual rotation of the fine adjustment knob **84**, the gear drive insert **88** orbits about the armature **87** by virtue of its direct connection to the knob through pins **89**. Since the motor unit **86** has a high resistance to externally induced rotation of the armature **87**, the first drive gear **92** remains fixed in position. Accordingly, the second and third drive gears **93**, **94** co-rotate in the same direction as the adjustment knob **84**, while the fourth drive gear **95** counter-rotates. Although this has a tendency to cause the drive shaft **81** to rotate in the opposite direction to the rotation of the fine adjustment knob **84**, due to the high gear ratio of the unbalanced differential drive train this counter-rotation is small compared with the orbital movement of the gear drive insert **88**. The net effect is to cause the drive gear **80** to rotate in the same direction as the fine adjustment knob **84**. This in turn permits manual movement of the positioning means, without backdriving or overdriving the motor unit **86**, allowing manual adjustment to take place even while the motor unit is in operation.

[0069] The unbalanced nature of the drive train arises from the planetary relationship of the first drive gear **92** with the second drive gear **93** and the fourth drive gear **95** with the third drive gear **94**. This planetary relationship tends to urge the gears out of enmeshment, creating a slightly non-parallel alignment between the axes of rotation of the gears. The wedging action produced by this non-parallel alignment causes a great deal of friction between the drive gears, even when not in operation. This friction is important in maintaining the positioning means in an upright orientation. Without this friction, the fine adjustment knob **84** could spin freely and the weight of the positioning means would backdrive the gear drive insert **88**, causing the positioning means to collapse under its own weight. However, during manual fine adjustment, the friction of the unbalanced drive train is easily overcome and the surgeon is permitted to make the desired changes to the positioning means.

[0070] In performing certain procedures, in particular brachytherapy or needle biopsy procedures, it is often necessary to insert more than one tool (eg: needle, scope, etc.) into the body simultaneously. To facilitate these types of procedures, it would be desirable that the apparatus allows the tool to be released once inserted to the correct position in order that the apparatus is made free for use in inserting a subsequent tool. In this manner, a plurality of tools can be inserted to the desired position simultaneously during a procedure.

[0071] Referring to FIG. **10**, a first embodiment of a tool release mechanism includes a stand-off **100** fixedly mounted to the first positioning means **20** proximal the hook joint **21** and extending towards the front of the apparatus. At the anterior end of the stand-off **100** is fixedly mounted a release block **101** having a pair of curved fingers **102** provided at one end thereof. The curved fingers **102** partially enclose an aperture **103** that is oversized compared with the tool (in this case, the needle **2**) that is to be inserted therethrough. The non-enclosed portion of the aperture **103** provides a slotted chordal opening that is large enough to permit the needle **2** to be removed from the aperture in a direction perpendicular to the axis of insertion **4**. A pair of side brackets **110** is secured to either side of the release block **101**. Each side bracket **110** includes a crescent shaped slot **111** with an open end that is roughly aligned with the slotted chordal opening. When inserted within the aperture **103**, the needle **2** seats at the apex of the crescent-shaped slots **111**. Residing within the aperture **103** is a cylindrical clamping block **104** having an elliptical interior slot **105** with an upper end that is offset from the center of the aperture. Upon rotation of the clamping block **104**, the upper end of the slot **105** approaches the center of the aperture **103** until it engages the needle **2** and wedges it against the apex of the crescent shaped slots **111**. The clamping block **104** is counter-rotated slightly prior to performing a procedure in order to un-lock the needle **2** and permit longitudinal sliding of the needle **2** along the axis of insertion **4**. The release mechanism is oriented such that, when the needle **2** is secured within the aperture **103**, the axis of insertion **4** is parallel with the guide axis **5**.

[0072] To facilitate rotation of the clamping block **104**, a block crank **112** is located at the center of the block and extends perpendicularly to its axis of rotation. A slider block **106** is confined by slide plates **107** to slide along the release block **101** in response to screw mechanism **108**. The screw mechanism **108** is equipped with stops **109** to prevent inadvertent over-tightening or disassembly of the release mechanism. Operation of the screw mechanism **108** causes the slider block to engage the crank **112** when slid along the release block **101**, thereby rotating the clamping block **104** and securing the needle **2** within the aperture **103**.

[0073] Referring to FIG. **11**, in a second embodiment of a tool release mechanism a mounting block **220** is provided that permits the telescoping guide **6** to move therewithin along the guide axis **5**. The mounting block **220** includes a T-shaped slot for receiving a complementary T-shaped mounting bar **222**. The T-shaped mounting bar **222** is able to slide within the slot parallel to the guide axis **5**. At the anterior end of the mounting bar **222** is fixedly mounted a release block **201** having a pair of curved fingers **202** provided at one end thereof. The curved fingers **202** partially enclose an aperture **203** that is oversized compared with the tool (in this case, the needle **2**) that is to be inserted therethrough. The non-enclosed portion of the aperture **203** provides a slotted chordal opening that is large enough to permit the needle **2** to be removed from the aperture in a direction perpendicular to the axis of insertion **4**. A pair of side brackets **210** is secured to either side of the release block **201**. Each side bracket **210** includes a crescent shaped slot **211** with an open end that is roughly aligned with the slotted chordal opening. When inserted within the aperture **203**, the needle **2** seats at the apex of the crescent-shaped slots **211**. Residing within the aperture **203** is a cylindrical clamping block **204** having an elliptical interior slot **205** with an upper end that is offset from the center of the aperture. Upon rotation of the clamping block **204**, the upper end of the slot **205** approaches the center of the aperture **203** until it engages the needle **2** and moves it toward the apex of the crescent shaped slots **211**. The release mechanism is oriented such that, when the needle **2** is secured within the aperture **203**, the axis of insertion **4** is parallel with the guide axis **5**.

[0074] The clamping block **204** is equipped with a threaded end **230** that engages with complementary interior threads within the aperture **203** to move the block longitudinally along the axis of insertion **4** upon rotation. The clamping block **204** includes a central shoulder **231** that engages adjustable stops **209** as it is advanced or retracted along the axis of insertion **4**. These stops **209** may be set to correspond to a particular diameter of needle **2** so that the clamping block **204** does not wedge the needle completely against the apex of the crescent-shaped slots **211**. This obviates the need for loosening the clamping block **204** prior to performing a procedure.

[0075] To facilitate rotation of the clamping block **204**, a block crank **212** is located at the center of the block on the shoulder **231** and extends perpendicularly to the axis of rotation. A slider block **206** is confined by slide plates **207** to slide along the release block **201** in response to longitudinal movement of a slide mechanism **208**. Pushing or pulling the slide mechanism **208** causes it to act directly upon the block crank **212**, thereby causing rotation of the clamping block **204**. The slide mechanism **208** is permitted to operate between the two pre-set stop points **209** to control the degree of clamping achieved by the clamping block **204**. The slide mechanism **208** may optionally include a bayonet style lock in place of or in addition to the fixed stops **209**; this allows a plurality of clamping positions to be achieved in order to accommodate a plurality of different needle diameters and provides positive confirmation that the needle is secured within the aperture **203**.

[0076] By loosening the locking knob **260**, the second embodiment advantageously permits the entire release mechanism to be moved along the guide axis **5** so that it is either closer to or further away from the patient. Also, the second embodiment permits the entire release mechanism to be removed and replaced, for example in the event that a tool is needed with a larger diameter than can be accommodated by the aperture **203**. The stops **209** are pre-set to a desired clamping condition, thereby obviating the need for releasing the needle by counter-rotation prior to performing the procedure. This advantageously increases the speed with which a needle may be inserted or removed from the mechanism as compared with the first embodiment, as the screw mechanism **108** is relatively time consuming to operate. However, the screw mechanism **108** has a wide range of adjustment and permits precise setting of the "feel" of the needle **2** as it slides through the aperture **103**. The features of the first and second embodiments may be combined in various sub-combinations in order to attain desired advantages.

[0077] During a prostate brachytherapy procedure, the ultrasound transducer **10** with internal rotation motor assembly is mounted on the base shaft **8** and inserted into the rectum, as is conventionally known. The surgeon, a physician or another healthcare professional then acquires a pre-therapy or pre-biopsy 3D TRUS image by rotating the transducer about its longitudinal axis, while 2D ultrasound images are digitally captured by the computer and reconstructed into a 3D image, as previously described. The 3D TRUS image is then viewed by the person acquiring the image and optionally saved to computer memory, as shown in FIG. **12**. The 3D TRUS image can then be recalled at any time, for example to plan the surgical procedure using therapy or biopsy planning software, during the procedure, or afterwards in comparison with post-operative images.

[0078] Referring to FIG. **13**, after the therapy or biopsy procedure is planned, the robot-aided therapy or biopsy procedure progresses as shown in FIGS. **13** and **14**. The surgeon selects a target (using the dose plan or biopsy plan) in the 3D TRUS image of the prostate. The 3D co-ordinates of the target are determined based upon a calibration between the coordinate systems of the apparatus and the 3D TRUS image. A path is then calculated for needle insertion that will reach the desired target. The path may be a straight line along a single vector or a compound path comprising multiple vectors; the latter is particularly useful in cases where interference from the pubic arch prevents direct access to the target. The computer then instructs the motors **9** to move the guide points a and b to the corresponding locations on their respective planes so that the needle will be inserted along the desired path. In addition, the computer may cause the ultrasound transducer **10** to rotate so that the needle can be viewed more clearly in the 2D ultrasound images as the needle is inserted. Alternatively, if the needle is to be inserted into the prostate on an oblique trajectory with respect to the ultrasound transducer axis, then continuous 3D TRUS images are acquired of the region through which the needle is inserted. In both situations, automated needle segmentation is performed to provide the surgeon with real-time or near-real time information on the trajectory of the needle during the procedure.

[0079] After the needle has been inserted into the prostate to the satisfaction of the surgeon (either manually, with automated assistance, or a combination thereof), the therapy is delivered through the needle or the lesion is biopsied. In the latter, a device such as a spring-loaded biopsy needle may be used. As shown in FIG. **2**, the image of the needle in the prostate can be recorded immediately while the therapy or biopsy is being delivered, and/or afterward. In a preferred embodiment, the computer automatically finds, records and displays the location of the needle tip on the 3D image as an aid to the surgeon.

[0080] As shown in FIGS. **12** and **14**, if another needle insertion is required to deliver therapy or biopsy to another location, the procedure is repeated. This process is repeated until the therapy or biopsy procedure is completed.

[0081] The foregoing describes preferred embodiments of the invention and is not to be construed in a limiting sense. Variants or mechanical equivalents to the way in which the invention works will be apparent to those skilled in the art, along with further features and sub-combinations, and are intended to be encompassed by the following claims.

1) An apparatus for the three-dimensional positioning of a guide for manual insertion of a medical tool within a body, the apparatus comprising:

a) an alignment axis;

b) a guide axis aligned with the guide;

c) a first plane orthogonal to the alignment axis;

d) a second plane orthogonal to the alignment axis and parallel to the first plane, the second plane spaced apart from the first plane along the alignment axis;

e) a first positioning means for positioning a first guide point on the first plane, the guide axis passing through the first guide point;

f) a second positioning means for positioning a second guide point on the second plane, the guide axis passing through the second guide point; and,

g) the first and second positioning means separately adjustable in order to provide a pre-determined angular relationship between the guide axis and the alignment axis.

2) The apparatus according to claim **1**, wherein the first and/or second positioning means are manually, automatically, or both manually and automatically adjustable.

3) The apparatus according to claim **1**, wherein the first positioning means comprises a means of adjusting the distance between the first guide point and the alignment axis and a means of adjusting the polar position of the first guide point on the first plane by rotating a first gear about a first rotation axis parallel to or collinear with the alignment axis.

4) The apparatus according to claim **3**, wherein the means of adjusting the distance between the first guide point and the alignment axis comprises:

a) a first link member having a first end pivotally attached to a first crank member of the first gear and having a second end;

b) a second gear spaced apart from the first gear along the alignment axis and rotatable about a second rotation axis parallel to or collinear with the alignment axis, the second gear having a second crank member;

c) a second link member having a first end and a second end, the first end of the second link member pivotally attached to the second end of the first link member, the second link member pivotally attached between its first and second ends to the second crank member at a link pivot point; and,

d) the first and second gears rotatable to adjust the distance between the first guide point and the alignment axis.

5) The apparatus according to claim **4**, wherein the first link member and the second crank member are parallel and wherein the first crank member and second link member are parallel, thereby forming a parallelogram linkage, and wherein the first and second rotation axes are collinear.

6) The apparatus according to claim **4**, wherein the first positioning means comprises a first locking means to selectively prevent movement of the second link member relative to the first link member about the link pivot point.

7) The apparatus according to claim **6**, wherein the first positioning means comprises a second locking means to selectively prevent movement of at least the first or second gear about its respective rotation axis.

8) The apparatus according to claim **7**, wherein the second positioning means is identical to the first positioning means.

9) The apparatus according to claim **4**, wherein the second end of the second link member comprises a universal joint or a spherical joint for connecting the guide means with the first link member.

10) The apparatus according to claim **1**, wherein the guide telescopes between the first and second guide points.

11) The apparatus according to claim **10**, wherein the guide is lockable to selectively prevent telescoping.

12) The apparatus according to claim **1**, wherein the guide includes release means operable to release the tool from the guide without adjusting the position of the tool or the apparatus.

13) The apparatus according to claim **1**, wherein the tool is a needle and wherein the needle passes through the guide means along the guide axis.

14) The apparatus according to claim **1**, wherein the angular relationship between the guide axis and the alignment means is determined with reference to a medical image of an interior of the body.

15) The apparatus according to claim **1**, wherein the apparatus further comprises at least one motor connected to the first positioning means and a computer interconnection means for use in automatically adjusting the position of the guide using the motor.

16) The apparatus according to claim **15**, wherein the apparatus comprises two motors connected to the first positioning means and two motors connected to the second positioning means.

17) An apparatus for the three-dimensional positioning of a guide for manual insertion of a medical tool within a body, the apparatus comprising:

a) at least one positioning means attached to the guide;

b) at least one motor connected to each positioning means, the motor comprising:

  i) an armature;

  ii) a gear shaft connected with the armature through a set of enmeshed gears;

  iii) a manual adjustment knob connected with the gear shaft;

  iv) a slip clutch connecting the gear shaft and the positioning means; and,

c) the manual adjustment knob rotatable to manually adjust the positioning means while the motor is in operation without overdriving the motor.

18) The apparatus of claim **17**, wherein the positioning means is both manually and automatically adjustable.

19) The apparatus of claim **17**, wherein the set of enmeshed gears comprises a differential drive train having a gear ratio greater than one.

20) The apparatus of claim **17**, wherein the apparatus comprises a position encoder for determining the rotational position of the gear shaft.

21) A method of positioning a guide for manual insertion of a medical tool within a body, the method comprising:

a) obtaining a medical image of an interior of the body;

b) providing the medical image to a computer in a digital form;

c) determining with the computer a desired angle for manual insertion of the tool based upon analysis of the image; and,

d) automatically positioning the guide at the desired angle using instructions provided by the computer to a motorized guide positioning apparatus.

22) The method according to claim **21**, wherein the method further comprises manually positioning the guide proximal the desired angle prior to automatically positioning the guide.

23) The method according to claim **21**, wherein the method further comprises manually adjusting the position of the guide while automatically positioning the guide.

24) The method according to claim **21**, wherein the tool is installed within the guide and wherein the method further comprises manually releasing the tool from the guide without adjusting the position of the tool or the guide.

25) The method according to claim **21**, wherein the medical image comprises a three-dimensional ultrasound image.

* * * * *

Appendix D: Health Canada, Ethics Approval Notices and Letters of Information for the clinical prostate biopsy studies.

Health Canada Santé Canada

Canada

Health Products and Food Branch
Direction générale des produits de santé et des aliments

Therapeutic Products Directorate

Direction des produits thérapeutiques

NOTRE MISSION : Nous contribuons à la santé des Canadiens et des Canadiennes et à l'efficacité du système de soins de santé en évaluant, en temps opportun, l'innocuité, l'efficacité et la qualité des produits pharmaceutiques et des instruments médicaux.

OUR MISSION: We contribute to the health of Canadians and to the effectiveness of the health care system by assessing the safety, efficacy and quality of pharmaceuticals and medical devices in a timely manner.

If you receive this fax in error, please advise the sender immediately.
Si vous recevez cette télécopie par erreur, veuillez en aviser immédiatement l'expéditeur.

TO/À

Name/Nom : **Kerry Knight**
Technical Specialist (RA)

Date : 27 March 2008

Organization/Organisme : The John P. Robarts Research Institute

Tel./Tél. :

Fax/Télécopieur :

No. of Pages, including this page/N° de pages, incluant cette page : 3

FROM/DE

Name/Nom : **Dragana Pantic**

E-Mail/Courriel :

Tel./Tél. :

Fax/Télécopieur :

TITLE	Acting Manager / Gestionnaire intérimaire	TITRE
Division	Device Evaluation Division / Division de l'évaluation des matériels	Division
Bureau	Medical Devices Bureau / Bureau des matériels médicaux	Bureau
Directorate	THERAPEUTIC PRODUCTS DIRECTORATE / DIRECTION DES PRODUITS THÉRAPEUTIQUES	Direction
Room		Pièce
Building		Édifice
Location		Lieu
Address Locator		Localisateur d'adresse
City/Province		Ville/Province
Postal Code		Code postal

MESSAGE

Health Canada / Santé Canada
Health Products and Food Branch / Direction générale des produits de santé et des aliments

Therapeutic Products Directorate

Date: MAR 2 8 2008

Application No. 129798

Kerry Knight

Investigational Testing Authorization - Class III

Dear Kerry Knight:

This is in reference to your application for Authorization to conduct Investigational Testing in Canada, received on 12 March 2008, and submitted pursuant to Part 3 of the *Medical Devices Regulations*. This pertains to the following;

Protocol:	An Improved Transrectal Ultrasound-guided Biopsy Procedure; Protocol Number: Rev. 2; Consent Dated: Ver. 5; 28 January 2008.
Objective:	(a) Validate a novel adaptation of standard 2D ultrasound for producing three-dimensional (3D) biopsy data, and (b) Determine if the results will produce data similar to general 3D ultrasound for recording the locations of biopsy cores, which are removed from the prostate during clinical biopsy procedures.
Device:	Three-Dimensional (3D) Ultrasound Prostate Biopsy Imaging System.
Number of devices:	One (1)
Number of subjects	Forty-five (45).

The information has been reviewed and you are hereby authorized under Section 83 of the *Medical Devices Regulations* to sell the subject device for investigational testing to the investigator(s) listed in the attached Appendix 1.

Sections 86, 87 and 88 of the *Medical Devices Regulations* impose additional requirements regarding the advertisement, record keeping and labelling of devices involved in investigational trials. Please advise the Bureau of any changes to the device, protocol or list of investigators. Any changes to the device or protocol that fall outside the scope of the risk assessment of this protocol will require a new application.

Yours sincerely,

Director
Medical Devices Bureau

RGR/mw
Attach.

Canada

Appendix 1 - List of Investigator(s)

Application No. 129798

Date: MAR 2 8 2008

Jonathan Izawa, MD, FRCPC

Office of Research Ethics
The University of Western Ontario

Use of Human Subjects - Ethics Approval Notice

Principal Investigator: Dr. J.I. Izawa
Review Number: **12669** **Revision Number:**
Protocol Title: An Improved Transrectal Ultrasound-guided Biopsy Procedure
Department and Institution: Urology, London Health Sciences Centre
Sponsor: CIHR-CANADIAN INSTITUTE OF HEALTH RESEARCH
Ethics Approval Date: September 26, 2006 **Expiry Date:** October 31, 2008
Documents Reviewed and Approved: UWO Protocol, Letter of information & consent form dated September 18/06
Documents Received for Information:

This is to notify you that The University of Western Ontario Research Ethics Board for Health Sciences Research Involving Human Subjects (HSREB) which is organized and operates according to the Tri-Council Policy Statement and the Health Canada/ICH Good Clinical Practice Practices: Consolidated Guidelines; and the applicable laws and regulations of Ontario has reviewed and granted full board approval to the above named research study on the approval date noted above. The membership of this REB also complies with the membership requirements for REB's as defined in Division 5 of the Food and Drug Regulations.

This approval shall remain valid until the expiry date noted above assuming timely and acceptable responses to the HSREB's periodic requests for surveillance and monitoring information. If you require an updated approval notice prior to that time you must request it using the UWO Updated Approval Request Form.

During the course of the research, no deviations from, or changes to, the protocol or consent form may be initiated without prior written approval from the HSREB except when necessary to eliminate immediate hazards to the subject or when the change(s) involve only logistical or administrative aspects of the study (e.g. change of monitor, telephone number). Expedited review of minor change(s) in ongoing studies will be considered. Subjects must receive a copy of the signed information/consent documentation.

Investigators must promptly also report to the HSREB:
a) changes increasing the risk to the participant(s) and/or affecting significantly the conduct of the study;
b) all adverse and unexpected experiences or events that are both serious and unexpected;
c) new information that may adversely affect the safety of the subjects or the conduct of the study.

If these changes/adverse events require a change to the information/consent documentation, and/or recruitment advertisement, the newly revised information/consent documentation, and/or advertisement, must be submitted to this office for approval.

Members of the HSREB who are named as investigators in research studies, or declare a conflict of interest, do not participate in discussion related to, nor vote on, such studies when they are presented to the HSREB.

Chair of HSREB: Dr. John W. McDonald
Deputy Chair: Susan Hoddinott

Version 4 August 20th 2007

London Health Sciences Centre

LETTER OF INFORMATION FOR PARTICIPANTS

Title of Study: An Improved Transrectal Ultrasound-guided Biopsy Procedure
Investigators: Drs. Jonathan I. Izawa, Joseph L. Chin, Aaron Fenster, and Cesare Romagnoli.

INTRODUCTION

You are invited to participate in this research study, which is for men who have been scheduled for prostate biopsy, which uses standard 2-dimensional ultrasound imaging to guide the biopsy needle. The prostate biopsy procedure is the standard care for men to test for prostate cancer, and it will be fully explained by Dr. Izawa, your urologist, or by Dr. Cesare Romagnoli, the radiologist. You will be able to ask Dr Izawa or Dr. Romagnoli, or their staff any questions you might have about your procedure. This research study involves taking some extra ultrasound images during the same session as your prostate biopsy.

PURPOSE

We are testing a new method of ultrasound imaging during prostate biopsy on 15 men to be done at London Health Sciences Centre. During standard prostate biopsy, the doctor can see the biopsy needle by using ultrasound and this helps to guide the needle into the correct place. The new method of ultrasound imaging we are trying will make 3-dimensional ultrasound images from standard 2-dimensional images by using one of three different tracking systems. Two of these systems are approved commercial devices, and one is an experimental, mechanical tracking system developed by Dr. Aaron Fenster's laboratory. All these tracking devices are entirely harmless and simply track the position of the biopsy needle during the biopsy procedure. Which tracking system is used will depend on which one performs the best during biopsy procedures. Each tracking system makes a map of exactly where the biopsy samples were taken in the prostate, so if patients need a repeat biopsy in the future, the doctor will be able to choose different areas to place the biopsy needle. This should improve the chances of finding small tumours that might have been missed during the first biopsy. We think this new method will prove to be easier and more accurate than the current method, which only makes 2-dimensional ultrasound images.

RESEARCH PROCEDURES FOR THIS STUDY

The procedure will be the same as for a regular prostate biopsy, but we will take a few extra regular ultrasound images, using one of the tracking devices so they can be made into 3D images. We will then do a real 3-dimensional ultrasound exam, so we can compare it to the one we will make with the tracking device.

The only difference between the regular 2-dimensional and the 3-dimensional ultrasound is that the 3-dimensional exam takes a little longer because the computer takes time to produce the 3-dimensional images. There are no extra visits to the hospital and the research is carried out during your prostate biopsy procedure. The extra time involved for this research study will be about 15 minutes on top of the time for your prostate biopsy, and you will remain in the same position for the 2-dimensional and the 3-dimensional ultrasound examinations.

RISKS AND DISCOMFORTS TO YOU IF YOU PARTICIPATE IN THIS STUDY
There are no known risks to the use of ultrasound in this way, and the procedure is completely painless.

ALTERNATIVES TO STUDY PARTICIPATION
The alternative to taking part in this study is to not take part.

THE BENEFITS TO YOU IF YOU PARTICIPATE IN THIS STUDY
There is no evidence that being part of this study will help your treatment, but the results may help future patients, because we believe this new method will give more information on the cancerous areas in the prostate and exactly where they are located. If this research study is successful, it will improve the chances of finding small cancerous tumours if a patient needs repeated biopsies.

CONFIDENTIALTY
Any information obtained from this study will be kept confidential and your name will not be identified in any way when the results are presented or published. The ultrasound images that are taken will be kept in a computer and your name and any other personal information will be made invisible. Any other information from this study will be kept in locked filing cabinets and only the research team and the University of Western Ontario Health Sciences Research Ethics Board (HSREB) will have access to the data. Representatives of HSREB may require access to your study-related records or may follow up with you to monitor the conduct of the study.

VOLUNTARY PARTICIPATION
Your participation in this study is voluntary. You may refuse to participate or withdraw from the study at any time with no effect on your future care.

WHO TO CONTACT IF YOU HAVE ANY QUESTIONS
If you have any questions, please feel free to contact us

If you have a question about your rights as a research participant or about the conduct of this study, you can contact the Vice President of Research c/o Lawson Health Research Institute (LHRI).

If you are already participating in another research study, please inform Dr. Izawa.

Please Note: You do not waive any legal rights by signing the consent form.
You will be given a copy of this letter of information and consent form to keep once it has been signed.

Version 4 August 20th 2007

London Health Sciences Centre

Consent Form for Participation

Title of Study: An Improved Transrectal Ultrasound-guided Biopsy Procedure

Investigators:
Drs. Jonathan I. Izawa, Joseph L. Chin, Aaron Fenster, and Cesare Romagnoli

I have read the letter of information, have had the nature of the study explained to me and I agree to participate. All questions have been answered to my satisfaction.

Dated in London, this__________day of________________, 20____

______________________________	______________________________
(Signature of Participant)	(Print name of Participant)
______________________________	______________________________
(Signature of Researcher)	(Print name of Researcher)
______________________________	______________________________
(Signature of Person Obtaining the Consent of the Participant)	(Print name of Person Obtaining the Consent of the Participant)

____
Patient Initials

Office of Research Ethics
The University of Western Ontario

Use of Human Subjects - Ethics Approval Notice

Principal Investigator:	Dr. J.I. Izawa		
Review Number:	**12669**	**Revision Number:**	**2**
Review Date:	March 5, 2008	**Review Level:**	Expedited
Protocol Title:	An Improved Transrectal Ultrasound-guided Biopsy Procedure		
Department and Institution:	Urology, London Health Sciences Centre		
Sponsor:	CIHR-CANADIAN INSTITUTE OF HEALTH RESEARCH		
Ethics Approval Date:	March 19, 2008	**Expiry Date:**	December 31, 2009
Documents Reviewed and Approved:	revised study end date, revised sample size, revised Letter of Information and Consent version 5 dated January 28, 2008		
Documents Received for Information:			

This is to notify you that The University of Western Ontario Research Ethics Board for Health Sciences Research Involving Human Subjects (HSREB) which is organized and operates according to the Tri-Council Policy Statement: Ethical Conduct of Research Involving Humans and the Health Canada/ICH Good Clinical Practice Practices: Consolidated Guidelines; and the applicable laws and regulations of Ontario has reviewed and granted approval to the above referenced revision(s) or amendment(s) on the approval date noted above. The membership of this REB also complies with the membership requirements for REB's as defined in Division 5 of the Food and Drug Regulations.

The ethics approval for this study shall remain valid until the expiry date noted above assuming timely and acceptable responses to the HSREB's periodic requests for surveillance and monitoring information. If you require an updated approval notice prior to that time you must request it using the UWO Updated Approval Request Form.

During the course of the research, no deviations from, or changes to, the protocol or consent form may be initiated without prior written approval from the HSREB except when necessary to eliminate immediate hazards to the subject or when the change(s) involve only logistical or administrative aspects of the study (e.g. change of monitor, telephone number). Expedited review of minor change(s) in ongoing studies will be considered. Subjects must receive a copy of the signed information/consent documentation.

Investigators must promptly also report to the HSREB:

a) changes increasing the risk to the participant(s) and/or affecting significantly the conduct of the study;
b) all adverse and unexpected experiences or events that are both serious and unexpected;
c) new information that may adversely affect the safety of the subjects or the conduct of the study.

If these changes/adverse events require a change to the information/consent documentation, and/or recruitment advertisement, the newly revised information/consent documentation, and/or advertisement, must be submitted to this office for approval.

Members of the HSREB who are named as investigators in research studies, or declare a conflict of interest, do not participate in discussion related to, nor vote on, such studies when they are presented to the HSREB.

Chair of HSREB: Dr. John W. McDonald

robarts
RESEARCH

To: Research Ethics Board

Date: January 28, 2008

From: Jackie Williams

Re: UWO Ethics Number 12669

Project Title: An Improved Transrectal Ultrasound-guided Biopsy Procedure

PI: Dr. Jonathan Izawa

Co-Investigators:
Dr. Joseph L. Chin, Dr. Aaron Fenster

Revision to Original Protocol

Study Design or Methods:

We would like to add 30 patients to the original number of 15. The original number was based on the research being a pilot study to test the feasibility of three different ultrasound tracking devices. The data thus far have shown that the tracking device developed in Dr. Aaron Fenster's laboratory is equivalent to the other two commercial trackers. We would like to extend the planned statistical analysis to include Analysis of Variance and regression/correlation analysis at the 0.05 alpha level. According to the Sample Size Table in Jacob Cohen's "A Power Primer", (Psychological Bulletin, 1992, Vol. 112, No. 1, pp155-159), the number of subjects required is 45. These changes will make the research more publishable.

Extension to the Study End Date:

We are requesting a new end of study date of December 31st 2009 to test the extra number of patients.

Changes to the Letter of Information

We have added the new number of participants in the Letter of Information.

Version 6 June 4th 2008

London Health Sciences Centre

LETTER OF INFORMATION FOR PARTICIPANTS

Title of Study: An Improved Transrectal Ultrasound-guided Biopsy Procedure
Investigators: Drs. Jonathan I. Izawa, Joseph L. Chin, Aaron Fenster, and Cesare Romagnoli.

INTRODUCTION

You are invited to participate in this research study, which is for men who have been scheduled for prostate biopsy, which uses standard 2-dimensional ultrasound imaging to guide the biopsy needle. The prostate biopsy procedure is the standard care for men to test for prostate cancer, and it will be fully explained by Dr. Izawa, your urologist, or by Dr. Cesare Romagnoli, the radiologist. You will be able to ask Dr Izawa or Dr. Romagnoli, or their staff any questions you might have about your procedure. This research study involves taking some extra ultrasound images during the same session as your prostate biopsy.

PURPOSE

We are testing a new method of ultrasound imaging during prostate biopsy on 45 men to be done at London Health Sciences Centre. During standard prostate biopsy, the doctor can see the biopsy needle by using ultrasound and this helps to guide the needle into the correct place. The new method of ultrasound imaging we are trying will make 3-dimensional ultrasound images from standard 2-dimensional images by using one of three different tracking systems. Two of these systems are approved commercial devices, and one is an experimental, mechanical tracking system developed by Dr. Aaron Fenster's laboratory. All these tracking devices are entirely harmless and simply track the position of the biopsy needle during the biopsy procedure. Which tracking system is used will depend on which one performs the best during biopsy procedures. Each tracking system makes a map of exactly where the biopsy samples were taken in the prostate, so if patients need a repeat biopsy in the future, the doctor will be able to choose different areas to place the biopsy needle. This should improve the chances of finding small tumours that might have been missed during the first biopsy. We think this new method will prove to be easier and more accurate than the current method, which only makes 2-dimensional ultrasound images.

We will also test a further group of 45 patients to check on the amount of deformation of the prostate gland caused by the pressure of the ultrasound transducer during the transrectal ultrasound examination. The procedure will be the same as for the first group, but we will add some extra 3-dimensional ultrasound images at the beginning of the procedure to check the baseline position of the prostate and then again at the end of the procedure to see if the position of the prostate has been pushed from the baseline position by the pressure from the transrectal ultrasound transducer, or if its shape has been otherwise deformed by this same pressure. It is important to know if this is occurring, as this will affect the measurements of the prostate.

RESEARCH PROCEDURES FOR THIS STUDY
The procedure will be the same as for a regular prostate biopsy, but we will take a few extra regular ultrasound images, using one of the tracking devices so they can be made into 3D images. We will then do a real 3-dimensional ultrasound exam, so we can compare it to the one we will make with the tracking device.

The only difference between the regular 2-dimensional and the 3-dimensional ultrasound is that the 3-dimensional exam takes a little longer because the computer takes time to produce the 3-dimensional images. There are no extra visits to the hospital and the research is carried out during your prostate biopsy procedure. The extra time involved for this research study will be about 15 minutes on top of the time for your prostate biopsy, and you will remain in the same position for the 2-dimensional and the 3-dimensional ultrasound examinations. For the group of 45 patients who will have additional 3D ultrasound images to check for movement of the prostate caused by the pressure of the ultrasound probe, this will add a further 10 minutes, for a total of 25 minutes added to the normal prostate biopsy time.

RISKS AND DISCOMFORTS TO YOU IF YOU PARTICIPATE IN THIS STUDY
There are no known risks to the use of ultrasound in this way, and the procedure is completely painless.

ALTERNATIVES TO STUDY PARTICIPATION
The alternative to taking part in this study is to not take part.

THE BENEFITS TO YOU IF YOU PARTICIPATE IN THIS STUDY
There is no evidence that being part of this study will help your treatment, but the results may help future patients, because we believe this new method will give more information on the cancerous areas in the prostate and exactly where they are located. If this research study is successful, it will improve the chances of finding small cancerous tumours if a patient needs repeated biopsies.

CONFIDENTIALTY
Any information obtained from this study will be kept confidential and your name will not be identified in any way when the results are presented or published. The ultrasound images that are taken will be kept in a computer and your name and any other personal information will be made invisible. Any other information from this study will be kept in locked filing cabinets and only the research team and the University of Western Ontario Health Sciences Research Ethics Board (HSREB) will have access to the data. Representatives of HSREB may require access to your study-related records or may follow up with you to monitor the conduct of the study.

VOLUNTARY PARTICIPATION
Your participation in this study is voluntary. You may refuse to participate or withdraw from the study at any time with no effect on your future care.

WHO TO CONTACT IF YOU HAVE ANY QUESTIONS
If you have any questions, please feel free to contact us

If you have a question about your rights as a research participant or about the conduct of this study, you can contact the Vice President of Research c/o Lawson Health Research Institute (LHRI).

If you are already participating in another research study, please inform Dr. Izawa.

Please Note: You do not waive any legal rights by signing the consent form.
You will be given a copy of this letter of information and consent form to keep once it has been signed.

Version 6 June 4th 2008

London Health Sciences Centre

Consent Form for Participation

Title of Study: An Improved Transrectal Ultrasound-guided Biopsy Procedure

Investigators:
Drs. Jonathan I. Izawa, Joseph L. Chin, Aaron Fenster, and Cesare Romagnoli

I have read the letter of information, have had the nature of the study explained to me and I agree to participate. All questions have been answered to my satisfaction.

Dated in London, this__________day of_______________, 20____

______________________________	______________________________
(Signature of Participant)	(Print name of Participant)
______________________________	______________________________
(Signature of Researcher)	(Print name of Researcher)
______________________________	______________________________
(Signature of Person Obtaining the Consent of the Participant)	(Print name of Person Obtaining the Consent of the Participant)

____
Patient Initials

Office of Research Ethics

The University of Western Ontario

Western

Use of Human Subjects - Ethics Approval Notice

Principal Investigator: Dr. J.I. Izawa
Review Number: **12669** **Revision Number:** **3**
Review Date: June 17, 2008 **Review Level:** Full Board
Protocol Title: An Improved Transrectal Ultrasound-guided Biopsy Procedure
Department and Institution: Urology, London Health Sciences Centre
Sponsor: CIHR-CANADIAN INSTITUTE OF HEALTH RESEARCH
Ethics Approval Date: June 17, 2008 **Expiry Date:** December 31, 2009
Documents Reviewed and Approved: Increase in number of participants, revised study methodology, and revised letter of information & consent form dated June 4/08
Documents Received for Information:

This is to notify you that The University of Western Ontario Research Ethics Board for Health Sciences Research Involving Human Subjects (HSREB) which is organized and operates according to the Tri-Council Policy Statement: Ethical Conduct of Research Involving Humans and the Health Canada/ICH Good Clinical Practice Practices: Consolidated Guidelines; and the applicable laws and regulations of Ontario has reviewed and granted approval to the above referenced revision(s) or amendment(s) on the approval date noted above. The membership of this REB also complies with the membership requirements for REB's as defined in Division 5 of the Food and Drug Regulations.

The ethics approval for this study shall remain valid until the expiry date noted above assuming timely and acceptable responses to the HSREB's periodic requests for surveillance and monitoring information. If you require an updated approval notice prior to that time you must request it using the UWO Updated Approval Request Form.

During the course of the research, no deviations from, or changes to, the protocol or consent form may be initiated without prior written approval from the HSREB except when necessary to eliminate immediate hazards to the subject or when the change(s) involve only logistical or administrative aspects of the study (e.g. change of monitor, telephone number). Expedited review of minor change(s) in ongoing studies will be considered. Subjects must receive a copy of the signed information/consent documentation.

Investigators must promptly also report to the HSREB:

a) changes increasing the risk to the participant(s) and/or affecting significantly the conduct of the study;
b) all adverse and unexpected experiences or events that are both serious and unexpected;
c) new information that may adversely affect the safety of the subjects or the conduct of the study.

If these changes/adverse events require a change to the information/consent documentation, and/or recruitment advertisement, the newly revised information/consent documentation, and/or advertisement, must be submitted to this office for approval.

Members of the HSREB who are named as investigators in research studies, or declare a conflict of interest, do not participate in discussion related to, nor vote on, such studies when they are presented to the HSREB.

Chair of HSREB: Dr. John W. McDonald

robarts
RESEARCH

To: Research Ethics Board **Date:** June 4, 2008

From: Jackie Williams

Re: UWO Ethics Number 12669

Project Title: An Improved Transrectal Ultrasound-guided Biopsy Procedure

PI: Dr. Jonathan Izawa

Co-Investigators:
Dr. Joseph L. Chin, Dr. Aaron Fenster

Revision to Original Protocol

Addition of Study Staff:

We would like to add a summer student, Vaishaly Karnak, to the list of collaborators. Ms. Karnak will assist Derek Cool, a doctoral student in gathering the images and in the analysis of data for the study.

Study Design or Methods:

We would like to extend this study by testing a further 45 patients (to the original 45) to check on the amount of deformation of the prostate gland caused by the pressure of the ultrasound transducer during the transrectal ultrasound examination. We will follow the original protocol on this new set of 45 patients who are already scheduled for prostate biopsy, but will add some extra 3-dimensional ultrasound images at the beginning of the procedure to check the baseline position of the prostate and then again at the end of the procedure to see if the position of the prostate has been pushed from the baseline position by the pressure from the transrectal ultrasound transducer, or if its shape has been otherwise deformed by this same pressure. It is important to know if this is occurring, as this will affect the results. This will not change the study end date of this project.

Changes to the Letter of Information

We have added the changes in the Letter of Information.

Version 7, March 1st 2010

LETTER OF INFORMATION FOR PARTICIPANTS

Title of Study: Hybrid Imaging for Prostate Biopsy Guidance

Principal Investigator: Dr. Jonathan Izawa

Co-Investigators:
Dr. Joseph L. Chin, Dr. Robert Bartha, Dr. Aaron Fenster, Dr. Cesare Romagnoli, and Dr. Charles McKenzie.

INTRODUCTION

You are being invited to participate in a research study, which is for men who have been scheduled for a prostate biopsy for suspected prostate cancer. That surgical procedure will be fully explained by Dr. Izawa and you will be able to ask him or his staff any questions. If successful, these new techniques will make small cancerous areas in the prostate easier to see, reducing the need for successive prostate biopsies, and allowing prostate cancer to be detected earlier than is possible at the present time.

PURPOSE

The research procedures for this study will be carried out at the Robarts Research Institute, which is located right next to London Health Sciences Centre, University Hospital. For this research, we are studying the different prostate regions involved in cancer using an advanced method of magnetic resonance imaging (MRI). The overall purpose of this study is to see if MRI will show areas of the prostate that exhibit metabolic changes due to cancer activity, helping to guide where to insert the biopsy needle to diagnose prostate cancer and pinpointing where the highest Gleason Grade cancer is most likely to be located. This study will use a similar machine that is used in regular MRI for patients, but we are using a higher magnetic field strength. MRI is thought to have good potential in diagnosing prostate cancer because it can show changes in the chemical activity of the prostate that are associated with prostate cancer. MRI is non-invasive tool that we believe will be able to: 1) detect cancer outside the gland, 2) detect specific areas within the prostate that contain cancer, 3) determine the aggressiveness of the cancer, and 4) direct the biopsy and treatment specifically to diseased areas. These changes are particularly noticeable at higher MRI field strengths, which is why we will be using a 3 Tesla (3T) scanner, which is twice the strength of the standard diagnostic 1.5 Tesla MRI. For the MRI scan we will also be using a contrast agent called Magnevist®, which will be injected into a vein in your arm. This contrast agent travels through the blood vessels, including the ones in the prostate gland, and makes the MRI images clearer. We hope the addition of contrast agent will make any small cancerous areas in the prostate easier to see.

We will also be using a 3-dimensional ultrasound exam in this study. The 3-dimensional images will be compared to the MRI scan to see if the abnormal areas in the prostate as shown by MRI also look abnormal on the ultrasound scan, and if any particular characteristics can be recognized. The results from the 3-dimensional ultrasound will also be compared to the regular pathology results after your prostatectomy surgery for the same purpose.

RESEARCH PROCEDURES FOR THIS STUDY

Participation in this study requires one visit that lasts about 2 hours. If you agree to take part, before you can be admitted into the study you will need to have a blood test to check your kidney function, and to screen you for certain types of anemia. This is to make sure it is safe for you to have an injection of a contrast agent during the study. The blood test will take place approximately 6 weeks before the study session. Your doctor (either Dr. Chin or Dr. Izawa) will ask you to attend their clinic to have two tubes (10 mls) of blood drawn. If your blood tests are normal, you will be asked to come to the Robarts Research Institute for the study session.

You will have an MRI scan inside the 3 Tesla scanner. Just before you go into the scanner, you will have an intravenous catheter (a tiny plastic tube) inserted into a vein in your arm, so that the contrast agent (dye) called Gd-DTPA (Magnevist®) can be injected into your vein. The contrast agent does not stay in your body, and it is completely cleared out through the urine within 48 hours. The scheduling of the MRI examination will depend on the times we are able to book the MRI scanner. The evening before the study you should take 30 mls of Milk of Magnesia, an over the counter laxative that will be provided to you. Just before the scan you will be given Buscopan (20mgs), which will be injected through the same catheter as the contrast agent. Buscopan is an approved antispasmodic that will minimize involuntary movements of your bowel or rectum during the scanning process. This is an approved drug commonly used during MRI procedures.

To reduce any discomfort, the doctor performing your prostate biopsy will apply Lidocaine gel, which is a topical anesthetic to the endorectal probe, and to your rectum. Then, you will have a small oval MRI endorectal probe inserted into your rectum, so it will lie close to the prostate gland. This probe picks up the MRI signal to give a very clear picture of the prostate gland.

This MRI machine uses a strong magnet and radio waves to make images of the body interior. You will be asked to lie on a long narrow couch for about an hour and a half while the machine gathers data. During this time you will be exposed to magnetic fields and radio waves. You will not feel either. You will, however, hear repetitive tapping noises that arise from the magnets that surround you. You will be provided with earplugs or headphones that you will be required to wear to minimize the sound and protect your hearing. The space within the large magnet in which you lie is somewhat confined, although we have taken many steps to relieve the "claustrophobic" feeling. There are no known significant risks with this procedure at this time because the radio waves and magnetic fields, at the strengths used, are thought to be without harm. The exception is if you have a cardiac pacemaker or a metallic clip in your body (e.g., an aneurysm clip in your brain), have severe heart disease, body piercings, tattoos containing metallic ink or slow release pharmaceutical skin patches.

There is a possibility that you will experience a localized twitching sensation due to the magnetic field changes during the scan. This is not unexpected and should not be painful. However, you can stop the exam at anytime. The magnetism and radio waves do not cause harmful effects at the levels used in the MRI machine. However, because the MR scanner uses a very strong magnet that will attract metal, all metallic objects must be removed from your person before you approach the scanner. In addition, watches and credit cards should also be removed as these could be damaged. (These items will be watched for you).

During your prostate biopsy you will also have a 3-dimensional ultrasound scan. This is the same as a regular ultrasound scan, except it takes a few minutes longer. The images from this 3D ultrasound exam will be combined with the MRI images and used to more precisely target the needle placement during the biopsy.

REASONS THAT MUST EXCLUDE YOU FROM THIS STUDY

MRI exclusion criteria

If you have any history of head or eye injury involving metal fragments, if you have some type of implanted electrical device (such as a cardiac pacemaker), if you have severe heart disease (including susceptibility to heart rhythm abnormalities), you should not have an MRI scan unless supervised by a physician. Additionally you should not have a MRI scan if you have conductive implants or devices such as skin patches, body piercing or tattoos containing metallic inks because there is a risk of heating or induction of electrical currents within the metal element causing burns to adjacent tissue.

Other reasons that must exclude you from this study are:

1. a known allergy to Magnevist,
2. sickle cell disease or other hemolytic anemias,
3. kidney disease.

THE LENGTH OF THIS STUDY AND HOW MANY PEOPLE WILL BE ENROLLED

We will be enrolling 75 men who are scheduled for prostate biopsy, including men who have already had one or more prostate biopsies, but whose pathology findings were normal from the previous biopsies, as well as men undergoing a first prostate biopsy. We will also be enrolling 20 other men whose pathology findings showed some prostate cell abnormalities that were not cancer cells, but which are thought to increase the risk of developing prostate cancer in the future. We will enroll these men over a period of about two years, and all of whom will be at this centre in London, Ontario. In total, there will be 95 men enrolled in this study.

RISKS AND DISCOMFORTS TO YOU IF YOU PARTICIPATE IN THIS STUDY
Part of your participation in this study will involve a research test with Magnetic Resonance Imaging (MRI) system, a common medical diagnostic tool that uses a strong magnetic field, a low frequency magnetic field, and a radio frequency field. No X-rays are used. As with any technology there is a risk of death or injury. For MRI the risk of death is less than 1 in 10 million and the risk of injury is less than 1 in 100,000. These risks do not arise from the MRI process itself, but from a failure to disclose or detect MRI incompatible objects in or around the body of the subject or the scanner room. It is therefore very important that you answer all the questions honestly and fully on the MRI screening questionnaire.

Almost all the deaths and injuries related to MRI scans have occurred because the MRI operator did not know that surgically implanted metal hardware (such as a cardiac pacemaker) was present inside the subject during the MRI scan. Other remote risks involve temporary hearing loss from the loud noise inside the magnet. This can be avoided with ear headphone protection that also allows continuous communication between the subject and staff during the scan.

For comparison, the risk of death in an MRI is similar to travelling 10 miles by car, while the risk of injury during an MRI is much less than the risks associated with normal daily activities for 1 hour.

You may not be allowed to continue in this research study if you are unable to have a MRI scan because, for example, you have some MRI incompatible metal in your body, you may be pregnant or attempting to become pregnant, or you may have a drug patch on your skin that contains a metal foil. Should you require a medically necessary MRI scan in the future, the final decision as to whether you can be scanned will be made by a qualified physician considering all the risks and benefits.

For the injection of contrast agent, there may be some mild discomfort or bruising at the intravenous or blood draw site with a minimal risk of local infection. The most common adverse events are headache (~5%), nausea (~3%), injection site coldness (~2%) and dizziness (~2%). Most headaches are transient and mild to moderate. Serious adverse reactions (e.g. anaphylaxis) occur at a rate of about 7/5,000,000.

Hemolysis (a breakdown of blood cells) has been reported following contrast agent administration in patients who have sickle cell disease, and in patients who have anemia (low red blood count). You will have a blood test prior to the study to make sure you do not have these conditions, and you will not be allowed to participate in this study if that is the case. Other side effects of the contrast agent are extremely rare but include nausea, a tingling sensation, headache, rash, and dizziness.

The risks and discomforts associated with the injection of Buscopan include dry mouth, dyshidrosis (a form of skin blisters), visual accommodation disorders (blurred vision), tachycardia (rapid heartbeat), dyspnea (shortness of breath), diarrhea, nausea, retinal pigmentation (abnormal colouring of the retina, which is the inner back wall of the eye), glaucoma and urinary retention. There have been rare reports of dizziness, decreased blood pressure and flushing. Skin reactions and other hypersensitivity, angioedema (swelling, similar to hives) and fixed drug eruptions (rash associated with injection site) have been reported rarely. There have been very rare reports of anaphylactic reactions and anaphylactic shock. Buscopan may cause blurred vision which may affect your ability to drive or operate machinery safely, and so we recommend that you bring someone with you to the study who will be able to drive you home afterwards, as if you are affected with blurred vision you should not drive or operate machinery.

You should consult your doctor immediately if you experience any of the following while after the Buscopan injection: red and painful eye, possibly with headache, loss of vision or blurred vision, or seeing haloes around lights. These symptoms may be caused by an increase in pressure inside the eyeball and require urgent investigation by your doctor.

The application of topical local anesthesia gel, Lidocaine, and its possible minor absorption through the rectal mucosa causes side effects very rarely. Signs of too much topical Lidocaine being absorbed into the body include blurred or double vision, dizziness, light-headedness, drowsiness, muscle twitching, trembling, nausea, vomiting, or feelings of hot, cold, or numbness in the rectal area.

There are no known risks to the use of ultrasound as it is used in this study and the procedure is completely painless.

ALTERNATIVES TO STUDY PARTICIPATION

The alternative to taking part in this study is to not take part. This will have no effect on your future care.

THE BENEFITS TO YOU IF YOU PARTICIPATE IN THIS STUDY

There is no evidence that being part of this study will help your treatment, but the results may help future patients, because we believe the MRI examination may tell us more definitely if there are cancerous areas in the prostate and exactly where they are located. If this research study is successful, we may be able to perfect the technique, and this may mean that patients in the future may not require repeated biopsies to check for cancer.

CONFIDENTIALTY

Any information obtained from this study will be kept confidential and your name will not be identified in any way when the results are presented or published. The information from this study will be kept in locked filing cabinets and only the research team will have access to the data, however, representatives of The University of Western Ontario Health Sciences Research Ethics Board may contact you, or require access to your study-related records to monitor the conduct of the research.

WHAT TO DO IF YOU WANT TO WITHDRAW FROM THIS STUDY
Your participation in this study is voluntary. You may refuse to participate, refuse to answer any questions, or withdraw from the study at any time with no effect on your future care. You will be reimbursed $30 for your participation in this study to cover any travel or parking costs.

WHO TO CONTACT IF YOU HAVE ANY QUESTIONS
If you have any questions about this study, please feel free to contact:
Dr. Jonathan Izawa

If you are participating in another research study, please inform Dr. Izawa.

If you have a question about your rights as a research participant or about the conduct of this study, you can contact Dr. David Hill, Scientific Director, Lawson Health Research Institute

Please Note: You do not waive any legal rights by signing the consent form.
You will be given a copy of this letter of information and consent form once it has been signed.

____
Patient Initials

robarts
IMAGING

Version 7, March 1st 2010

Consent Form for Participation

Title of Study: Hybrid Imaging for Prostate Biopsy Guidance

Investigators:
Dr. Jonathan Izawa, Dr. Joseph L. Chin, Dr. Robert Bartha, Dr. Aaron Fenster, Dr. Cesare Romagnoli and Dr. Charles McKenzie.

I have read the letter of information, have had the nature of the study explained to me and I agree to participate. All questions have been answered to my satisfaction.

Dated in London, this__________day of________________, 20____

______________________________	______________________________
(Signature of Participant)	(Print name of Participant)

____
(Signature of Researcher)

______________________________	______________________________
(Signature of Person Obtaining the Consent of the Participant)	(Print name of Person Obtaining the Consent of the Participant)

Appendix E: Health Canada and Ethics Approval Notice for the clinical prostate therapy study.

Therapeutic Products Directorate

Health Canada | Santé Canada

Health Products and Food Branch | Direction générale des produits de santé et des aliments

DATE: JUL 0 7 2011

Application No. 178857

Chandima Edirisinghe

Investigational Testing Authorization - Class II

Dear Chandima Edirisinghe:

This is in reference to your application for Authorization to conduct Investigational Testing in Canada, received on 10 March 2011, and submitted pursuant to Part 3 of the *Medical Devices Regulations*. This pertains to the following:

Protocol: An Improved Prostate Imaging and Cancer Treatment Procedure
Objectives: (1) To determine the accuracy improvement to the treatment delivery using 3-dimensional imaging
(2) To determine the effectiveness of the intra-operative delivery adjustment to compensate for prostate movement, and
(3) To determine whether only ultrasound imaging can be used throughout the procedure and instead of combination of CT imaging and ultrasound imaging.
(4) To determine whether better delivery can be done using the flexibility of the non-template mechanical device.
Device: "3D Ultrasound Prostate Imaging and Cancer Treatment Planning System"
No. of devices: One (1)
No. of subjects: Ten (10)

The information has been reviewed and you are hereby authorized under Section 83 of the *Medical Devices Regulations* to sell the subject device for investigational testing to the institution(s) listed in the attached Appendix 1.

Sections 86, 87 and 88 of the *Medical Devices Regulations* impose additional requirements regarding the advertisement, record keeping and labelling of devices involved in investigational trials. Please advise the Bureau of any changes to the device, protocol or list of investigators. Any changes to the device or protocol that fall outside the scope of the risk assessment of this protocol will require a new application.

Yours sincerely,

Medical Devices Bureau

RGR/mw
Attach.

Canada

Appendix 1 - List of Investigator(s) and Institution(s) **Application No. 178857**

Date: JUL 0 7 2011

Dr. David D'Souza

Research
Western

Use of Human Participants - Ethics Approval Notice

Principal Investigator: Dr. David D'Souza
Review Number: 18147
Review Level: Full Board
Approved Local Adult Participants: 10
Approved Local Minor Participants: 0
Protocol Title: Mechatronic assisted 3D transrectal ultrasound guided adaptive prostate brachytherapy
Department & Institution: Oncology,London Health Sciences Centre
Sponsor: Ontario Institute for Cancer Research "1mm challenge"

Ethics Approval Date: September 07, 2011 **Expiry Date:** December 31, 2013

Documents Reviewed & Approved & Documents Received for Information:

Document Name	Comments	Version Date
UWO Protocol		
Letter of Information & Consent		2011/08/15

This is to notify you that the University of Western Ontario Health Sciences Research Ethics Board (HSREB) which is organized and operates according to the Tri-Council Policy Statement: Ethical Conduct of Research Involving Humans and the Health Canada/ICH Good Clinical Practice Practices: Consolidated Guidelines; and the applicable laws and regulations of Ontario has reviewed and granted approval to the above referenced study on the approval date noted above. The membership of this HSREB also complies with the membership requirements for REB's as defined in Division 5 of the Food and Drug Regulations.

The ethics approval for this study shall remain valid until the expiry date noted above assuming timely and acceptable responses to the HSREB's periodic requests for surveillance and monitoring information. If you require an updated approval notice prior to that time you must request it using the UWO Updated Approval Request form.

Member of the HSREB that are named as investigators in research studies, or declare a conflict of interest, do not participate in discussions related to, nor vote on, such studies when they are presented to the HSREB.

The Chair of the HSREB is Dr. Joseph Gilbert.

The **University** ***of*** **Western Ontario**
Office of Research Ethics

Appendix F: Copyright Release

Hi Jeffrey,

Thank you for your email. Yes, you may have permission to reprint the two articles for your PhD thesis.

Penny Slattery
Journal Manager

I am seeking permission to reprint the following two articles that were published in the Medical Physics journal into my PhD thesis:

1) Jeffrey Bax, Derek Cool, Lori Gardi, Kerry Knight, David Smith, Jacques Montreuil, Shi Sherebrin, Cesare Romagnoli, Aaron Fenster, "Mechanically Assisted 3D Ultrasound Guided Prostate Biopsy System", Med Phys., vol 35, no 12, pp 5397-5410, 2008.

2) Jeffrey Bax, David Smith, Laura Bartha, Jacques Montreuil, Shi Sherebrin, Lori Gardi, Chandima Edirisinghi, Aaron Fenster, "A Compact Mechatronic System for 3D Guided Prostate Interventions", Med Phys., vol 38, no 2, pp 1055-69, 2011.

Sincerely,

Jeffrey Bax

Curriculum Vitae

Jeffery S. Bax

Academic Background

2006 – Present **The University of Western Ontario**
London, Ontario
- PhD Candidate: Biomedical Engineering program.

1989 – 1994 **The University of Western Ontario**
London, Ontario
- BESc in Mechanical-Manufacturing Engineering
- Completed 51 courses in mechanical engineering design, advanced mathematics, thermodynamics, industrial engineering and communications.

1995 - 2000 **Fanshawe College**
London, Ontario
- Completed 32 courses in machine shop, metallurgy, welding, computer networking and programming (C++).

1987 – 1988 **Aero Academy Inc.**
London, Ontario
- Canadian Private Pilot License.

Honors and Awards

Graduate studies

2008 – Present	Alexander Graham Bell Canada Graduate Scholarship (CGS)
2007 – 2008	NSERC PGS-M
2006 – Present	Western Graduate Research Scholarship
2006 – 2007	Ontario Graduate Scholarship in Science and Technology

Undergraduate studies

1994	NSERC Undergraduate Research Award
1992 – 1993	Faculty Association Award, University of Western Ontario
1990 – 1994	Dean’s Honor List
1990	APEO Scholarship
1989 – 1993	Canada Scholarship
1989	UWO Entrance Scholarship
	Bell Canada Award
	Ontario Scholarship

Refereed Publications

- Ryu B, **Bax J**, Edirisinge C, Lewis C, Chen J, D'Souza D, Fenster A, Wong E. Prostate brachytherapy with oblique needles to treat large glands and overcome pubic arch interference. International Journal of Radiation Oncology • Biology • Physics (IJROBP). Under Review.
- Karnik V V, Fenster A, **Bax J**, Romagnoli C, Ward AD. *Evaluation of Intersession 3D-TRUS to 3D-TRUS Image Registration for Repeat Prostate Biopsies*. Med Phys. In Press.
- De Silva T, Fenster A, **Bax J,** Romagnoli C, Izawa J, Samarabandu J, Ward A. *Quantification of prostate deformation due to needle insertion during TRUS-guided biopsy: Comparison of hand-held and mechanically stabilized systems.* Med Phys. In press.
- **Bax J**, Smith D, Bartha L, Montreuil J, Sherebrin S, Gardi L, Edirisinghe C, Fenster A. *A Compact Mechatronic System for 3D Ultrasound Guided Prostate Interventions*. Med Phys. 2011 Feb; 38(2):1055-69.
- Karnik V V, Fenster A, **Bax J**, Cool DW, Gardi L, Gyacskov I, Romagnoli C, Ward AD. *Assessment of image registration accuracy in three-dimensional transrectal ultrasound guided prostate biopsy*. Med Phys. 2010 Feb; 37(2):802-13.
- Thakur Y, **Bax JS**, Holdsworth DW, Drangova M.*Design and performance evaluation of a remote catheter navigation system*. IEEE Trans Biomed Eng. 2009 Jul; 56(7):1901-8.
- Ma K, Kornecki A, **Bax J**, Mundt Y, Fenster A. *Development and validation of a new guidance device for lateral approach stereotactic breast biopsy*. Med Phys. 2009 Jun; 36(6):2118-29.
- **Bax J**, Cool D, Gardi L, Knight K, Smith D, Montreuil J, Sherebrin S, Romagnoli C, Fenster A. *Mechanically assisted 3D ultrasound guided prostate biopsy system*. Med Phys. 2008 Dec;35(12):5397-410.
- **Bax J,** Wehlau W, Sharpe S. *Another Look at the Delta Scuti Star FM Comae*. The Journal of the Royal Astronomical Society of Canada. 1995 89(6): 245-56.

Conference Abstracts /Proceedings

- De Silva T, **Bax J**, Fenster A, Samarabandu J, Ward A, *Quantification of prostate deformation due to needle insertion during TRUS-guided biopsy: comparison of hand-held and mechanically stabilized systems.* Proceedings of the SPIE International Symposium on Medical Imaging, Orlando, FL: Vol. 6918, February 12-15, 2011: 7968-29, Oral.
- **Bax J,** Gardi L, Montreuil J, Smith D, Fenster A. *A Compact Mechatronic System for 3-D Ultrasound Guided Prostate Interventions*. OICR Annual Scientific Meeting, Imaging Commercialization Session, February 09-11, 2011, Invited talk.
- Karnik V, Fenster A, **Bax J**, Gardi L, Gyacskov I, Montreuil J, Romagnoli C, Ward A. *Evaluation of inter-session 3D-TRUS to 3D-TRUS image registration for repeat prostate biopsies*. MICCAI 2010 Proceedings, Poster
- Waring C, **Bax J**, Montreuil J, Lacefield J, Fenster A. *3D Image-Guided Robotic Needle Positioning System for Small Animal Interventions.* Proc of the Imaging Network of Ontario Annual Imaging Symposium (ImNO), Toronto, ON: 2010, Poster.

- **Bax J,** Williams J, Cool D, Gardi L, Montreuil J, Karnik V, Sherebrin S, Romagnoli C, Fenster A. *Mechanically Assisted 3D Prostate Ultrasound Imaging and Biopsy System*. Proceedings of the SPIE International Symposium on Medical Imaging, San Diego, CA: Vol. 7625, February 14-16, 2010, Poster.
- Karnik V, Ward AD, **Bax J**, Cool DW, Gardi L, Gyacskov I, Romagnoli C, Fenster A. *Assessment of Image Registration Accuracy in Three-Dimensional Transrectal Ultrasound Guided Prostate Biopsy*. American Institute for Ultrasound in Medicine (AIUM) Proceedings, San Diego, CA: Abstract # 730552, 2010, Oral.
- Karnik V, Ward A, **Bax J**, Cool DW, Gardi L, Gyacskov I, Romagnoli C, Fenster A. *Assessment of Registration Accuracy in Three Dimensional Transrectal Ultrasound Images of Prostates*. American Association of Physicists in Medicine (AAPM). Anaheim, CA. 2009, Oral.
- **Bax J,** *Clinical Evaluation of a Mechanically Assisted 3D Prostate Ultrasound Imaging and Biopsy System* Proc of the Imaging Network of Ontario 7th Annual Imaging Symposium (ImNO), Toronto, ON: Sept 29-Oct 1, 2008, Invited talk.
- Karnik V, Bax J, Cool DW, Gardi L, Gyacskov I, Romagnoli C, Fenster A. *Assessment of Registration Accuracy in 3D Transrectal Ultrasound Images of Prostate Biopsies: Comparison of Rigid and Non-Rigid Registration.* Proc of the Imaging Network of Ontario 7th Annual Imaging Symposium (ImNO), Toronto, ON: Sept 29-Oct 1, 2008, Poster.
- Ma K, Fenster A, Kornecki A, Mundt Y, **Bax J**. A new lateral guidance device for stereotactic breast biopsy using an add-on unit to an upright mammography system. Conf Proc IEEE Eng Med Biol Soc. 2008: 3653-6, Oral.
- **Bax J**,Cool J,Gardi L, Montreuil J, Gil E, Bluvol J, Knight K, Smith D, Romagnoli C, Fenster A. *3D Transrectal Ultrasound Prostate Biopsy using a Mechanical Imaging and Needle-Guidance System.* Proceedings of the SPIE International Symposium on Medical Imaging, San Diego, CA: Vol. 6918, February 17-19, 2008: 6918, Poster.
- **Bax J,** Gardi L, Montreuil J, Smith D, Fenster A. *A Compact Robotic Apparatus and Method for 3-D Ultrasound Guided Prostate Therapy*. Proceedings of the SPIE International Symposium on Medical Imaging, San Diego, CA: Vol. 6509-88, February 17-22, 2007, Poster.
- **Bax J,** Wehlau W, Sharpe S. *Another Look at the Delta Scuti Star FM Comae*. Conference abstract, CASCA, The University of Western Ontario, London, ON, May 1994, Poster.

Patents

- **Bax J,** Gardi L, Montreuil J, Smith D, Fenster A. *Apparatus and Method for Guiding the Insertion of a Medical Tool.* US. Application No. US11/427,121: Filed June 28, 2006. (Pending)
- **Bax J,** Cool D, Gardi L, Fenster A. *Apparatus for guiding medical tools*. International Application under the Patent Cooperation Treaty Application No. WO 2007/147232 A1: Filed June 19, 2007. (Pending)
- **Bax J**, Fenster A. *Counterbalance Assembly*. International Application under the Patent Cooperation Treaty Application No. PCT/CA2008/001716: Filed Sept. 26, 2007. (Pending)

Work Experience

2005 – Present **Robarts Research Institute** London, Ontario

Research Technician

- Develop and support the mechanical design of novel surgical mechatronic systems for cancer diagnosis and therapy.

2004 – 2005 **Clark Robotic Systems Inc.** St. Catharines, Ontario

Contract Engineering Services: Industrial Robotics / Automation

- Design robotic end of arm tooling, and integrate into assembly lines.

2000 – 2005 **Sciencetech Inc.** London, Ontario

Consulting Engineer: Optical Research Equipment / Systems

- Develop optical positioning and tracking systems to withstand the harsh environments encountered in space exploration.

1994 – 2004 **Triad Industries Inc.** London, Ontario

Machine Designer: Special Purpose Industrial Machinery / Equipment

- I was part of a conceptual development / quotation team.
- Mechanical design of high-speed assembly machines, and precision tooling.

1993 – 1995 **UWO Department of Astronomy** London, Ontario

Research Assistant

- Analyzed data from distant stars collected over a period of five years.
- The results were first presented at the CASCA meeting in 1994.